Universidad Autónoma de Nuevo León

FACULTAD DE INGENIERÍA MECÁNICA Y ELÉCTRICA

ALL SPRAY-PYROLYSIS COATED PHOTOVOLTAIC STRUCTURE USING COPPER ANTIMONY SULFIDE ABSORBER AND ZINC OXYSULFIDE WINDOW LAYERS

POR

PAULOSUTTY ABRAHAM

2032336

COMO REQUISITO PARA OBTENER EL GRADO DE

DOCTOR EN INGENIERÍA DE MATERIALES

SEPTIEMBRE 2023

I

UNIVERSIDAD AUTÓNOMA DE NUEVO LEÓN

FACULTAD DE INGENIERÍA MECÁNICA Y ELÉCTRICA

SUBDIRECCIÓN DE ESTUDIOS DE POSGRADO

ALL SPRAY-PYROLYSIS COATED PHOTOVOLTAIC STRUCTURE USING COPPER ANTIMONY SULFIDE ABSORBER AND ZINC OXYSULFIDE WINDOW LAYERS

POR

PAULOSUTTY ABRAHAM
2032336

**COMO REQUISITO PARA OBTENER EL GRADO DE
DOCTOR EN INGENIERÍA DE MATERIALES**

SEPTIEMBRE 2023

CERTIFICATE

UNIVERSIDAD AUTÓNOMA DE NUEVO LEÓN
Facultad de Ingeniería Mecánica y Eléctrica
Posgrado

Los miembros del Comité de Evaluación de Tesis recomendamos que la Tesis "All spray-pyrolysis coated photovoltaic structure using copper antimony sulfide absorber and zinc oxysulfide window layers", realizada por el estudiante Paulosutty Abraham, con número de matrícula 2032336, sea aceptada para su defensa como requisito parcial para obtener el grado de Doctor en Ingeniería de Materiales.

El Comité de Evaluación de Tesis

Dra. Bindu Krishnan
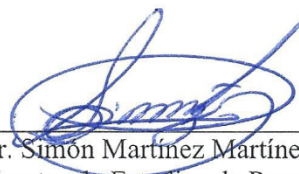Director

Dr. Sadasivan Shaji
Revisor

Dr. David Avellaneda Avellaneda
Revisor

Dra. Shadai Lugo Loredo
Revisor

Dr. Andrés Manuel Garay Tapia
Revisor

Dr. Jorge Oswaldo González Garza
Revisor

Vo.Bo.

Dr. Simón Martínez Martínez
Subdirector de Estudios de Posgrado

Institución _____190001_____

Programa _122608_

Acta Núm. _334_

Ciudad Universitaria, a 15 de Noviembre de 2023.

Dedications

*Mr. **ABRAHAM GEORGE** and Mrs. **ANITHA PAUL***

&

*Mr. **GEORJUTTY ABRAHAM** and Mrs. **SNEHA HARRISON***

Acknowledgements

First of all, I am overwhelmed by the journey of being research scholar, where I have found myself, I never expected to reach. I would like to express my deepest gratitude to a few people and institutions that have made it worth.

I am here quoting a famous recite before I mention few people as it follows like this: If I have seen further, it is by standing upon the shoulder of giants who trod before us.

Dra Bindu Krishnan, my doctoral guide whom I deeply owed for the aid to fulfil my research journey through these years. I am expressing my sincere thankful to her vision, effort and time with guidance and valuable lessons benefited both personal and professional life. Also, I express my profound gratitude to Dr Sadasivan Shaji and Dr David Avellaneda for the full pledge of attention and advice shared throughout these years. Dr. Josue Amilcar Aguilar Martinez, Dr. Selene Sepulveda Guzman and Dr. Edgar Garcia for the help and support for accessing XRD, Raman and SEM equipment. I am deeply thankful to Dr. Simon Martinez Martinez and Dr. Azael Martínez de la Cruz FIME departments heads who have provided immense help for simplifying the administrative procedures.

My sincere thanks to Dr. Manju T, who guided my master's project, providing me with an opportunity to explore the fundamentals of research career and to the professors at Sree Sankara College Kalady, and St Peter's College Kolenchery, India for their support to pursue my goal.

CONTENTS

ABSTRACT

Thin film solar cells play a vital role in the field of photovoltaic applications and energy conversion research. In the current scenario, Si based solar cells face certain limitations such as high production cost, issues with waste disposal and limited resources. These challenges have accelerated the investigation into low cost, nontoxic and earth abundant materials. In this insight, solar cells based on chalcogenides prove better performance due to their tunable optoelectronic properties. While copper indium gallium selenide and Cadmium telluride solar cells reported conversion efficiencies comparable to Si based solar cell, their scarcity of raw materials, toxicity and expensive deposition methods hinder their broader applications. To address these challenges, researchers have explored semiconductors composed of nontoxic constituents and earth abundant elements. Among them, Cu based compounds such as copper zinc tin sulfoselenide (CZTSSe), copper zinc tin sulfide (CZTS) have been investigated recently. However, complex cation stoichiometry and structural polymorphism have limited the PV device performance based on these absorber layers.

In such scenario, copper antimony sulfide chalcogenides exhibit suitable photo physical properties as a potential photovoltaic absorber, near ideal optical band gaps (1.2 - 1.8 eV) with absorption coefficient ($>10^5$ cm^{-1}). Different attempts have been made recently to focus on the low-cost deposition of these films ranging from vapour based methods to solution-based deposition techniques. Additionally, transparent conductive oxides layers play a vital role as window layers in solar cell devices. Mainly, Cd based chalcogenide have been explored for the window layers. Due to Cd toxicity and production wastage of these films, researchers have turned to investigate on natural oxides like ZnO, InO_2, SnO_2. Among them ZnO features nontoxic, earth abundant and easily tunable optoelectronic properties. Sulfur anion substitution in ZnO lattice makes the effort for easy tuning of the optical band gap and electrical properties, helping to solve the major limitation of p-n junction i.e., conduction band offset. Among solution-based deposition techniques, ultrasonic spray pyrolysis deposition is a low cost, large area compatible and low chemical wastage method. Using the application of ultrasonic generator, the solvent is atomized into finely tuned spray droplets directed to heated substrates via carrier gas.

In this thesis, a systematic analysis of structural, chemical, and optoelectronic properties of the window and absorber layers using ultrasonic spray pyrolysis was explored. All films were deposited at ambient condition and exposed to conventional vacuum annealing to enhance the properties of the deposited films. Initially ZnO, Zn (O, S), Sb_2S_3 and copper antimony sulfide thin films were deposited, and various characterization techniques were employed for the analysis. During the deposition highly oriented hexagonal ZnO and Zn (O, S), orthorhombic Sb_2S_3 and two unique phase of copper antimony sulfide: cubic $Cu_{12}Sb_4S_{13}$ and orthorhombic $CuSbS_2$ thin films were successfully deposited. In addition, the theoretical simulation of the respective materials using First principles calculations using density functional theory were employed, including density of states, electronic band diagram, phonon dispersion and optical spectra. Finally, heterojunction devices were fabricated using the ZnO/Zn (O, S) as window layer and copper antimony sulfide absorber layers, all deposited by ultrasonic spray coating, for PV and photodetector applications. The results demonstrate the scope of this thesis in relation to the development of photovoltaic structures and photodetectors using low toxic-materials obtained through a simple, cost-effective large area compatible process.

RESUMEN

Las celdas solares de películas delgadas desempeñan un papel vital en el campo de las aplicaciones fotovoltaicas y la investigación de conversión de energía. En el escenario actual, las celdas solares basadas en Si enfrentan ciertas limitaciones, como el alto costo de producción, problemas con la eliminación de desechos y recursos limitados. Estos retos han acelerado la investigación de materiales de bajo costo, no tóxicos y abundantes en la tierra. En esta idea, las celdas solares basadas en calcogenuros demuestran un mejor rendimiento debido a sus propiedades optoelectrónicas ajustables. Si bien las celdas solares de seleniuro de cobre-indio- galio y telururo de cadmio reportaron eficiencias de conversión comparables a las celdas solares basadas en Si, su escasez de materias primas, toxicidad y costosos métodos de deposición evitan que se tengan mayor aplicación. Para abordar estos retos, los investigadores han explorado semiconductores compuestos de componentes no tóxicos y elementos abundantes en la tierra. Entre ellos, recientemente se han investigado compuestos a base de Cu como sulfoseleniuro de estaño, cobre y zinc (CZTS). Sin embargo, la estequiometría catiónica compleja y el polimorfismo estructural han limitado el rendimiento del dispositivo fotovoltaico basado en estas capas absorbedoras.

En tal escenario, los calcogenuros de sulfuro de antimonio de cobre exhiben propiedades fotofísicas adecuadas como un potencial material absorbedor fotovoltaico, tales como una brecha de energía ideal (1.2 - 1.8 eV), y un alto coeficiente de absorción óptica ($>10^5$ cm^{-1}). Recientemente se han hecho diferentes intentos para centrarse en la deposición de bajo costo de estas películas que van desde métodos basados en vapor hasta técnicas de deposición basadas en soluciones. Además, las capas transparentes de óxidos conductores desempeñan un papel vital como capas de ventanas en dispositivos de celdas solares. Principalmente, se han explorado calcogenuros basados en Cd para las capas de ventanas. Debido a la toxicidad del Cd y el desperdicio de producción de estas películas, los investigadores han recurrido a la investigación de óxidos naturales como ZnO, InO$_2$, SnO$_2$. Entre ellos, el ZnO presenta buenas propiedades optoelectronicas que son facilmente ajustables, ademas de abundancia en la tierra y baja toxicidad de sus elementos precursores.

. La sustitución de aniones de azufre en la red de ZnO hace el esfuerzo para facilitar el ajuste de la banda prohibida óptica y las propiedades eléctricas, ayudando a resolver la limitación principal de la unión pn, es decir, el desplazamiento de la banda de conducción.

Entre las técnicas de deposición basadas en soluciones, la deposición por pirólisis por pulverización ultrasónica es un método de bajo costo, compatible con grandes áreas ademas de que es un método de bajos residuos químicos. Usando la aplicación de un generador ultrasónico, el solvente se atomiza en gotas de pulverización finamente ajustadas dirigidas a sustratos calentados a través de gas portador.

En esta tesis, se ha sintetizado un análisis sistemático de las propiedades estructurales, químicas y optoelectrónicas de las capas ventana y absorbedor mediante pirólisis por pulverización ultrasónica. Todas las películas se depositaron en condiciones ambientales y se fueron sometidas a tratamientos térmicos en vacío para mejorar las propiedades de las películas depositadas. Inicialmente se depositaron películas delgadas de ZnO, Zn (O, S), Sb_2S_3 y sulfuro de antimonio y cobre, y se emplearon diversas técnicas de caracterización para el análisis. Durante la deposición hexagonal altamente orientada de peliculas delgadas de ZnO y Zn (O, S), se depositaron con éxito películas delgadas ortorrómbicas Sb_2S_3 y dos fases únicas de sulfuro de antimonio de cobre: $Cu_{12}Sb_4S_{13}$ cúbico y $CuSbS_2$ ortorrómbico. Además, se empleó la simulación teórica de los respectivos materiales utilizando cálculos de los primeros principios utilizando la teoría del funcional de la densidad, incluida la densidad de estados, el diagrama de bandas electrónicas, la dispersión de fonones y los espectros ópticos. Finalmente, los dispositivos de heterounión se fabricaron utilizando el ZnO / Zn (O, S) como capa de ventana y capas absorbedoras de sulfuro de antimonio y cobre, todas depositadas por recubrimiento por pulverización ultrasónica, para aplicaciones fotovoltaicas y fotodetectores. Los resultados demuestran el alcance de esta tesis en relación con el desarrollo de estructuras fotovoltaicas y fotodetectores utilizando materiales de baja toxicidad obtenidos a través de un proceso sencillo, de bajo costo y compatible para realizar en grandes áreas.

LIST OF FIGURES

LIST OF TABLES

ABBREVIATIONS

a-Si: Amorphous Si

BE: Binding energy

CBM: Conduction band minimum

CdTe: Cadmium telluride

CIGS: copper indium gallium selenide

CZTS: Copper zinc tin sulfide

EDS: Energy Dispersive X-Ray Spectroscopy

FF: Fill factor

FTO: Fluorine doped tin oxide

JCPDS: Joint Committee on Powder Diffraction Standards

Jsc: Short circuit current density

J-V: Current density: voltage

PCE: Power conversion efficiency

PV: Photovoltaics

Sb_2S_3: Antimony sulfide

SCAPS-1D: Solar Cell Capacitance Simulator-1 dimensional software

SEM: Scanning Electron Microscopy

TCO: Transparent conductive oxide

UV-Vis-NIR: Ultraviolet-Visible-Near Infra Red

VASP: Vienna Ab-initio Simulation Package

Voc: Open circuit voltage

W-H: Williamson- Hall

XPS: X-Ray Photoelectron Spectroscopy

XRD: X-Ray diffraction

Chapter 1

Thin Film Solar Cells

1.1. Introduction

Energy harnessing is a set of processes in which energy is converted from environmental or mechanical sources to usable forms such as electrical energy. Mainly, the sources are divided into two categories: non-renewable (exhaustible and polluting) and renewable (inexhaustible and non-polluting) resources. According to research, the consumption of resources has a severe impact on economic growth, but polluting emissions do pose a threat to nature. At the same time, overconsumption and the prolonged reliability of natural resources affect the economy's status [1]. The solution to this problem is the replacement of non-renewable resources with renewable sources. The major renewable resources are solar, wind, hydropower, tidal, geothermal, and biomass energies. The energy from these sources is either used directly or stored in a storage device. Energy harnessing using photovoltaics is a single-step conversion process to generate electrical energy from solar radiation.

1.2. Photovoltaics

 The mechanism includes the following steps:

- The radiation is being absorbed by a material (absorbers), which excites the material from its ground state to its excited state, creating electron-hole pairs.
- The electron-hole pairs are swept in different directions because of the charge diffusion.
- The photogenerated holes and electrons at two collecting electrodes dissipating energy at a load.
- The combination of a negative-positive charge pair at the anode returns the absorber to the ground state.

The incident photons from the sun can be mapped in a solar spectrum depending on latitude, atmospheric conditions, the position of the earth (apogee and perigee), wavelength etc.

1.3. History of photovoltaics

Light – electric current conversion basically defined by photovoltaic effect was observed by French physicist Alexandre Edmond Becquerel in 1839, while experimenting an electrolyte

and metal electrode. He observed a spike in the conductance under illumination. Later 1873, Willoughby Smith recorded selenium can be effectively utilized to convert illuminated radiation to electric current. The most intriguing part comes after the discovery of William G Adams illuminating a junction with selenium and platinum, recorded better performance than from predecessors. Amongst all the discoveries, the generation of charge carrier from photons was well achieved on the material defined as semiconductors. When a light illuminated on a semiconductor with appropriate optical band gap, the radiation is absorbed by the material and converted to charge carriers, finally extracted to external contacts.

The most intriguing part of semiconductor component production is the material used in manufacturing. Silicon (Si), an elemental semiconductor that is abundant, cheap, and nontoxic. Si possesses an optical band gap of 1.12 eV, and its electrical conductivity could be tailored by the doping process. The thermal conductivity value proves that Si is an adequate material to transfer heat generated inside the circuits. The feasibility of engineering silicon films to possess various electrical properties helps them to integrate, providing isolation and lower capacitance in Integrated chips (ICs). Natural silicon crystals were melted, purified to 99.999999999% purity, and finally grown into ingots using the Czochralski technique. The ingots are cut into slices called wafers and the wafers with a thickness of microns (10^{-6}) to nanometers (10^{-9}) were used to produce the components for the ICs. Si technology based solar cells can produce high power conversion efficiency by optimizing the device structure design, and optoelectronic properties, and lowering the recombination losses and resistance of the electrodes. Among the Si-based solar cells, passivated emitter rear solar cell (PERC), interdigitated back contact cell (IBC), heterojunction with intrinsic thin layer cell (HIT) reached maximum efficiency of 23.3 %, 25 % and 23.5 % respectively so far [2,3].

Although Si has a lot of advantages, it still faces many drawbacks. They are highly sensitive to electrostatic discharges in circuits and radiation, and they poorly respond to the high-frequency range. An unfavorable amount of heat is generated on high power switching, causing shortened life cycles. The thickness must be sufficient (between 200 – 500 in microns) to generate its intrinsic optoelectronic properties. Also, expensive toxic substances are used in the manufacturing and purifying processes. These are all the reasons that make

researchers revisit and divert their focus to different elements and compounds for photovoltaics and other optoelectronic applications. Even if we acknowledge profoundly the history of the technology reaped, we need to focus on addressing the paramount challenge of modern life, which drives toward harnessing and providing efficient and clean energy.

1.4. Thin film solar cells

1.4.1. Thin Films

Thin films are materials that possess tunable chemical and physical properties apart from their bulk, arising mainly from the variation of thickness ranging from micrometers to nanometers. The thickness difference can influence the optical and electronic properties, The surface-to-volume ratio of thin films is higher compared to bulk leading to affect many chemical activities such as catalysis, adsorption, and diffusion.

Thin films deposition and formation via the nucleation growth process, mainly follow three steps [4]:

- Incorporation of atomic/molecular/ionic species and their transport through a medium towards a fixed substrate where chemical species lose the velocity component towards the normal of substrates and absorbed on the surface.

- Formation of clusters depending upon the thermal equilibrium between surface and adsorbed species leads to chemisorbed, stable nuclei that have critical grain sizes.

- To reduce the surface energy, the nuclei start to coalesce with each other which defines as the agglomeration stage depending on the substrate temperature, thermal diffusion, rate of adsorption/desorption etc.

- The rate of coalescence leads to a continuous, holes and boundaries filled network type structure leading to the formation of thin films.

The anisotropic or isotropic growth can take place in normal or parallel to the substrates depending on nucleation density. The re-nucleation of nuclei at the surface led to layered structures which eventually grows to a thin film.

There are different techniques used to deposit thin films and they are mainly characterized by two: vapor and solution-based techniques. Vapor deposition techniques are further

classified into physical vapor deposition (PVD) and chemical vapor deposition (CVD). Classification of various thin film deposition methods are shown in Figure 1.0.
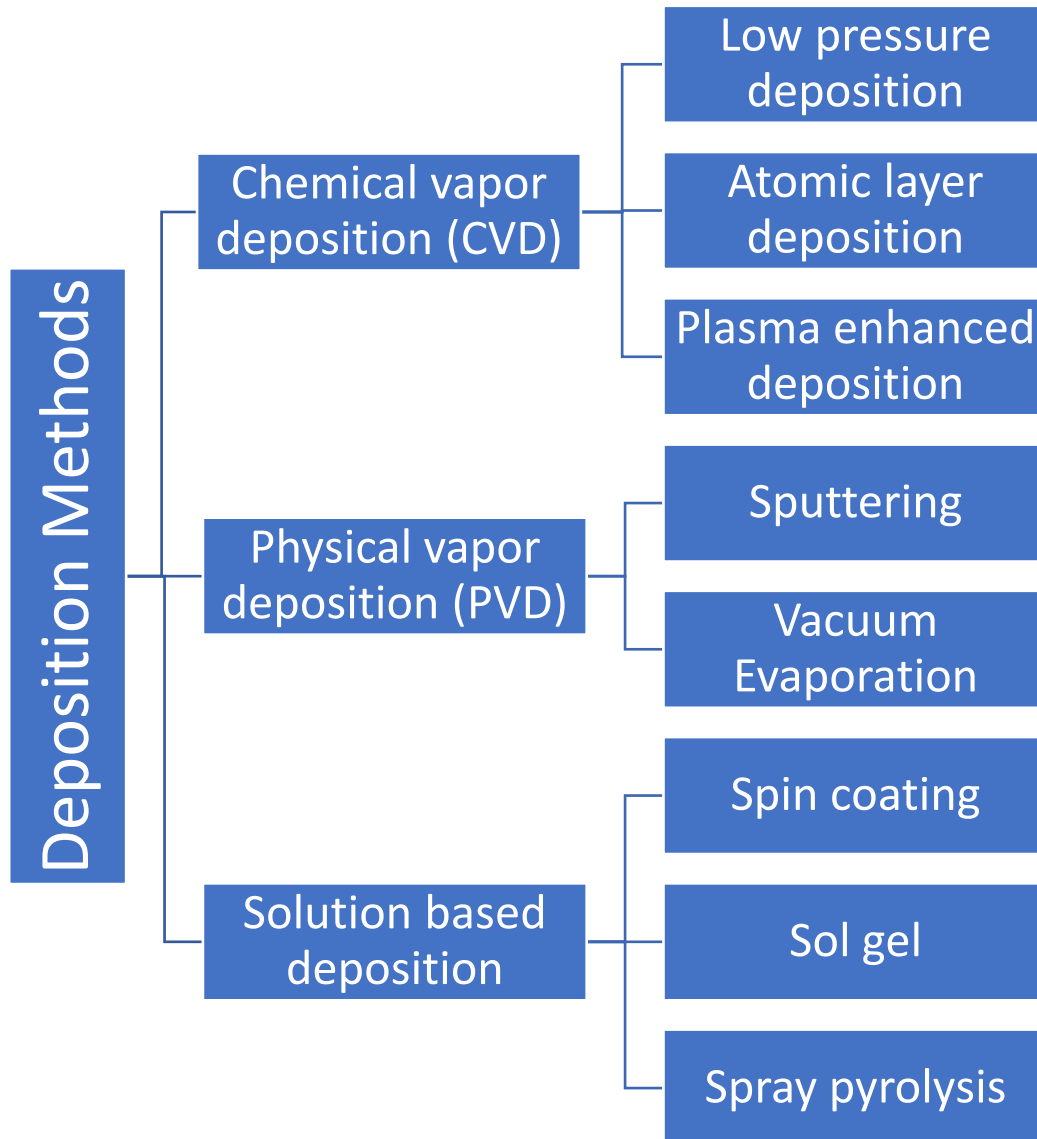
Figure 1.0 Schematics of various thin film deposition techniques.

1.4.2. Thin Film Photovoltaics

A conventional photovoltaic or solar cell is a solid-state electronic device that employs a p-n semiconductor junction. In a thin film solar cell, different materials can be used to form a p-n junction to convert the incident radiation to electrical energy. Among them,

1) Absorber materials are capable of undergoing absorption-caused excited states, which are formed by photons with energy that lie within the solar spectrum. The excited states that are generated must be mobile or excitons that are capable of dissociating into free electrons and free holes. Absorber materials could be organic or inorganic semiconductors, dye molecules, or quantum dots.

2) Window/Buffer layers enable better admittance of incident radiation to the junction possessing wide band gap and comparable refractive index to reduce the optical losses. Effective charge transfer can be guaranteed on the suitable band alignment with absorber material. In addition, an antireflection substance is used as an optical impedance matching medium to couple light into the structure of the solar cell in an effective manner. Plasmonic materials including metals and photonic materials, such as insulators, semiconductors, and metals, are used as optical components to control scattering, reflection, interference, and diffraction, thereby influencing the optical electric field and, consequently, the absorption distribution within the absorber.

3) Cell electrodes are conductive materials that provide ohmic contacts which are necessary for transporting current from the cell to the external load with minimal voltage loss. As contact electrodes, metals, or transparent conducting oxides (also known as TCOs) are normally utilized, the electrical and optical loss caused by these materials must be minimized [5].

In general, the photovoltaic effect in thin film solar cells is originated from:

1) <u>Presence of electric field:</u> The absorption of electromagnetic radiation is modeled by Beer-Lambert law while the recombination of charge carrier is taken by the S-R-H mechanism together with the difference in the work function of contact arises a built-in electric field. The

charge carrier accelerates under an electric field, so an effective field sweeps the photogenerated charge carriers toward the contacts.

2) <u>Presence of effective force field</u>: The origin of drift and diffusion current, defined by the hole – electron current density reveals a change in hole – electron affinities that give rise to corresponding hole-electron effective force fields. The hole – electron effective force field has a significant role in carrier transport at bulk as well as on interface.

3)The diffusion of charge carriers: The difference in the electron and hole mobilities gives rise to inhomogeneous distribution or gradient throughout the materials. The photogenerated charge carriers chose the gradient as transport influence thereby the diffusion coefficient of the carriers increases. However, the diffusion-assisted photovoltaic effect is insignificant because of the non-directional charge transport. Thus, solar cells are designed in a way to have a built-in electrostatic field, and effective force fields.

A thin film solar cell is designed on layer-by-layer regions with donor-acceptor regions separated for carrier diffusion which is in the order of nanometers. The donor-acceptor interfacial areas permit the charge carrier separation within the induced effective field leading to better charge carrier extraction. The incident photon is absorbed and the photogenerated carriers need to be collected at the opposite electrodes otherwise the carriers get trapped in the donor or acceptor domain and recombined. Thus, poor charge transfer through layers with imbalanced charge carrier mobility contributes to the lowering of the efficiency of solar cells [6]. Initially in the 1960, a Schottky junction was proposed for solar cell structure which was reported lower than 0.1% efficiency [7]. Later towards the end of the 20th century, heterojunction solar cells achieved a power conversion efficiency higher than 10% and the latest record efficiency of 30% as given in Figure 1.1 by NREL labs.
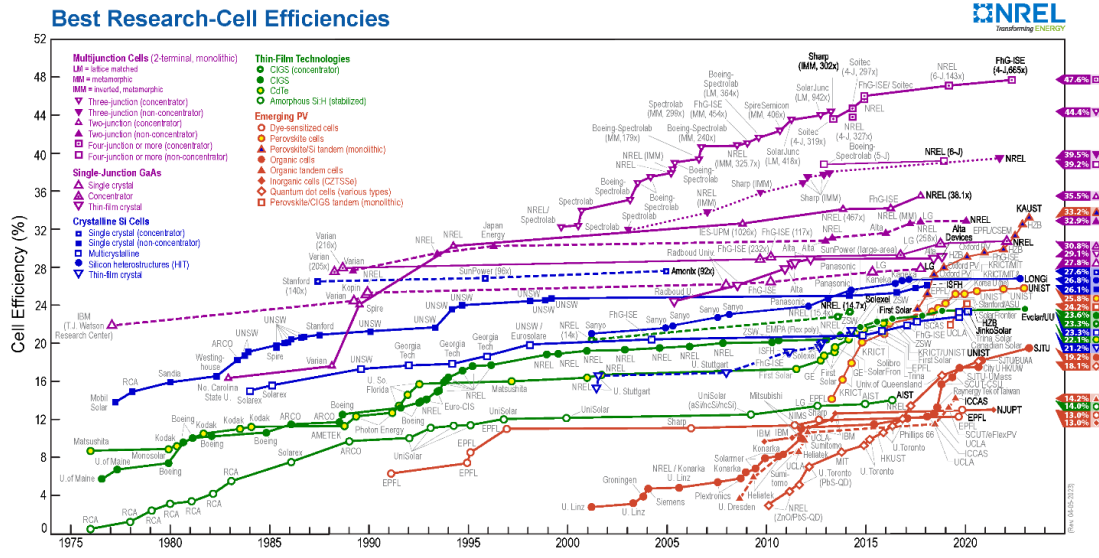
Figure 1.1 Research cell efficiencies NREL labs, USA   https://www.nrel.gov/PV/cell-efficiency.html. (Accessed on 31 July 2023)

1.4.3 Solar Cell Characteristics
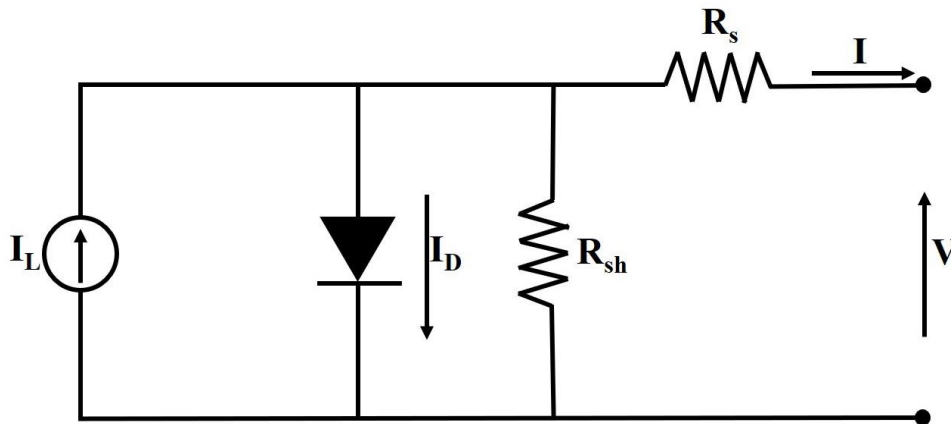
Figure 1.2 Equivalent circuit of solar cell with photo current source I_L, diode current I_D, shunt and series resistances (R_{sh} and R_S).

The equivalent current – voltage characteristics of a solar cell (Figure 1.2) defined on the parameters, are given as follows: The maximum current surpass through circuit when the end terminals are shorted is defined as short circuit current (I_{sc}) and current per area is current density (J_{sc}). While the terminals are open, then the maximum voltage extracted from the

circuit is defined as open circuit voltage (V_{oc}). V_{oc} gives an idea of the Fermi energy separation at the equilibrium stage of electron hole generation.

The ratio of output electrical power (P_{out}) over input power (P_{in}) is defined as efficiency (η) of the solar cell device shown in equation (1),

$$\eta \ = \frac{P_{out}}{P_{\ in}} \ = \ \frac{V_{oc}I_{sc}FF}{P_{in}} \qquad\qquad (1)$$

Where fill factor (FF) defines as the output power to ideal power ratio. Fill factor calculated by the equation (2) as follows.

$$FF \ = \ \frac{V_m I_m}{V_{oc}I_{sc}} \qquad\qquad (2)$$

The I-V characteristics of solar cell consist of shunt (R_{sh}) and series (R_s) resistances depicted in Figure 1.1 is represented in equation (3) given below:

$$I = I_L - \ I_0 \left[\exp\left[\frac{e}{nKT}(V + IR_s) \right] - 1 \right] - \frac{V + IR_s}{R_{sh}} \qquad\qquad (3)$$

Where I_o is the reverse saturation current and *n* is the diode factor.

1.4.4. Dye sensitized solar cells

Dye-sensitized thin film solar cells (DSSC) convert solar radiation into electricity with the aid of a sensitizer that uses synthetic or natural dyes [8]. The principle of operation of a dye-synthesized solar cell is as follows: the dye molecule absorbs incident photons and generates excited electrons. Excited electrons are transferred from the conduction band to the nano porous semiconductor using a sensitizer. Then, using an anode or working electrode, electrons are extracted towards a load, where electrical energy is collected, while a cathode or counter electrode dissipates an electron, completing the circuit [9]. The development of a solar cell with an efficiency of 7.1% by Oregan and Gratzel in 1991 was a pivotal moment in the history of DSSC. DSSCs are a prospective substitute for Si solar cells owing to their inexpensive manufacturing costs, simple structure, and easily accessible ingredients. Their current power conversion efficiency is recorded of 13.6% with triazatruxene based sensitizers [10,11].

1.4.5. Perovskite solar cells

Perovskite solar cells (PSCs) have recently attracted a great deal of interest due to their increasing power conversion efficiency (PCE), facile manufacturing, and inexpensive material components. Perovskites have a basic crystal structure represented by the formula ABX_3, in which the species A and B are cations and X acts as an anion. The reported optoelectronic properties have high carrier mobility(>4 cm^2/Vs), absorption coefficient ($>10^5$ cm^{-1}), and moderate recombination losses [12,13]. In these types of solar cells, the excitons generated in the perovskite absorber shift from high concentrations to low concentrations as they diffuse their way to the donor/acceptor (D/A) interface. This process is known as the diffusive process. At the D/A interface, charge carriers undergo dissociation to generate free charges. The electrons reach the cathode via an electron transport layer [14]. In 2009, Miyasaka *et al.* demonstrated the first perovskite solar cell with an efficiency of 3.81%. Since then, the efficiency of PSCs (FTO/MAPbI$_3$/Spiro OMeTAD/Ag)has increased to 26.8% [15] because of numerous startling developments. However, there are several limitations that impede the commercialization of PSCs, such as their low structural stability and the fact that they are particularly sensitive to environments including water, heat, and oxygen. In addition, the difficulty of covering large areas and the use of toxic substances such as lead [16] are other major concerns.

1.5. Thin Film Chalcogenide solar cells

The increasing demands for novel device properties and applications have stipulated the thin films researchers led to the investigation of chalcogenide compounds. Chalcogenides thin films were employed in various devices like solar cells, lasers, ultraviolet light emitters, spin functional devices, microelectronics, optical and magnetic wave devices. In this thesis, focuses on the application of chalcogenides in thin film solar cells. Chalcogenide thin films are defined as compounds containing at least one of the VI group elements (sulfur (S), selenium (Se) and tellurium (Te)). Initially pilot production of thin films with low-cost fabrication methods and better absorption of incident light led to the investigation on binary and ternary thin films.

1.5.1. Cadmium Telluride

Cadmium telluride based solar cell is a highly competitive thin-film PV technology on the global market. Some of the most important features of CdTe as a photovoltaic material are its direct bandgap of 1.45 eV, high absorption coefficient, and chemical stability [17–19]. Production of the first CdTe solar cells began in 1972, owing to the initiatives of Bonet and Rabenhorst. The CdS/CdTe heterojunction was made using a three-step process, and its efficiency was 6% [20]. High-temperature CdTe deposition, $CdCl_2$ activation treatment, Cu doping, etc. have been used to boost the efficiency of CdTe-based solar cells, resulting in a conversion efficiency of 15%. The National Renewable Energy Laboratory's Wu *et al.* [21] achieved a 16.5% improvement in efficiency. Over the past five years, the efficiency of CdTe solar cells has increased dramatically by implementing novel methods such as bandgap grading and copper embedding. As a consequence of the redesign, productivity and power conversion efficiencies increased by 21.2% [22]. However, cadmium toxicity and scarcity are two of the most pressing issues which turn the attention to materials composed of abundant and low toxic elements.

1.5.2. Copper indium gallium sulfo-selenide (CIGS)

Copper indium gallium selenide, typically referred to as CIGS or Cu (InGa)Se_2, is a very promising material for solar applications due to its high absorption coefficient (10^5 cm $^{-1}$), direct optical bandgap of 1-1.2 eV [23]. These characteristics make CIGS an excellent candidate to use in photovoltaic devices. In 1980, Mickelsen and Chen fabricated a cell using a CdS/CuInSe$_2$ heterojunction using thermal evaporation, which led to a cell having an efficiency of 5.7%. In CIGS, the bandgap aligned with the solar spectrum by substituting Ga for indium [24–28]. Due to the intrinsic band bending and Fermi position alignment in CIS, the CIS-based cell exhibited a high J_{sc} [29]. Subsequently, numerous reported analysis showed enhanced CIS-based cell efficiency, resulting in the production of solar cells with 12.2% conversion efficiencies [23]. Due to the possibility of bandgap engineering by grading the composition in CIGS, CIS has been replaced with CIGS. In tetragonal CIGS, which has lattice parameter c/a ratio of 2, lattice distortion occurs because of the presence of In-Se, Cu-Se, and Ga-Se bonds. Thereby CIGS can absorb most of the

radiation within just one millimeter of its thickness, and the amount of material needed to fabricate devices out of CIGS can be drastically reduced by only requiring a layer of thickness less than 1 μm. Sequential deposition, co-evaporation, and ambient atmospheric conditions are viable to deposit CIGS [30].

In 1976, Kazmerski *et al.* successfully fabricated the first solar cell based on CIGS with a conversion efficiency of 4.5 % to 12.5 % [31]. Currently, the efficiency of CIGS-based cells has increased to over 20 % through enhancements to the absorber-buffer interface, optimizations of the window layer, and new deposition methods etc. The maximum CIGS solar- cell efficiency has been measured in the lab to be 23.5 % [32]. Scarcity and toxicity of the components create a shortage and health issues on fabrication of CdTe and CIGS solar cells. Compared to silicon based solar cells the economic feasibility on large scale production and fabrication methods reported is a growing concern with telluride, indium, and germanium availability.

1.6. Emerging Chalcogenide thin films for Photovoltaics

1.6.1. Copper zinc tin sulfo selenide

Cu_2ZnSnS (CZTS) is a quaternary p-type semiconductor that shows a direct bandgap of about 1.5 eV, a carrier concentration that is comparable to that of CIGS, and a significant absorption coefficient of order 10^4 cm^{-1} at wavelengths in the visible spectrum and p-type conductivity that can be achieved due to the presence of intrinsic defects, such as copper vacancies [33–35]. CZTS photovoltaic devices have the potential to attain an efficiency of 28 % in compliance with the Shockley-Queisser limit [36–38].

Katagiri *et al.* developed a sputtering procedure that resulted in the production of CZTS solar cells with an efficiency of 0.66 % [39]. In a later work, Shin used vacuum processing to obtain an efficiency of 8.4 % [40]. Recent studies have shown that incorporating Se into CZTS results in an alloy known as $Cu_2ZnSn (S_xSe_{1-x})_4$ (CZTSSe). The modification in the S/Se ratio causes both the structural and optoelectronic characteristics of the compound [41,42][43]. The best efficiency that has been recorded so far for a CZTSSe solar cell is 12.6 % [44]. Cation disorder defects are the most significant issues that impact

the efficiency of CZTS cells. These defects lower open circuit voltage and hence the solar cell efficiency [45].

1.6.2. Copper tin sulfide /selenide (Cu-Sn-S/Se)

Among ternary chalcogenides, I-IV-VI group elements are widely explored due to their high absorption coefficient ($>10^5$ cm^{-1}), intrinsic p-type conductivity and tunable optical band gap ranging from 0.9 -1.7 eV [46,47]. Amidst, copper tin sulfide (CTS) thin films have been investigated for their photovoltaic application rendering unique optoelectronic properties on solar cells initially reported a 0.11 % power conversion efficiency in 1987 by Fakolujo *et al.* [48]. Recently, up to 6.7 % efficiency has been achieved on CTS solar cells and a theoretical power conversion efficiency of 30 % hence further studies have been intensified on CTS solar cells [49]. Apart from the photovoltaic application, CTS thin films were reported as effective photoactive materials such as photodetectors and photocatalysis and dye-synthesized solar cells [50–53]. The major deposition techniques for the fabrication of CTS thin films are based on chemical solution method such as solvothermal, spin coating, chemical bath deposition and electrodeposition to produce nanosized and porous films with high surface area [50,52,54,55]. At the same time copper tin selenide thin films have been investigated for their tunable optical band gap in the range of 0.8-1.1 eV, high absorption coefficient (10^4-10^5 cm^{-1}) with electron and hole mobilities of the values 10 cm^{2}V^{-1}s^{-1} [56–59].

1.6.3. Antimony sulfide

Antimony sulfide (Sb_2S_3) has gained popularity as an absorber material due to its earth-abundant, low toxicity, and long-term stability [60]. It exhibits desirable characteristics, such as optimum bandgap (1.5–1.7 eV), a high absorption coefficient ($> 10^5$ cm^{-1}), and inherent p-type semi conductivity [61]. As a result, Sb_2S_3 can potentially be utilized in a wide variety of optoelectronic applications, including thin films, nanoparticles, and nanostructures.

Bera *et al.* fabricated the Sb_2S_3 thin film on spiro- OMeTAD photodiode with a photo response time of less than 25 milliseconds results in self-powered low visible light photodetector [60]. One-dimensional Sb_2S_3 nanostructures were synthesized by solvothermal approach, and these nanostructures display strong photocatalytic activity for the breakdown

of methyl orange [60]. the exceptional optoelectronic characteristics of Sb_2S_3 make it a possible candidate for application as an absorber material junction or tandem solar cells [60]. Seok group has succeeded in achieving a power conversion efficiency (PCE) of 7.5 % using sensitized Sb_2S_3/TiO_2/FTO/Glass configuration [62]. To improve the efficiency of the device, a significant amount of work has been put in, with the primary emphasis being placed on the development of new synthesis methods for producing high-quality Sb_2S_3. The approaches used include chemical bath deposition, solution deposition, fast thermal evaporation, atomic layer deposition, thermal evaporation. For instance, by utilizing chemical bath deposition, the efficiency of an Sb_2S_3 solar cell was enhanced from 2.56% to 5.5% [63–65]. Song *et al.* generated a thin layer of high-quality Sb_2S_3 by using rapid thermal evaporation (RTE), which resulted in a power conversion efficiency of 5.4% [66]. Another vacuum method was atomic layer deposition, which produced a PCE of 5.77% [67].

1.6.4. Silver antimony sulfoselenides

Among the chalcogenides, silver-based chalcogenides are explored due to their nontoxicity, earth abundant, low thermal conductivity and tunable optoelectronic band gap which are favorable for thermoelectric and photovoltaic applications [68], Optoelectronic applications can be engineered using by doping to increase the carrier concentration, mobility, conductivity etc [69]. $AgSbSe_2$ and $AgSbS_2$ are reported with p type conductivity with band gap in the range of 0.93 – 1.6 eV [70–72]. The device application in solar cells was first investigated on chemical bath deposited Sb_2S_3 onto which Ag evaporated layers closed with selenium films [73]. Using insitu gas solid reaction approach solar cell device with configuration TiO_2/$AgSbS_2$/Au obtained an enhanced external quantum efficiency (EQE) of 15% was reported [74]. The dye sensitized $AgSbS_2$ liquid junction solar cells showed, 1.3 % PCE [75,76]. A systematic control over Se/S ratio on chemical bath synthesized $AgSbS_{2-x}Se_x$ thin film absorber achieved a maximum efficiency of 4.2 % [77].

1.6.5. Cu-Sb-S thin films: Promising candidates for thin film photovoltaics

Copper antimony sulfide (Cu-Sb-S) belongs to a family of I-V-VI group-type semiconductors. Different phases of Cu-Sb-S compounds have been known with distinct optical and electrical properties that arise from their crystalline structures and atomic

compositions [78]. Most of them have optimal band gaps for sunlight absorption and hence high device efficiency. The family of ternary Cu–Sb-chalcogenides offer a rich selection of potential candidates for earth- abundant low toxic photovoltaic (PV) absorber materials [79]. Moreover, a high absorption coefficient $> 10^5$ cm^{-1} is another distinguishing feature of Cu-Sb-S compounds [80]. Different Cu-Sb-S ternary phases are identified in a phase diagram given in Figure 1.3. In general, monoclinic, orthorhombic, cubic, and tetragonal possesses with covalently bonded planar structure connected by Van der Wall's force arise from the high lone pair density [79]. And the main contributors to the lone pair electron densities are from Sb (III) ions which can block a binding direction. From Figure 1.3 the Cu-Sb-S phases are mapped so closely that the temperature, composition, and chemical reaction highly influence the stability and formation of the phases. The copper-antimony- sulfide compounds exist in four phases viz. $CuSbS_2$ (chalcostibite), Cu_3SbS_4 (fematinite), Cu_3SbS_3 (skinnerite) and $Cu_{12}Sb_4S_{13}$ (tetrahedrite). From the elemental composition of copper antimony sulfide compounds, the phase diagram exhibits all major four phases aligned close to each other. The reported phases possess different optoelectronic properties depending on varied composition present in the compounds.
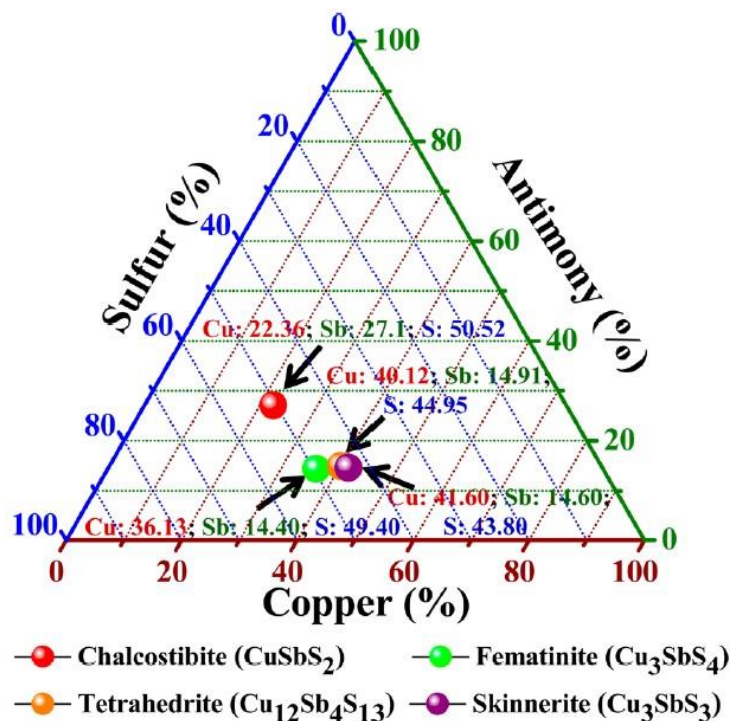
Figure 1.3. Phase diagram of the Cu-Sb-S system (Reprinted permission[81] J. Alloys Compd. 694 (2017) 132–135. https://doi.org/10.1016/J.JALLCOM.2016.09.307)

The experimental evaluation of the behavior of four phases and the temperature dependence on the phase stability were reported [82,83]. The Cu-Sb-S phases (monoclinic, orthorhombic, cubic, and tetragonal) have high optical absorption with optical band gap lying at 1.1 -1.7 eV which is essentially required for PV absorber materials [84,85]. Both physical and chemical methods have been implemented for deposition for Cu-Sb-S thin films of different phases. This thesis work mainly focuses on tetrahedrite ($Cu_{12}Sb_4S_{13}$) and chalcostibite ($CuSbS_2$) phases of copper antimony sulfide. The following section summarizes synthesis and characterization of copper antimony sulfide thin films on the photovoltaic and photodetector applications.

1.6.5.1. Tetrahedrite ($Cu_{12}Sb_4S_{13}$)

$Cu_{12}Sb_4S_{13}$ poses a unique structure with a metal to semiconductor transition around 85 K attributed to the structural transition from cubic to tetragonal [86,87]. $Cu_{12}Sb_4S_{13}$ poses a non-centrosymmetric cubic space group I43m (217) and reported feature of tetrahedrite crystals

is attributed to the copper occupancies bonded to sulfur atoms and Sb localized lone pair [88]. This bond forms a trigonal plane, which favors an anisotropic atomic motion of atoms perpendicular to triagonal plane. This anisotropic motion of atoms favors the low lattice thermal conductivity and phonon scattering in tetrahedrites [89,90]. Mainly, tetrahedrite phase is explored for thermoelectric properties due its low dislocation density, high band degeneracy and low thermal conductivity suitable for thermoelectric applications [91–94].

Mechanical, physical as well as chemical methods have been implemented on the synthesis of $Cu_{12}Sb_4S_{13}$ compounds. Bulk $Cu_{12}Sb_4S_{13}$ powders were synthesized using mechanical alloying and ball milling method. Among the reported methods, mechanical alloying and ball milling have been focused to synthesize $Cu_{12}Sb_4S_{13}$ in its bulk powder form, mainly for thermoelectric applications [91–93]. Only a few multistage processes have been known for thin film deposition. One method was electron beam evaporation of pellets made of ball milled powder on the bulk compound pre-synthesized by mechanical alloying. Another method was a two-stage process of radio frequency (RF) sputtered Cu-Sb layers followed by sulfur vaporization at 140 °C. On glass substrates, good quality thin films were formed by annealing Sb_2S_3/CuS stacked layers deposited by physical vapor deposition [93,95]. Further, solution-based deposition techniques such as spin coating, hot injection and drop casting were also used to obtain the tetrahedrite thin films. A separate stock solution of Cu/Sb powder mixed with S in hydrazine (highly toxic) was made, from which Cu-Sb-S precursor solution to form spin coated films. The precursor solution was prepared on nitrogen filled glovebox with water and N_2 kept under 1ppm. During preheating the substrate, the hydrazine solution was deposited on the substrate where the reacting agents react with precursor solution during spin coating, forming the thin films [96]. A similar approach was done using thermolysis of Cu-Sb thiocarbonate solutions or Cu-Sb xanthates to deposit $Cu_{12}Sb_4S_{13}$ thin films. The precursor decomposition of a mixture of *bis*(*O*-ethylxanthato)copper(II) and *tris*(*O*-ethylxanthato)antimony(III) with tuning of copper and antimony xanthates molar ratio produced single-phases of either chalcostibite or tetrahedrite were obtained [97].
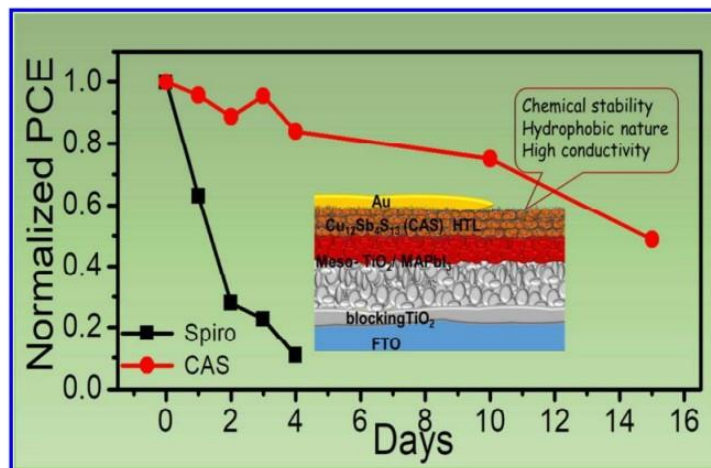
Figure 1.4. PV device using $Cu_{12}Sb_4S_{13}$ hole transport layer[98]

By drop casting metal xanthates as precursor, mesoporous $Cu_{12}Sb_4S_{13}$ thin films with band gap of 1.7 eV and their transient absorption spectra with broad absorption towards higher wavelength signified better electron injection in the interfaces [99]. The charge recombination kinetics (difference in optical density, versus time profile) in tetrahedrite revealed long-lived charge separation (lifetime in the range of 1 ms–10 ms) that is well-suited to use as light absorbers in semiconductor-sensitized solar cells.

Among solution based techniques, spray pyrolysis is a cost-efficient and environmentally benign deposition technique that produces uniform and homogenous thin films[79,100,101]. Panitee *et al.* demonstrated a photo electrocatalytic device using doped In^{3+} on $Cu_{12}Sb_4S_{13}$ thin film with porous morphology using perfume atomizer [102]. Ternary chalcogenide–$Cu_{12}Sb_4S_{13}$ thin films were fabricated by adding anhydrous copper (II) into the stock solution of antimony (III) sulfide dissolved in methanol: as sources of Cu^{2+}, Sb^{3+} and S^{2-} ions, respectively. On In^{3+} doping, optical band gap was reduced. Thus, in the literature, despite the evaluation of optical and thermoelectric properties $Cu_{12}Sb_4S_{13}$ thin films formed by different methods, a systematic analysis of their optoelectronic properties and their device applications are yet to be accomplished.

1.6.5.2. Chalcostibite (CuSbS$_2$)

CuSbS$_2$ has been suggested as a promising absorber material due to its high absorption coefficient ($>10^5$ cm^{-1}), near ideal band gap (1.4-1.6 eV) and possess an intrinsic p-type semi conductivity, comparable properties as that of CIGS[103]. Copper antimony sulfide (CuSbS$_2$) exists in orthorhombic structure with space group 62. The material is studied for the stability and charge transport properties to form interface structures[95]. The copper vacancies in the lattice act as shallow defects with the lowest formation energy as reported to be ionized rapidly and generate hole carriers leading to the intrinsic p type semi conductivity[104].

Several deposition methods have been widely implemented for the fabrication of nanocrystals and thin films for photovoltaic and photodetector application. Adam W. Welch *et al.* reported the RF magnetron sputtering of the self-regulated growth of CuSbS$_2$ with improved optoelectronic properties [105]. Shi *et al.* reported fabrication of CuSbS$_2$ with particle size of 25 nm using solvothermal method and the films showed an optical band gap of 1.45 eV. The controlled formation mechanism was based on the chelating and reducing agents with expense of reactants [81]. Liu *et al.* studied quantum dot sensitized solar cell using CuSbS$_2$ films with 1.3 eV optical band gap and particle size of 15 nm formed via hot injection method [78].

Chemical bath deposition (CBD) was used for CuSbS$_2$ thin film fabrication. CBD is a suitable option for the growth of affordable, large-area thin films for solar applications. In a typical chemical bath deposition, the substrates retained within the bath containing cations and anions to form the thin films [106,107]. Chemical bath deposition is a wet chemical process where precursor chemicals react on substrate surfaces. Most of the reported crystal growth is amorphous in nature and re-crystallize in post thermal treatments. At higher annealing temperatures, can result in an increase in carrier concentration or a copper deficiency. Carrie L. McCarthy et. al reported CuSbS$_2$ thin films from annealing Cu$_2$S and Sb$_2$S$_3$ binary phase by spin coating using thiol-amine mixtures by varying deposition temperatures [108]. Like CBD, spin coating is a simple and cost-effective method for depositing thin films on flat substrates [109].

Only a few reports are available in the literature related to spray deposition of $CuSbS_2$ for photovoltaic and photodetector applications [110–113]. Thin films of TiO_2 and $CuSbS_2$ were spray deposited and evaluated the performance of a 3D solar cell comprising TCO, dense TiO_2, and $CuSbS_2$ sandwiched between layers of graphite. However, the photovoltaic response of the cells was severely dampened by the existence of an impure Sb_2S_3 phase and a porous structure [100]. The optical bandgap value for all the films deposited under different conditions were found to be between 1.15 and 1.7 eV [110]. Using precursor solutions containing $SbCl_3$, $CuCl_2$, $CS(NH_2)_2$, on glass substrates at 200 °C led to the formation of $CuSbS_2$ thin films along with an impure Cu_2S phase [101]. The resulting films showed a direct optical bandgap of 1.45 eV and a carrier concentration of 5×10^{20} cm^{-3}.

1.6.6. Cu-Sb-S based PV devices

The highest performing PV devices using Cu-Sb-S shows open circuit voltage of V_{oc} = 0.622 V, Short circuit current J_{sc} = 17.9 (mA/cm^2), FF= 28 %, with an efficiency of 3.2 [79,114]. Most of the Cu-Sb-S devices use CdS as window/buffer with Glass/Mo/$CuSbS_2$/CdS/ZnO: Al configuration. In such cases, Cu diffusion into CdS window layer creates deep trap states for holes lowering the short circuit current. Correlated issues, for example the band alignment shows a cliff led to low V_{oc} with high recombination rate [115]. Due to toxicity and elemental diffusion, CdS was replaced with transparent conductive oxides viz., ZnO, MgO, TiO_2 [116]. Riha *et al.* reported V_{oc} of 0.02 V and J_{sc} of 0.045 mA/cm^2 for Glass/ITO/TiO_2/$CuSbS_2$/Au configuration. The reported study confirms annealing treatment enhance the crystallinity of the film growth and increase in the carrier life time from 0.5 to 0.7 ns thereby a rise in V_{oc} = 0.300 V [117]. Maiello *et al.* reported V_{oc} of 0.03 V and J_{sc} of 1.6 mA/cm^2 on ITO/i-ZnO/CdS/Cu_3SbS_3/Mo/glass configuration [118] and Franzer *et al.* reported V_{oc} of 0.24 and J_{sc} of 7.1 (mA/cm^2) for Glass/FTO/CdS/Cu_3SbS_4/Cu/Ag. Further, Wang *et al.* reported V_{oc} of 0.03 (V) and J_{sc} of 7.65 (mA/cm^2) on Glass/FTO/ZnMgO/$Cu_{12}Sb_4S_{13}$/gold [96]. The highest power conversion efficiency of 3.22 % for $CuSbS_2$ thin films have been known in the configuration Mo/ $CuSbS_2$/CdS/i-ZnO/n-ZnO/Al using hybrid ink nanoparticles[119]. The limiting factor on the power conversion factor is the Cu/Sb composition which controls the growth of phases [119].

1.6.7. Challenges to address

Current photovoltaic research focuses on building highly efficient PV devices based on low-cost materials using economically feasible manufacturing methods. When the low-cost materials are used as commercial solar cells, their performance is often argued because the fabricated and reported cells are on laboratory standards. As the scenario persists, we propose copper antimony sulfide thin films as absorber material incorporated on solar cell devices for PV applications. Copper chalcogenides such as $Cu_{12}Sb_4S_{13}$ and $CuSbS_2$ have gained research interest worldwide due to their low-cost and environmentally beneficial constituents. From the literature, systematic growth control of the thin film's optoelectronic properties for photovoltaic applications have not been widely reported. $Cu_{12}Sb_4S_{13}$ and $CuSbS_2$ falls into excellent candidates for the p type absorber material having an optical band gap range from 1.3 - 1.7 eV with high absorption coefficient ($>10^5$ cm^{-1}). Tunable optoelectronic properties, reproducibility and stability of the films incorporated in PV devices are yet to be explored. An optimal hetero-junction design with minimal current loss and enhanced open circuit voltage, improving the efficiency is yet to be achieved. Factors affecting the efficiency of the solar cell device are parasitic resistances (series and shunt resistance) along with better band alignment in the layered hetero-junction solar cell. The conduction band offset with cliff and spike shaped alignments reduce the charge carrier transfer from the depletion region to the extraction terminal, hence the charge carrier collection and overall solar cell device performance diminishes [120,121]. The band alignment offset can be improved to a great extent by choosing the hetero-junctions with appropriate band gap and electron affinity values which ensure the unhindered charge carrier transport. Lowering recombination centers on controlled crystal growth can help to attain enhanced power conversion factors. To meet the challenges, the present thesis work proposes the following.

1.7. HYPOTHESIS

Copper antimony sulfide thin films with varying compositions can be formed on zinc oxysulfide thin films by controlling sulfur to copper-antimony concentrations in the precursor solution resulting fully ultrasonic spray coated heterojunctions with photovoltaic and photodetection properties.

1.8. OBJECTIVES

1.8.1. General Objective:

To fabricate thin‑film solar cells u s i n g copper antimony sulfide thin films as absorber and zinc oxysulfide as window layers, a fully ultrasonic spray pyrolyzed device.

1.8.2. Specific Objectives:

➢ Simulation of Cu-Sb-S/ Zn (O, S) PV junction performance using SCAPS I D software.
➢ Theoretical calculation of the electronic band structures of the absorber and the window layers using MedeA software and DFT calculation using VASP.
➢ Synthesis of Zn (O, S) thin films with suitable optoelectronic properties by ultrasonic spray.
➢ Evaluation of structure, morphology, and optoelectronic properties of Zn (O, S) films.
➢ Spray deposition of Sb_2S_3 thin films by spray pyrolysis, no copper in the precursor solution
➢ Analyze Cu-Sb-S thin film deposition by incorporating Cu in the Sb_2S_3 precursor.
➢ Deposition of copper antimony sulfide thin films with varying S to (Cu-Sb) ratios in the precursor solution to evaluate the optical and electrical properties of Cu-Sb-S films with varying electrical properties.
➢ Evaluation of photovoltaic and photodetection properties of the heterojunctions of copper antimony sulfide thin films with varying electrical properties using different window layers of CdS, Zn (O, S) films
➢ A comparative analysis of theoretical and experimental results.

1.9. Justification

Photovoltaics is considered one of the effective methods of power generation. While progressing the research on the new compounds and its fabrication methods to incorporate on devices, scarcity and toxicity have posed major problems. Earth abundant and environmental benign at the same time stable and reproducibility of the device fabrication have been a challenge. Among them, copper-based chalcogenides can address to a great extent and the investigation on their optoelectronic properties can improve their performance and further meet the challenges previously not attended. From the literature survey, Cu-Sb-S thin films of different phases show potential scope as photovoltaic absorber material, but the incorporation into solar cells is not efficiently explored. Ultrasonically assisted chemical

spray pyrolysis is an excellent thin film deposition technique , using less amount of chemicals and advantage of covering large area of substrates. In the present thesis, an intense investigation on the different components of   solar cell devices is included: ZnO, Zn (O, S) transparent conductive oxide layers as the window layer and Cu-Sb-S thin films ($Cu_{12}Sb_4S_{13}$ and $CuSbS_2$) as absorber layers. ZnO and Zn (O, S) layer with tunable optoelectronic properties have been chosen as a replacement for CdS to overcome Cd toxicity, and thermal instability and also to prevent Cu diffusion from the absorber layer. An intrinsic Sb_2S_3 layer can provide a channel in the depletion region where an effective electric field can sweep the charge carriers to terminal electrodes. It is known that $Cu_{12}Sb_4S_{13}$ and $CuSbS_2$ thin films possess high absorption coefficient ($>10^5$ cm^{-1}) and band gaps in the range 1.3-1.6 eV respectively predicting their potential application in photovoltaics as well as photodetection. Hence, this thesis mainly focuses on the synthesis, characterization of ZnO, Zn (O, S), Sb_2S_3, $Cu_{12}Sb_4S_{13}$ and $CuSbS_2$ thin films and their device applications, using the method of ultrasonic spray pyrolysis.

Chapter 2

Materials and Methods

In this chapter, details of theoretical approach to calculate electronic band structure, vibrational spectra and photovoltaic performance are first explained. Also, experimentation details for the synthesis and characterization of zinc oxide, zinc oxysulfide, antimony sulfide and copper antimony sulfide thin films are also included as follows. Computational simulation of molecular structure was achieved using the Schrodinger equation for many bodies within the density functional theory. Using DFT methodology by Vienna Ab initio simulation package helps to define properties of structure by first principal quantum mechanical calculation. Moreover, using SCAPS 1D, a solar cell simulation software developed for the simulation of photovoltaic structures, PV devices using ZnO/Zn(O,S) window and $CuSbS_2$ absorber layers were simulated. The basic algorithm for the simulation which governs the photogeneration and recombination of charge carriers are based on Poisson's and electron/hole continuity equation.

Experimental analysis of thin films is initiated by utilizing the advantages of ultrasonic spray pyrolysis deposition technique. By spray pyrolysis, uniform and homogenous thin films can be produced.

2.1. Computational Methods

Computational methodology provides a mathematical model solved numerically to define a physical phenomenon. The core reason for many physical properties such as optical, electrical, and magnetic properties of semiconductors arise from the electronic charge distribution of material. The limitation of macro dimension analysis can be overcome to a great extent by correlating with the respective computational data.

2.1.1 MedeA Environment

MedeA architecture is designed for quantum mechanical atomistic simulation combining experimental and computed data with sophisticated computer job management and graphical workflow. MedeA Graphical User Interface combined with job server and task server handles the computational job control and data preprocessing. The software helps for material screening,

design experiment and scientific analysis in simplified output files. The software includes crystal structure data and structure building tools. In the present thesis, crystal structures were imported from structural database and then optimized by the structural minimization calculation as explained below. The optimized structures are modelled for electronic properties calculation using VASP code brief details as given below.

2.1.2. Crystal Structure

MedeA is equipped with a graphical user interface to the databases ICSD, COD Pauling and Pearson's data. They contain over 1.1 million structural entries comprising the largest solid-state structure database. It includes lattice parameters, atomic positions, symmetry, stoichiometry, partial disorder, phase diagram etc. The cell stage allows adjustment of the cell dimensions to define periodicity.

2.1.3 VASP

Vienna *Ab initio* Simulation package is a density functional code for quantum mechanical computational simulation program. Computational simulations using density functional theories have successfully reported in-depth analysis of structural, electronical, and vibrational properties of molecules. Even though precision of the calculation has been a challenge, using first principle calculation with pseudo potentials, projected augmented wave and plane wave basis set methods, VASP combines with the key feature of frozen core electron models guarantees lower time consumption and accuracy of the calculations [122]. VASP 5.4. software calculation approximates the many-body Schrodinger equation using density functional theory by solving Kohn Sham equations for non-interacting electrons. In this case, the one-electron orbitals' charge densities and local potentials are defined in plane wave basis sets. The electron and ion interaction is defined using either pseudopotential or projector-augmented wave methods [123].

2.1.3.1. Algorithm

The algorithm used in the VASP is defined in an iterative matrix diagonalization scheme based on a conjugate gradient scheme, block Davidson scheme or direct inversion in the iterative subspace (RMM-DIIS). The flow chart of electronic minimization by VASP calculations is shown in Figure 2.1. Initially, the charge densities and wavevectors are independent quantities that are set according to INIWAV and INCAR files. After each self-consistency loop the charge density is set

as a Hamiltonian, to create the optimized iterative wavefunctions accurately matching with the wavefunction of the Hamiltonian. The finalized wavefunctions' new charge density is calculated to patch up with the initial wavefunctions. A unitary transformation of wavefunctions was calculated for Hamiltonian because of the diagonal-spanned subspace. The subspace diagonalization transforms the wave function accordingly.

```
┌─────────────────────────────────────────────────┐
│     Trial Charge density CHGCAR and wavevector   │
└─────────────────────────────────────────────────┘
                        │
                        ▼
          ┌─────────────────────────────────────┐
          │  Set up Hamiltonian by choosing      │
          │  exchange correlation/Hartree        │
          │  functional.                         │
          └─────────────────────────────────────┘
                        │
                        ▼
          ┌─────────────────────────────────────┐
          │  Diagonalization in iterative        │
          │  subspace and optimize the wavevector.│
          └─────────────────────────────────────┘
                        │
                        ▼
          ┌─────────────────────────────────────┐
          │  Finding new partial occupancies     │
          │  and free energy (E) with new        │
          │  charge density                      │
          └─────────────────────────────────────┘
                        │
                        ▼
     If No            ◇ ΔE < E ◇
```
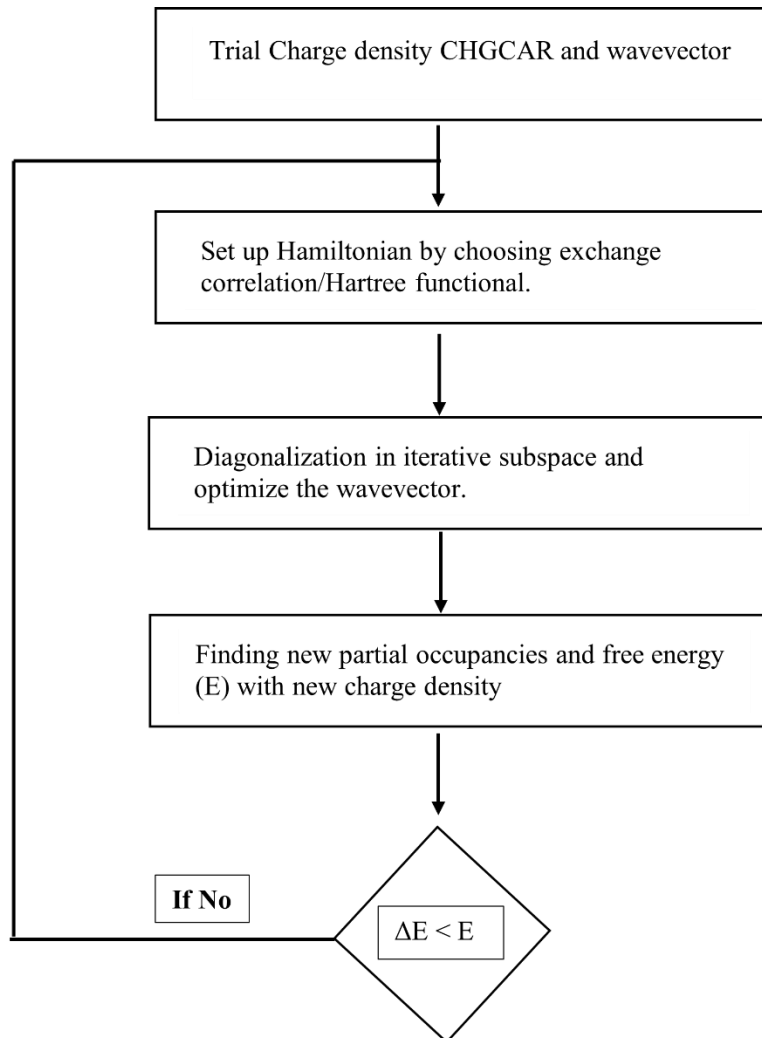
Figure 2.1 Algorithm of electronic minimization using VASP.

2.1.4. General steps explored for the simulation of unit cells.

2.1.4.1. Structure optimization

To evaluate the minimal force and energy by relaxing atomic positions and cell parameters with or without constraints. The calculation evaluates the bulk equilibrium structure at T = 0K (ground

state structure). The atoms are relaxed until the forces reach a minimal value than the input convergence. The cell volume changes the lattice parameters (a, b, c, and cell angles). The conjugate gradient iteration method was used for structure relaxation to minimize the force and energy return of the local minimum of the total surface energy as shown in the user interface in Figure 2.2.
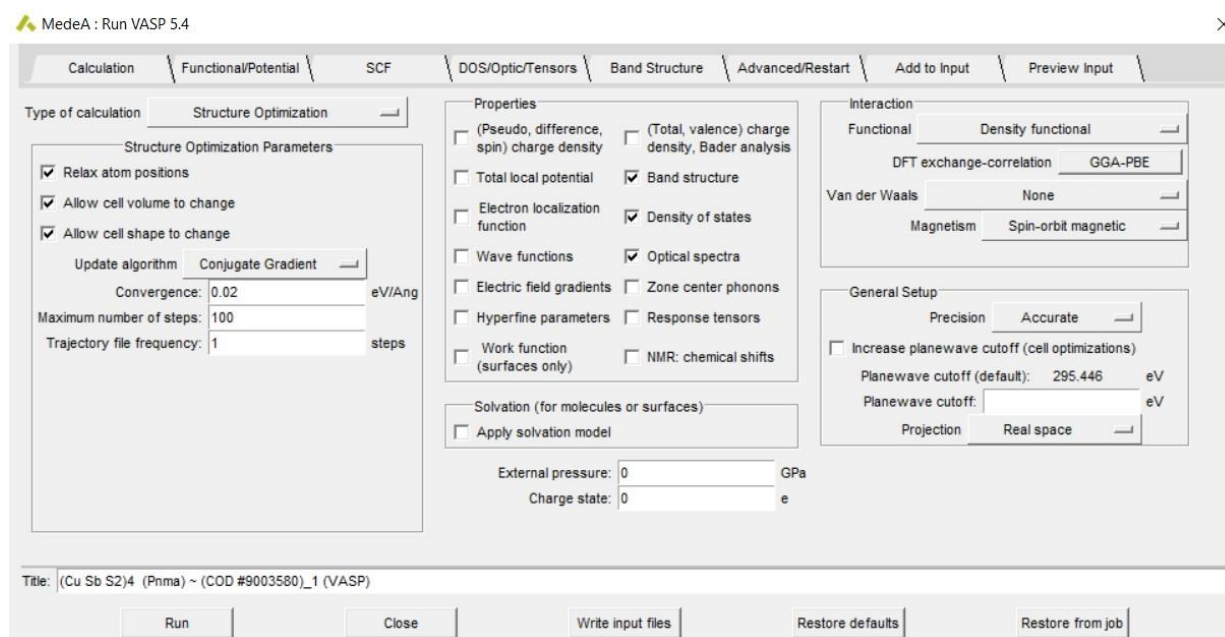
Figure 2.2 The graphical user interface for structural optimization.

A convergence upper limit of 0.02 eV/Å was used for the allowed residual force between atoms in the cell. A maximum number of 100 geometry steps are selected to be executed for the iteration. The definition of quantum physical interaction of electron-electron and electron–nuclei are defined exchange – correlation functional which allows to selection of the degree of locality, from local density approximation to Hartree Fock with several steps. For the structure optimization process, density functional of generalized gradient approximation – Perdew, Burke and Ernzerhof (GGA-PBE) [124] was used.

During the cell optimization, an increased plane wave cutoff was chosen due to the converging slowness of stress tensors with atomic forces value between the atoms. For structural optimization, a normal precision option was implored for the calculation. To save time, projection operators in real space were used. A self-consistent field calculation solving the Kohn Sham

equation was utilized for the evaluation of total energy, force, stress tensors and electron density to the corresponding atomic arrangements. The k point sampling for the electronic structure calculation was chosen explicitly allowing the definition of subdivision in X, Y and Z direction of k space. The origin of the mesh was shifted to the gamma point. An odd-sized grid was used for a cubic crystal structure. The density of states that are integrated by choosing the integration schemes depends upon whether the material of interest is a metal, semiconductor or insulator. The fractional occupation was considered on occupied and unoccupied states in space and integrated over a definite volume was achieved by choosing the option of integration scheme.

For semiconductors, the smearing of the electronic occupation around the Fermi energy was improved on the convergence value by choosing the Gaussian smearing method. Convergence was attained on the value between total energy and electronic eigenvalue, lower than the input field value between two iterations. A default value of 1×10^{-6} eV was chosen for the relaxation process. A maximum iteration step of 100 is normally used before the self-consistent field convergence. Later the program was set to the structural optimization process.

2.1.5. Electronic structure: Density of states and Band diagram

The relaxed structure is fed into the single point calculations for the density of states and band diagram. The dispersion relation between the electronic eigenvalues as a function of momentum within Brillouin zone is depicted as a band diagram. A total number of 40 k points are chosen for the band diagram calculation to plot the band structure while each line segment denotes a different direction in k space. The number of electronic eigenvalues as a function of energy is plotted as the density of states. To generate a converged charge density, a self-consistent calculation was chosen as shown in figure 2.3. A denser k mesh was selected by opting to reduce the spacing of 0.1/Å. Gaussian smearing method with a width of 0.2 eV was opted for semiconductor density of state calculation. A projection scheme of the plane wave method (PAW) sphere was chosen to get the angular momentum projected density of states for s, p, d, and f orbitals. Spin orbit coupling was considered during the calculation due to the contribution of 3d orbitals where degeneracy of orbital angular momentum can influence the optical and magnetic properties of the materials.
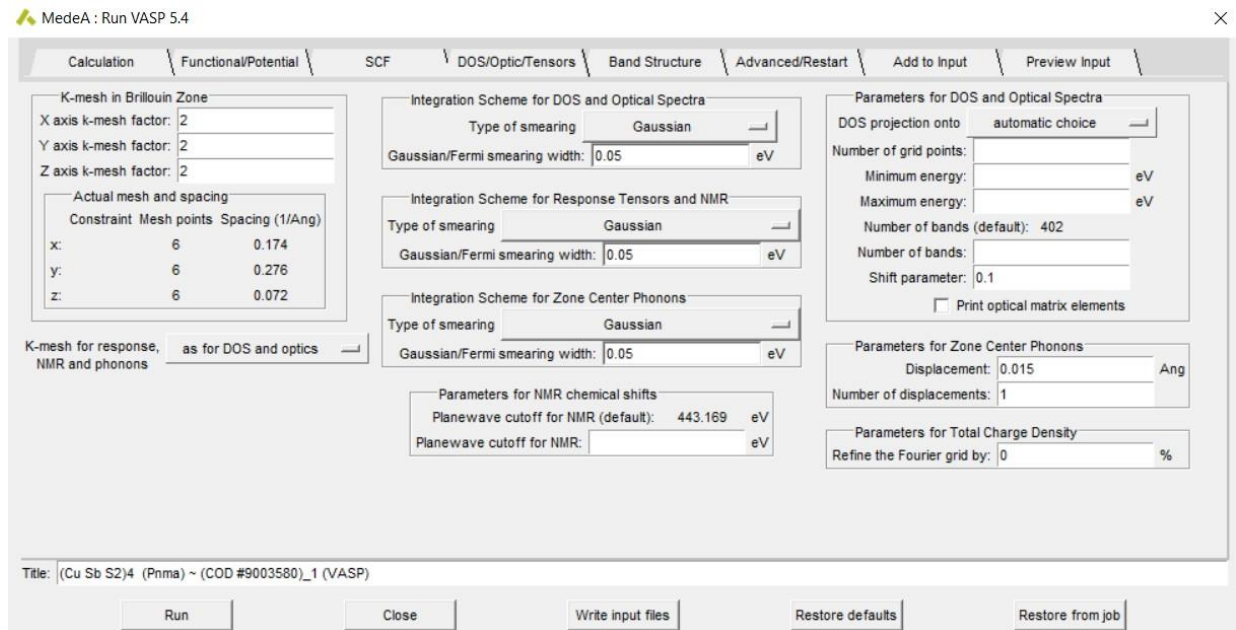
Figure 2.3. Density of states, band diagram and optical band diagram calculations tab on VASP 5.4 software

2.1.6. Optical spectra

Frequency dependent complex dielectric function gives an insight into optical properties of semiconductors. The excited state calculation of electron which defines the optical properties of the structure is compiled using the exitonic effect on quasi particle spectra. Calculations using the Casida equations and the Bethe-Salpeter equation on top of quasiparticle computations (GW) are different ways to generate very precise response functions and, as a result, optical spectra that include excitonic effects. Integration scheme and smearing method with k point sampling were commonly given with density of states calculation as shown in Figure 2.3. Interactions between electrons and holes can have a profound impact on the optical spectrum. The imaginary and real part of dielectric function was solved using Kramers - Kronig relation. The integration schemes and self-convergence field calculation parameter are commonly employed for density of states and optical spectra calculations.

2.1.7. Phonon spectra

During phonon calculation, a large supercell was kept at equilibrium where the symmetrical atoms were displaced for the force constant calculation. Then a dynamical matrix

constructed and diagonalized the phonon frequencies for points in k space to obtain corresponding eigenvectors and atomic movements. A full Brillouin zone calculation was selected to include the entire Brillouin zone kept at equidistant as shown in the interface of phonon calculation (Figure 2.4). The interaction range determines the size of the supercell opted. The displacement of atoms was chosen as 0.02 Å such that the force is large enough and the calculation should not extend out the harmonic regime and also a negative displacement for the displaced atoms move in opposite directions. The linear response from the dielectric tensor and born effective charge led to the longitudinal optics (LO) and transverse optic (TO) splitting in the gamma point and resulted in infrared (IR) spectra. Raman spectra resulted in the linear response of atoms in supercell defined from Raman tensor and corresponding intensity vs wavenumber is plotted.
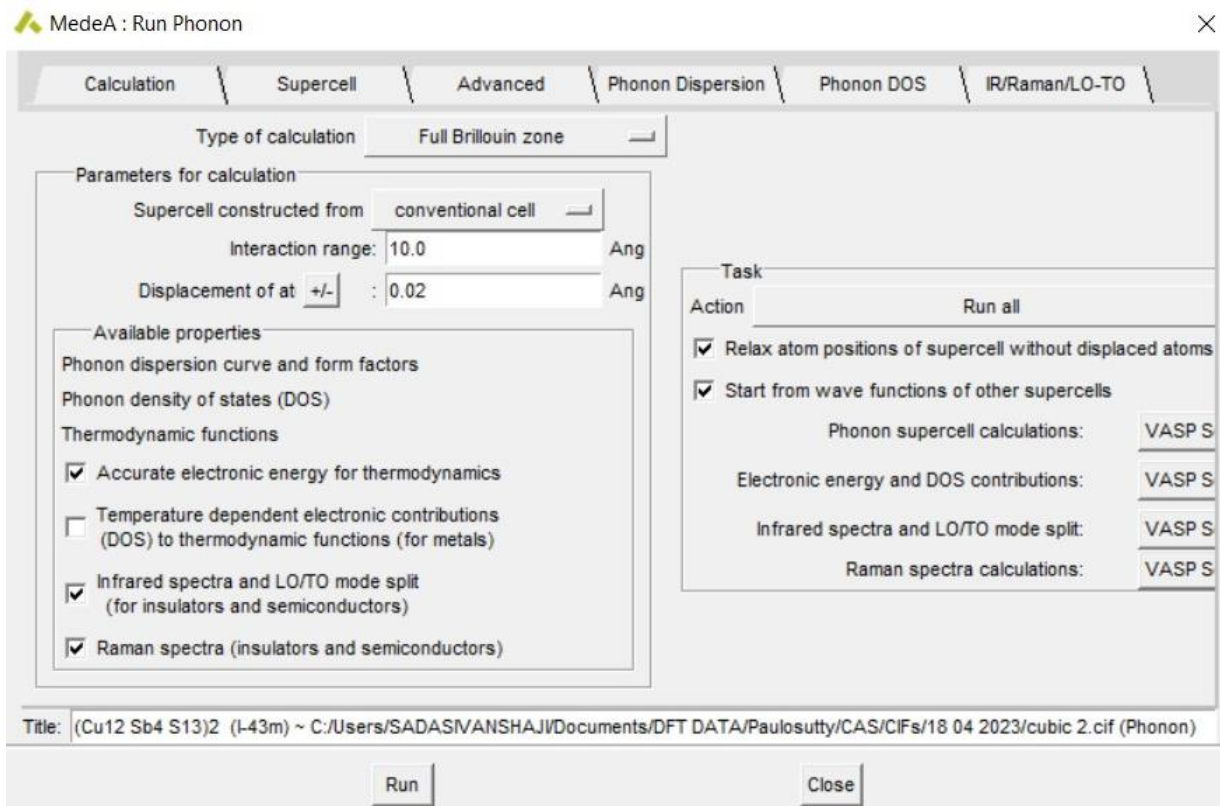
Figure 2.4 User interface of phonon calculations

2.2. SCAPS 1D

SCAPS 1D is a one-dimensional solar cell simulation package developed at Electronic and Information Systems (ELIS) of the University of Gent, Belgium. The program is developed for

CIGS semiconductors, crystalline and amorphous semiconductors. The simulation of solar cells consists of band-to-band, SRH and Auger recombination gives an insight into the recombination loss at the bulk as well as interfacial layers equivalent to the physical space.

The basic equation used for modeling the semiconductor is the Poisson equation which relates the electric charge to the electrostatic potential and continuity equation for electrons and holes [125]. The equation follows a 3N non-linear equation where the total cell is divided into N intervals with one can choose potential, quasi Fermi energy levels for electrons and holes independently. It is possible for discontinuities in the energy bands E_c and E_v, and consequently in the band gap E_g, to exist at the interfaces between the layers. This makes it possible for interface recombination to take place. Figure 2.5 shows the general working algorithm of SCAPS1D. In the initial point the solar structure is fed to the software using the required material with properties shown in Table 1.
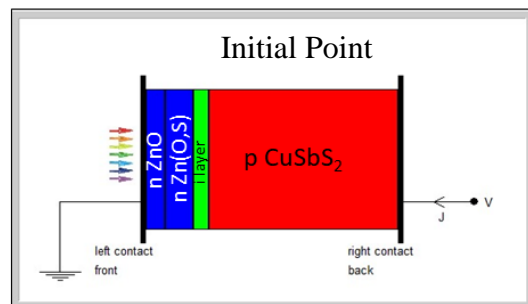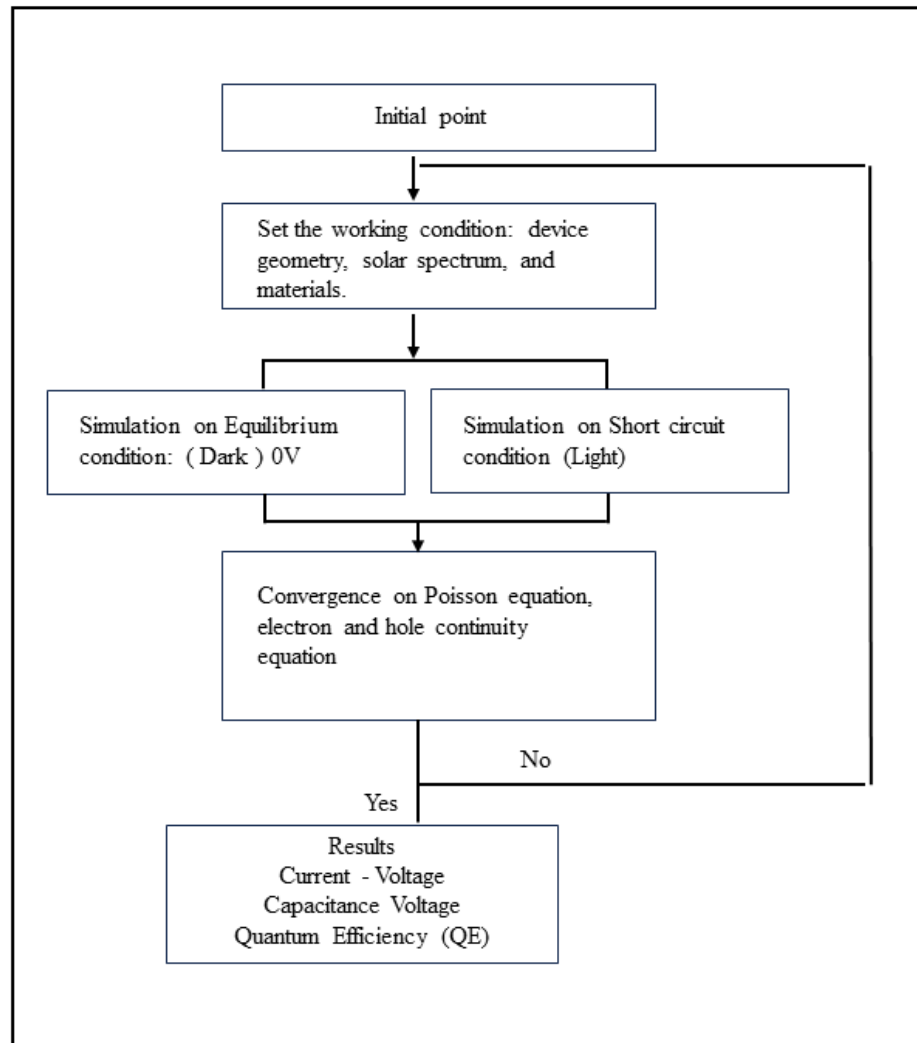
Figure 2.5. General working principle of SCAPS 1D with simulation of FTO/ZnO/Zn (O, S)/Sb_2S_3/$CuSbS_2$

2.2.1. Simulation of solar cell FTO/ZnO/Zn (O, S)/Sb_2S_3/$CuSbS_2$

The simulation of solar cell structure FTO/ZnO/Zn (O, S)/Sb_2S_3/$CuSbS_2$ was modeled on SCAPS 1D software. At the working condition point, temperature was set at 300 K in correlation with the parameters of thermal velocities, thermal voltage, $N_c(T)$, and $N_v(T)$. Solar cell layers defined by the ASCII files of the materials, which can be edited with the data corresponding to the layers, interfacial layer, and contact properties etc. The device was illuminated from the back contact layer of ZnO/Zn (O, S) window layers copper antimony sulfide as absorber layer. The

parameters used for the simulation which define the properties of the material are listed in Table 1.

Table 1 SCAPS 1 D parameter of layered structure for solar cell simulation

Properties	Materials			
	ZnO [126]	**Zn (O, S)** [127]	**Sb$_2$S$_3$** [128]	**CuSbS$_2$** [129]
Thickness, [nm]	40	30	80	250
Band gap E$_g$ [eV]	3.2	2.7	1.7	1.45
Permittivity ε$_r$	9	8.5	7	4.0
Density of states N$_C$ [cm^3]	2.2×10^{18}	2.2×10^{18}	4.7×10^{15}	1.23×10^{20}
Density of states N$_V$ [cm^3]	1.8×10^{19}	1.8×10^{19}	4.7×10^{15}	1.78×10^{20}
Thermal velocity V$_{th, e}$ [cm/s]	1.0×10^7	1.0×10^7	1.0×10^6	6.8×10^6
Thermal velocity V$_{th, p}$ [cm/s]	$1{\cdot}0 \times 10^7$	1.0×10^7	1.0×10^6	6.07×10^6
Mobility μ$_n$ [cm^2/Vs]	100	100	10.2	16
Mobility μ$_P$ [cm^2/Vs]	25	25	9.8	8
Donor defect density N$_D$ [cm^{-3}]	1.0×10^{14}	1.0×10^{16}	5.7×10^{13}	0
Acceptor defect density N$_A$ [cm^{-3}]	0	0	4.7×10^{13}	5.7×10^{16}

2.3. Materials

The chemicals for the preparation of the precursor solution for the ZnO, Zn (O, S), Sb$_2$S$_3$ and Cu$_{12}$Sb$_4$S$_{13}$ / CuSbS$_2$ thin films were reagent grade and utilized as such without any purification. The solutes for precursor solution used were zinc acetate dihydrate salt (Zn (CH$_3$COO)$_2$.2H$_2$O; 99.7% purity), thioacetamide salt (C$_2$H$_5$NS), antimony chloride (SbCl$_3$; 98%) and copper chloride dihydrate (CuCl$_2$.2H$_2$O; 99.1%). The solvents used for the precursor solutions were methanol

(CH$_3$OH; 99.6%) and acetone (C$_2$H$_6$CO; 99.7%). The solvents used were of reagent grade and distributed by Fermont. The salts were supplied by Fermont and Sigma Aldrich.

2.4. Experimental methods

Synthesis

This section includes the complete experimental methodology implemented for the synthesis and characterization of ZnO/Zn (O, S), Sb$_2$S$_3$, Cu$_{12}$Sb$_4$S$_{13}$ and CuSbS$_2$ thin films and their photovoltaic devices. All these thin films were grown via ultrasonic spray pyrolysis.

Ultrasonic spray pyrolysis

Spray pyrolysis is an excellent deposition technique for the thin film deposition for mono or bi-layer films either denser or thinner, porous, uniform, homogenous films. Basically, the spray technique uses droplet generation from the precursor solution induced by external atomization with properties including cost effectiveness, deposition rate, scalability etc. The most attractive features of spray techniques are the high stability, adhesive to the substrates and fabrication over large areas. Ultrasonic wave induced droplets of the precursor solution deposited directly over a heated substrate produces high quality films. A schematic diagram of the ultrasonic spray pyrolysis set up used in this thesis is shown in Figure 2.6. For metal oxide precursors, nitrates, acetates, and chlorides can easily be dissolved in alcoholic and aqueous solutions and readily be sprayed into the substrates.

Principle:

During ultrasonic atomization Newtonian fluids with low viscosities are passed over a vibrating surface which is an electromechanical device that vibrates at high frequency and converts the solution into droplets. The capillary wave mechanism is used to describe the process of ultrasonic nebulization where the formation of capillary waves on the surface of a liquid is supported by a vibrating solid. The equation (4) relating capillary wavelength (λ), surface tension (σ), fluid density (ρ), frequency (f) and fluid depth (h) is formulated by Kelvin shown below:

$$\lambda \left[\tanh\left(\frac{2\pi h}{\lambda}\right)\right]^{-1/3} = \left[\frac{2\pi\sigma}{\rho f^2}\right]^{1/3} \tag{4}$$

From the above equation the capillary frequency (λ) and the droplet size (D) of the fluid can be correlated by R.W Wood and A.L. Loomis and then experimentally Land *et al.* derived the average droplet size and ultrasonic frequency as given below (5).

$$D = \kappa \left[\frac{8\pi\sigma}{\rho f^2}\right]^{1/3} \tag{5}$$

Where κ corresponds to the number of droplets produced on the ultrasonic frequency of 10-100 kHz[130].

The ultrasonic spray pyrolysis equipment with a program assisted controller was purchased from Zhengzhou CY Scientific Instrument Ltd. The equipped machine for the deposition of thin films is shown in Figure 2.6. The technical parameters used for the deposition are included in Table 2.
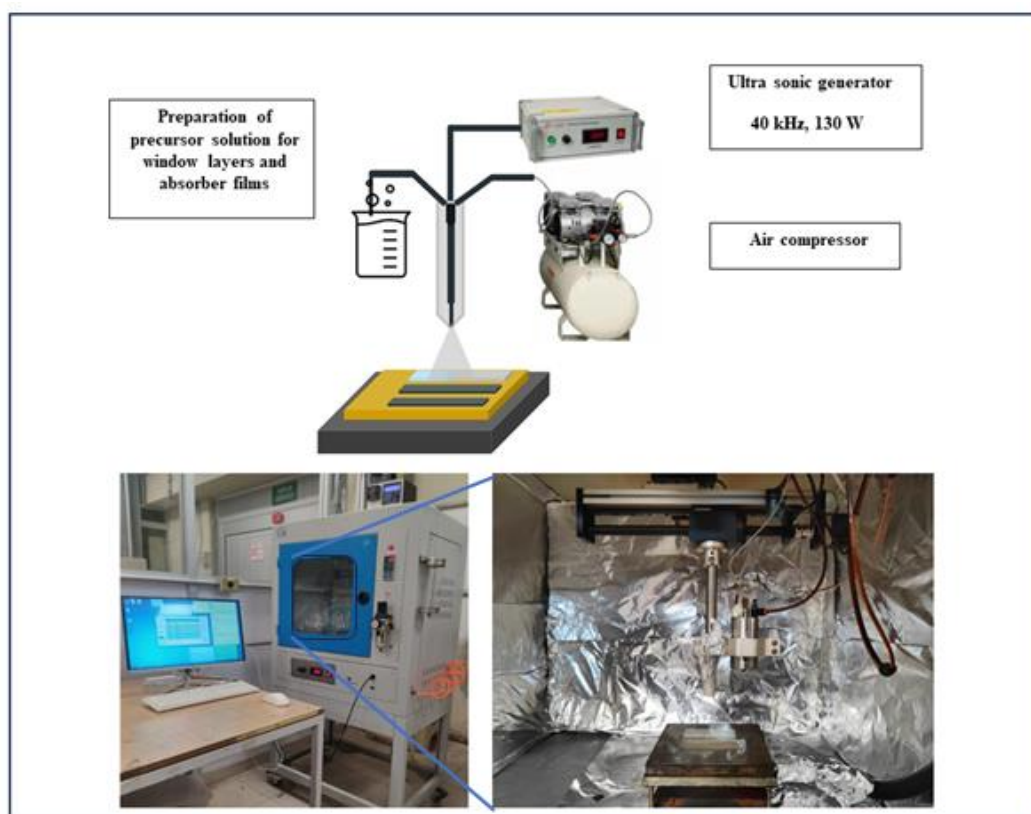
Figure 2.6 Schematic diagram of spray deposition technique with images of ultrasonic spray pyrolysis system with program assisted controller and the spray nozzle.

Table 2.0 Technical parameters implemented for the Ultrasonic spray pyrolysis.

Spray pyrolysis Model	CY-USP130-A
Control Method	Industrial Computer + Instrument Panel
Ultrasonic Sprayer	40 kHz 130 W
Substrate Heater Plate	150 mm $\times$ 150 mm
Nozzle Stroke	X-Y Axis up to 190 mm
Supply Voltage	AC 220 V, 50 Hz
Max Temperature	500 °C
Ultra sonic nozzle stroke frequency	40 KHz
Speed of nozzle stroke	50 mm/s
Distance between substrate and nozzle	9.5 cm
Compressed air pressure	0.02 MPa
Glass Substrate	(Fisher Scientific: 25 mm x 75 mm x 1 mm
Load current	0.03 A

2.4.1. Fabrication of ZnO/Zn (O, S) thin films

Thin films of ZnO and ZnO:S were synthesized using the precursor solutions containing zinc acetate and zinc acetate with thioacetamide, respectively. To prepare the precursor solutions, to 80 milliliters (ml) of methanol, 0.1 ml of zinc acetate dihydrate was diluted. The solution was stirred for 15 minutes at a time maintaining the temperature at 27 °C. In the same manner, the precursor

solution for Zn (O, S) was made by dissolving zinc acetate dihydrate salt and thioacetamide (C_2H_5NS) in methanol. Thin films of ZnO and ZnO:S were deposited by spraying the precursor solution on to the substrates. Microscope glass slides supplied by Fisher Scientific were used as substrates. These slides were of dimensions of 25 mm × 75 mm × 1 mm. After being ultrasonically cleaned-for 15 minutes in distilled water. The substrates were then washed with a neutral soap solution for 2 minutes and dried in warm air for ten minutes. The clean glass substrates were placed on a hotplate at 400 °C for 25 minutes. A peristaltic pump with a dispensing rate of 15 ml/min was used to pump the precursor solution into ultrasonic spray nozzle. The spray nozzle stroke was electrically connected to an ultrasonic generator producing varied current loads. Hence, inducing the frequency with which the transducer in the nozzle stroke vibrates and converts the precursor solution into spray droplets. Table 3 displays parameters employed during spray and sample identification. The samples were exposed to different annealing condition listes as follows: Vacuum annealing (450 °C/ 30 min), Air annealing (450 °C/ 30 min) and Rapid thermal process (450 °C/ 5 min).

Table 3 Sample identification of ZnO/Zn (O, S) thin films

	0.1 M Zinc acetate	
Molarity	**0.006, 0.008 and 0.016 M Thioacetamide**	
Substrate temperature	**400 °C**	
Precursor solution	**80 ml**	
Post thermal treatments	Vacuum annealing and Air annealing at 450 °C for 1 h Rapid thermal processing at 450 °C for 1-3 min	
Spray rate	**15 ml/min**	
Sample ID	**ZnO**	**Zn(O, S)**
	As prepared: **ZO**	As prepared: **ZOS**
	Vacuum annealed: **VA ZO**	Vacuum annealed: **VA ZOS**
	Air annealed: A**A ZO**	Air annealed: A**A ZOS**
	RTP: **RT ZO**	RTP: **RT ZOS**

The spray was directed towards the heated substrate using compressed air. The pre-programmed motion sequence was set to the microprocessor which controls the spray nozzle stroke to move along the X-Y direction. The nozzle stroke motion was designed in such a manner that one spray cycle was 100 mm in the positive X direction, follows 10 mm in the positive Y direction, and then 100 mm in the negative X direction. There was a total of 8 deposition cycles performed to get uniform deposition on three substrates. The 80 ml precursor solution was sprayed in 15 spray cycles until they were fully covered.

2.4.2. Antimony sulfide (Sb$_2$S$_3$) thin films

Reagent grade chemicals were used to prepare the precursor solution as mentioned 2.3. To prepare the precursor solution, 0.017 M antimony trichloride (SbCl$_3$) and approximately 4 times [0.07 M] thioacetamide (C$_2$H$_5$NS) were combined in 60 ml of acetone and stirred for 20 minutes in a glass beaker. The pH of the solution was 3.

Table 4 Sample identification of Sb$_2$S$_3$ thin films

Molarity	**0.003, 0.008, 0.011, 0.014, 0.017 M SbCl$_3$**	
	0.03, 0.04, 0.05,0.06, 00.07 M C$_2$H$_5$NS	
Substrate temperature	**170, 200 and 230 °C**	
Precursor solution	**60 ml**	
Spray rate	**7 ml/min**	
Sample ID	As prepared Sb$_2$S$_3$ **(Deposition temperature °C)**	**170** **200** **230**
	Vacuum annealed	**350 °C / 30 min**
	Rapid thermal process	**400 °C / 1 min**

The spray parameter was kept constant throughout the spray as mentioned in Table 4. For film deposition, the substrates temperature was 170 °C. The movements of the spray head were

programmed in a step-by-step manner so that the spray nozzle would move 90 millimeters in the positive X direction, then 10 millimeters in the Y direction, and then continue 90 millimeters in the negative X direction to finish 1 deposition cycle and 8 such deposition cycles for 1 spray cycle over 3 substrates. A combined total of 25 spray cycles were carried out to achieve the desired thickness on all three substrates. The general spray parameter and sample identification were given in Table 4.

2.4.3. Copper antimony sulfide thin films

General and technical spray parameters for spray deposition are included in Table 5. To deposit the film, substrate temperature of 200 °C for twenty minutes was kept constant at the hot plate. Using a peristaltic pump, the spray rate was set at 4 ml per minute. The thin films were deposited by concurrently adjusting volumes of copper chloride and antimony chloride in an 80 ml precursor solution, for a given quantity of thioacetamide. We referred to this phenomenon as a fluctuating S/(Cu+Sb) ratio, and we considered the high volatility of sulfur to keep the S concentration in the precursor solution (0.01 M thioacetamide) at a high level. In addition, we increased the amount of the precursor to 100 milliliters to confirm the fabrication of the thin film.

Table 5 Parameters employed for the deposition of copper antimony sulfide thin films.

Molarity	**0.0004, 0.0018, 0.003, 0.007, 0.01M CuCl$_2$.2H$_2$O**
	0.0015, 0.0038, 0.005, 0.008, 0.01 M SbCl$_3$
	0.07 M C$_2$H$_5$NS
Substrate temperature	**200 °C**
Precursor solution	**60 – 100 ml**
Spray rate	**4 ml/min**
Post thermal treatments	**350 °C/30 min**
	400 °C/ 30 min

2.5 Characterization techniques

2.5.1. X-Ray diffraction (XRD)

The crystal structure of the samples were analyzed using X-ray diffraction technique. A PANanalytical EMPYREAN diffractometer with Cu K_α radiation source was used to record the diffracted pattern. The operating conditions were 40 kV and 40 mA respectively under normal atmospheric conditions. The extracted data were further correlated with standard JCPDS data and Rietveld refined GSAS software. The average crystalline size (D) and the micro strain of the films can be calculated using the Williamson Hall plot.

2.5.2. Raman Spectroscopy

Phase and molecular interactions were analyzed using Raman spectroscopy. In Raman spectroscopy, Rayleigh scattering which are elastically scattered photons together inelastically scattered photons (Stoke and Anti-Stoke) can be used to define the chemical bonds of the samples. When a molecule possesses an electric dipole with polarizability induced by the incident photon, a vibration is said to be active. The detector measures the frequency and maps it into a specific wavenumber. In this work, samples were analyzed using a Thermo Scientific DXR Raman microscope equipped with a 532 nm laser.

2.5.3. X-Ray photoelectron spectroscopy (XPS)

A surface analysis method used to determine elemental composition and chemical states provides an in-depth analysis of the chemical environment of the sample. The surface of the samples is irradiated using an X-ray source (Al Kα: Energy:1486.68 eV, Voltage: 12 keV, Current: 3×10^{-3} A), and interacts with atoms to induce a photoelectric effect, ejecting the electron. The emitted electrons with binding energy given in the equation (6) were measured as photoelectron spectra.

$$KE = h\nu - BE - \Phi_s \tag{6}$$

Where hν is defined X-ray photon energy, BE is the binding energy of electron, and Φ_s is the work function of spectrometer. The BE was calculated from the spectrometer work function and incident photon energy. The core level photoelectrons were mapped into spectra from a sample having

energy which further quantifies the elemental composition. The base pressure in the analysis chamber was 1 x 10^{-9} mBar while spectra were being analyzed. This pressure was reached by combining a 3-filament titanium sublimation pump with two different 260 l/s turbo molecular pump systems. The analysis area was that of the focused X-ray beam spot size, which was 400 μm. The voltage was 12 keV, and the current was 3×10^{-3} A. The B.E values of the photoelectrons were analyzed with a 180-degree double-focusing hemispherical analyzer and had a work function of 4.2 eV and a 128-channel electron detector. Etching the surface of the sample was achieved using an Ar^+ ion gun at an etching rate of 1.22 /second. The parameters used for the etching were 2 keV at an angle of incidence 30 degrees.

2.5.4. Scanning electron microscopy(SEM)

Scanning electron microscopy was used to determine surface morphology. In SEM a high-energy electron source or electron gun emits electrons that are accelerated by an applied voltage. Secondary electrons, backscattered electrons (BSE), and distinctive X-rays are produced because of the high-energy electron beam's interaction with the specimen. The secondary and BSE are mainly used for sample surface imaging. Secondary electrons are produced when the electrons on the surface get excited and lose some of the energy due to interaction with incident electrons. The morphology and topography of the sample surface were produced by these secondary electrons. Backscattered electrons were produced, when the electrons hit the sample producing elastically scattered (no loss of energy) primary electrons with high energy that rebound from the sample surface. The rapid phase discrimination or contrasts in composition is illustrated by BSE. In many materials the mean free path length of secondary electrons was 10Å, so in comparison with BSE the volume of production of secondary electrons is small. Hence, the secondary electrons were perfect for examining the topography. The production of secondary electrons depends upon the atomic number of targets and the angle of incidence of the electron beam. In BSE, brighter signals are produced for specimen surfaces composed of atoms with higher atomic numbers.

2.5.5. UV Vis NIR spectroscopy

UV-Vis-NIR spectrometers measure light intensity at a certain wavelength to determine a material's transmission or reflection. The absorption coefficient of the material can be calculated from the equation (7) given below.

$$\alpha = \frac{1}{d} \, ln \, [\frac{(1-R)^2}{T}] \tag{7}$$

Where α is the absorption coefficient, T is the transmittance, R is the reflectance and d were the average thickness of the thin film. The average thickness of the film was measured using the profilometer technique. From the absorption coefficient the energy bandgap can be calculated from the equation (8) given below.

$$(\alpha h\nu)^n = A\left(h\nu - E_g\right) \tag{8}$$

Here A is a constant, ν is the frequency and E_g is the optical bandgap. With an optical transition, the value of *n* changes; it is 2,1/2, and 2/3 for direct allowed, indirect allowed, and direct forbidden transitions, respectively. The bandgap was determined by extrapolating $(\alpha h\nu)^n$ vs (hν) curve to the X - axis, where $(\alpha h\nu)^n = 0$ gives the optical bandgap. In this work the optical transmittance, reflectance and absorbance of the films were recorded using a UV-Vis-NIR spectrophotometer (JASCO-V770). The thin film was placed in the sample holder with a reference substrate (plain glass). Two glass substrates were used for the baseline measurement for transmittance vs wavelength spectra, one in the reference path and the other in the sample path.

2.5.6 Electrical characterization

The electrical properties of the thin films and devices were examined by measuring the photocurrent response. Electrical contacts of 7 mm in length separated by 7 mm were painted using silver paints. The electrical measurements were performed using a computer interfaced Keithley 6487 Pico ammeter/voltage source. The measurements were done using a halogen lamp (50 W) and LEDs of different wavelengths, The measurements were done sequentially in both dark and illumination at an interval of 20 seconds.

2.5.7. Hall effect measurement

The electrical properties such as carrier concentration, carrier mobility, resistivity and conductivity of the samples were measured using a Hall effect measurement system (Ecopia HMS-3000) equipped with a 0.55 Tesla magnet. Four contacts were painted at the corners of the sample, which was placed on SPCB-1 spring clip board. The spring-loaded tips were made in contact with the sample through the silver contacts. The sample holder along with sample was placed inside the

sample in a compartment. The Hall effect measurements were done at room temperature by applying a magnetic flux density of 0.55 Tesla.

2.5.8. J-V-Characteristics

The characterization of solar cells was done by J-V characteristics using a Keithley 6487 Pico ammeter/voltage source. The measured voltage and current density (current per unit area) were plotted. Open circuit voltage (V_{oc}) is represented by the intersection at the X axis where current is zero, while short circuit current is represented by the intersection at the Y axis when voltage is zero (I_{sc}). The back contact was made using silver paint and a front contact from FTO. During the voltage sweep, voltage and current were monitored using these top and bottom electrodes. The PV structures were illuminated using an Oriel solar simulator with AM 1.5G radiation at an intensity of 1000 W/m^2.

The following chapter includes the theoretical discussion on simulated structures of ZnO, Zn (O.S), Sb_2S_3, $Cu_{12}Sb_4S_{13}$ and $CuSbS_2$. Theoretical discussion includes the structural characteristics, density of states, band diagram and optical properties, in some cases vibrational spectra.

Chapter 3

Results and Discussion: Theoretical Simulations

This chapter discusses the theoretical simulation of different layers developed in this thesis for photovoltaic applications. Density functional theory calculation using VASP code that is implemented to MedeA material design graphical user interface. Solar cell capacitance simulator (SCAPS) 1D software designed for 1 dimensional solar cell simulations is implemented for the PV measurements, as mentioned in the previous chapter.

3.1. Ab initio calculation using Density Functional Theory (DFT)

3.1.1. ZnO and Zn (O, S) unit cells

The hexagonal crystal structure of ZnO supercell which belongs to the space group P63/mc and C_{6v}^4 symmetry is employed in the structural optimization calculation. The above structure has lattice parameters of a = b = 3.3249 Å, c = 22.7589 Å, and α = β = 90 ° and γ = 120 °. The Zn and O atoms occupied at 1a Wyckoff position. The optimized structure exhibited the following lattice parameters: a = b = 3.2589 Å, c = 20.7540 Å, and α= β = 90 °; γ = 120 °, volume = 142.3615 Å^3 (Figure 3.1 a). Using the method of random substitution, 0.8% of O atoms in the structure were substituted by sulfur to create a similar crystal structure to the one obtained experimentally. ZnO unit cell constitutes a tetrahedron polyhedral, where two zinc atoms bonded with two oxygen atoms at the vertex of a tetrahedron. For the calculation, a super cell consisting of four-unit cells (Figure 3.1 a) is used. Three oxygen atoms connected to zinc atoms at the basal plane of the cell have an average bond length of 1.97 Å and a bond angle of 110.45 °. Additional oxygen atoms formed covalent bonds with zinc that has an average bond angle of 108.47 ° and a bond length of 1.99 Å. The process of optimizing the S-incorporated ZnO super cell (Figure 3.1 b) led to a modification in the lattice parameter, which resulted in the change in lattice parameters: a = b = 3.2843 Å and c = 21.4547 Å and α = β = 90 °; γ = 120 °, volume = 144.1236 Å^3. The substitution of S atoms resulted in the rearrangement of the supercell. There are three S atoms bonded to the Zn at an average bond length of 1.98 Å and at an angle of 110.45 °, while there is one S atom attached to the Zn at a bond length of 1.99 Å and at an angle of 108.47 °. It is observed that the presence of

S^{2-} species in the lattice produces an increase in both the lattice parameter and bond length. The dangling connection formed between the zinc ion and the sulfur ion contributes to the charge density distribution and, as a result, increases the structural stability.
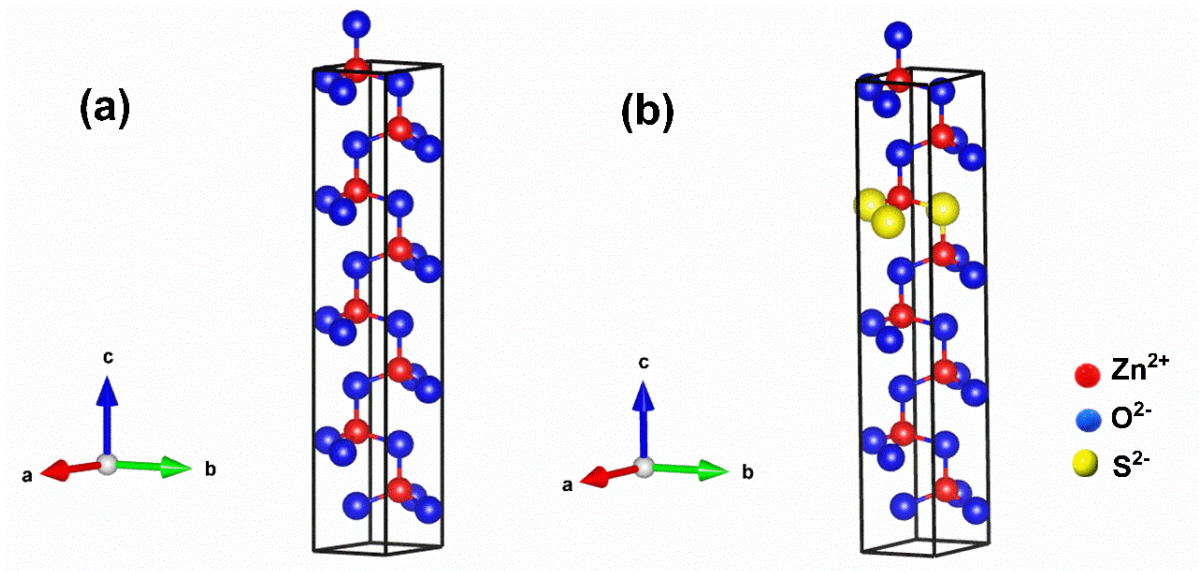
Figure 3.1 Supercells preferentially oriented towards c axis (a) ZnO and (b) Zn (O, S)

3.1.1.1. Density of states and band structure

Figures 3.2. a) and c) show the partial density of states and total density of states vs energy for the valence orbitals of zinc and oxygen atoms. From the figure, the valence band maximum (VBM) potential energy levels are mostly composed of the O p orbitals and from the Zn atoms both d and p orbitals are involved at the valence band maximum. The conduction band edge has a low energy level and is equally composed of Zn and O valence orbitals. The estimated band diagram of the ZnO unit cell is marked in Figure 3.2.e). In this diagram, the symmetry points of the Brillouin zones are in the direction; A > H > L > A > g > K > M. The valence band edges are at -0.13 eV, and the conduction band edges at 3.1 eV. These band edges coincide at (0,0,0) point, and as a result, a band gap of 3.2 eV and a direct electron transition from valence band to conduction band is predicted.

Figures 3.2 b) and d) show the partial and total density of states vs. energy of the S incorporated ZnO unit cell. The figure clearly shows the influence of S 2p orbitals in valence band where the strong overlap of S atoms introduces discrete energy levels narrowing the band gap

compared to ZnO density of states. The E vs. k diagram of the S-incorporated ZnO unit cell is shown in figure 3.2 (f), and the symmetry points in the direction of F> g > B > G. According to the dispersion relation, the valence band edge is located at -0.09 eV, and the conduction band edge is located at 2.8 eV. Together, these two band edges result in a band gap of 2.8 eV, corresponding to a direct transition as marked in the figure.
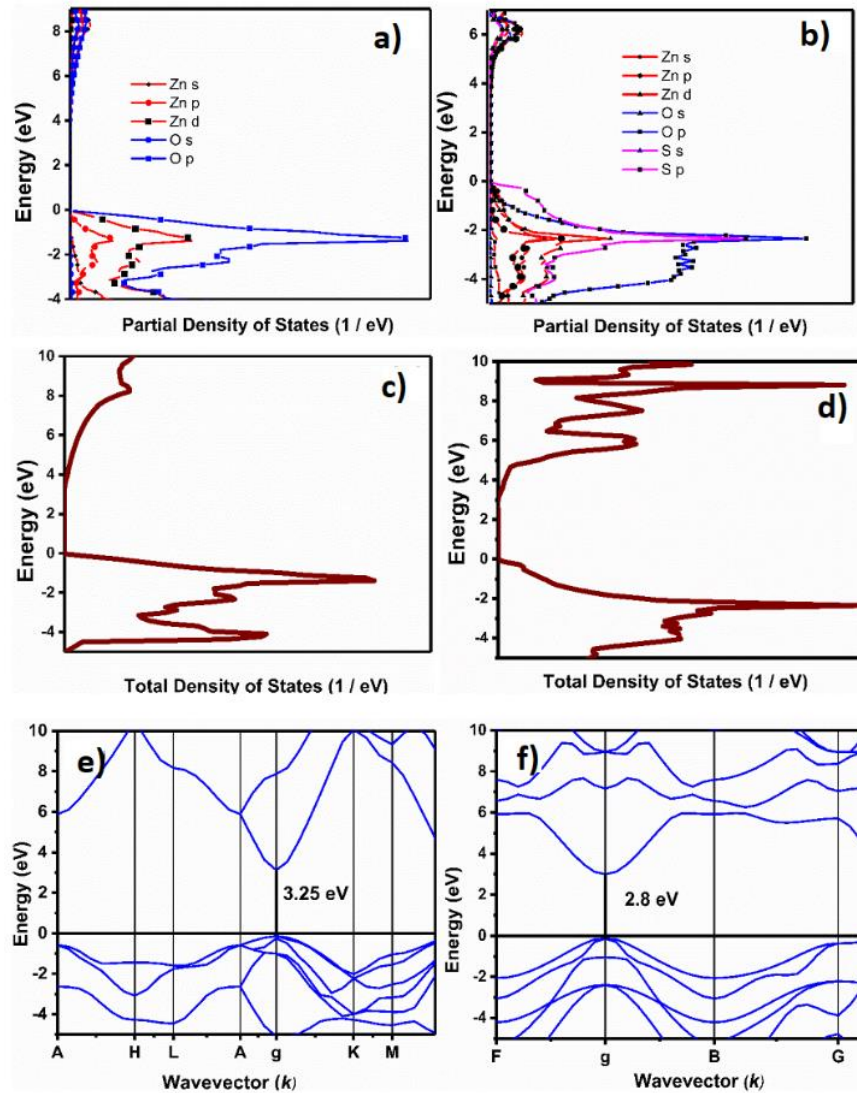
Figure 3.2 a), c) and e) Energy vs. partial and total density of states and band diagram of ZnO unit cell. b), d) and f) Energy vs. partial and total density of states and band diagram of S incorporated ZnO unit cell

3.1.2. Sb₂S₃ unit cell

The orthorhombic Sb_2S_3 unit cell (matching with the experimental results) was imported from the structure database available in MedeA Materials design Inc. The unit cell belongs to the Pnma 62 space group and D_{2h} point group, and all the atoms at the 4c Wyckoff positions. The lattice parameters of the structure are (JCPDS data # 421393, informatica ID 9007048) a = 11.3130 Å, b = 3.8411 Å, c = 11.2390 Å and α = β = γ = 90 °, volume = 488.3 Å ^{3}. According to Figure 3.3, Sb is occupied in in two lattices (Sb1 and Sb2), whereas S is identified in three positions (S1, S2 and S3). In the figure, the trigonal $Sb1S_3$ is formed with one Sb atom bonded to three S atoms with an average bond length of 2.5 Å. Also, each Sb2 atom is bonded to five S atoms, and the average bond length is 2.4 Å, forming the tetragonal pyramids composed of Sb-S₅ units. In the Figure, atom Sb1 has two bonds of Sb-S2 and one bond of Sb-S3, which both form a quasi-fourfold coordination with an average bond angle of 44.2 °. In comparison, atom Sb2 has three bonds of Sb-S1 and two bonds of Sb-S3, which has accomplished a quasi-sixfold coordination with an average bond angle of 46.06 °. The ground state properties of the structure for DFT calculations were done based on this structure, and the optimized structure parameters of $(Sb_2S_3)_4$ were lattice parameters of a = 11.3425 Å, b =3.8143 Å, and c=11.9723 Å with the volume and density of unit cell were 522.37 Å^3 and 4.3 mg/m^3 respectively.
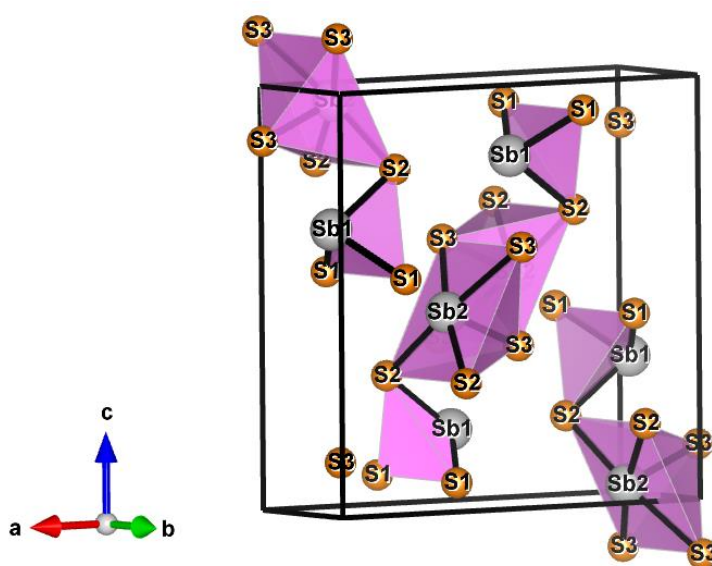
Figure 3.3 Orthorhombic Sb₂S₃ unit cell

3.1.2.1. Density of states and band diagram

Within the scope of this thesis, the HSE06 hybrid functional is used both as a short-range screened and a global hybrid functional. The hybrid functionals provide enhanced energy functionals where the LDA or GGA energy functional is combined with the Hartree Fock (HF) energy, resulting an improved capability of defining a broad spectrum of material properties. Improved exchange functional combined with a reduction in errors caused by self-interaction helps the hybrid functional HSE06 have precise measurements for semiconductors. The calculated partial density of states vs. E and E vs. k diagrams are presented in Figure 3.4. a and b, respectively. As can be seen in Figure 3.4 a), the s orbitals of the Sb1 and Sb2 atoms contribute to the density of states at the valence band edge, while the p orbitals contribute to the density of states at the conduction band minimum.
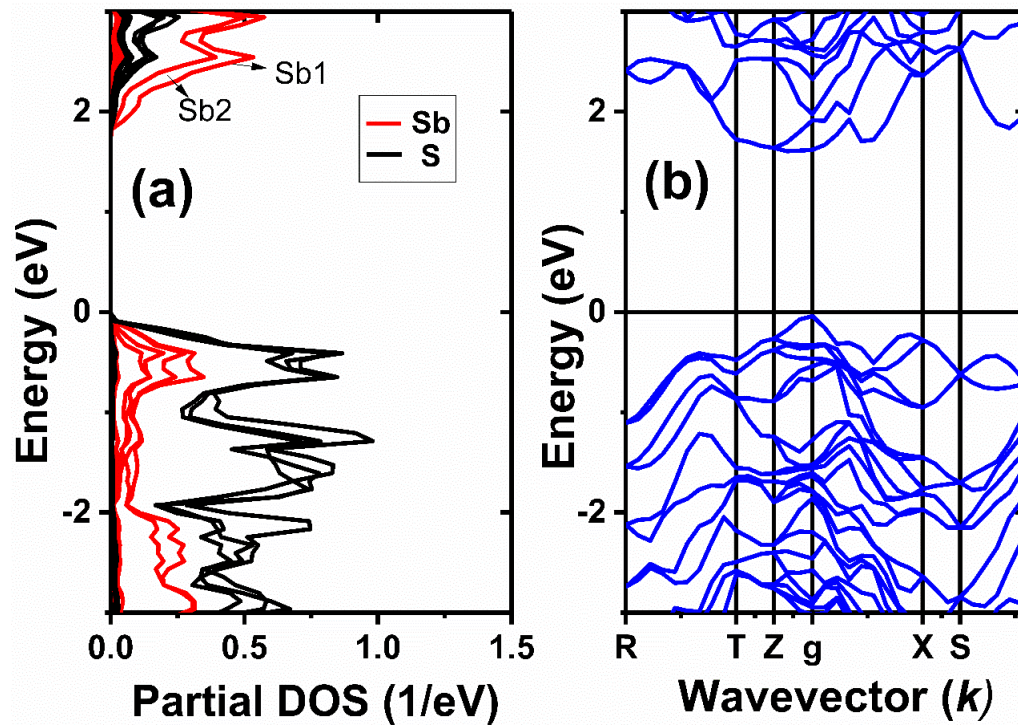
Figure 3.4. Density of states and band diagram of Sb_2S_3 unit cell

The contribution of Sb-d orbitals in the band edges was not influential. In the cases of S1, S2, and S3, the s orbitals contribute to the density of states at the edge of the conduction band, while the highly occupied p orbitals contribute to the density of states at the valence band edge. As a result,

the density of states of S p orbitals dominates the valance band, while the density of states of S 2p orbitals dominates the conduction band, as seen in a direct allowed transition from the point of the valence band, which is located at -0.06 eV, to the point of the conduction band, which is located at 1.56 eV leading to a band gap of 1.6 eV that is indicated in Fig. 3.4b) along the symmetric points R → T → Z → Γ→ X → S → Y.

The computed band diagram describes a flat conduction band minimum and a narrow valence band maximum (VBM), both coincide with the gamma point which defines a direct transition of electron from the valence band to the conduction band. Recent reports given in Table 6 predict an indirect optical band gap on using low accurate functionals except with mBJ and HSE06.

Table 6 Optical band gap reported for different functional.

Exchange-Correlational functional	E_g (eV)	Type of bandgap	Reference
PBE	1.2	Indirect	[131]
mBJ	1.71/1.74	Indirect/direct	[132]
HSE 06	2.15	Indirect	[133]
TB-mBJ	1.6	Indirect	[134]
LDA	1.1	Indirect	[135]
TB-mBJ	1.8	Direct	[136]
HSE 06	1.6	Direct	Present thesis

3.1.2.2. Vibrational band structure

Although there have been reports on the theoretical simulations of electronic and vibrational band structures, the parameters connected to the structure and Exchange-correlational functionals differ in each study; therefore, the nature and the properties vary appropriately. The precision of

the parameters that are employed in this thesis is a key contributor to the similarity between the outcomes obtained from the computations and experiments. The theoretical calculations (k point sampling using $2 \times 4 \times 2$ mesh) for Sb_2S_3 are one of the few that use more accurate DFT and incorporate hybrid exchange-correlational functionals of HSE06 for semiconductors.
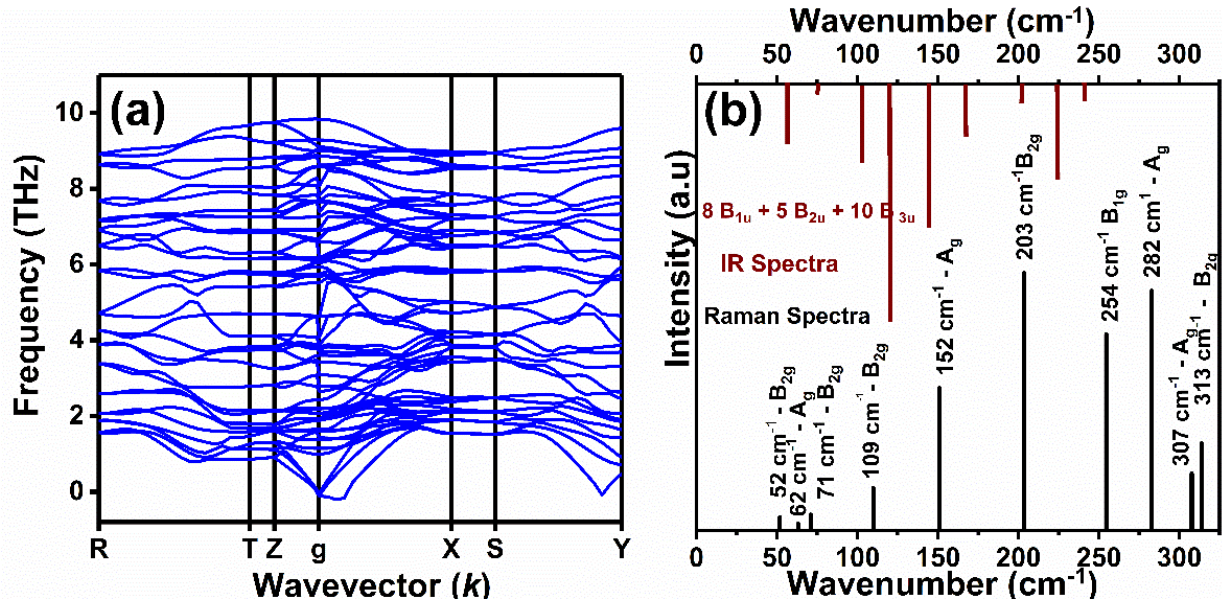
Figure 3.5. Vibration spectra of Sb_2S_3 based on the orthorhombic unit cell a) dispersion relation E vs. k b) Raman and IR spectra

The simulated dispersion curves of the vibrational frequency vs wave vector based on the structure and the lattice dynamics of Sb_2S_3 is shown in the figure 3.5. The unit cell contains a total of 4 molecules thereby 60 vibration modes are expected. Among 60 modes 3 are defined as acoustic modes (2TA, 1LA) and 57 are optical modes (39LO, 18TO). Among the 57 optical modes, 37 are Raman active and 22 IR active and 5 silent modes. From group theory, the irreducible representation of the vibration modes can be expresses as:

$$\Gamma_{vib} = 30\ \Gamma_{Raman} + 22\ \Gamma_{IR} + 3\ \Gamma_{acoustic} + 5\ \Gamma_{silent} \qquad (9)$$

The reported vibration modes consist of 10 A_g, 5 B_{1g}, 10 B_{2g} and 5 B_{3g} defining Γ_{Raman} and 22 IR modes. The Raman active A_g, B_{1g} and B_{2g} modes originated from the symmetry on inversion modes. Corresponding modes of S – Sb – S bending vibrations labelled at 62, 152, 282, and 307 cm^{-1} are categorized as A_g vibrational modes. The Sb – S stretching vibrations correspond to the antisymmetric modes B_{2g} and B_{1g} at 52, 71, 109, 203, 254 and 313 cm^{-1}. The IR active modes

comprised of $4B_{1u}$, $9B_{2u}$ and $9B_{3u}$ symmetry modes with irreducible representation $\Gamma_{IR} = 4\ B_{1u} + 9\ B_{2u} + 9\ B_{3u}$. The origin of LO - TO mode splitting in Sb_2S_3 unit cell arises from the Born effective charges. The reported study shows similar LO TO splitting in phonon dispersion with discrepancy in degeneracy of vibrational modes [137].

3.1.3. Cubic $Cu_{12}Sb_4S_{13}$

Figure 3.6 shows the cubic crystal structure of $Cu_{12}Sb_4S_{13}$ unit cell belonging to I-43m space group 217. The lattice parameter of the imported structure (Figure 3.6 a) from database has lattice parameter; a=10.35930 Å with volume of 1121.8 Å^3. Copper and sulfur atoms occupy two lattice sites: Cu1 at 12d Wyckoff position and Cu2 at 12e Wyck position. At the same time sulfur occupies two position S1 24g and S at 2a Wycoff positions while Sb occupies at 8c Wyckoff positions. Figure 3.6 b) displays the structural optimized unit cell with lattice parameter a=10.34930 Å with volume of 1108.8 Å^3
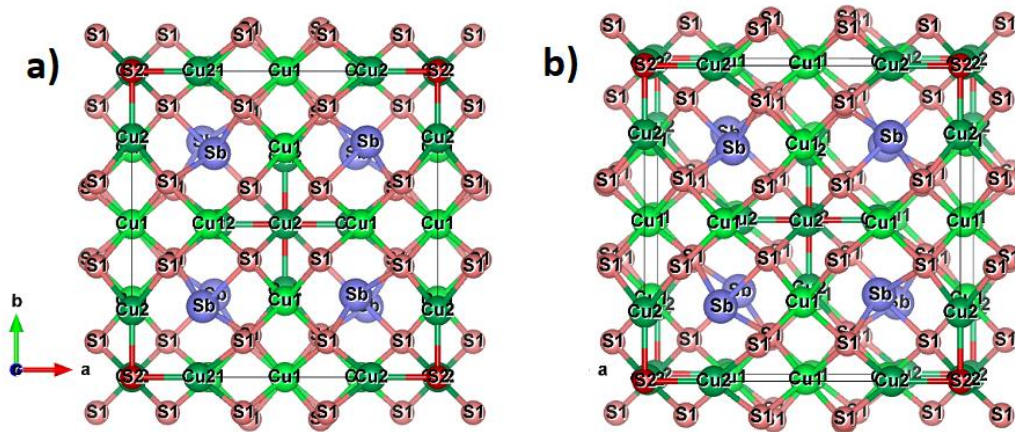
Figure 3.6 a) The initial structure of cubic unit cell of $Cu_{12}Sb_4S_{13}$ b) optimized structure of cubic $Cu_{12}Sb_4S_{13}$.

3.1.3.1. Density of States and band diagram

Figure 3.7 denotes the density of states and the electronic band structure. Electronic states as a function of energy are simulated using the cubic structure composed of Cu, Sb and S atoms. The valence band maximum is highly contributed by the orbitals of Cu2, S1 and S2 s while Sb and Cu1 have lower influence in the highly occupied orbitals. From the figure, conduction band minimum can be seen as highly influenced from the Sb p orbitals. The dispersion relation plotted

in the g → H → N → P → g → N direction predicts a direct electron transition from valence band to conduction band. The calculated band structure predicts an optical band gap of 1.4 eV.

3.1.3.2. Optical Spectra

Figure 3.8 corresponds to the frequency dependent optical constants of the structure. The electronic excitation of electron can be derived from the equation reported in following references [138]. The complex dielectric function over wavelength (equation 10) was resolved using Kohn Sham equation of energy levels yielding a matrix with imaginary and real parts of dielectric constant.

$$\varepsilon(\omega) = \varepsilon_r + \varepsilon_i \qquad (10)$$

Where $\varepsilon(\omega)$ denotes the complex dielectric function with real dielectric constant ($\varepsilon_r = n^2-k^2$) and imaginary dielectric constant ($\varepsilon_i = 2nk$).
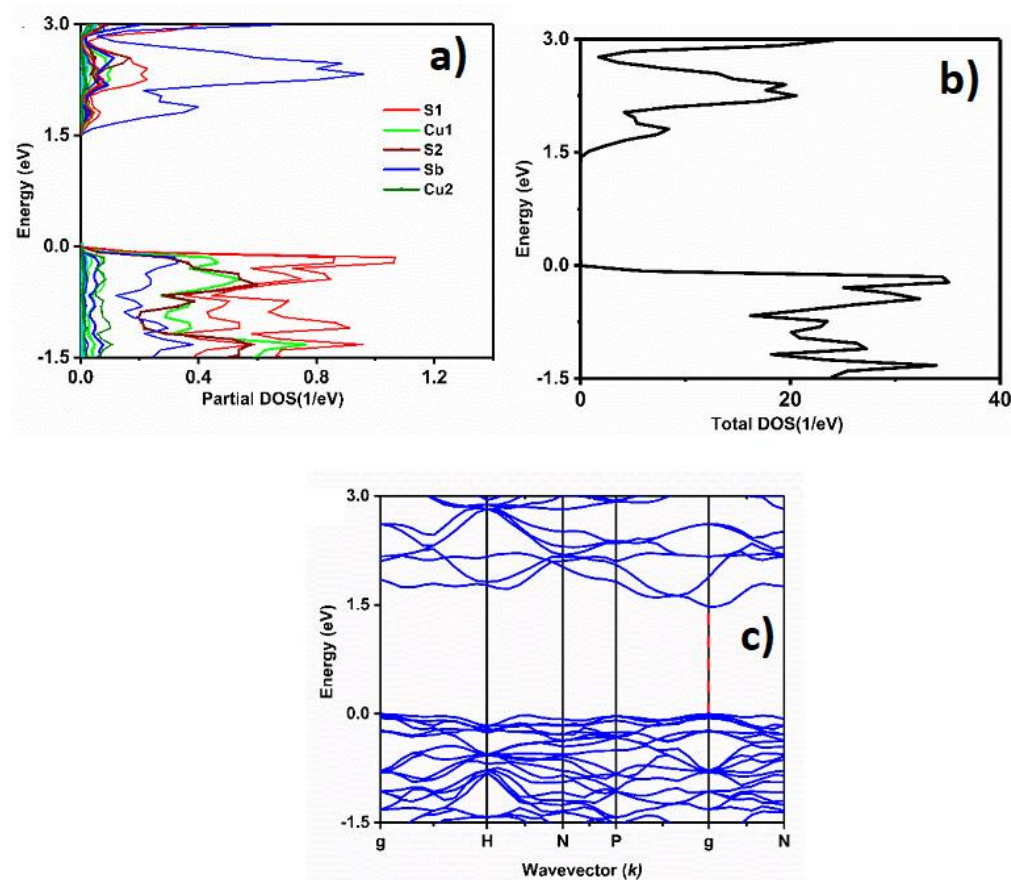
Figure 3.7 Density of states a) partial DOS vs. Energy b) Total DOS vs. Energy c) Energy band diagram, for the $Cu_{12}Sb_4S_{13}$ unit cell.

From figure 3.8, the real part of the dielectric constant has higher values (~11) at shorter wavelengths (~ 250 – 700 nm) indicating high energy storing capability on applied electric field while longer wavelength such property diminishes. While the imaginary dielectric constant increase at longer wavelength (> 800 nm) indicates the absorptive nature of the material in visible spectrum.
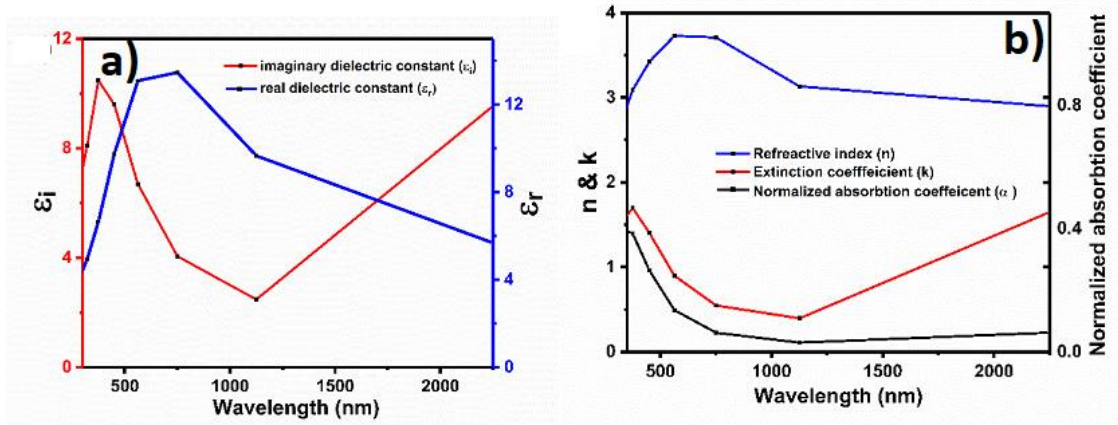
Figure 3.8 Wavelength dependent optical constants of the simulated $Cu_{12}Sb_4S_{13}$ unit cell a)real and imaginary parts of the calculated dielectric constants b) refractive index, (n) extinction (k) and coefficients and normalized absorption coefficient.

3.2. SCAPS 1D

SCAPS 1D software is used to simulate the solar cell structure of configuration FTO/ZnO/Zn (O, S) /Sb_2S_3/$CuSbS_2$ as shown in Figure 3.9. Simulation is modelled in one dimension throughout the layers with junctions formed in physical space. During simulation, parameters which affect the efficiency of the solar cell were varied. Transparent conductive oxides (TCOs) window layer layers are ZnO and ZnO (O, S). Copper antimony sulfide ($CuSbS_2$) is used as absorber layer while antimony sulfide (Sb_2S_3) layer is introduced between absorber and window layer. The effect on variation in structural and electronic parameter on the above layers on simulation can give an insight to the experimental fabrication of solar cell devices.
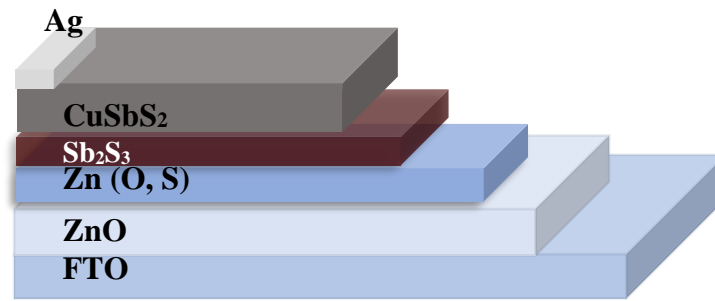
Figure 3.9 Schematic representation of solar simulation on structure ZnO/Zn (O, S)$/Sb_2S_3/CuSbS_2$

i) Effect of thickness of absorber layer in power conversion efficiency

The thickness of the absorber layer has a significant effect in the cell performance as shown in the J-V characteristics shown in figure 3.10. As the thickness of the absorber layer increases the 100 nm to 250 nm, the short circuit current density increases significantly while the open circuit voltage remains constant.
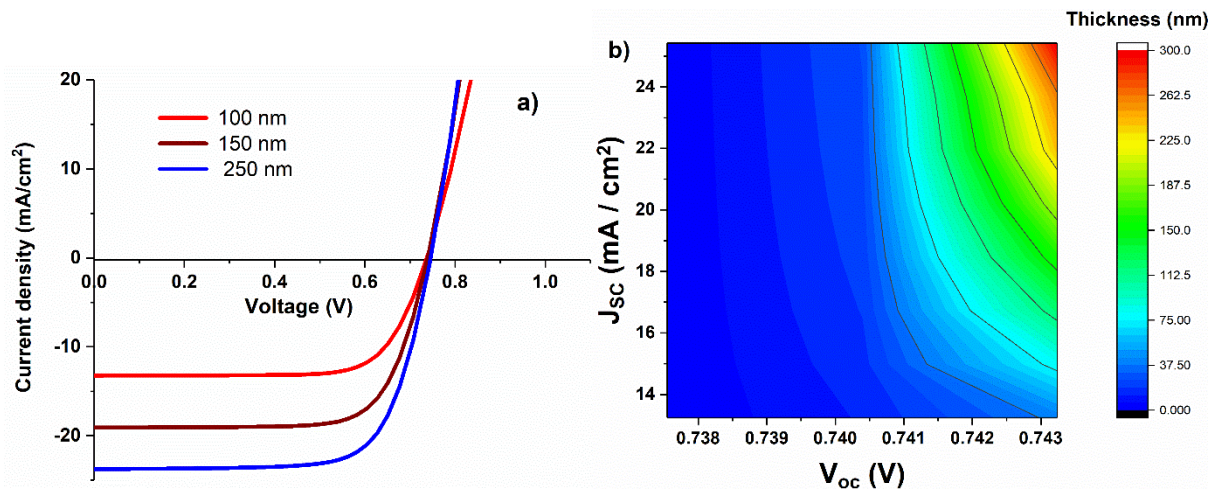
Figure 3.10 The effect of thickness in the absorber layer and contour graph on the effect of thickness in J_{sc} and V_{oc}

The increase in J_{sc} is attributed to the increase in the absorption of photon thereby the photogenerated charge carriers[139]. The contour zone shown in Figure 3.10 signifies the highest J_{sc} value lies around 250 nm to 300nm where beyond 300 nm a saturation of J_{sc} as well as V_{oc} is observed. The corresponding efficiency and fill factor are given in Table 7.

Table 7. Effect of variation of absorber thickness in the solar cell structure

Absorber Thickness (nm)	J_{sc} (mA/cm^2)	V_{oc} (V)	Fill factor (FF)	Efficiency (%)
100	13	0.706	62	5.6
150	19.4	0.742	64	9.2
250	23.73	0.754	65.5	11.7

ii) Effect of carrier concentration in absorber and window layers

The carrier concentration of absorber and window layer plays a significant parameter influencing the power conversion of solar devices. The carrier concentrations varied from 10^{12} to 10^{18} (1/cm^3) in absorber layer and window layers as shown in Figure 3.11. From the figure, increase in the carrier concentration in absorber layer directly reduces the J_{sc} and V_{oc} and this effect is primarily attributed to the carrier recombination loss at the bulk material and interface. The increase in the concentration of acceptor charge carrier proportionally reduces the charge life time of photogenerated carrier resulting in the reduction of carriers at the interface [140]. Also, the stagnation of low V_{oc} and J_{sc} by high carrier concentration suggests a lightly doped material can effectively act as an efficient absorber material as seen in the figure.
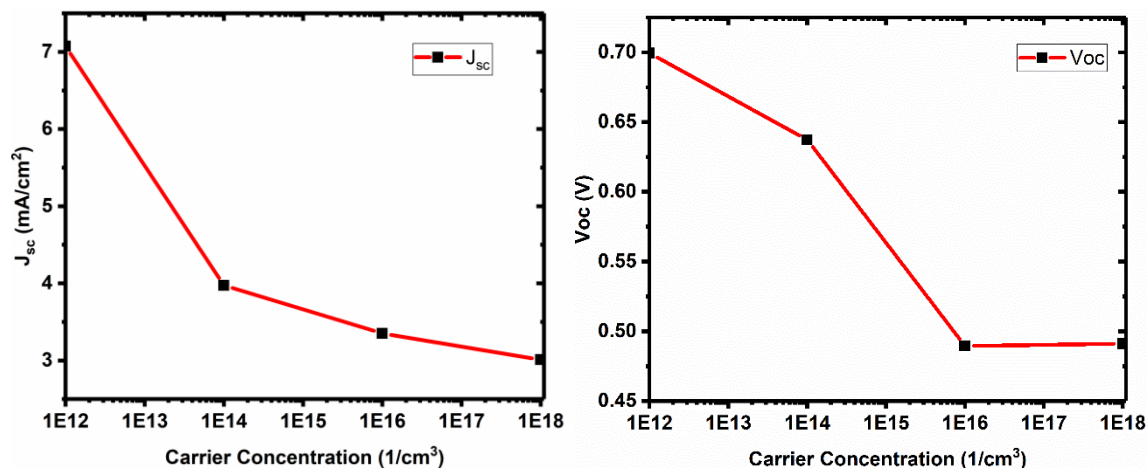
Figure 3.11 Effect of carrier concentration of absorber layer in J_{sc} and V_{oc} of the solar cell

Figure 3.12 shows the effect of carrier concentration in the window layers on V_{oc} and J_{sc}. J_{sc} and V_{oc} increment on increased carrier concentration can be achieved by doping and post annealing treatments. High carrier concentration in window layer allows the depletion region to be more penetrated towards the lightly doped p-type $CuSbS_2$ absorber layer, thereby allowing enhanced photo carrier generation within the depletion region and effective charge separation because of existing electric field, causing enhanced J_{sc}[141].
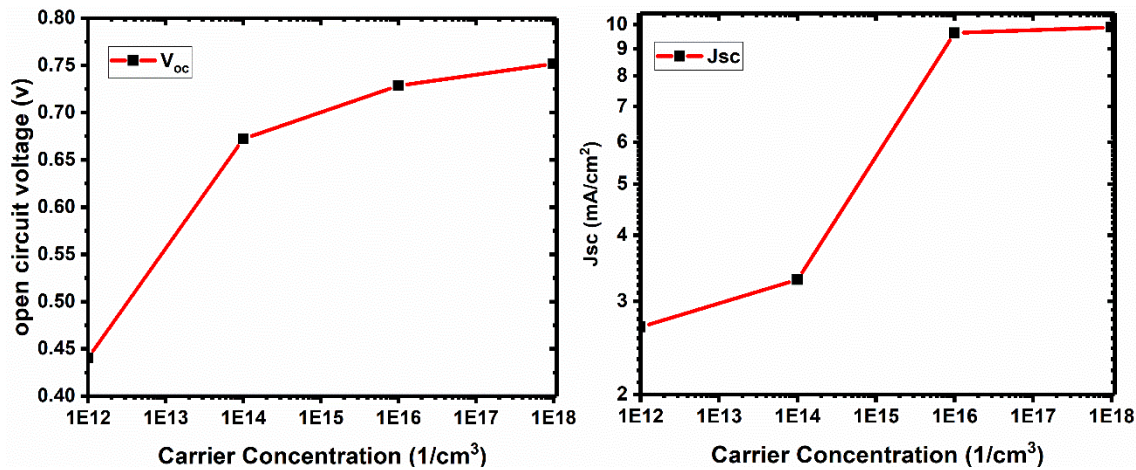
Figure 3.12 Effect of carrier concentration of window layer in J_{sc} and V_{oc} of the solar cell.

iii) Effect of Sb_2S_3 near intrinsic layer

In the proposed structure, Sb_2S_3 layer with low carrier concentration acts as near intrinsic layer with a goal to optimize the interfacial and bulk recombination via passivation of absorber bulk defect. The losses in fill factor and recombination are the main efficiency limiting parameters in solar cell devices. Passivation of bulk defect density in absorber layer can enhance the current density and thus control the efficiency of the solar cell [142]. In the figure 3.13, the open circuit voltage has been improved attributed to the better band alignment by the insertion of Sb_2S_3 between absorber and CdS window layers by chemical bath deposition as reported by Y. Rodríguez-Lazcano *et al.* [143]. The short circuit current density rises by the passivation of charge

carriers due to the extension of depletion region near intrinsic layer, which in turn increases the lifetime thereby enhanced charge extraction. Teimouri *et al.* reported simulation using CuSbS$_2$ layer as hole transport layers due to their high absorption coefficient and high hole mobility. A low cost, nontoxic and earth abundant materials like copper chalcogenides were proposed as absorber and hole transport layers in perovskite solar cells [141]. In the simulation analysis it was reported that ternary CuSbS$_2$ layer possesses a lower HOMO level (-5.25 eV) compared to copper indium sulfide compounds (-5.43 eV). The major limiting factor of hetero junction solar cell was the conduction band offset (CBO). The value of CBO lies between -0.7 – 0.4 eV shows constant J$_{sc}$ while CBO >0.4 eV cause significant reduction in the J$_{sc}$. Sadanad *et al.* reported the simulation studies of CBO of CuSbS$_2$ film in the hetero junction with transparent conductive oxides are well matched of the enhanced J$_{sc}$ [144].
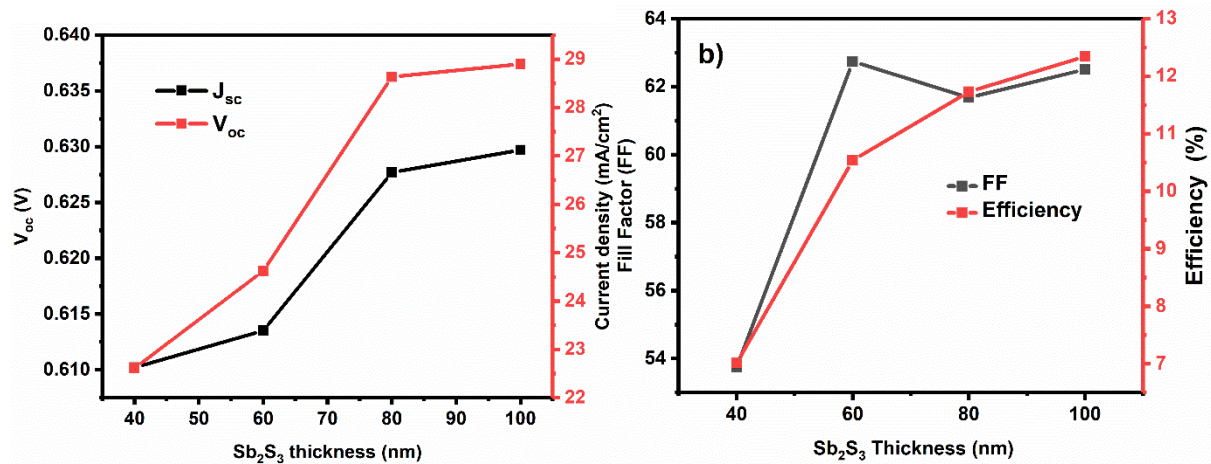
Figure 3.13 Effect of Sb$_2$S$_3$ thickness in the solar cell parameter

Thus, after knowing the theoretical properties, in the forthcoming chapters, experimental results on synthesis, characterization of optical and electronic properties of ZnO, Zn(O,S), Sb$_2$S$_3$, different phases of copper antimony sulfides and the devices formed by incorporating these thin films are discussed.

CHAPTER 4

Results and Discussion: Ultrasonically spray pyrolyzed ZnO and Zn (O, S) window layers

In this chapter, deposition of ultrasonically spray pyrolyzed ZnO and S incorporated ZnO thin films are described. Transparent conductive oxide (TCO) layers exhibit high optical transparency and electrical conductivity. Hence TCOs can easily transmit incident radiation to the p-n junction and at the same time act as an electrode for the photogenerated charge carrier extraction. In hetero junction devices conduction band offset (CFO) is defined as the mismatch in the conduction band minimum edges when semiconductors are aligned. To reduce the mismatch this study focuses on anion doping (S^{2-}) in host lattice (ZnO TCOs) which can alter the structural, optical and electrical properties thereby improving the band alignment.

4.1. X - Ray diffraction (XRD)

Figure 4.1 shows the diffraction patterns of ZnO and Zn (O, S) thin films deposited at a substrate temperature of 400 °C. Sample marked as ZO assigned for the undoped ZnO thin films while S incorporated thin films were marked as ZOS. Thioacetamide was used as the S source for the anion doping with weight percentage 0.8 and 1.6 % of zinc acetate denotes as ZOS 0.8% and ZOS 1.6% as shown in the Figure. In all the cases, only one peak located at 2θ =34.5° is detected which is indexed to (002) plane of the hexagonal crystal structure of ZnO (JCPDS # 790205), There are no peaks corresponding to any other planes or other crystalline phases present in the films. The strong reflection of the (002) plane suggests a preferred orientation of the film growth along the c axis perpendicular to the substrate plane, which has the potential to increase charge carrier transport. During the process, the film growth tends to reduce the surface energy by diffusing atoms into the surface layer with the lowest energy of a specific crystallite. According to the Van der Drift model, the nuclei that have the greatest potential for rapid expansion on the substrate have a preference for expanding in a certain direction[145]. Nevertheless, the hypothesis that is based on the growth to minimize the surface energy, or in this instance (002) planes, is the one that is more applicable. Therefore, crystallite development occurs mostly in the direction [002], which is perpendicular to the surface of the substrate. This results in an increase in thickness, while the orientation distribution shifts towards the crystallographic direction of the surface which has the lowest energy[146,147]. During the spray pyrolysis process, it requires greater mobility

for the surface atoms, which is a requirement that could be readily achieved through adjusting the substrate temperature properly.

As can be observed in Figure 4.1 a, the diffraction angle (2θ) changes in the case of ZnO:S, shifting towards smaller values. Compared to that of the pure ZnO film, the presence of 0.8% sulfur (ZOS 0.8%) caused the location of the (002) peak to shift from 34.5 to 34.4°, and then to 34.33 ° when the sulfur percentage become to 1.6% (ZOS 1.6%). The incorporation of S into ZnO results in the deformation of the lattice as well as the presence of (100) and (101) planes that have a very low intensity. These planes grow at the cost of (002) oriented crystallites, as seen by the decrease in peak intensity shown in the graph. This can be attributed to the possibility that the S^{2-} (184 pm) anions occupying the interstitial or O^{2-} (140 pm) anion sites of the ZnO lattice [148,149].
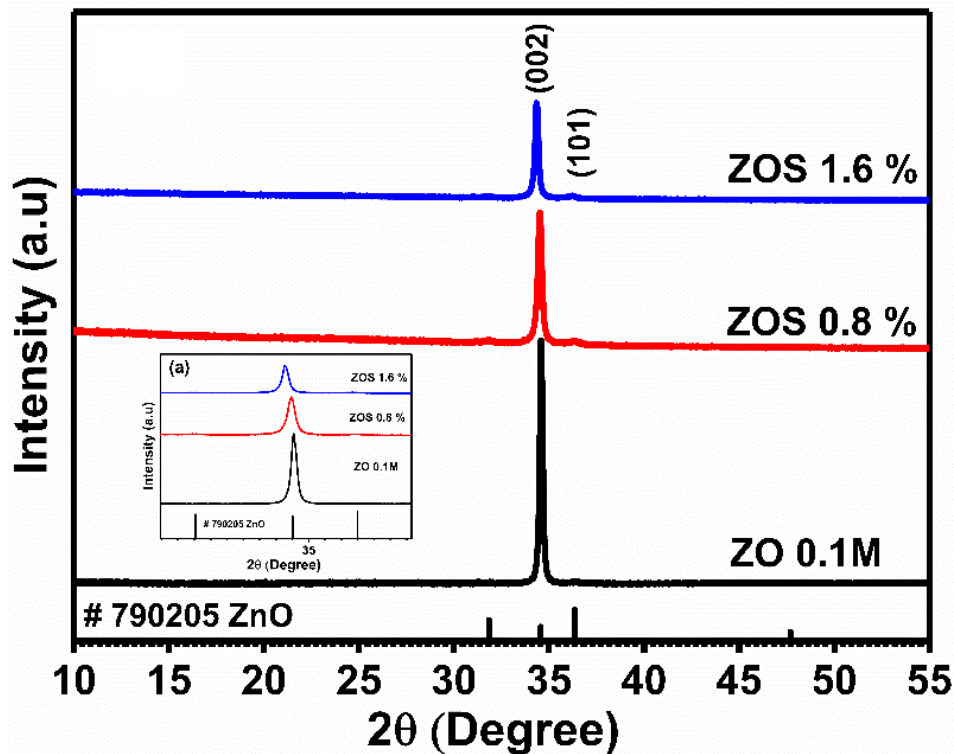
Figure 4.1 The diffraction patterns of ZnO and S incorporated ZnO thin films (Zn (O, S)) with zoomed inset graph shows the variation on peak position on S incorporation.

It is observed a rise in distortion as more S^{2-} was incorporated into the film. Figure 4.2b) demonstrates that the peak intensity varies with post thermal treatments (mentioned in section **2.4.1.**) indicating improved crystallinity. The influence of thermal treatments on the structure of

ZnO:S (0.8%) can be seen in Figure 4.2c). The peak intensity is lowered by vacuum annealing and air annealing, but it is increased by rapid thermal treatment. The incorporation of S into the ZnO lattice increases the peak broadening, which indicates a decrease in crystallinity compared to Figure 4.2 b).
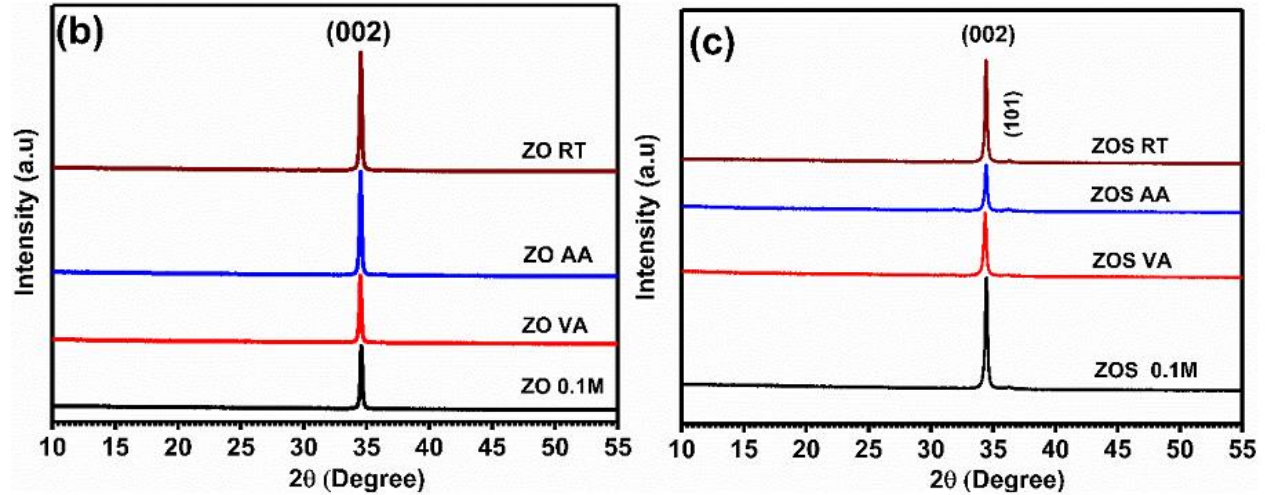
Figure 4.2 Post thermal (Vacuum annealed (VA), Air annealed (AA) and Rapid thermal process (RTP) treated samples of b) ZnO and c) S incorporated ZnO thin films.

The crystallite size was calculated using Scherr's formula given below (equation 11).

$$D = \frac{K\lambda}{\beta cos\theta} \qquad (11)$$

where D is the crystallite size, λ is the wavelength of the X-ray source, β is the full width half maximum of the peak and θ is the diffraction angle, K is the shape factor. Table 8 shows the calculated crystallite size from Scherr's equation.

The crystallite size is increased on different annealing condition. At elevated temperature on annealing the atoms in the grains achieve higher mobility which in turn allows the enhanced migration and grains tends to rearrange themselves. This can lead to coalescence of smaller grains to larger grains which can be evident in Table 8.

Table 8. Crystaline size of the ZnO and Zn (O, S) thin films

Samples	Crystallite size (nm)
ZO 0.1M	38
ZO VA	41
ZO AA	40
ZO RT	38.5
ZOS 0.1M	30
ZOS VA	36
ZOS AA	32
ZOS RT	35

4.2. Energy Dispersive X-Ray Spectroscopy (EDS)

Using energy dispersive X-ray spectroscopy, semi-quantitative elemental analysis was performed on the samples. Figure 4.3 shows the EDS spectra (Figure 4.3 a) and elemental mapping (Figure 4.3 b) and c) of 0.1M ZO thin films. The atomic percentages of zinc and oxygen in ZnO thin films are 49 and 50.4 %, respectively, validating the stoichiometry of zinc oxide thin films, and no additional impurities were detected. The EDS spectra (Figure 4.4 a) show the purity of the films with Zn, O and S and EDS mapping shows the uniform distribution of Zn, O and S elements throughout the samples. The atomic percentage of sulfur in the ZnO (ZOS 0.8%) thin films is 0.9% along with 47% zinc and 51% oxygen. Table 9 summarizes the atomic percentages of ZnO and S incorporated ZnO thin films. The atomic percentages of Zn and O in ZO films remained same while ZOS films atomic percentage of Zn is lowered due to the evaporation. The presence of O can be summed up from the substrate. So, it can be concluded that the S can occupy the Zn interstitials which can be one reason for the lower mobility of the charge carriers in ZOS films.
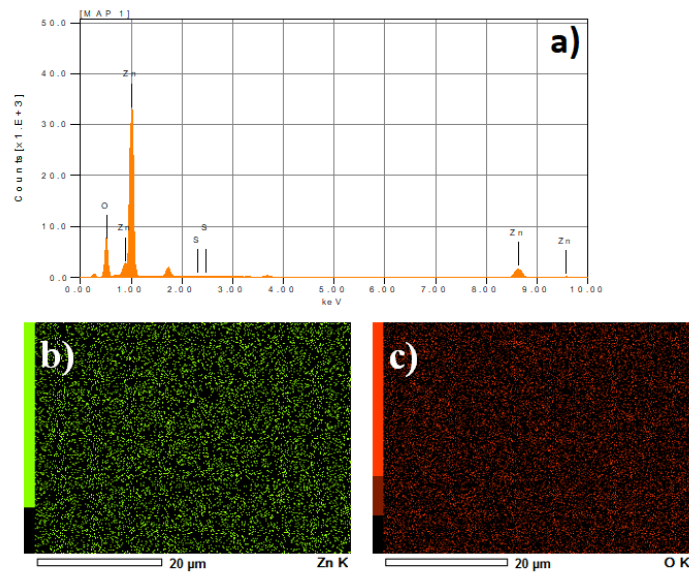
Figure 4.3 a)EDS spectra and mapping of the elements b) Zn c) O detected from the sample 0.1M ZnO.
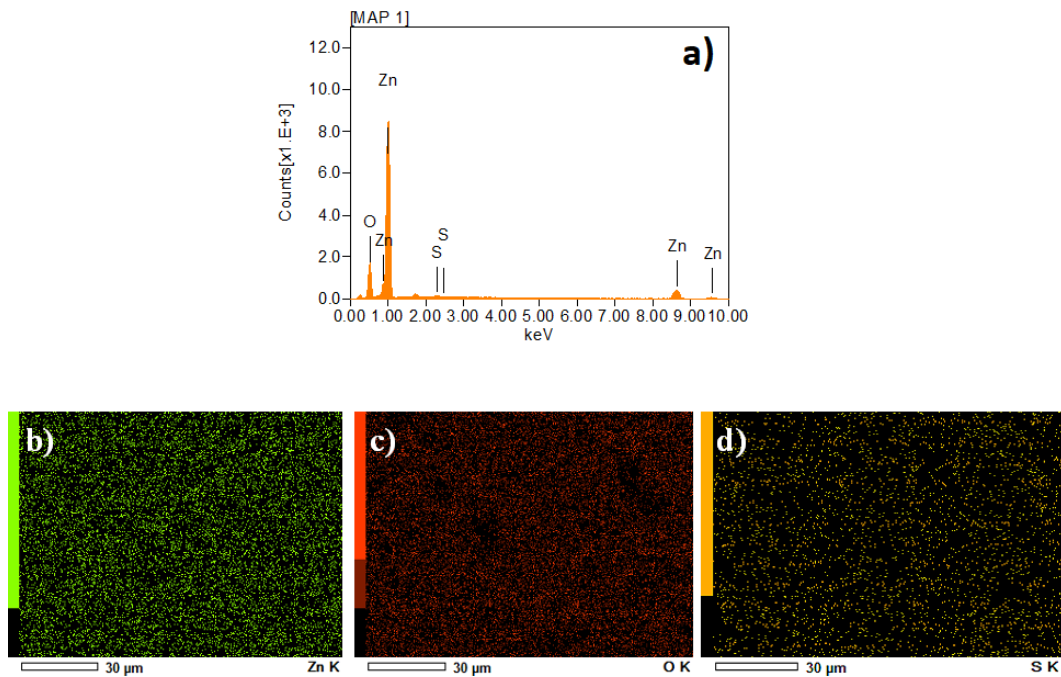
Figure 4.4 a) EDS spectra and mapping of the elements b) Zn c) O and d) S from the sample 0.1 M ZOS

Table 9. Atomic composition of elements recorded in ZnO thin films.

Samples	Zn %	O %	O/Zn	Samples	Zn %	O %	S%	S/O
ZO	49.5	50.5	1.02	ZOS	47.0	51.7	1.2	0.02
ZO-VA	49.9	50.1	1.0	ZOS-VA	48.0	51.3	0.6	0.01
ZO-AA	49.1	50.9	1.03	ZOS-AA	46.9	52.0	1.1	0.02
ZO-RT	49.6	50.2	1.01	ZOS-RT	47.9	51.5	0.7	0.01

4.3. X-Ray photoelectron spectroscopy (XPS)

The XPS analysis was used to evaluate the elemental composition of the surface and the respective chemical states of elements in ZnO and ZnO:S samples. The X-ray source AlKα (Energy:1486.68 eV, Voltage: 12 keV, Current: 3×10^{-3} A) was coupled with micro-focused X-ray monochromator. The binding energy scale calibration and linearity were confirmed using Ag $3d_{5/2}$ peak with FWHM 0.9 eV. A flood gun was used for the charge compensation in sample surface. Analysis includes the survey spectrum, high resolution spectra and depth profile.

Figure 4.5 a) shows the survey spectrum, fitted peaks of high-resolution Zn and O core levels of as prepared and post-thermal treated ZnO thin films. The survey spectrum reveals the elemental presence in the sample surface. It was evident from the figure that all peaks identified as the Auger and core electron peaks of the elements Zn and O. In Figure.4.5 b, the core level spectra of the as-prepared films consist of Zn $2p_{3/2}$ (B.E-1021 eV and $2p_{1/2}$ (B.E-1044.6 eV) doublet peaks separated by 23.1 eV. The B.E values can be ascribed to Zn^{2+} state in ZnO [150]. Figure. 4.5. c) shows O 1s core level, which can be fitted into two symmetric singlets: O_I with lower binding energy (530.2 eV) corresponding to the O^{2-} state [151], bonding with Zn^{2+} in the hexagonal wurtzite lattice, and O_{II} with higher binding energy (B.E-532.1 eV) corresponds to the weakly bonded O atoms at vacancy sites where theses site can act as electron donor sites, as marked in the figure . In the annealed samples, Zn $2p_{3/2}$ and $2p_{1/2}$ binding energy values are apparently the

same as in the pristine, but the O 1s peak are shifted towards higher values due to changes in the chemical environment induced on neighboring oxygen 1s orbitals by the oxygen vacancies [152,153]. The vacuum annealed film (ZO VA) exhibit the highest B.E of O 1s peak at 531.2 eV and 532.9 eV, as shown in the figure. The relative drop in intensity implies that the atomic concentration of O_{II} is lowered, indicating that vacuum annealing created lattice vacancies by removing oxygen. In the case of air-annealed samples (ZO AA), O_{II} peak value remains unchanged as that of ZO VA. Moreover, rapid thermal treated film (ZO RT) O 1s core level B.E values are identical to that of pristine film, indicating no major change in the chemical environment due to vacuum annealing or rapid thermal processing. Figure 4.5d) shows the uniform distribution of Zn and O present in the sample via depth profile analysis. The peaks position of Zn and O orbital confirms the chemical states of Zn^{2+} and O^{2-}
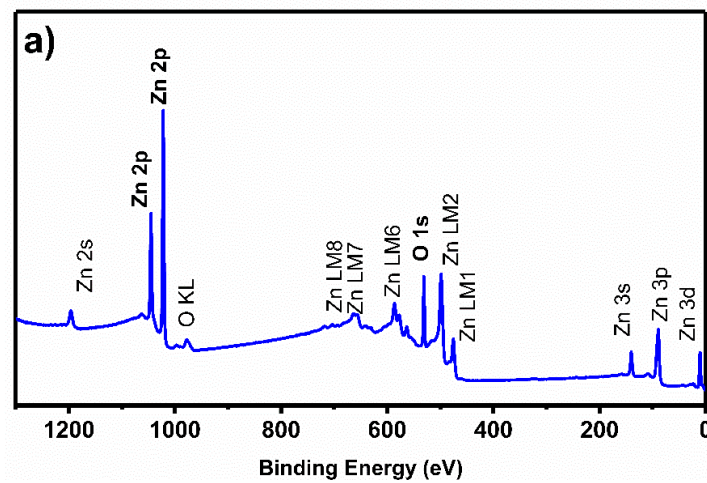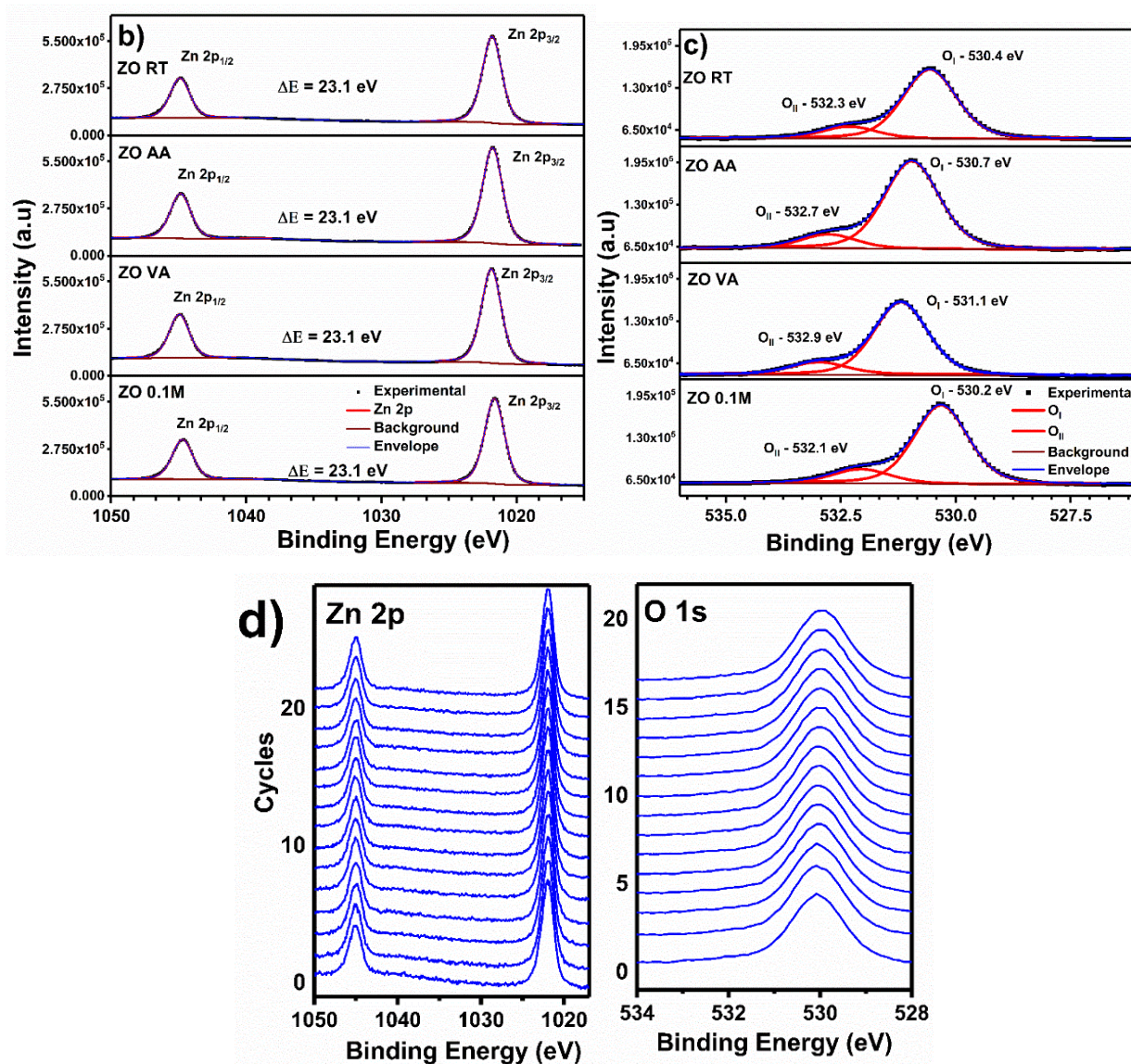
Figure 4.5 XPS spectra of ZnO thin films a) survey spectrum, high resolution spectra of zinc 2p b), and oxygen 1s c), and d) depth profile of the elements detected from ZO 0.1M sample substrate to surface.

Figure 4.6 a) displays the survey spectrum of a typical ZnO:S (ZOS 0.8%) thin film. Figure 4.6 b) shows high-resolution core level spectra of Zn 2p levels of as prepared and post-thermal treated films of ZnO:S (ZOS 0.8%, ZOS VA, ZOS AA, and ZOS RT). As mentioned earlier, ZnO:S (ZOS 0.8%) Zn 2p peak B.E corresponds to $2p_{3/2}$ (1021 eV) and $2p_{1/2}$ (1044 eV) peaks with B.E separation of 23.1 eV. The B.E values are related to the presence of Zn^{2+} as specified above. The

fitted O 1s peaks (O_I - 530.1 eV and O_{II} - 531.8 eV) are given in Figure 4.6 c. Oxygen ions in ZnO lattice correlates to O_I peaks. Fig. 4.6 d) shows weak intense peaks the corresponding S 2p core level spectra that can be fitted to 2 $p_{3/2}$ with B.E of 161.7 eV and 2 $p_{1/2}$ of 162.9 eV separated by 1.1 eV as marked. From the Figure, it is observed that post-thermal treatments reduce S 2p peak intensity. In sample ZOS VA, no change in B.E of Zn 2p is noticed, whereas O_I (530.7 eV) peak is shifted to higher B.E than that that in ZOS. The oxygen peak at B.E 529.9 eV suggests sulfur replacement with oxygen due to air annealing. Rapid thermal treated films (ZOS RT) can lose sulfur with less oxygen replacement due to reduced O 1s B.E (530.6 eV). Figure 4.5 e) shows the depth profile with Zn and O detected throughout the film with the presence of S from the surface to substrate.
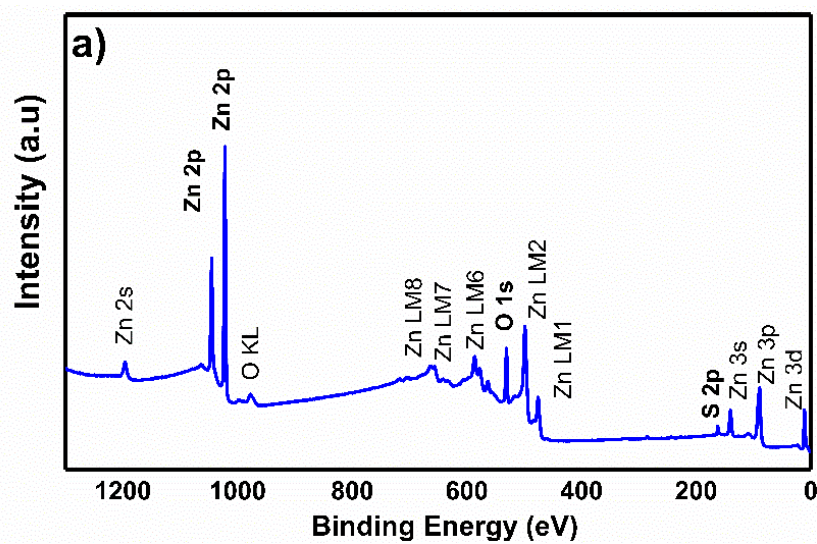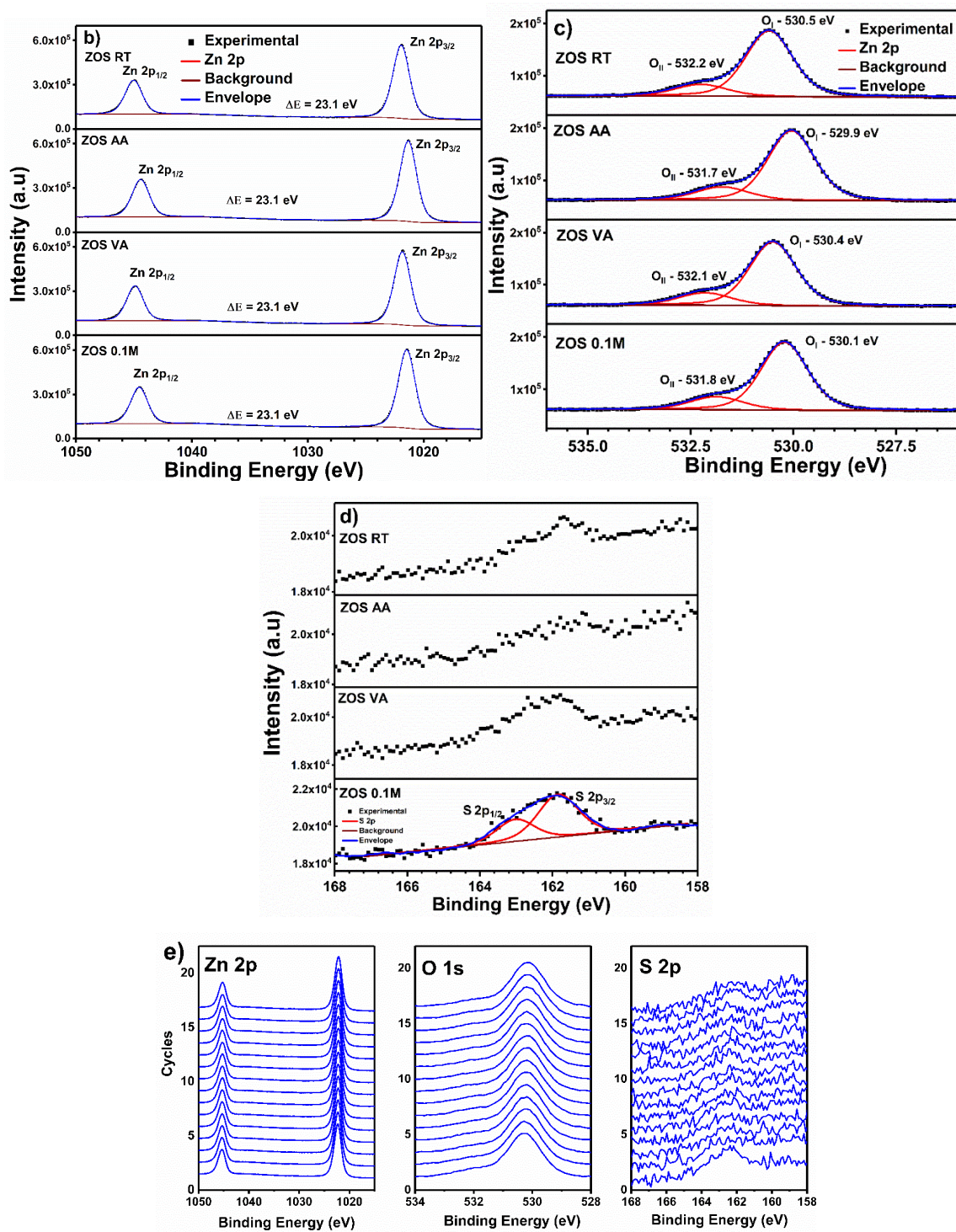
Figure 4.6 XPS spectra of S incorporated Zn (O, S) thin films with a) survey spectrum, high resolution spectra of Zn 2p b), O 1s c) and S 2p d) ions, and depth profile of the elements in ZO 0.1M detected from substrate to sample surface.

4.4. Scanning Electron Microscopy (SEM)

Figure 4.7 shows the SEM images which reveal morphology of as prepared and post thermal treated ZnO thin films. In general, the film surfaces are of uniform and compact morphology. ZO (Figure 4.7a) and ZO-VA (Figure 4.7 b) samples possess similar features of uniformly distributed spherical grains. ZO-AA (Figure 4.7 c) and ZO-RT (Figure 4.7 d) thin film have flake-like or faceted grain distributions. Thermally induced grain development mechanism increases kinetic energy of atoms or molecules enable them to mobile freely led to facilitate the crystal growth [154]. The diffusion rate of grains were directed to the coalescence of grains which can be related from the crystallite size calculation. The incorporation of sulfur affects ZnO grain development (Figure 4.8 a–d). The inhibition of grain growth can be observed on the morphology of S incorporated ZnO thin films (Figure 4.7). From the diffraction pattern, crystallite size calculation showed reduced size (<34 nm), which can be attributed to retarded crystal growth by S incorporation to the ZnO lattice. The larger ionic radii of S^{2-} anions slowed ZnO grain development, where anion dopants can promote localized stress field that act as barrier for the grain boundary migration [155]. Using spray pyrolysis deposition method, morphology of the films is highly influenced by substrate temperature, type of precursors and annealing temperature. Kenankis *et al.* reported thin films composed of surfaces with inhomogeneously distributed smooth granular grains using ultrasonic spray pyrolysis, in which the molarity and the substrate temperature where highly influenced on the optoelectronic properties[156]. While Ma *et al.* reported that in ultrasonic spray pyrolysis the sequential increment of substrate temperature led to the variation in morphology from closed packed nanosheets to dense equiaxed nanograins [157].
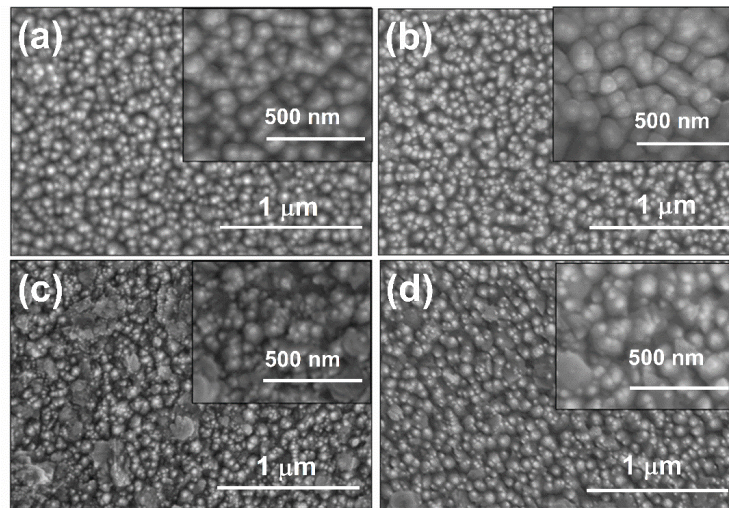
Figure 4.7 Surface morphology of ZnO thin films: a) ZO b) ZO VA c) ZO AA d) ZO RT
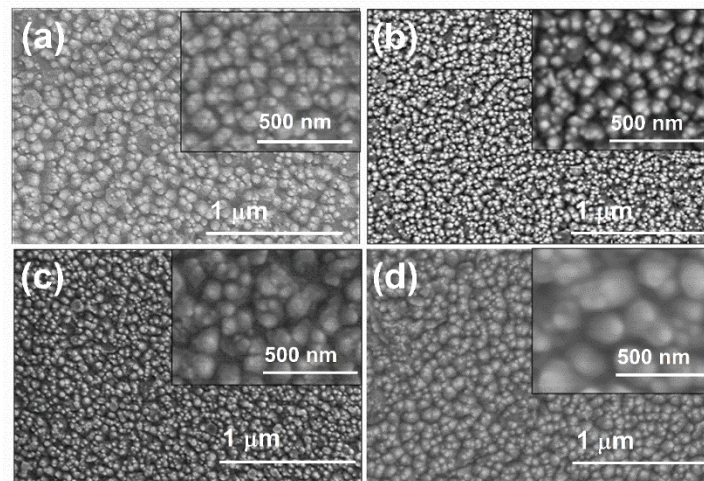
Figure 4.8 Surface morphology of S incorporated ZnO thin films; a) ZOS b) ZOS VA c) ZOS AA d) ZOS RT

4.5. Optical Properties

The optical properties ZnO and ZnO:S thin films are shown in Figure. 4.9 (a-d). Figure. 4.9 a) shows the transmittance (T%) and reflectance (R%) spectra of ZnO thin films on posting thermal treatments. The visible and NIR (non-absorbing region) spectra of the ZnO thin films reveal above 80% transmittance and ~15% reflectance (Figure 4.9 a). ZnO:S films show transmittance was

reduced (<80%) on S incorporating in thin films (Figure. 4.9c). The introduction of scattering centers on the anion incorporation on host lattice affect the grain boundaries can also attributed to the lower transmittance of the incident radiation. In the Figure, interference patterns composed of the transmittance maxima coincides with reflectance minima indicating specularly reflecting nature of homogeneous and smooth surfaces of the films, that prevent scattering due to surface roughness. Figure. 4.9b) illustrates absorbance vs. wavelength spectra where absorbance is calculated using the equation (12) given below:

$$Absorbance = ln\frac{(1-R)^2}{T} \tag{12}$$

Where T indicates transmittance and R as reflectance at a specific wavelength obtained from the respective spectra of the films. The optical band gap corresponding to a direct allowed transition is calculated using the given equation (15).

$$(\alpha h\upsilon)^2 = A(h\upsilon - E_g) \tag{13}$$

where α denotes the absorption coefficient at frequency ν, n reveals the nature of the transition involved, and possible values of n are 2, 1/2, and 2/3 for direct allowed, indirect allowed, and forbidden direct transition respectively and where E_g defines the optical band gap. Fig 7b) displays absorption spectra of as prepared and post thermal treated ZnO thin films. The optical band gap values are computed from the Tauc plots of $(\alpha h\nu)^2$ vs hν. as given inset in Figure 4.9 b). In the Figure, optical band gap (E_g) is calculated by linearly extrapolating the $(\alpha h\nu)^2$ to hν axis. The linear plots show a straight line spanning to hν axis at 3.2 eV corresponding to αhν = 0   for ZnO thin film. Similarly, the optical band gap of Zn (O, S) thin films is also evaluated as shown in Figure. 4.9 d). From the figure it is clear that S incorporation in ZnO reduces the optical band gap to 2.8 eV and this may be due to S doping-induced intra band states which in turn decreases the optical band gap [158]. For Zn(O,S) vacuum annealed (VA) and air annealed (AA) films, the absorption edge shows a shift to longer wavelength in the spectra due to an increase in the defect states present in the thin films [159] and change in the structural disorder induced bond angle and length creates defects near band edges due to dopants [160]. Substitutional dopant ions can produce empty electron states in the conduction band, which shifts the absorbance spectra to longer wavelengths. Incorporation of S in the ZnO lattice can alter the electronic density of states which affects the probability of electronic transition from

valence band to conduction band and that can influence in the absorption of incident radiation [161]. Together, the localized energy states introduce in the band gap by the incorporation of S in the ZnO lattice led to the shift in the absorption edges which was evident in the theoretical simulation of density of states and band diagram of ZnO and Zn (O, S) unit cells.
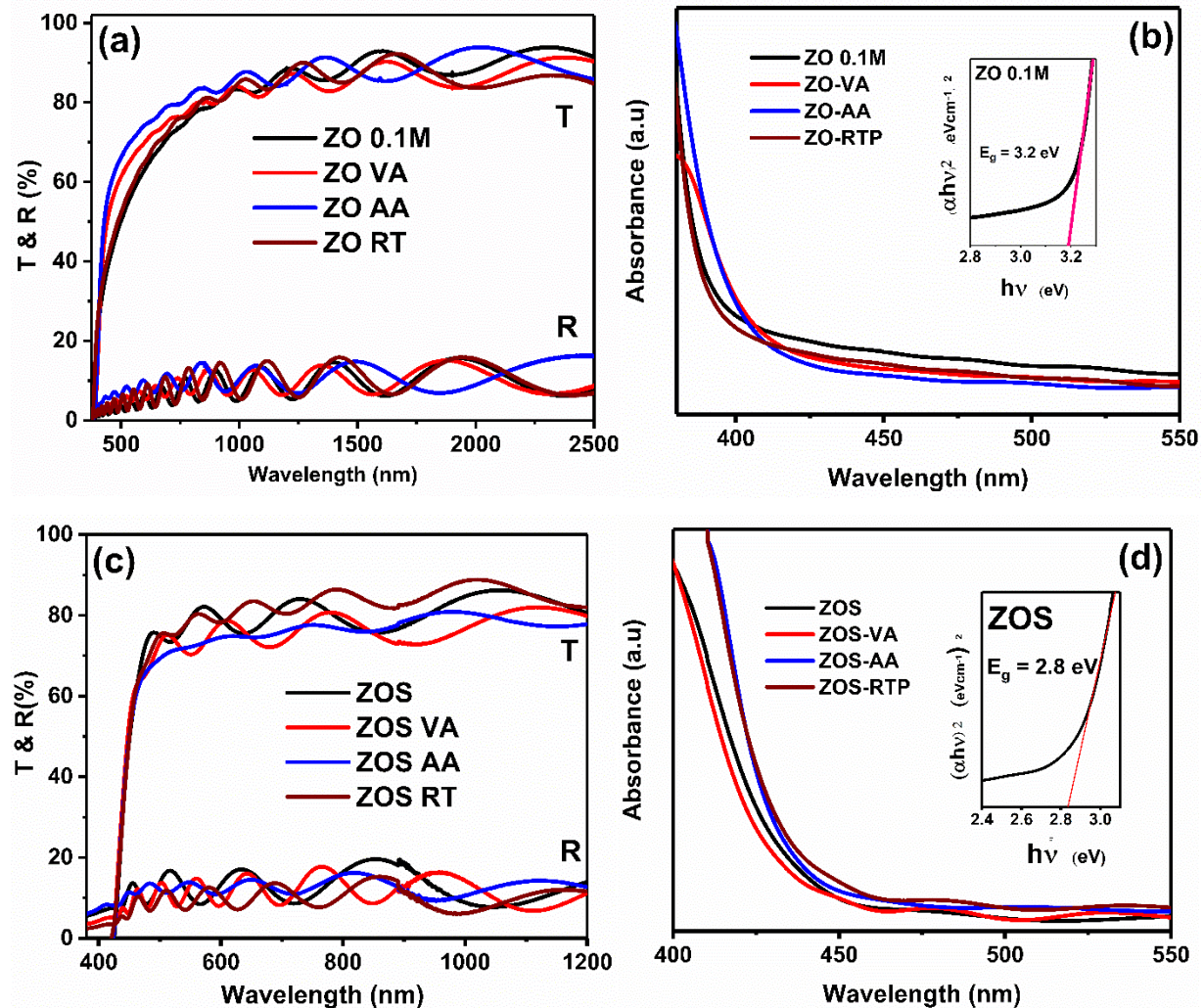
Figure 4.9 Optical properties of ZnO and Zn(O,S)thin films: Transmittance(T) and Reflectance (R)spectra of a) ZnO thin films(ZO 0.1M, ZO VA, ZO AA, ZO RT) b) absorption spectra of ZnO films with optical band gap is given as inset, c) Zn (O, S) thin films (ZOS 0.1M, ZOS VA, ZOS AA, ZOS RT) d) absorption spectra with optical band are given as inset in the graph.

4.6. Electrical Properties

Electrical properties of the thin films; resistivity, carrier concentration, and mobility of ZnO and ZnO:S thin films were evaluated as listed in Table 10. All the samples exhibit negative Hall coefficients, indicating that the bulk charge carriers are electrons, and hence the conductivity is n-type. Due to their limited mobility and low carrier concentration, samples ZO 0.1M and ZOS 0.1M show comparatively high resistance, as seen in the Table. The vacuum annealed films (ZO VA and ZOS VA), on the other hand, exhibit the highest conductivity due to their high carrier concentration and mobility. The sheet resistance values of 67 and 470 $\Omega/\square$ for ZO VA and ZOS VA are among the lowest values reported for such TCO films. The reported value shows sheet resistance of ZNO TCO layers were 0.7 - 1.2 $\times 10^3 \, \Omega/\square$ [76]. This may be due to annealing induced oxygen vacancies and Zn interstitials, both of which are donor states, to form in ZO VA, increasing the electron concentration [162] and changing both the optical and electrical properties of the material.

Apart from ZO AA and ZOS AA films, all the samples exhibit high mobility, which can be attributed to the high crystallite nature of the films. The mobility of the electrons is restricted by the scattering centers of the ionized atoms [163]. During the analysis of substrate and annealing temperature of the highly oriented thin film, it was reported that lowered resistivity of the films varied from $(1.1 – 6.3 \times 10^{-2})$ (Ωcm). The main reason can be attributed to the presence of oxygen vacancies and reduced density of grain boundary scattering centers raised mainly from adsorbed oxygen [164,165]. The overall resistivity of S incorporated ZnO thin films were reported to increase due to the decrease in electron carrier mobility arise from the scattering introduced by the disorder [166] reflected in the diffraction pattern of crystal growth discussed in section 4.1.

Table 10. Electrical properties of the ZnO and Zn (O, S) thin films

Samples	Resistivity (Ωcm)	Bulk Concentration (cm^{-3})	Mobility (cm^2/Vs)	Sheet Resistance (Ω/$\square$)
ZO 0.1 M	1.4×10^{-1}	7.5×10^{18}	5.7	3×10^3
ZO VA	1.5×10^{-3}	4.2×10^{20}	14	67
ZO AA	12×10^{-1}	2.0×10^{18}	2.7	16.6×10^3
ZO RT	3×10^{-2}	1.2×10^{19}	16	350
ZOS 0.1M	8.3×10^{-2}	6.4×10^{19}	1.1	3×10^4
ZOS VA	5.2×10^{-3}	8.7×10^{19}	12	4.7×10^2
ZOS AA	65×10^1	1.9×10^{18}	5×10^{-1}	48×10^4
ZOS RT	5.2×10^{-2}	1.6×10^{19}	10	9.8×10^2

Thus, after setting up the spray for TCO films, deposition of antimony sulfide thin films were explained in the next chapter. In this case, before starting with copper antimony sulfide thin

films, a systematic study on the thin film formation using a precursor containing only Sb and S sources. Effects of substrate temperature, annealing temperature and time, variation in molar ratio of precursor solution are analyzed.

CHAPTER 5

Results and discussion: Sb_2S_3 thin film growth by ultrasonic spray pyrolysis

This chapter discusses the growth and optoelectronic properties of Sb_2S_3, prepared as a first step towards the synthesis of Cu-Sb-S films and thus to understand the growth dynamics due to variation in Sb/S ratio in the precursor solution prior to incorporating copper. Moreover, Sb_2S_3 possesses a near-ideal optical band gap (1.6-1.9 eV) and a high absorption coefficient ($>10^5$ cm^{-1}) for PV applications. Sb_2S_3 films are known for their structural and thermal stability [167] reported as a crucial role in solar cell devices especially in interface engineering in heterojunction devices with improved charge extraction and reduced recombination losses.

5.1. X-Ray diffraction (XRD)

Figure 5.1. shows the diffraction patterns of thin films obtained by ultrasonically sprayed precursor solutions containing $SbCl_3$ and C_2H_5NS at different conditions. The patterns of the films formed at substrate temperatures of 170, 200, 230, 260, and 290 °C are given in Figure 5.1 a) along with photos of the respective samples. Low intense peaks are present at 2θ = 11.1, 15.7, 17.5, 22.3, 24.8, 28.5, 32.6, 35.6, 40.3, 45.4 and 47.3 ° and the respective peak intensity increases as the substrate temperature increases from 170 °C to 200 °C. These peaks are indexed as (110), (200), (120), (220), (130), (320), (140), (420), (141), (440), and (151) planes corresponding to orthorhombic Sb_2S_3 (JCPDS # 42-1393) as given in the figure. For the films formed at 200 °C, all the peaks are more pronounced implying increased crystallinity as depicted in the figure. As the substrate temperature increases from 230 to 260 °C, the intensity of Sb_2S_3 peaks diminishes and Sb_2O_3 peaks (JCPDS # 721334) originate, and at 290 °C, oxide phase predominates as marked in the figure. In addition, the dark Sb_2S_3 films become transparent due to the formation of Sb_2O_3 as seen in the inset photos. The diffraction patterns also indicate that Sb_2S_3 thin films grow along (220) directions perpendicular to the substrate.

Moreover, crystallographic characterization is also analyzed for the films formed by changing the Sb/S molar ratio in the precursor solution as depicted in Figure 5.1 b) and c). By adjusting Sb concentration (for a given S concentration of 0.07M) and S concentration (for a given Sb molarity 0.017M), the films formed using solutions containing Sb/S ratios 0.25, 0.2, 0.15, 0.11,

0.28, 0.34 to 0.4. Further increase in the molar ratio of Sb/S > 0.4, there was precipitation in the precursor solution. In most of the reports of Sb_2S_3 prepared by spray deposition technique, as-prepared Sb_2S_3 films were amorphous [168] due to the presence of a complexing agent. The complexing agent could lead to the formation of the amorphous structure due to the binding of Sb and S ions forming coordination complexes. The complexing agent with metal ions could disrupt the regular crystallization forming stable complexes, such a complexes stabilizes the solution but reduced mobility and disrupt the nucleation of the particle [169].
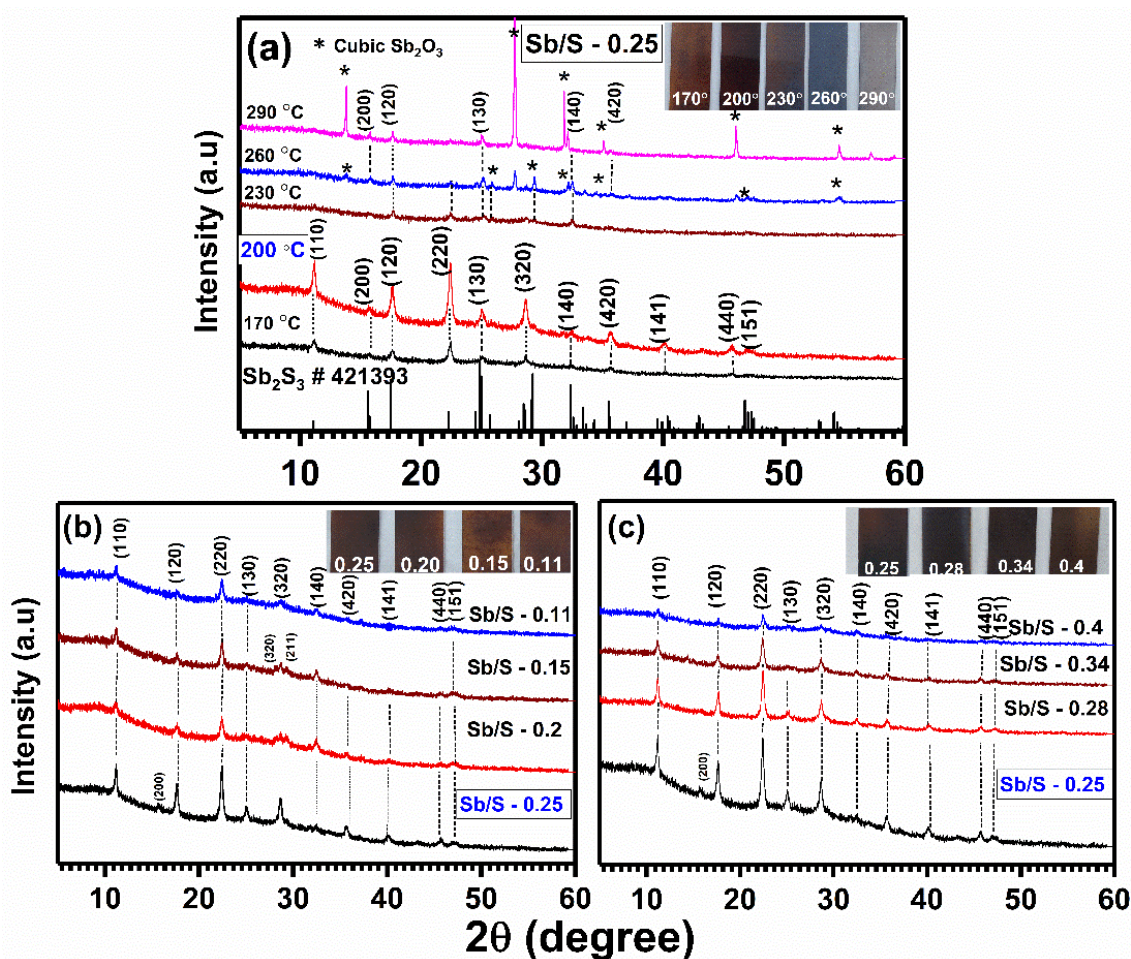
Figure 5.1 Diffraction pattern of sample deposited at different substrate temperature b) sample deposited at 200 °C with Sb molar variation b) Variation of S molar ratio.

According to the XRD analysis, optimized thin films were produced at 200 °C using a precursor solution with a molar ratio of 0.017 M $SbCl_3$ / 0.07 M C_2H_5NS. Further studies were done on the effect of postdeposition treatments, as given in Figure 5.2 in which the diffraction

patterns of the films vacuum annealed at 350, 375, and 400 °C for 30 min are plotted. For 350 °C annealed films, (220) planes show relatively higher intensity. Further, as the annealing temperature increased, weak Sb_2O_3 peaks (marked by * in the figure) appear in the case of 375 °C sample. Also, both Sb_2S_3 and Sb_2O_3 peaks strengthen as the temperature rises to 400 °C, reducing the respective FWHMs. However, rapid thermal processing of the films at 400 °C for 1, 3, and 5 minutes display only Sb_2S_3 peaks. Thus, rapid treatment at 400 °C increases crystallinity and orientation without changing the composition or decomposition of Sb_2S_3 thin films.

Further insight into the growth process was quantified in terms of the texture coefficient (TC) calculated for (220) plane. TC (220) corresponds to the as prepared, 350 °C vacuum, and 1 min RTP annealed samples, which are 1.4, 1.7, and 1.8, respectively. These values of texture coefficient (TC) >1 indicate a preferential orientation of (220) perpendicular to the substrate plane[169].
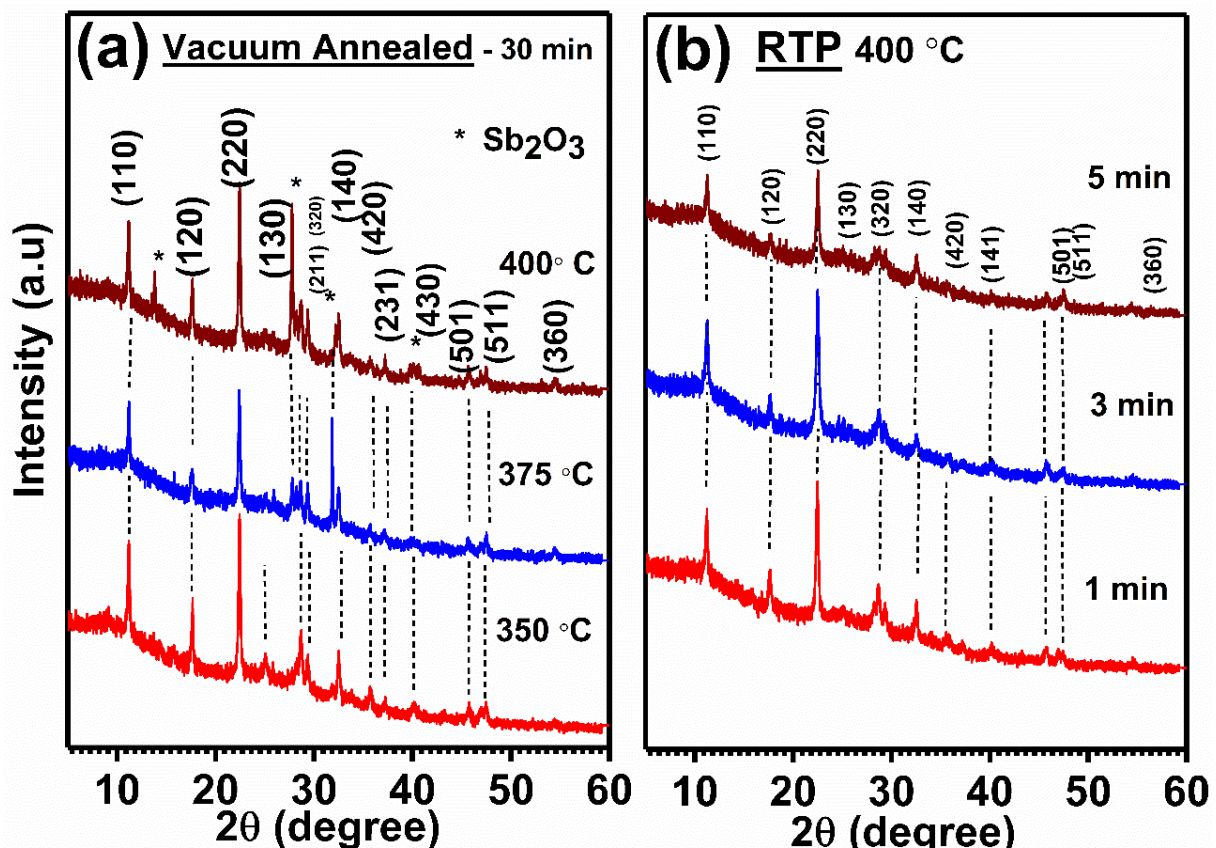
Figure 5.2. Post thermal treatments of as prepared sample a) vacuum annealed b) RTP.

To confirm the phase identification, Rietveld refinement analysis of the diffraction pattern of the in situ grown film at 200 °C was performed as in Figure 5.3, using the structural analysis program on the GSAS-II software [56]. The result supports the phase purity of the sample. The weighted profile factor (Rw) and goodness of fit (GoF) showed discrepancy indices of 3.55% and 1.16, respectively. The weighted profile factor (R_w) indicates covariance of the variables within experimental and standard profile. The lower the Rw value better the observed data is aligned to standard profile. Goodness of fit (GoF) shows how standard data fit to the observed data. The lower the value of GoF, the higher the fitting parameters matches with experimental and observed data. Rw and GoF data show refinement accuracy, validating the formation of pure orthorhombic Sb_2S_3 with the lattice parameters a = 11.3206 Å, b = 3.7947 Å, and c = 11.9326 Å.
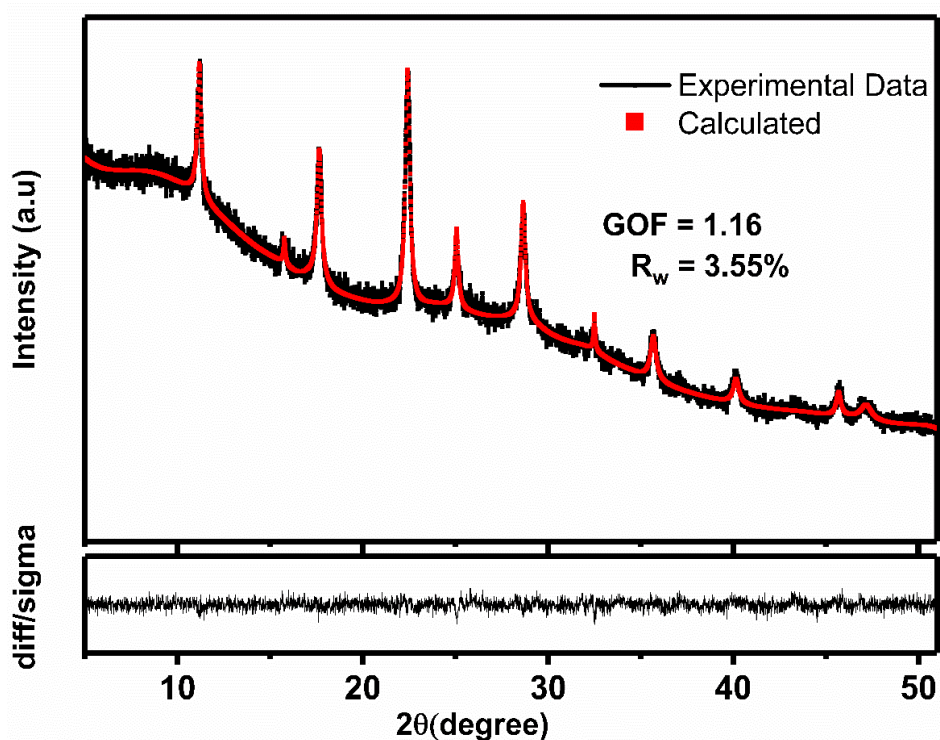
Figure 5.3. Rietveld refinement of Sb_2S_3 thin film deposited at 200 °C.

The diffraction peak broadening analysis was done to evaluate the respective crystallite size and lattice strain values of the films. For this, Williamson-Hall (W-H) plots were made using the following equations (14) from the corresponding XRD pattern. The contribution from the instrumental broadening was determined using a LaB_6 reference. Figure 5.4. shows the W-H graphs for the 200 °C as sprayed and post treated films (vacuum annealed at 350 °C and 1 min

RTP at 400 °C). The plots are based on the dominant planes (110), (120), and (220). From the intercepts and slopes of the W-H straight-line plots, crystallite size (D) and lattice strain (ε), are directly calculated.

$$\beta cos\theta = \varepsilon sin\theta + \frac{K\lambda}{D} \qquad (14)$$

where β is the total FWHM due to crystallite size and strain, K is the shape factor (0.9), and λ is the X-ray wavelength (1.54056 Å). β is the FWHM of the diffraction peak. The crystallite size values of the as prepared, 350 °C vacuum annealed, and 1 min RTP Sb₂S₃ films were 26, 32, and 40 nm. Corresponding strain values of the thin films were ε = 0.00224, 0.000710, 0.0009. The increased crystallite size (D) and TC (220) value greater than unity for annealed samples indicate improved thin film grain growth along preferential oriented plane.
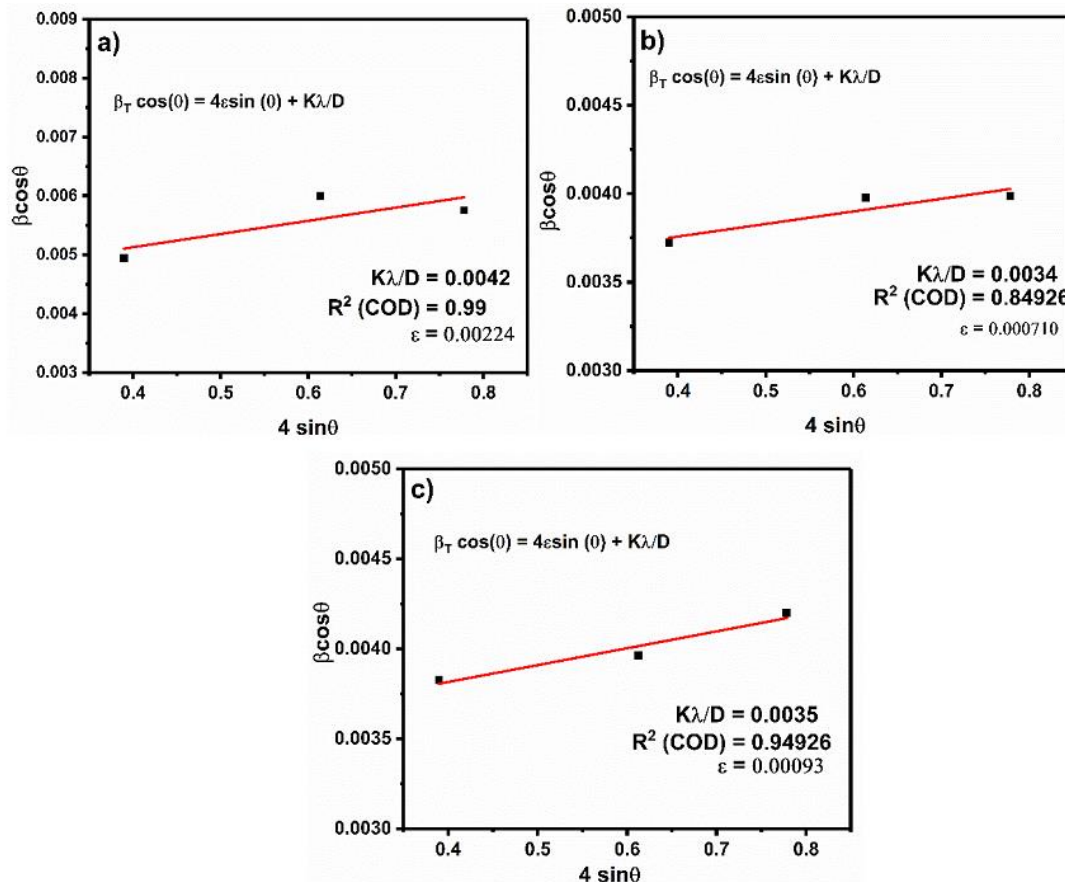
Figure 5.4. W-H plot a) as prepared samples at 200 °C b) vacuum annealed sample 350 °C / 30 min c) rapid thermal processing 400 °C / 1 min.

Thus, by ultrasonic spray pyrolysis, polycrystalline Sb_2S_3 thin films were formed *in situ* at substrate temperatures of 170, 200 and 230 °C by the dissociation and reaction of $SbCl_3$ and C_2H_5NS. In other solution based techniques, amorphous Sb_2S_3 thin films were formed [170] During chemical bath the orientation of crystal growth directed to (130) planes was reported. The texture coefficient increased with post-deposition treatments [171].

5.2. Raman Spectroscopy

The Raman spectra of the as prepared and annealed films are shown in Figure 5.5. It can be observed from the figure that there are nine Raman peaks that correspond to the frequencies 51, 62, 72, 109, and 254 cm^{-1} as well as a broad peak that is mostly centered about 300 cm^{-1}. These bands have vibrational frequency value ranges that are consistent with our theoretical calculations (section 3.2.2. and Figure 3.5) as shown in the Figure. The S-Sb-S bending vibrations (A_g) are accountable for the formation of the symmetric modes at 62, 72, 150, 270, and 287 cm^{-1}, whereas the antisymmetric modes for the Sb-S stretching bond are involved in the formation of the wider peaks at 51, 109, 304, and 312 cm^{-1}. The occurrence of a strong preferred orientation of the Sb_2S_3 films is reflected in a higher number of symmetric (A_g) modes in the Raman spectra. One of the characteristics features of the Raman spectrum of Sb_2S_3 is the broad peak around 300 cm^{-1}. The broad peak are be originated from the Sb-S and S=S vibrational modes [172,173].
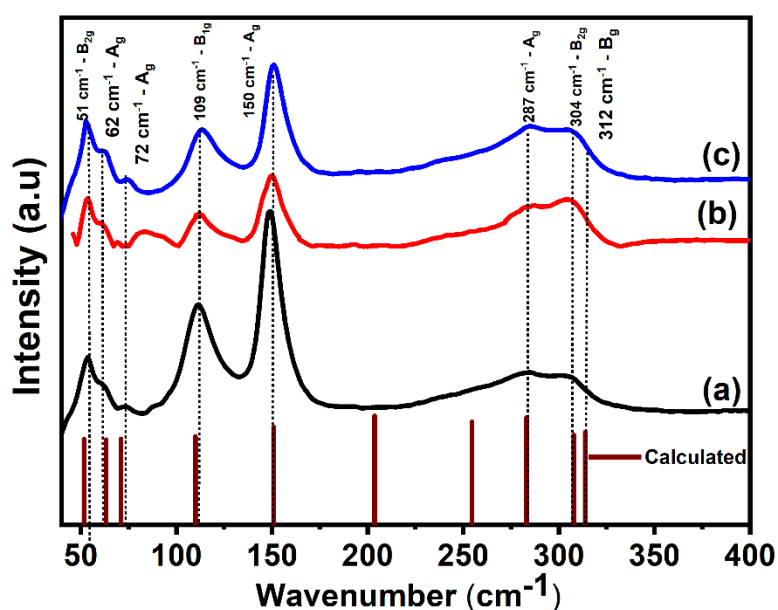
Figure 5.5. Raman spectra of a) as prepared sample, b) vacuum annealed and c) RTP sample.

5.3. Energy Dispersive Spectroscopy (EDS)

The ratio of atomic percentages (Sb/S) obtained from EDS was 0.64 for the as-prepared films, implying, nearly stoichiometric elemental ratio in correlation with stibnite phase Sb_2S_3 as shown in Table 11. The elemental ratios of the Sb_2S_3 films that were deposited at 170 and 230 °C are shown Table. The same stoichiometric ratio remains constant at 170 ° C as it does at 200 °C. Since oxygen is incorporated into the compound at higher temperatures (230 °C), the ratio grows. This is evidenced by the presence of Sb_2O_3, which is apparent from diffraction patterns. It is plausible that an insignificant quantity of sulfur was evaporated during the annealing process, which led to a gradual increase in the ratio after annealing (0.68 and 0.67). The EDS mapping shown in figure 5.6 confirms the uniform distribution of elements by the visual representation. The regions of scans were 1×1 cm^2 which reveals no variation of compositions and thus relative concentration of elements were constant. As the substrate temperature increases to 230° C the S presence diminishes compared to Sb because of the decomposition of Sb_2S_3. In post thermal treatments, the relative atomic concentration in the samples was constant, and the elemental distribution was observed uniform.

Table 11 Atomic percentage of sample deposited at different substrate temperatures (170- 230 °C) and post thermal treated samples.

Samples	Sb	S	Sb/S
170 °C	40.44	59.56	0.68
200 °C	38.4	59	0.65
230 °C	54.52	45.52	1.2
Vacuum Annealed 350 °C / 30 min	37.22	54.45	0.68
RTP 400 °C/ 1 min	38.23	56.41	0.67
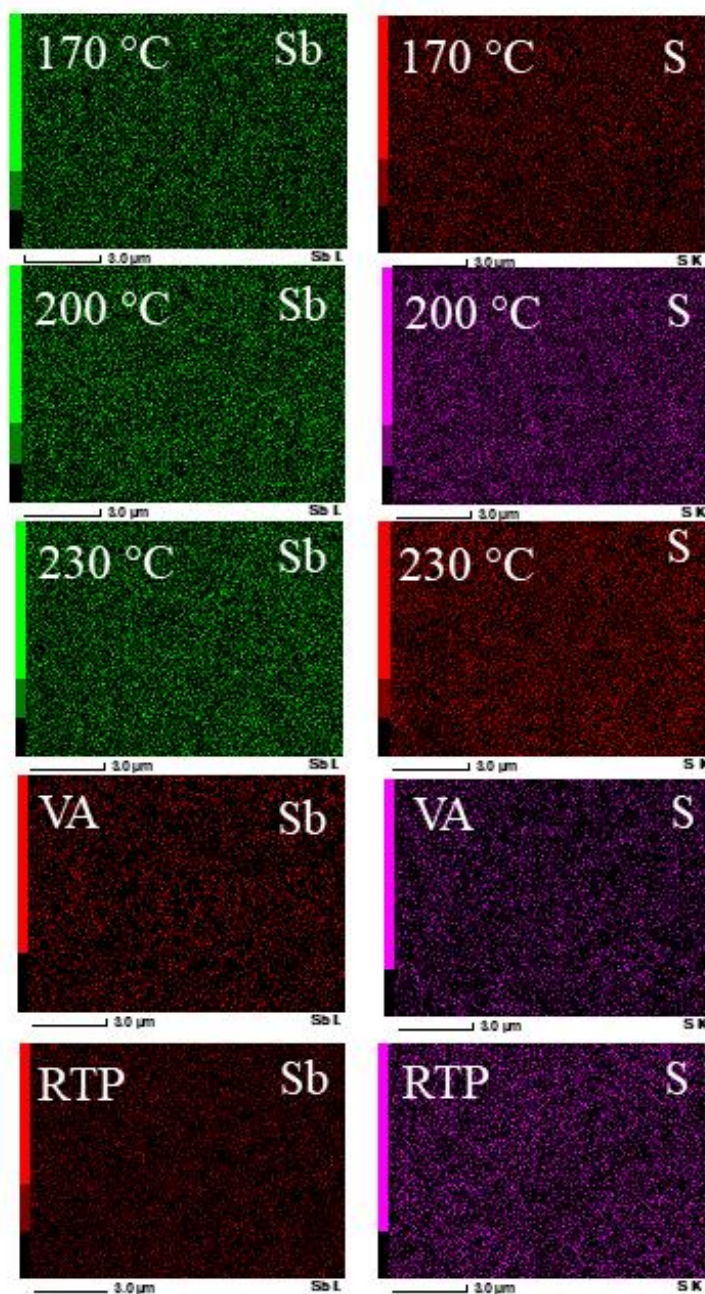
Figure 5.6. EDS mapping of the Sb₂S₃ samples with mapping of the samples deposited at different substrate temperature 170, 200, 230 °C and post thermal annealed samples (vacuum annealed and RTP)

5.4. X - ray photoelectron spectroscopy (XPS)

XPS analysis was used to confirm the elemental composition and the respective chemical states of Sb_2S_3 sample. Both survey spectrum and high-resolution core level spectra were recorded after sample surface etching using Ar^+ (2 keV) ion. The survey peak pattern indicates the core level and Auger peaks of Sb and S in the sample, which are shown in Figure 5.7. Figure 5.7 (a) shows the survey spectrum of a typical film (200 °C sprayed sample). High resolution core level spectra of Sb 3d and S 2p are analyzed as shown in Figure. 5.7 (b) and (c) to comprehend the different chemical states. The adventitious carbon (C1s) peak at 284.6 eV used for the calibration of binding energies from the core peaks, together a flood gun coupled with the spectrometer for the charge compensation. As seen in the Figure, the Sb 3d and S 2 p core level spectra are fitted using the Gaussian-Lorentzian sum function and Shirley type background. The doublet peaks intensity ratio and FWHM were maintained for the peak fitting. Sb 3d is a doublet composed of spin orbit couples $3d_{3/2}$ and $3d_{5/2}$ peaks that are 9.4 eV apart according to Figure. 5.7(b). Peaks with binding energies of 539.28 and 529.88 eV may be attributed to Sb^{3+} states in Sb_2S_3 [174–176]. As seen in the Figure, the additional shoulder peaks at 538.18 and 528.88 eV and are those of metallic antimony (Sb^0), which may have been formed by a sputter-induced reduction action brought on by Ar+ etching. The fitted peaks marked at 163.17 and 162.01 with B.E separation of 1.16 eV, are S 2p (Figure. 5.7(c)) doublet comprises spin orbit peaks of 2p 1/2 and 2p 3/2, which are consistent with the properties of sulfides (S^{2-} state) [177]. The presence of Sb and S can be seen from the film surface to the depth at which Si and O from the substrate were detected in Figure. 5.7 d) using the depth profile analysis.
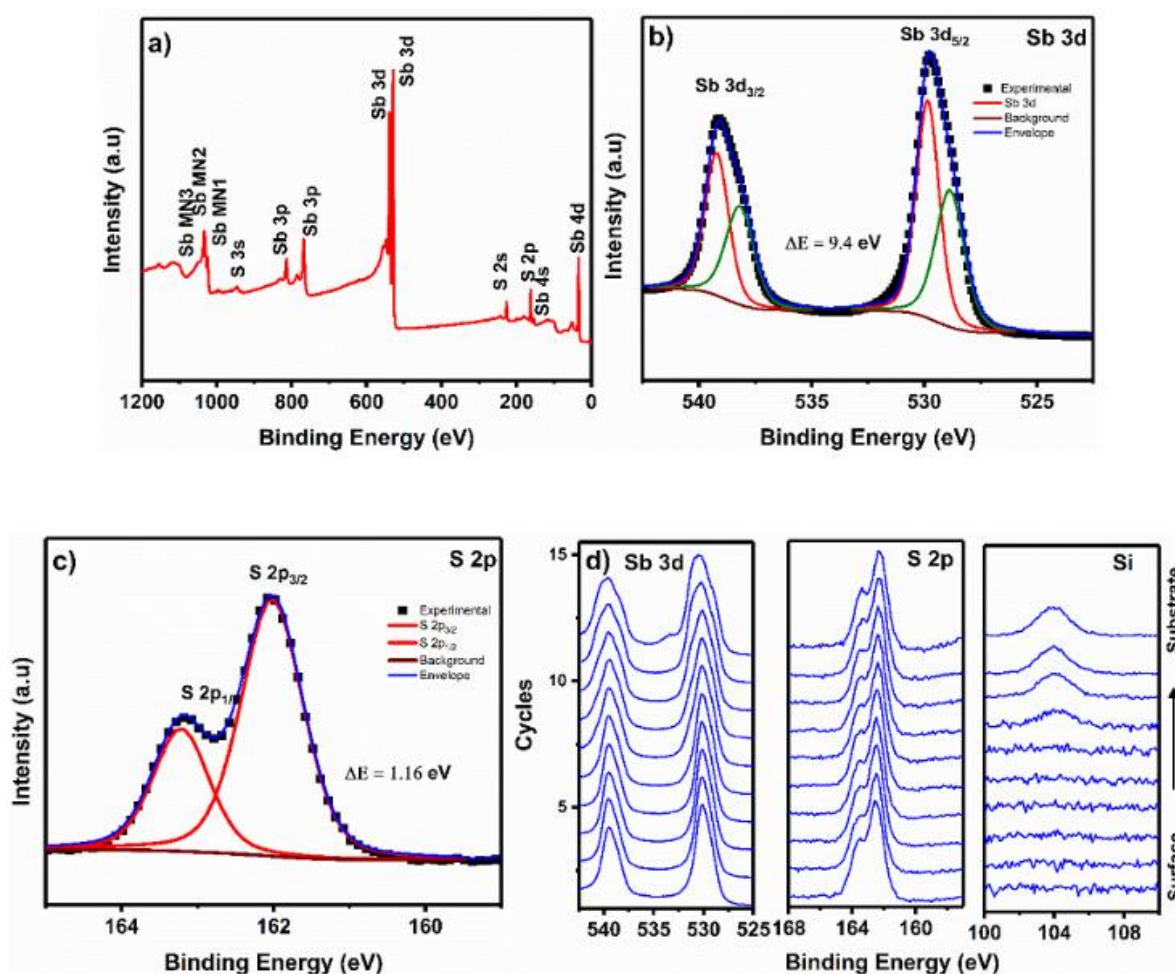
Figure 5.7: XPS analysis of Sb_2S_3 thin films at 200 °C (a) survey spectrum, high resolution core level spectra of (b) Sb 3d and (c) S 2p and (d) depth profile binding energy analysis.

5.5. Morphology

Morphology of Sb_2S_3 films were analyzed using SEM given in Figure 5.8. The micrographs of the phase pure films deposited at 200 ° C (as prepared (Figure 5.8.a)), vacuum annealed (Figure 5.8. b) and RTP (Figure 5.8.c) are seen. Figure 5.8 a) shows grain size approximately 40 nm distributed uniformly. The vacuum annealed sample (Figure 5.8 b) produced tight grain boundaries and less porous surface morphology while RTP treated sample (Figure 5.8 c) is composed of surface with coalesced grains. The annealing process led to the coalescence of grains to form compact structure which can affect the electrical charge carrier transport. Sb_2S_3 films recrystallize by vacuum

annealing and rapid thermal processing as evident from the respective morphologies of high spatial homogeneity and compact grain nature [57]. Figure 5.9 a) and b) shows the samples deposited at different substrate temperatures 170 and 230 °C. Sample possess rod shape structure with nonuniform distribution of grains throughout the sample surfaces. In spray pyrolysis, substrate temperature affects surface morphology by changing grain shape and size [56]. Figure 5.9 c) shows the cross-section image of as deposited thin film with measured thickness of 480 nm.
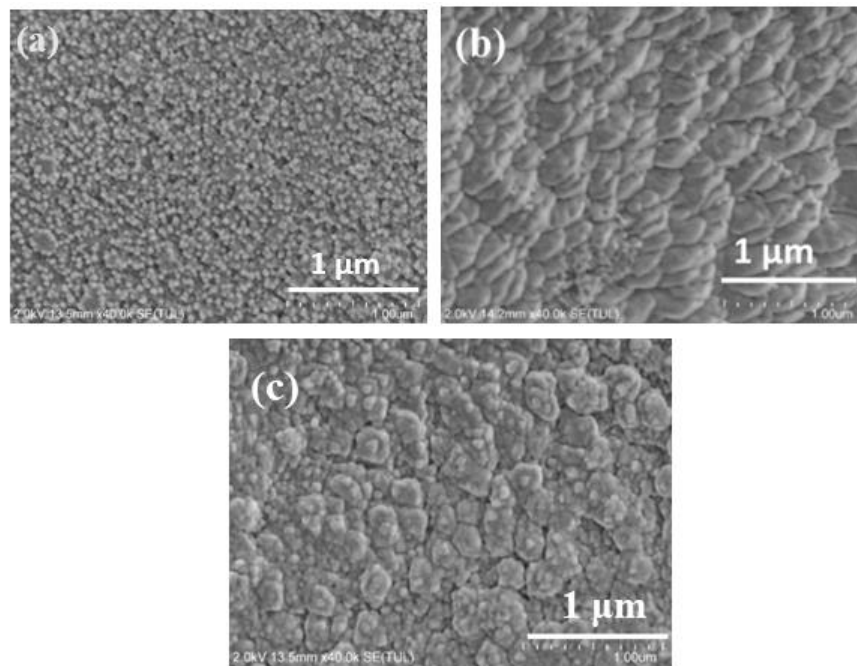
Figure 5.8 As prepared sample of Sb_2S_3 thin films with as prepared sample (a), vacuum annealed (b) and RTP (c)
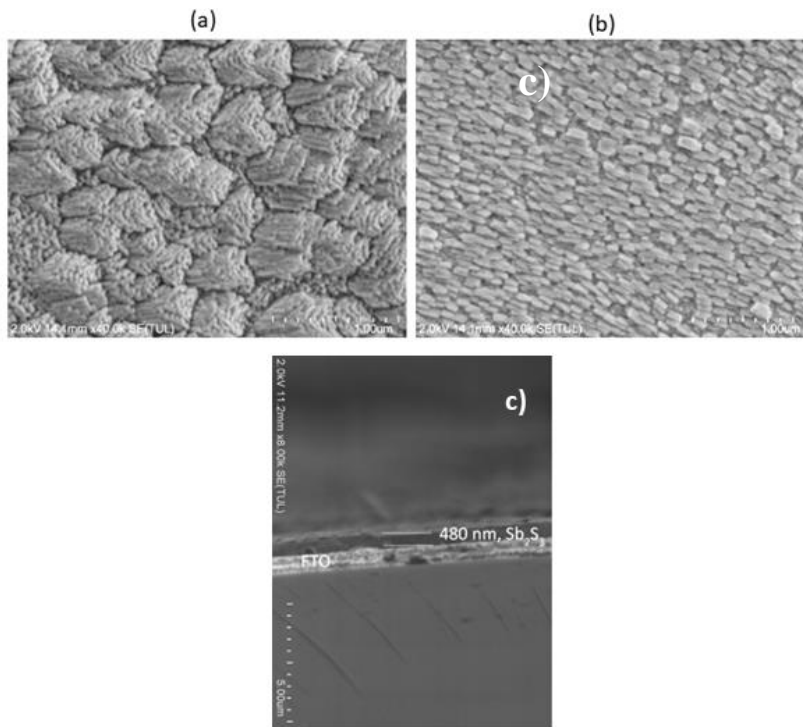
Figure 5.9 Morphology of the samples deposited at a) 170 °C and b) 230 °C, c) Sample cross section with thickness 480 nm.

5.6. Optical properties

The transmittance and reflectance spectra in the wavelength range of 400-2500 nm of the phase pure samples are analyzed to evaluate optical characteristics. Figure 5.10 shows the transmission spectra of 200 °C sprayed sample and the thermal treated films. In the figure, samples exhibited interference patterns at longer wavelengths and a steep curve around the absorption edge near visible range (600 -750 nm). The transmission maximum and reflectance minimum (vice versa) at the same incident wavelength ensured optical homogeneity of the films. Figure 5.10 b) displays the respective absorbance spectra calculated absorbance as a function of incident wavelength for phase pure sample with post thermal treated sample and optical bandgap value is determined using Tauc plot in Figure 5.10 (c-e). Equation (15) shown in section 4.5 shows the equation used for the calculation of optical band gap. For the direct electronic transition from valence band to conduction band; n = 2 values are assigned.
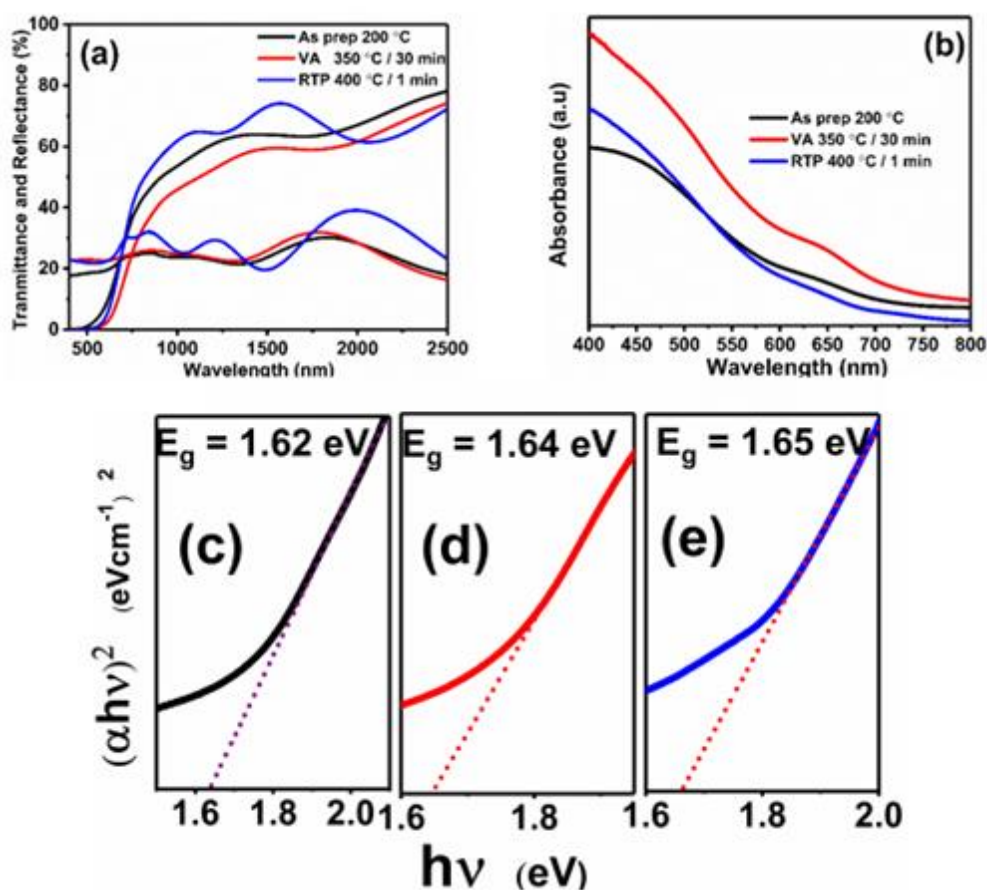
Figure 5.10 Optical properties of the Sb₂S₃ thin films; a) Transmittance and reflectance vs wavelength of as prepared thin films with post thermal treated samples b) Absorbance vs wavelength of the as prepared sample with post thermal treated samples. Tauc plots to evaluate optical band gaps c) as sprayed deposited at 200 °C d) sample vacuum annealed at 350 °C/30 min and e) RTP treated sample 400 °C/ 30 min.

Theoretical studies on density of states and band diagram predict the direct electron transition from valence band to conduction band. From Figure 5.10 (c-e) the band gap value of the prepared sample deposited at 200 °C was determined and the value of optical band gap is calculated as 1.63 eV for as the prepared, 1.62 eV for vacuum annealed and rapid thermal processed samples consistent with our theoretical calculations. There is no significant change in the optical band gap observed on post thermal treated samples. The presence of hump-like curve in absorbance vs wavelength spectra can be attributed to the presence of defective states where intra band electron

transitions occur. Strong absorbance caused by accelerated electronic transitions and morphologically, a reduction in the crystallite size might be responsible for the modest shift in the band gap value edge. Figure 5.11 shows the variation of transmittance and reflectance vs wavelength of as prepared sample deposited at 170 and 230 °C substrate temperature shows lower interference patterns, revealing the powdery surfaces. Effect of different vacuum annealing condition on the thin films are shown in Figure 5.11 b) and effect of rapid thermal annealing is shown in Figure 5.11 c).
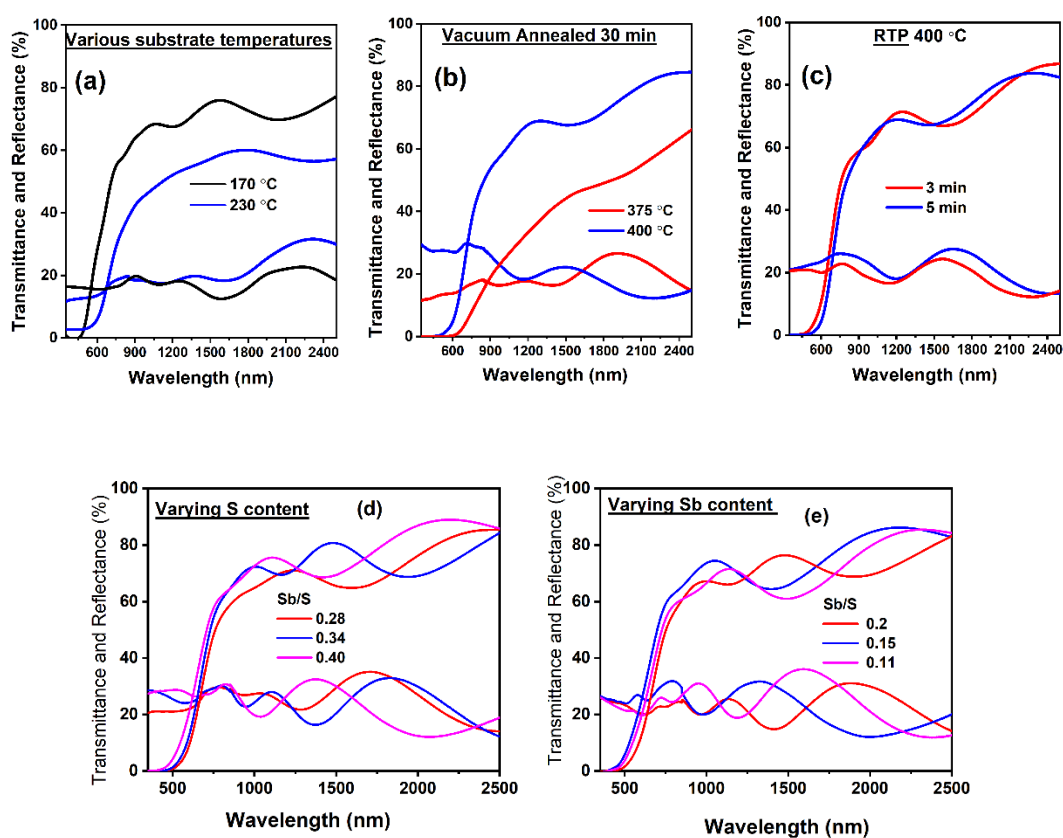
Figure 5.11 Transmittance and reflectance vs wavelength a) various substrate temperature 170 and 230 °C b) samples exposed to various vacuum annealing temperature c) effect of varied time on rapid thermal annealing d) thin films with variation of S d) and Sb e) molar ratio on precursor solution.

The S and Sb variations on the precursor solution provide different optical properties on the films in Figure 5.11 d) and e). By varying Sb/S ratio, the optical band gap varies from 1.6 – 2.3 eV which can be attributed to the presence of oxides of antimony widens the band gap. The optical band gap was reported as tuned from 1.4 – 2.2 eV using different spray parameters (spray rate and carrier gas pressure) attributed to the different morphologies by spray pyrolysis[178–180]. Using chemical bath deposition and spin coating methods, the reported optical band gap lies in the range of 1.5 – 1.8 eV, mostly indirect band gap[170,181,182].

5.7. Electrical properties

Table 12 Electrical properties of Sb_2S_3 thin films

Sb_2S_3 thin films	Carrier concentration $\times 10^{13}$ (cm^{-3})	Conductivity $\times 10^{-4}$ (Ω^{-1}cm^{-1})	Mobility (cm^2 / Vs)
As prepared (200 °C sprayed)	0.02	3.35	2
350 °C/ 30 min vacuum annealed	2.1	4.64	7
RTP 400 °C / 1 min	9.3	5.64	3

Table 12 reveals the Hall effect measurements of as sprayed and post thermal treated Sb_2S_3 thin films. From the table, all the films show p type conductivity and carrier concentrations are relatively very low. The as sprayed Sb_2S_3 thin films possess lower carrier concentration and lower mobility of carriers hence lower conductivity observed. The post thermal treated samples show enhanced Hall effect measurements. As the diffraction pattern reveals the crystallinity of the samples were improved thereby carrier concentration and mobility were improved reflected in the conductivity. Thereby low conductivity of the as prepared samples is enhanced by post thermal conditions. Improved crystallinity can contribute to the better mobility of the charge carrier together with the presence of donor defect (sulfur vacancies) can cause holes in valence band thereby hole carrier concentration can be increased [183].

The cyclic photocurrent response (8 cycles) was measured using 50 W halogen lamp (30 W/cm^2) at a bias of 10 V of samples; a) as prepared sample deposited at 200 °C b) vacuum annealed sample at 350 °C/ 30 min c) rapid thermal annealed sample at 400 °C/1 min as shown in Figure 5.12. In the figure, as prepared and posted thermal treated samples are photoconductive. The photogenerated current is enhanced on annealing which can be attributed to the better crystallinity and charge carrier transport of the thin films which can be correlated to the diffraction pattern and morphology analyzes. In the figure the photosensitivity of the samples was calculated using equation 15:

$$S(\%) = \frac{I_{light} - I_{dark}}{I_{dark}} \times 100 \qquad (15)$$

Where S defines the photosensitivity, I$_{light}$ and I$_{Dark}$ are the illuminated and dark current. The sensitivity values correspond to 200 °C sprayed sample, vacuum annealed sample at 350 °C / 30 min and rapid thermal sample at 400 °C / 1 min are 186, 275 and 220 (%) respectively. A rapid photocurrent, rise and decay under ON and OFF conditions and this suggests Sb$_2$S$_3$ thin films as photodetector in the photoconductive mode. Rise time defined as the time required for the current to reach 90 % of the photocurrent and decay time defined as the time required to reach the current to the 10% of photocurrent were calculated; for the as prepared sample rise / decay time was 0.9/1 sec and for the vacuum annealed and rapid thermal processed films 0.3/0.38 and 0.25/0.29 seconds respectively.

The photocurrent response of the films formed by varying the substrate temperatures, Sb/S molar ratios, vacuum annealing temperature (350 – 400 °C), rapid thermal processing time (1-5 min) are also analyzed as displayed in Figure 5.13. Figure corresponds to the photoresponse variation of substrate temperature from (170 – 260 °C). Sample deposited at 200 °C shows the highest photocurrent at bias of 10 V compared to lower and higher deposition temperature. Variation of vacuum annealing temperature from 350 – 200 °C on the sample deposited at 200 °C is recorded and inferred that sample annealed at 350 °C as well as the rapid thermal annealed sample at 400 °C for 1 min shows enhanced photocurrent. Improved photocurrent during the deposition and annealing temperature and time confirms the carrier life time was improved under these conditions, similar reports states the same observations [178,184,185]
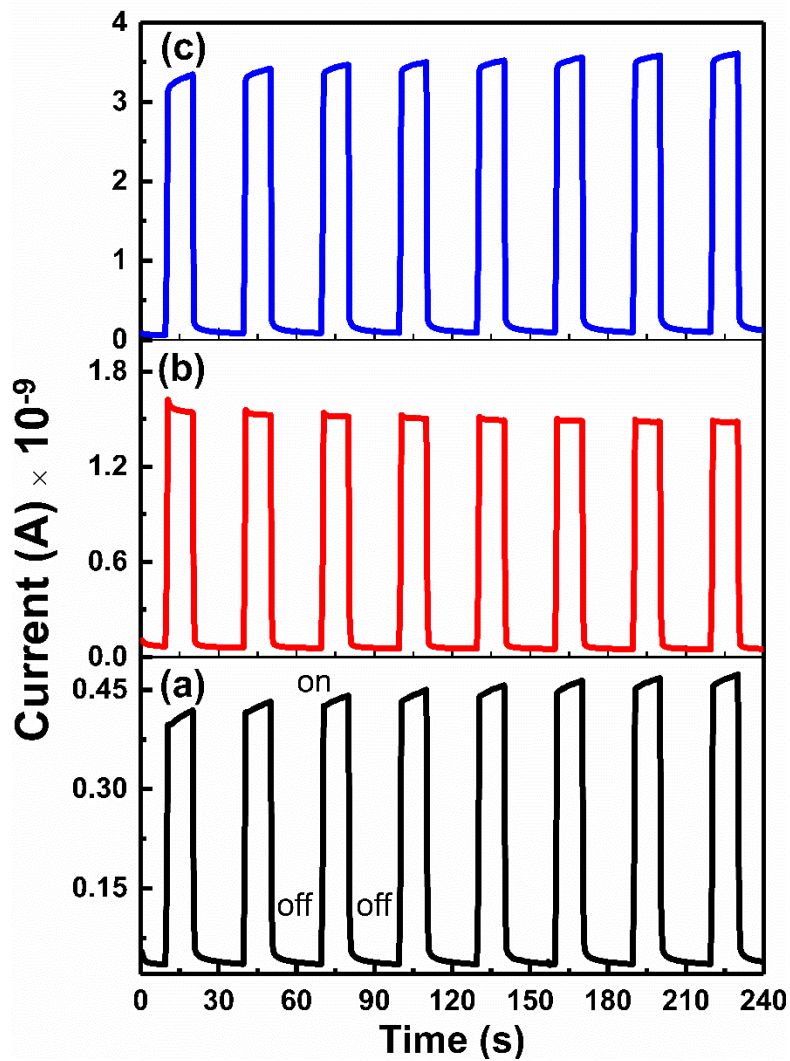
Figure 5.12 Photo response of the Sb$_2$S$_3$ samples deposited at 200 °C b) vacuum annealed sample at 350 °C/ 30 min c) rapid thermal annealed sample at 400° C/1 min.
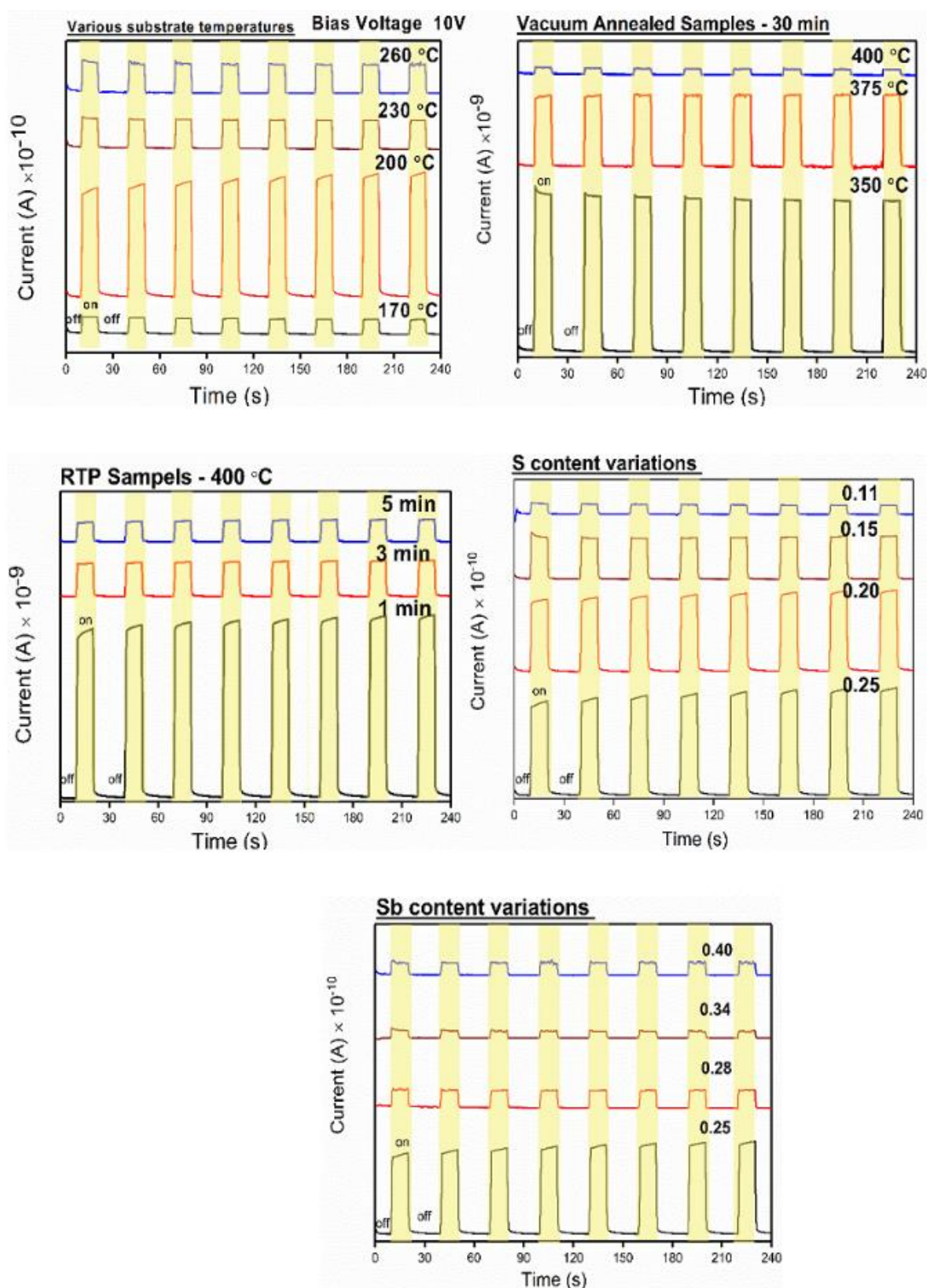
Figure 5.13 Photo response of the samples corresponding to substrate temperature deposited at 170 – 260 °C, vacuum annealed and rapid thermal annealed sample and varied Sb/S molar ratio.

Using ultrasonic spray pyrolysis deposition technique, Sb_2S_3 thin films were deposited on glass substrates at different substrate temperatures (170 – 230 °C), From the diffraction pattern the crystallization of film was slowly begins at 170 °C and improved on higher temperature but beyond 230 °C, diffraction pattern confirms the presence of oxides. This can be reasoned that at higher temperature the film decomposed, and film growth led to the oxide formation. Later the sample deposited at 200 °C were exposed to post thermal treatments, vacuum annealing (350 °C /30 min and rapid thermal treatments (400 °C/ 1 min). Diffraction pattern analysis revealed an i*n-situ* crystallization of thin films. Annealing treatments improve the crystallinity of the samples which was evident from the texture coefficient and W-H plots. Morphology analysis reveals a uniform distribution of spherical particles over the sample surface which can enhance the charge carrier transport. The chemical analysis confirmed the elemental and chemical states of the elements present in the samples. The optical and electrical properties revealed the effect of substrate temperature, annealing temperature, time and atomic composition are highly influential to the Sb_2S_3 thin films. In this section reveals a systematic analysis on controlled crystal growth of Sb_2S_3 thin film and optoelectronic properties of antimony sulfide thin films. The key factor affecting the crystal growth of Sb_2S_3 thin films was suitable thermal energy provided for the decomposition of constituent chemicals during the deposition and later led to the nucleation of films growth. Spray pyrolyzed deposition technique is a facile method to tune the film growth by varying different parameters such as temperature, spray rate, carrier gas pressure etc. Hence a direct method to influence the optoelectronic properties of the films were widely reported for the chalcogenide thin films[186–189].

Binary Sb_2S_3 faces intrinsic defect lowers the PV application. Such device properties can be engineered to incorporation of transition metal. The following chapter includes the analysis of incorporating transition metal (Cu) into antimony sulfide thin films and formation of different phases of copper antimony sulfide .

CHAPTER 6

Results and discussion

***In situ* growth of different phases of copper antimony sulfide thin films by ultrasonic spray pyrolysis**

This chapter describes deposition of different phases of copper antimony sulfide thin films using a single step ultrasonic spray pyrolysis. It includes identification of phases and evaluation of optoelectronic properties of copper antimony sulfide thin films formed at a given substrate temperature by varying systematically precursor concentrations. Further, electrical conductivity of the thin films can also be controlled to exhibit semiconducting or semi metallic behavior. This chapter is organized into two parts, the first part focuses on investigation on synthesis of tetrahedrite ($Cu_{12}Sb_4S_{13}$)   thin films and the second part discusses the formation of chalcostibite ($CuSbS_2$) thin films.

6.1 Phase identification

6.1. 1 Varying Copper in Sb_2S_3 precursor

Figure 6.1 shows the diffraction patterns of copper incorporated Sb_2S_3 thin films, a systematic approach. The concentration of copper chloride dihydrate varied from 0.0004 – 0.02 M as labelled in the figure. The molar ratio of antimony and sulfur was 0.017 M and 0.07 M respectively as optimized for the deposition of phase pure Sb_2S_3 thin films. It was observed that all peaks corresponded to the binary phases of copper and antimony and diffraction peaks were well matched with the standard binary phases: orthorhombic Cu_2S (JCPDS data #230961) and Sb_2S_3 (JCPDS data # 421393). In the case of 0.0004 M Cu, only weak peaks of Sb_2S_3 (#421393) are detected as marked in the figure. As the molarity increases (0.0008 and 0.00012), along with Sb_2S_3 peaks, peaks due to Cu_2S start to emerge. Interestingly, a gradual increment of copper molarity (0.0004 M) diminishes the Sb_2S_3 crystallite growth, and Cu_2S phase becomes dominant as seen in the figure. XRD results reveal that for the given concentration of Sb, and S, the sole variation of Cu molarity produces only binaries.   Also, it is evident that the significant structural changes leading to the crystal growth take place in the region of Cu molarity 0.0012 – 0.004M (shaded in figure

6.1). So, it is necessary to vary molar ratios of both copper and antimony simultaneously while keeping the sulfur molar ratio kept constant due to high volatility of sulfur.
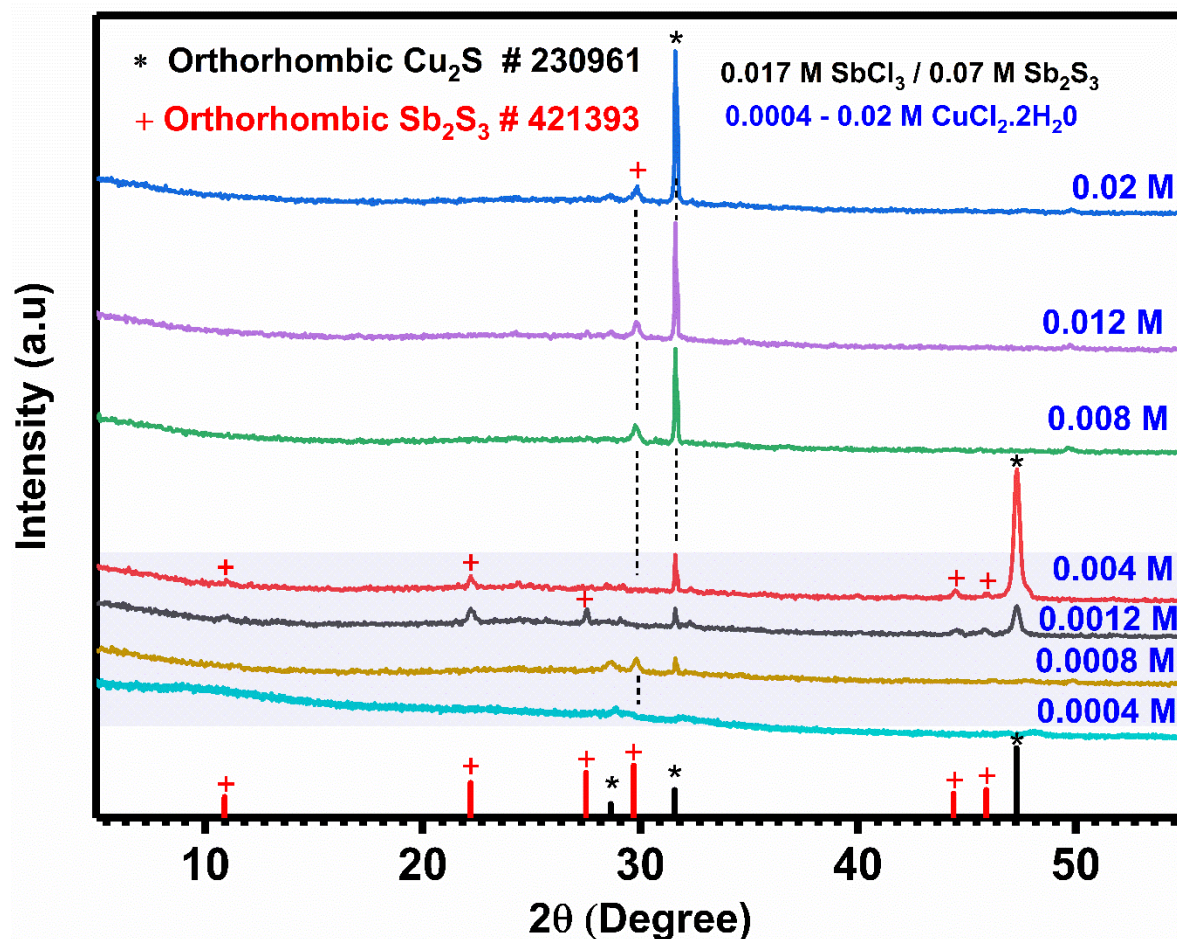
Figure 6.1 Diffraction pattern of the thin films formed by varying copper chloride, molar ratio from 0.0004 – 0.02M, on 0.017M antimony and 0.07 M sulfur.

Figure 6.2 displays the structure analysis of Cu-Sb-S thin films deposited by simultaneously varying (Cu and Sb). Thin films with varied (S/Cu+Sb) molar ratio are labelled as **CAS12.5, CAS 8.8, CAS 4.7** and **CAS3.5**.

6.1. 2 Varying S/(Cu+Sb) ratio in the precursor

The copper and antimony molarities were varied simultaneously in the precursor solution. The varied molar ratio is equated to (S/Cu+Sb)

Figure 6.2 a) represents the thin films deposited at 200 °C. The diffraction patterns recorded for the as-prepared thin films exhibit poor crystallinity. From the figure, there is an indication of a peak at 2θ = 29.9 ° in both CAS12.5 and CAS8.8 and this feeble peak disappears as the ratio decreases further. Figure 6.2 b) reveals the corresponding Raman spectra in which peaks at 267, 325, 352 and 480 cm^{-1} are detected in all the samples as marked. The peaks centered at 480 cm^{-1} are correlated with the presence of binary phase of Cu_2S which was absent in the diffraction pattern [190] and peaks centered at 267, 325 and 352 cm^{-1} could be due to amorphous Sb_2S_3 [187]. The diffraction patterns recorded for vacuum annealed films are given in Figure 6.3.
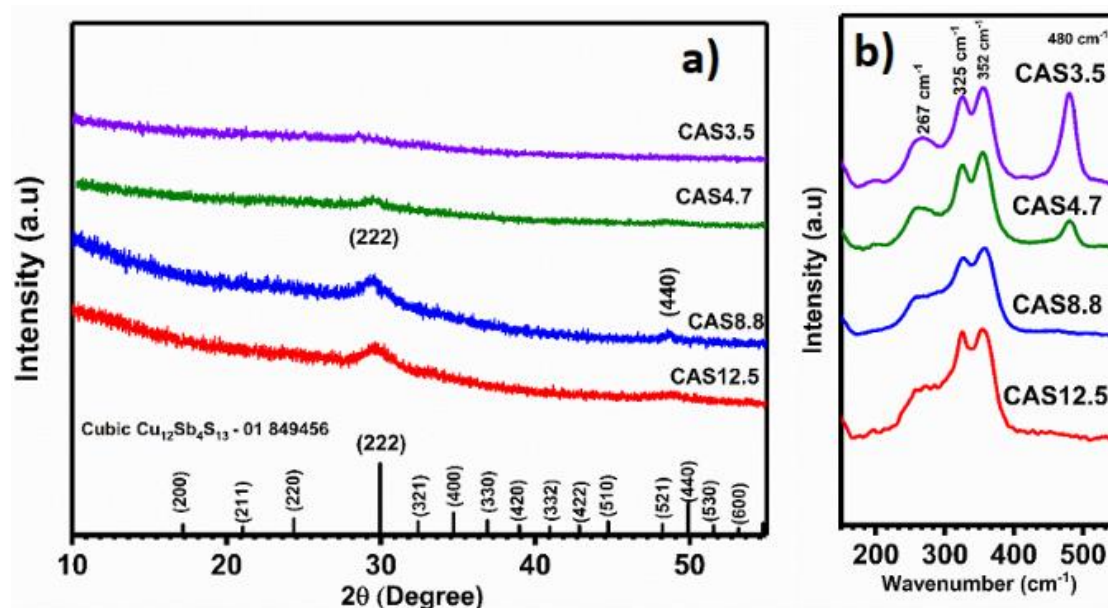
Figure 6.2 a) Diffraction pattern of as prepared Cu-Sb-S thin films prepared by varying S/(Sb+Cu) molar ratio 12.5, 8.8, 4.7 and 3.5 and b) Raman spectra of the corresponding films.

From the Figure, 400 °C annealed films (**400CAS12.5, 400CAS8.8, 400CAS4.7**, and **400CAS3.5**) display polycrystalline nature with well-defined diffraction peaks. In 400CAS12.5 sample, peaks at 2θ = 17.7, 24.4, 29.9, 32.4, 34.7, 36.9, 44.7, 48.2, and 49.9 ° are detected as marked in the figure. These peaks can be indexed with (200), (220), (222), (321), (400), (330), (510), (521), and (440) planes corresponding to bcc $Cu_{12}Sb_4S_{13}$ (ICDD # 01-084-9456) as indicated in the Figure. In 400CAS8.8, similar peaks with improved intensity are observed and intensity

decreases as the ratio is 4.7 and less. Further, it can be seen that all the films are likely to grow the (222) planes perpendicular to the substrate plane. Figure 6.3 b) illustrates the crystalline nature of the film grown by spraying the precursor volume to 100 ml. In this case, the presence of discrete peaks, as noted in the figure, provides compelling evidence of *in situ* growth of polycrystalline $Cu_{12}Sb_4S_{13}$ thin films. These peaks are well-defined even in the as sprayed films highlighting the importance of increasing the spray solution volume to 100 ml to obtain sufficient thickness to grow crystalline films.

Considering the significance of reduced device processing temperatures, XRD analysis of CAS12.5 and CAS8.8 films annealed at 350 °C is performed as shown in Figure 6.3 c. The pattern demonstrates that as sprayed films turned to polycrystalline even at lower annealing temperature. In the case of other methods based on various multistage procedures of powder synthesis followed by spin coating, or physical vapour deposition required higher temperature (350-400 °C) post-treatments to obtain polycrystalline $Cu_{12}Sb_4S_{13}$[96,191,192].

Rietveld refinement was utilized to investigate the phase purity of 400CAS12.5 and 400CAS8.8 samples as shown in Figure 6.3 e) and f) respectively. Refinements were made to obtain the structural characteristics, including atomic position, preferential orientation direction, profile function, and partial orientation correction. In both samples, the profiles are the bcc structured $Cu_{12}Sb_4S_{13}$ belonging to space group *I-43m* (217) with lattice parameter a = b = c = 10.3432 Å and α = β = γ = 90 °. These results well matched with our theoretical simulation and corresponding crystal structure is given in Figure 6.3 h).

Based on the characteristics of the unit cell, density of $Cu_{12}Sb_4S_{13}$ was calculated as 5.0005 g/cm^3, and its mass absorption 186.6 cm^2/g. As shown in the respective figures (Figure 6.3 e) and f), the discrepancy indices of the refinement determined by the weighted profile factor (Rw) and goodness of fit (GOF) are 5.55 % and 1.6 for 400CAS8.8, and 3.23 % and 1.12 for 400CAS12.5. In comparison with that of CA12.5, higher values of Rw and GOF for sample 8.8 can be due to the presence of 1.3 % weighted fraction of $Cu_{1.8}S$ which is marked as (*), along with 98.7% of $Cu_{12}Sb_4S_{13}$, Figure 6.2 f).

Moreover, the texture coefficient (TC) corresponding to the film growth is calculated using equation (16) proposed by G.B. Harris. The value of TC $_{(hkl)}$ greater than unity signifies crystal growth is oriented towards the *(hkl)* plane.

$$TC(222) = \frac{I_{(222)}/I_{o(222)}}{\frac{1}{m}\sum_{i=1}^{m}\frac{I_{(h_i k_i l_i)}}{I_{o(h_i k_i l_i)}}} \qquad (16)$$

where *m* defines the number of peaks, I_{hkl}: intensity of the peak defined by (hkl) in the diffraction pattern, and $I_{0(hkl)}$ is the corresponding intensity in the standard diffracted pattern. The texture coefficient TC (222) values determined for films 400CAS 12.5, 400CAS8.8, 400CAS4.7, and 400CAS3.5 are respectively 1.03, 1.43, 1.23, and 1.17. A preferential orientation of (222) planes during the deposition is indicated by TC greater than 1.
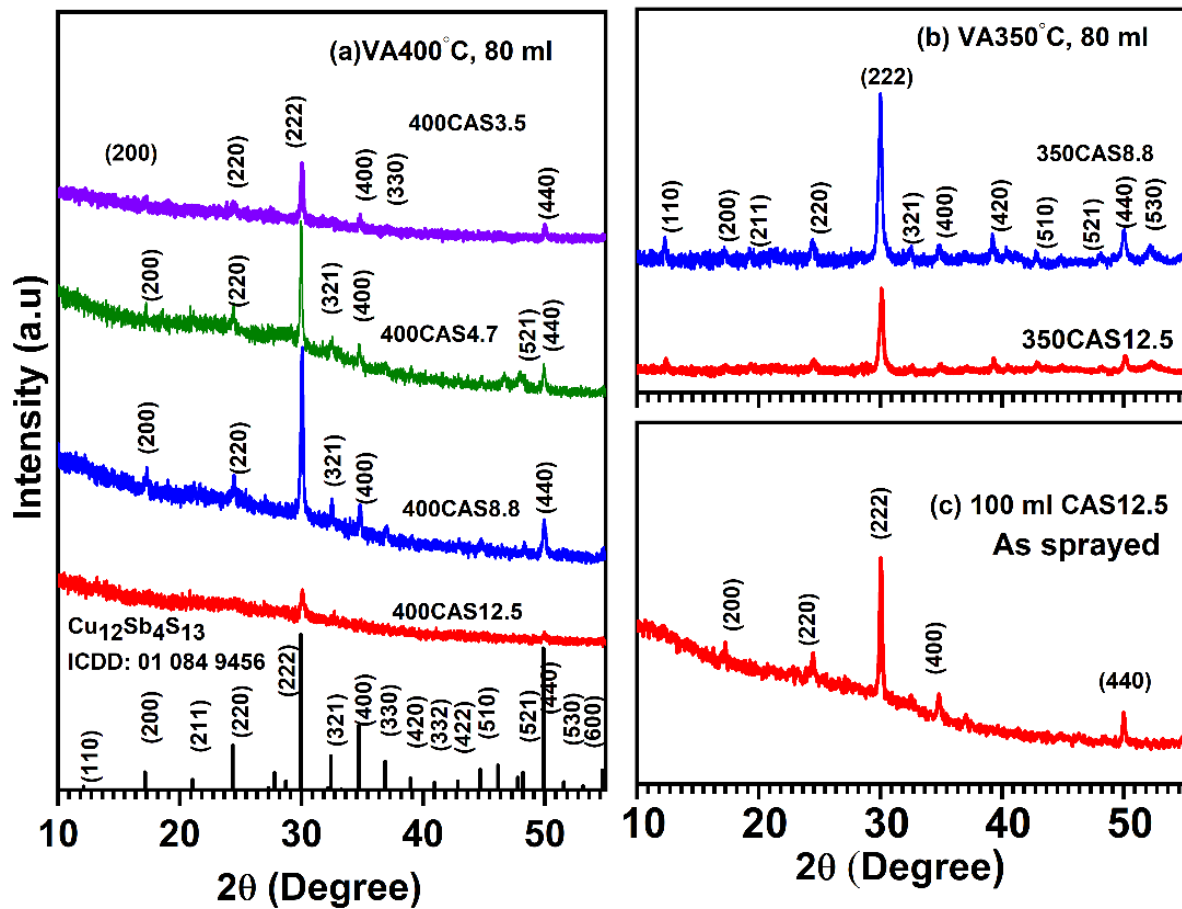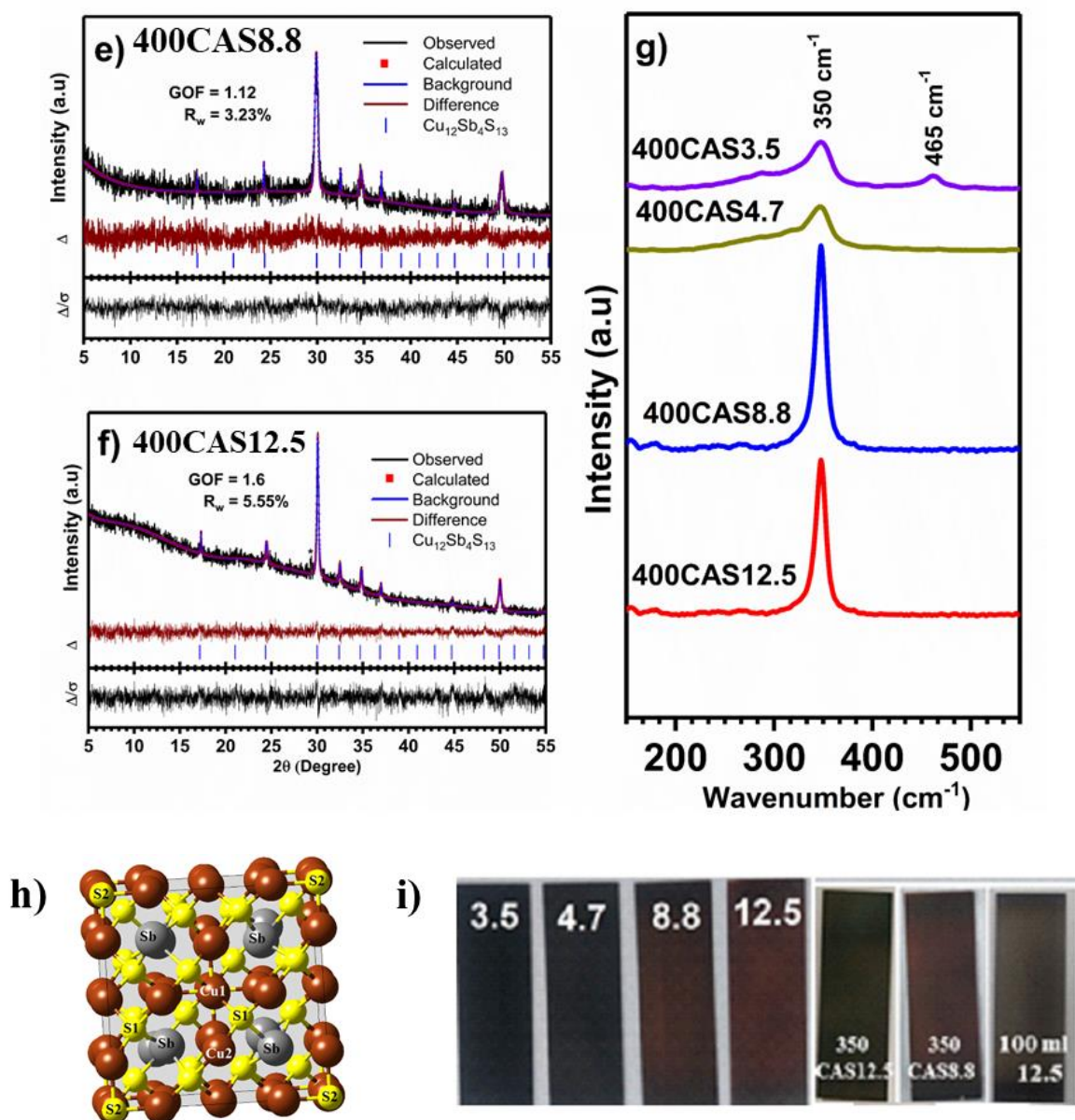
Figure 6.3: Diffraction patterns of the thin films (a)deposited with varying S/(Cu + Sb) molar ratios (400 CAS12.5, 400CAS8.8, 400CAS4.7, 400CAS3.5) (b) as-deposited and vacuum annealed thin films using 100 ml solution CAS12.5 and 100400CAS12.5 c) thin films 350 °C CAS12.5 and CAS8.8 annealed at e) and (f) Rietveld refinement of the 400 °C annealed films (400CAS12.5, 400CAS8.8)(g) Raman spectra of 400 °C annealed films (400 CAS12.5, 400CAS8.8, 400CAS4.7, 400CAS3.5) h) $Cu_{12}Sb_4S_{13}$ unit cell i) samples photos of films deposited at different deposition conditions .

The crystallite size was calculated using Scherrer equation (13) mentioned section **4.1**. For the samples annealed at 400 °C, 400 CAS 12.5, 400CAS8.8, 400CAS4.7, and 400CAS3.5 samples are composed of crystallites of sizes of 33, 38, 37, and 36 nm respectively. The crystallite diameters of the *in situ* crystallized films deposited using 100 ml precursor solution (100 ml CAS 12.5 as prepared figure 6.3 c) was 35 nm.

Raman spectra were used to analyze the chemical structure of annealed thin films. As shown in the figure 6.3 g, a strong vibrational mode can be observed at a frequency of 350 cm^{-1} in the case of films with a comparatively higher (S/Cu+Sb) ratio (CAS12.5 and CAS8.8) [193,194]. The peak at 350 cm^{-1} in our experimental spectra can, however, be attributed to the formation of $Cu_{12}Sb_4S_{13}$ with reference to the Rruff data (RRUFF ID: R070423) for the tetrahedrite mineral sample ($Cu_6(Cu_6Zn_2)$ Sb_4S_{13}). Also, in other reports of $Cu_{12}Sb_4S_{13}$ synthesized by electron beam evaporation and spin coating of copper-antimony mixed precursors in chlorobenzene, , the peak at 350 cm^{-1} can be attributed to the vibrational mode that originates from Sb-S bond stretching [95,195].

6.1 2 Precursor solution with copper poor concentration

From the diffraction pattern discussed in Figure 6.3, it was observed that the maximum molar ratio (S/Cu+Sb) required for the tetrahedrite ($Cu_{12}Sb_4S_{13}$) was 3.5 beyond the molar ratio the precursor precipitates uncontrollably. Considering the formation of polycrystalline thin films with sufficient thickness, and the structural changes detected in Figure 6.1 (Between 0.0014 and 0.004M) and 6.2 (3.5 of S/(Cu+Sb), the thin films obtained with poor Cu, in Sb rich precursor, at Cu/Sb ratio 0.17. Interestingly the diffraction pattern given in Figure 6.4 confirms the chalcostibite ($CuSbS_2$) phase of copper antimony sulfide. In as prepared sample deposited at 200 °C labelled as as prep, diffraction pattern shows *in situ* polycrystalline nature with peaks marked at 2θ =28.7, 29.9, 30.3, 32.1, correspond to the (111) (410), (301) and (120), all the peaks match with standard the orthorhombic $CuSbS_2$ (#441417) data. After posting thermal treatments at temperature 350 and 400 °C (labelled as VA 350 and VA 400), shows enhanced crystallinity. After annealing respective peaks were dominated as marked at 2θ = 12.2, 19.1, 34.5, 35, 39.05, 40.2, 43.3, 47.8 and 49.7 ° corresponds to (200), (210), (400), (220), (320), (501), (221), (520) and (002) planes. There were no binary phases formed by Cu, Sb and S are detected. The crystallite size of the thin films was

calculated and the average crystallite size to be 35, 42 and 45 nm for as prepared, VA 350 and VA 400 respectively.
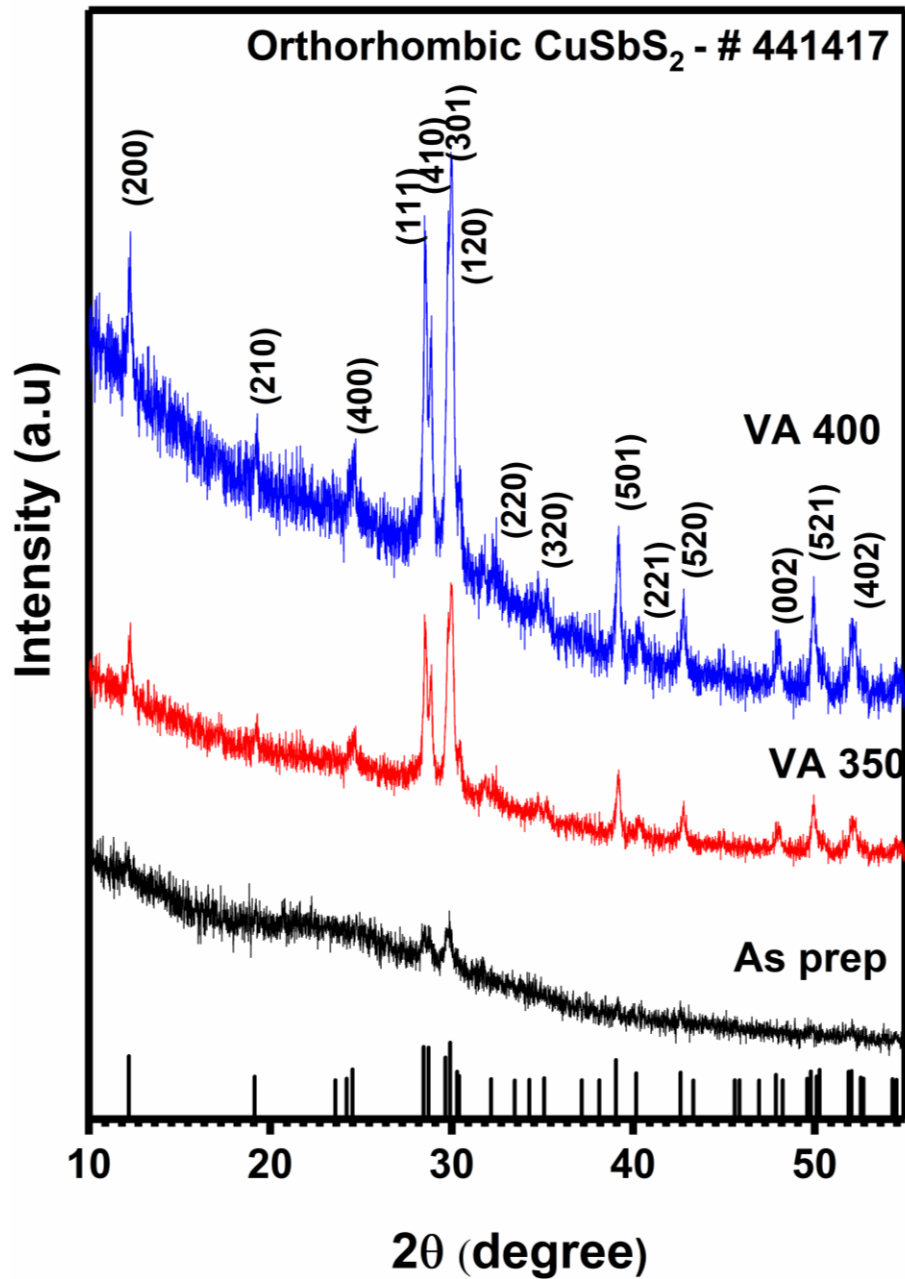
Figure 6.4 Diffraction pattern of CuSbS$_2$ samples a) as prepared deposited at 200 °C (As prep), vacuum annealed samples b) annealed at 350 °C and c) annealed at 400 °

6.2 Tetrahedrite $Cu_{12}Sb_4S_{13}$

6.2.1 Chemical composition

       Figure 6.5 presents the elemental composition as well as the EDAX mapping for the thin films of 400CAS 12.5 and 400CAS8.8. In both instances, the mapping reveals a uniform distribution of Cu, Sb, and S across the films. Table 13 provides the relative semi quantification of atomic percentages for the elements copper, antimony, and sulfur. From the table, the S/(Cu+Sb) ratio in the films is 0.7 for 400CAS12.5 and 0.8 for 400CAS8.8, both values are relatively close to the stoichiometric formula. According to the formula, the Cu/Sb ratio greater than one indicates the possibility of a copper-rich composition. Figure 6.5 contains EDS spectra displaying Cu, Sb, and S signals, respectively. There was no sign of any additional elements, such as chlorine or nitrogen, that were present in the precursor solutions in the thin films and the elements were uniformly distributed.
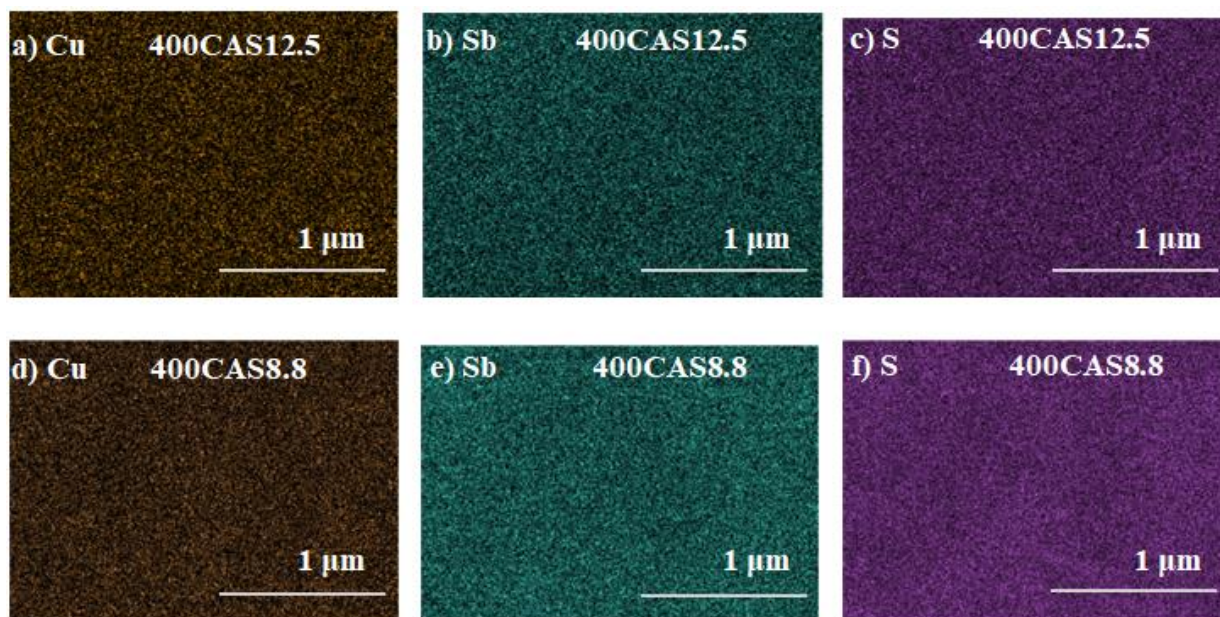
Figure 6.5: Elemental mapping of Cu, Sb and S in $Cu_{12}Sb_4S_{13}$ thin films (a-c) 400CAS12.5 and (d-f) 400CAS 8.8

Table 13: Elemental composition in percentage present in the typical CAS12.5 and 400CAS 8.8 thin films

Sample	Element			S/(Cu+Sb)	Cu/Sb
	Cu K	Sb L	S K		
400CAS12.5	35.2	23.1	41.7	0.7	1.5
400CAS8.8	38.3	17.7	44	0.8	2.2

   XPS was used to investigate the compositional analysis $Cu_{12}Sb_4S_{13}$ films, as well as the respective chemical states and depth-wise elemental composition. During the analysis the samples were kept for 18 hours in a parking chamber under vacuum of 1×10^{-6} mbar. Ag $3d_{5/2}$ with FWHM 0.9 eV using a silver foil kept inside the spectrometer was used for the calibration and linearity of the binding energy scale. A low electron energy flood gun was used for the charge compensation. A pass energy of 200 eV was used for survey spectra and 50 eV for high resolution spectra and both were spectra recorded   after one cycle of Ar^+ etching to reduce the surface contamination on the sample.

   Figure 6.6 a) is the survey spectra of the CAS12.5 and CAS8.8 thin films, both as prepared and annealed at 400 °C. Only peaks of copper (2s, 2p, 3s, 3p), antimony (3p, 3d, 4d), and sulfur (2s, 2p) along with their Auger peaks are detected in the survey spectra. After annealing, intensity of all the peaks improved. The peak fitting was accomplished with the use of the Gaussian-Lorentzian sum function and the Shirley-type background calculations.

   High resolution Cu 2p core level spectra of 400CAS12.5 (Figure 6.6b) and 400CAS8.8 (Figure 6.6c) are composed of spin-orbit doublets constituted of Cu $2p_{3/2}$ and Cu$2p_{1/2}$ at 952.6 and 932.8 eV and is separated by $\Delta E = 19.8$ eV. These binding energy values can be assigned to Cu^+ state   results that were previously reported [196,197]. Similarly, Sb core level spectra of the samples are shown in Figure 6.6 (d – e). The spin-orbit coupled $3d_{5/2}$ and $3d_{3/2}$ doublets constitute the Sb 3d peaks. Each of the doublets can be further fitted into separate peaks, as shown in the figure. In 400CAS12.5 contains 3d ($3d_{3/2}$:$3d_{5/2}$) doublet pairs with binding energies (540.1 : 530.7 eV), (538.7 ; 529.3 eV) and (537.8 : 528.4 eV), respective peaks for 400 CAS8.8 were marked at (539.9 ; 530.5 eV), (538.5 ; 529.1 eV) and (537.6 ; 528.2 eV) [191,198]. It is possible that these peaks can be formed by the presence of Sb^{5+}, Sb^{3+}, or Sb^0 [96]. Core level spectra of antimony

based compounds are commonly reported the presence of Sb^0 due to sputter induced effect by Ar^+ etching [170,177]. Also, at a B.E of 531.5 eV, oxygen peak was originated from adsorbed oxygen [199] or hydroxyl group [200] on the surface of the film. The adsorbed oxygen was removed from the film as the etching process continues, as seen in the depth profile. According to the stoichiometry relation of $Cu_{12}Sb_4S_{13}$ phase, it is possible two oxidation states for Sb3d (Sb^{3+} and Sb^{5+}) [96]. For sample 400CAS12.5, the S 2p peaks are fitted by two peaks corresponding to 2 $p_{3/2}$ (163.08 eV) and 2 $p_{1/2}$ (161.88 eV) components respectively. A doublet appears for sample 400CAS8.8 at 162.98 and 161.78 eV, which correspond to S $2p_{3/2}$ and S $2p_{1/2}$, respectively, with a separation of B.E 1.2 eV. These values are in correlation with those of S^{-2} ionic state [201]. Therefore, the analysis of the results of high-resolution core level spectra formation of $Cu_{12}Sb_4S_{13}$ is confirmed as indicated by the chemical states of Cu^+, Sb^{3+}/Sb^{5+} and S^{2-}. Wang et al reported the tetrahedrite phase by spin coating possess dual ionic states of antimony (Sb^{5+}/Sb^{3+}) which preserve the charge neutrality[96]. While, Emden *et al.* reported the $Cu_{12}Sb_4S_{13}$ nanocrystals by hot injection method possess dual ionic states of copper (Cu^+/Cu^{2+}) [202].
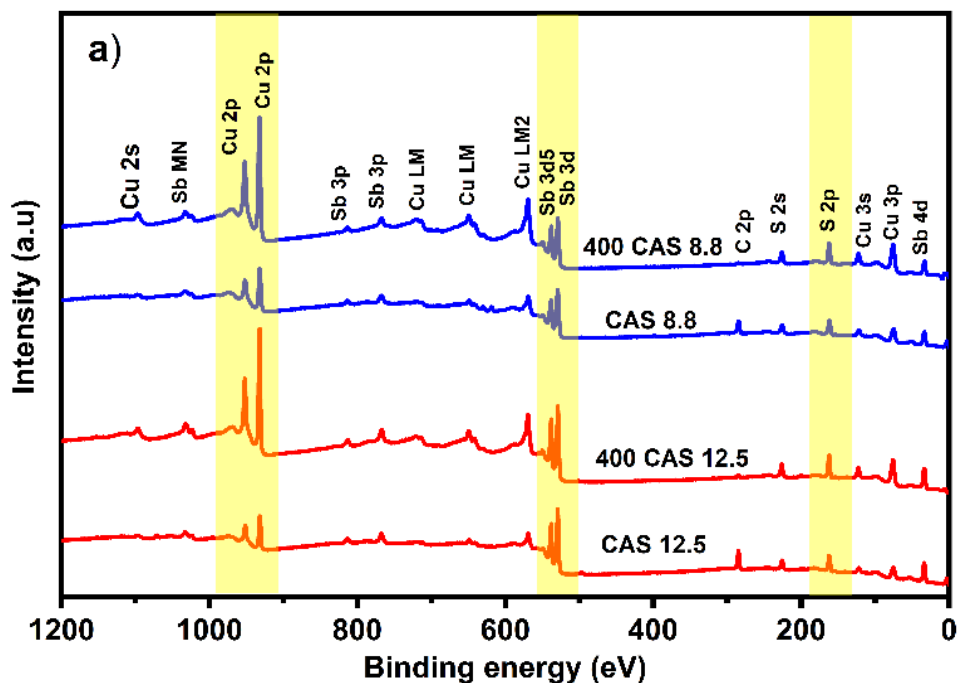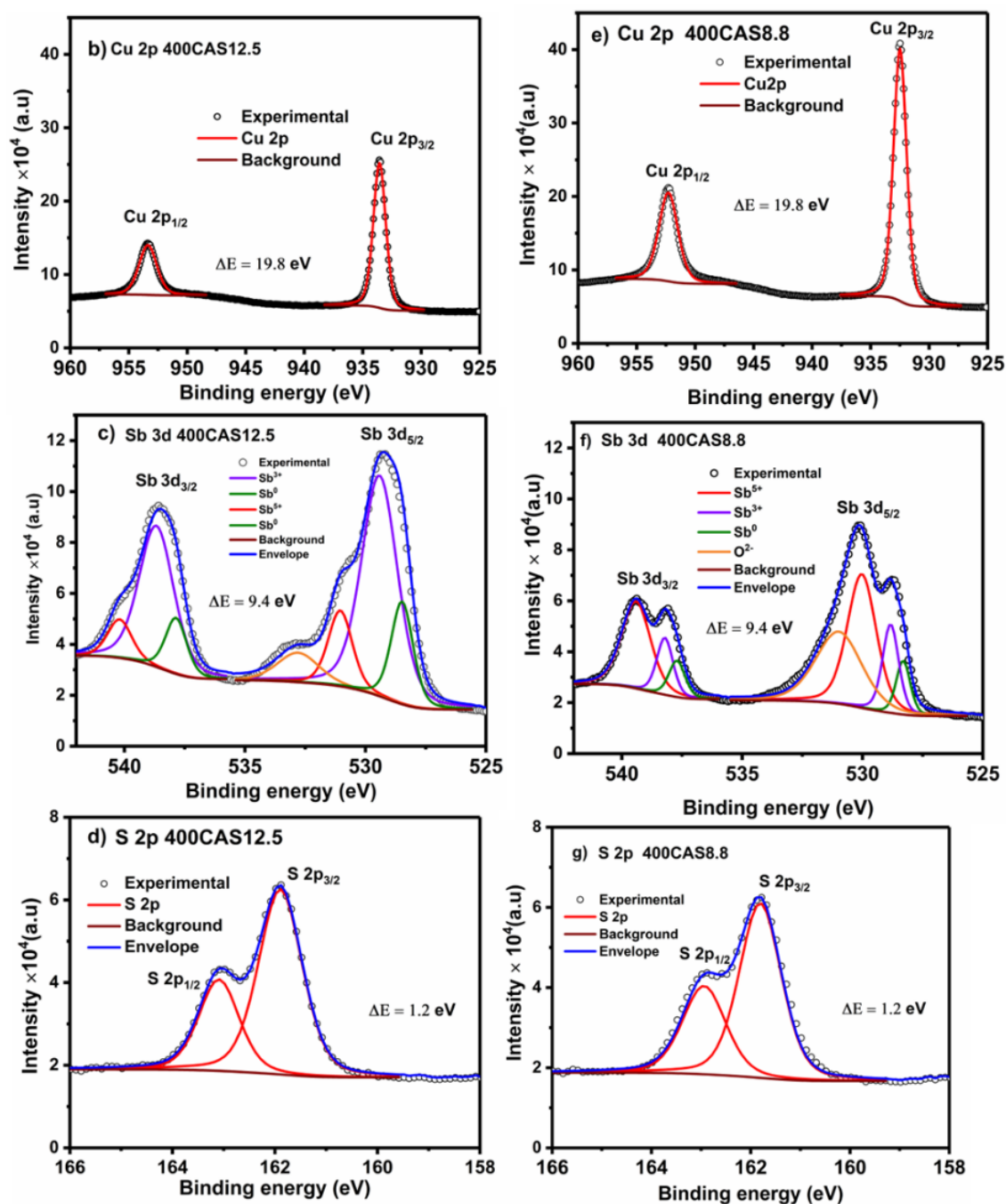
Figure 6.6 a) The survey spectra of $Cu_{12}Sb_4S_{13}$ thin films (CAS12.5, CAS8.8, 400 CAS12.5, 400CAS8.8) (b, d, f) High-resolution spectra of Cu 2p, Sb 3d and S 2p core levels of 400CAS12.5 (right column) and (c, e, g) High-resolution spectra of Cu 2p, Sb 3d and S 2p core levels of 400CAS8.8 (left column)
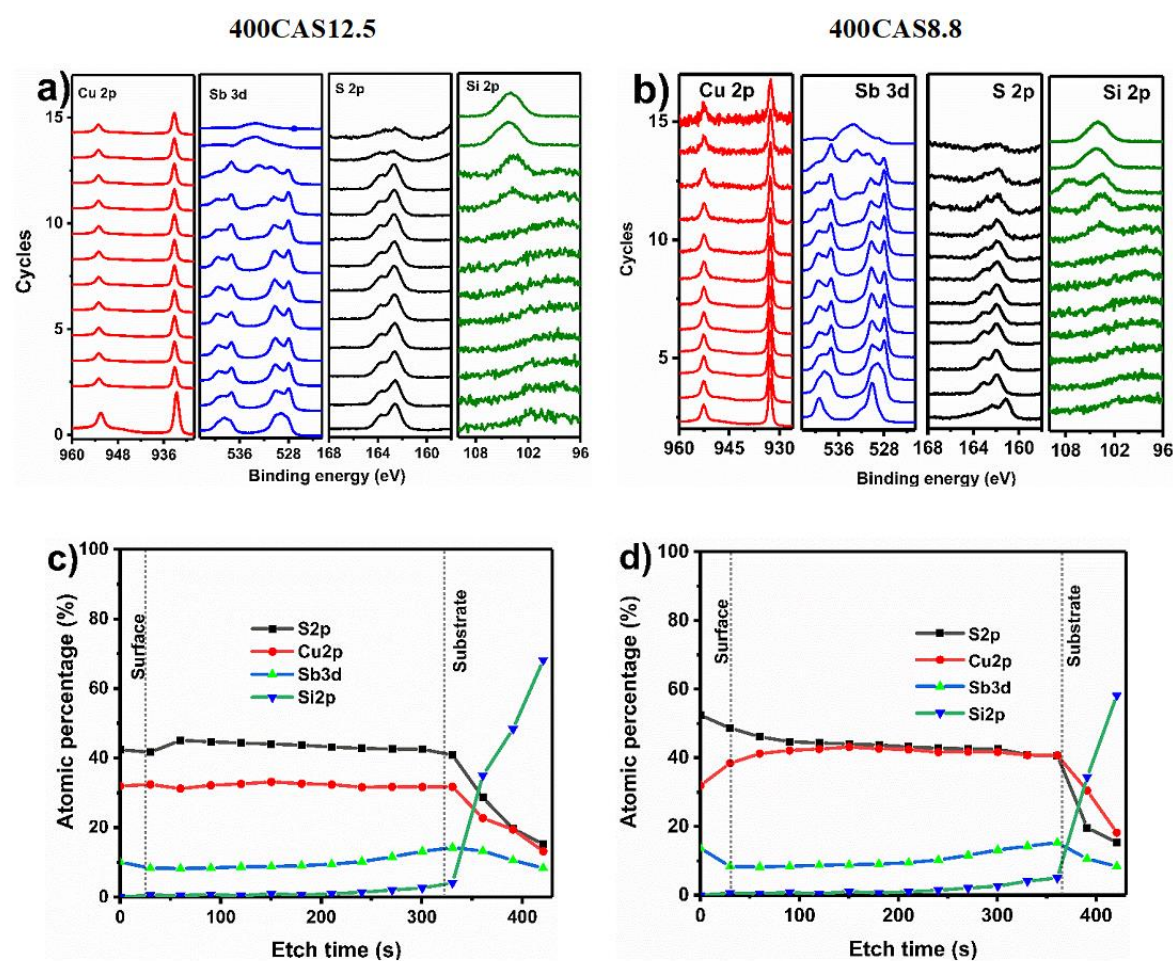
Figure 6.7: (a, b) Depth profile of the $Cu_{12}Sb_4S_{13}$ thin films; 400CAS12.5 and 400CAS8.8 (c, d) The calculated atomic compositions of 400CAS12.5 and 400CAS8.8.

The depth profiles of 400CAS12.5 and 400CAS8.8, are shown in figures 6.7 b) and c), respectively. Cu, Sb, and S elements are present in the samples throughout thickness, from the surface to the substrate. Si peaks originated from the glass substrate. The atomic compositions of the films, from the surface down to the substrate, are represented by c) and d) in figure 6.6, respectively. In the 400CAS12.5 sample, Figure 6.7 c) reveals that there is roughly 32 % copper, 15% antimony, and 45% sulfur throughout the depth of the sample. As a result, the S/(Cu+Sb) ratio that was calculated to be 0.9 consistent with the EDAX measurements. In the case of 400CAS8.8, as shown in Figure 6.7 d, identical proportion of copper and sulfur (40%) are found throughout the sample, however the proportion of antimony is 16%. In this instance, the

compositional ratio, written as S/(Cu+Sb), is 0.7 which is comparable with the respective EDAX results.

6.2.2 Morphology

The surface morphology of as prepared samples of CAS12.5 and CAS8.8 is given in Figure 6.8 (a- d) as marked, under different magnifications (a and b for CAS 12.5; c and d for CAS 8.8). A uniform distribution of compact spherical grains can be seen. Figure 6.9 (a) and Figure 6.9 (b), respectively, display the surface morphologies of 400CAS12.5 and 400CAS8.8. In the figure, 400CAS12.5 sample has roughly spherical grains that are scattered evenly throughout the surface, leading to improved carrier transport. As seen in the figure, the surface of 400CAS8.8 (the film composition that is high in copper) is composed of spherical grains that are interwoven to form flower-like structures that have concave centers. These grains are uniformly distributed across the surface.
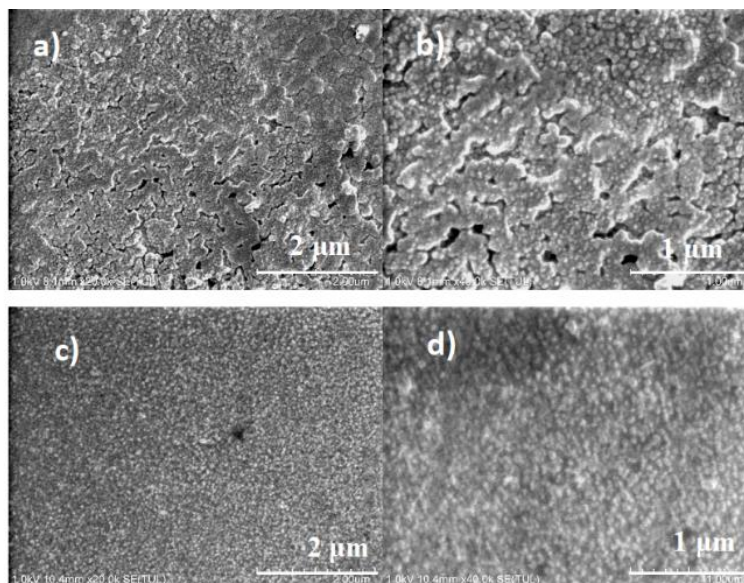
Figure 6.8 SEM images of as prepared (a-b) CAS12.5 and (c-d) CAS8.8
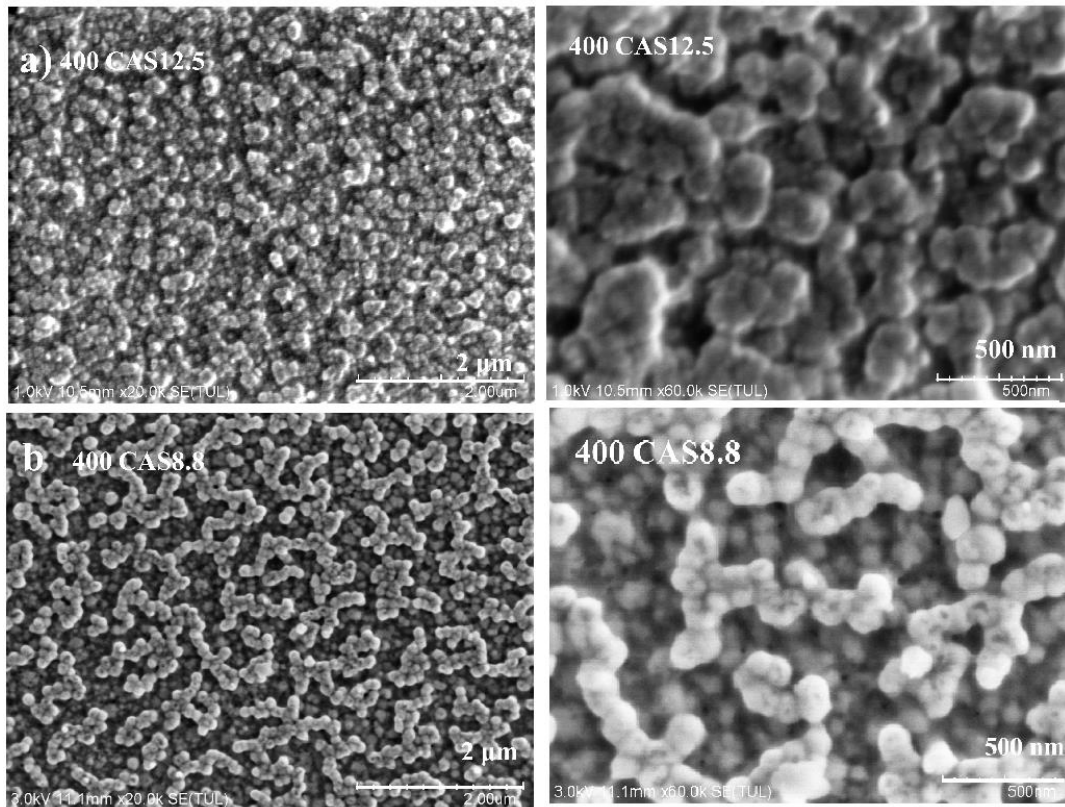
Figure 6.9: SEM images of $Cu_{12}Sb_4S_{13}$ films thin films a) 400CAS12.5 b) 400CAS8.8

6.2.3 Optical properties
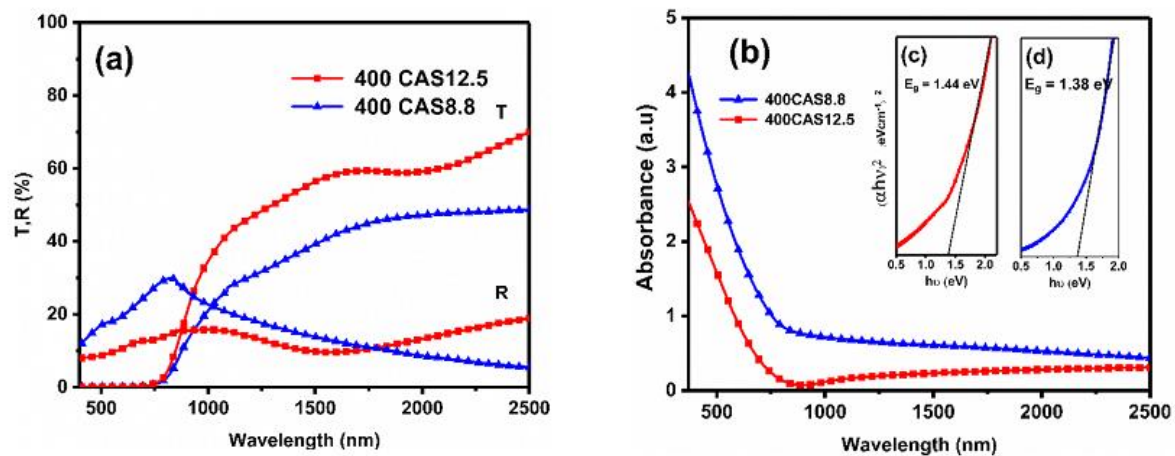
Figure 6.10 a) Transmittance and reflectance spectra of $Cu_{12}Sb_4S_{13}$ thin films (400CAS12.5 and 400CAS8.8) b) Absorbance vs wavelength spectra (CAS12.5 and CAS8.8) along with Tauc plots as inset.

The transmittance (T%) and reflectance (R%) spectra of $Cu_{12}Sb_4S_{13}$ thin films (400CAS12.5 and 400CAS8.8) were measured in the wavelength range of 400-2500 nm to determine the optical characteristics of the films shown in Figure 6.10. The corresponding absorption spectra are depicted in Figure 6.10 (b). As can be seen in the Figure, the absorption edge moves from the region around 700 nm to the NIR region around 850 nm as increase in the Cu/Sb ratio in the films. By applying equation (15) (section 4.5) to the T and R spectra of the samples, the absorption coefficient of the samples may be determined.

The optical band gap values of the films are calculated using the Tauc plots (Figure 6.10, inset), and the values are 1.44 and 1.38 eV respectively for CAS12.5 and 400CAS8.8. These results are in accordance with the data that are reported for tetrahedrite $Cu_{12}Sb_4S_{13}$ thin films. The optical band gap of the films that were formed by sulfurization through RF magnetron sputtered metal precursors or spin coating using hydrazine solutions was measured to be 1.47 eV [90,202]. It was reported that the electron beams evaporated films had a value of 1.8 eV higher than the other films. According to the observations of the diffraction pattern, the higher crystallinity of the copper-rich film's theoretical simulation of density of states and band diagram, it was observed that presence of Cu and Sb 3d orbitals are heavily occupied in the band edges contributes to low band gap value compared to other phases of copper antimony sulfide structure.

6.2.4. Electrical properties

The electrical conductivity, carrier concentration, and charge carrier mobility of the polycrystalline $Cu_{12}Sb_4S_{13}$ thin films (CAS12.5100 ml, 400CAS12.5100 ml, 400CAS8.8) from Hall effect experiments were performed and the results are shown in Table 14. From the Table, the carrier concentrations for 400CAS12.5 films is in the order of 10^{18} cm^{-3}, which reveals that these films have a semiconducting behavior with electrical conductivity in the range of 1-3 (Ωcm)$^{-1}$ The fact that the carrier concentration of sample 400CAS8.8 is one order greater (10^{19} cm^{-3}) and, conductivity (12.5 Ωcm)$^{-1}$ of 400CAS8.8 to show semi-metallic nature. In binary and ternary copper chalcogenides, copper vacancies, in general, are responsible for the presence of shallow acceptor defects [81,203,204]. Additionally, the presence of Cu_2S which is p-type, even though extremely minimal amount, in copper-rich films can also result in increased electrical conductivity [205–208].

Table 14: Hall effect measurements of $Cu_{12}Sb_4S_{13}$ thin films deposited at various conditions.

Sample	Carrier concentration $(cm^{-3}) \times 10^{18}$	Mobility $(cm^2/V.s)$	Conductivity $(\Omega cm)^{-1}$
CAS12.5100 ml	1.3	4.2	1
350 CAS12.5100 ml	3.9	4.7	2.9
400CAS12.5100 ml	6.6	5.7	5.8
400 CAS8.8	16.3	4.3	12.1

Further, the photocurrent response carried out on thin films with CAS12.5100ml employing a tungsten halogen light of 50 W is shown in Figure 6.11. A bias voltage of 0.5 V was supplied, and the current was measured while the light source was cycled ON and OFF for ten cycles, in the dark for 60 sec, in the light for 20 sec, and in the dark for 100 seconds. Because of their persistent photo conducting nature, a longer time period of 60 -100 seconds was given under dark after switching off the illumination in order to check the electrical stability in the dark and its decay to the initial value at the OFF stage. Figure 6.11 depicts the photo responses of CAS12.5100 ml and 400CAS12.5100 ml, both of which have been determined to be polycrystalline by XRD (Figure 6.3). In both instances, the photo response current for 10 cycles indicates a behavior that is consistent and stable throughout.

In addition, photocurrent response studies were carried out utilizing LEDs of various wavelengths, ranging from UV (400 nm) through Vis (blue-465 nm, green-520 nm, and red-620 nm), and NIR (740 nm) spectrum. The films have a photocurrent response that is similar for all wavelengths (UV, VIS, and NIR) and for NIR even higher magnitude. Equation (17) (section 5.5) is used to determine the photosensitivity of the samples, which quantifies the conversion of light into an electrical signal and, thus, the photodetection property mentioned in section 5.5.
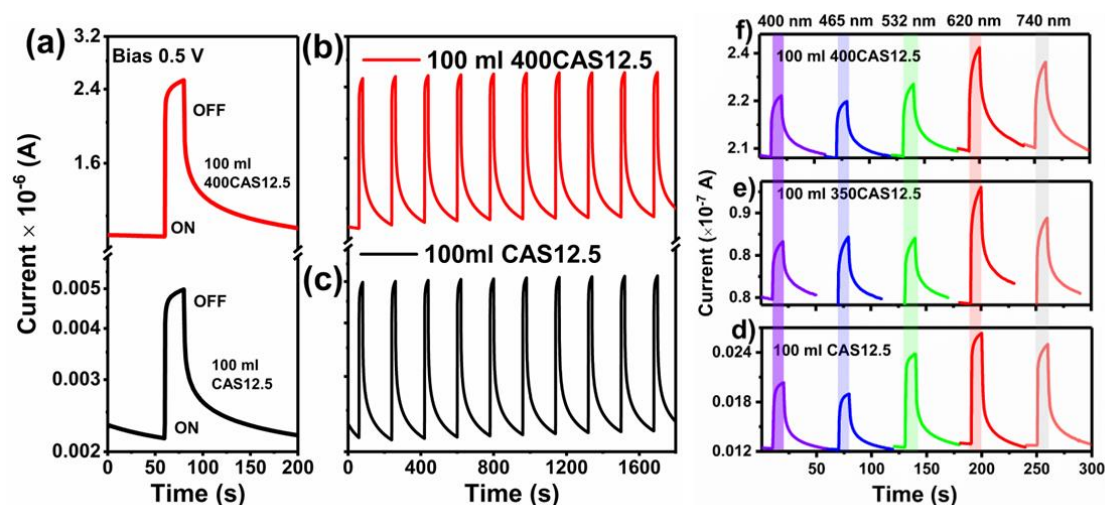
Figure 6.11: a) Photo response of polycrystalline $Cu_{12}Sb_4S_{13}$ thin films (100ml CAS12.5, 100ml 350CAS12.5 and 100ml 400CAS12.5)

The sensitivity values of 100 ml CAS12.5 and 100 ml 400CAS12.5100 were 133% respectively. In addition, the rise and decay times   were calculated for 100 ml CAS12.5and the 100ml 400 CAS12.5 from Figure 6.11a. The rise/decay time value as 1.1 seconds and 0.7 seconds, respectively the samples undergo a post-thermal treatment, which results in an improvement in the photocurrent rise time due to charge carrier movement. However, decay time for CAS12.5 is more than 50 seconds as seen in the figure. This may be, explained by the presence of deep trap states caused by intrinsic defects, as described in transition metal-based compounds [7,40] The deep acceptor trap states (antimony vacancies, copper interstitials) which have low formation energy were highly thermal stable, they can act as centers of charge compensators in the thin films. The photostability of the thin films is demonstrated by the cyclic measurements that are shown in Figure 6.11 b) and c),

The photodetection sensitivity for various wavelengths using LEDs, as follows: Figure 6.11 d), e), and f) demonstrates photo response of 100 ml CAS12.5, 100 ml 350CAS12.5, and 100 ml 400CAS12.5, respectively, under illumination using 30 W LEDs with varied wavelengths that ranged from ultraviolet (400 nm) to near infrared (740 nm), as indicated in the figure. It can be seen from the plots that the semiconducting curves show essentially wavelength independent photodetection, particularly in the visible area of the spectrum. The fundamental absorption edge of the sample is located at 880 nm, which correlates with the region of enhanced photocurrent in

the red/NIR spectrum. In section 6.4 discuss the optical properties while the band gap is calculated as 1.45 eV, which means the absorption edges lies around 880 nm. This can be the reason for the enhanced absorption at red/NIR region. Therefore, the semiconducting $Cu_{12}Sb_4S_{13}$ thin films can function as a single photodetector for a wide range of wavelengths, from the visible to the near infrared.

The following section discusses the composition analysis and photophysical properties chalcostibite $CuSbS_2$ phase.

6.3 Chalcostibite CuSbS₂

6.3.1 Composition

The EDS mapping and spectrum were employed for the elemental compositional analysis of the as prepared (As prep) and vacuum annealed (VA 350) samples. Figure 6.12 (a – c) shows the EDS mapping of the as prepared sample together, Figure 6. 12 (e-f) shows the mapping of vacuum annealed sample. EDS mapping shows a uniform elemental distribution throughout the samples. There could observe a reduction in the atomic concentration which could be attributed from the diffusion of elements or recrystallization in the sample from the sample during annealing. The atomic concentration and then Cu/Sb ratio from the EDS spectra are tabulated as shown in Table 15. Both atomic concentration and Cu/Sb ratio confirm the near stoichiometry of the $CuSbS_2$ thin films. Absence of signals from the residues such as chlorine or nitrogen which were present in the precursor solution , confirms the phase purity of the sample.

Table 15 Atomic concentration of as prepared (As prep) and vacuum annealed sample (VA350)

Sample	Element			Cu/Sb
	Cu K	Sb L	S K	
As prep	31.4	29	39.6	1.08
VA 350	28.8	27.5	43.7	1.04
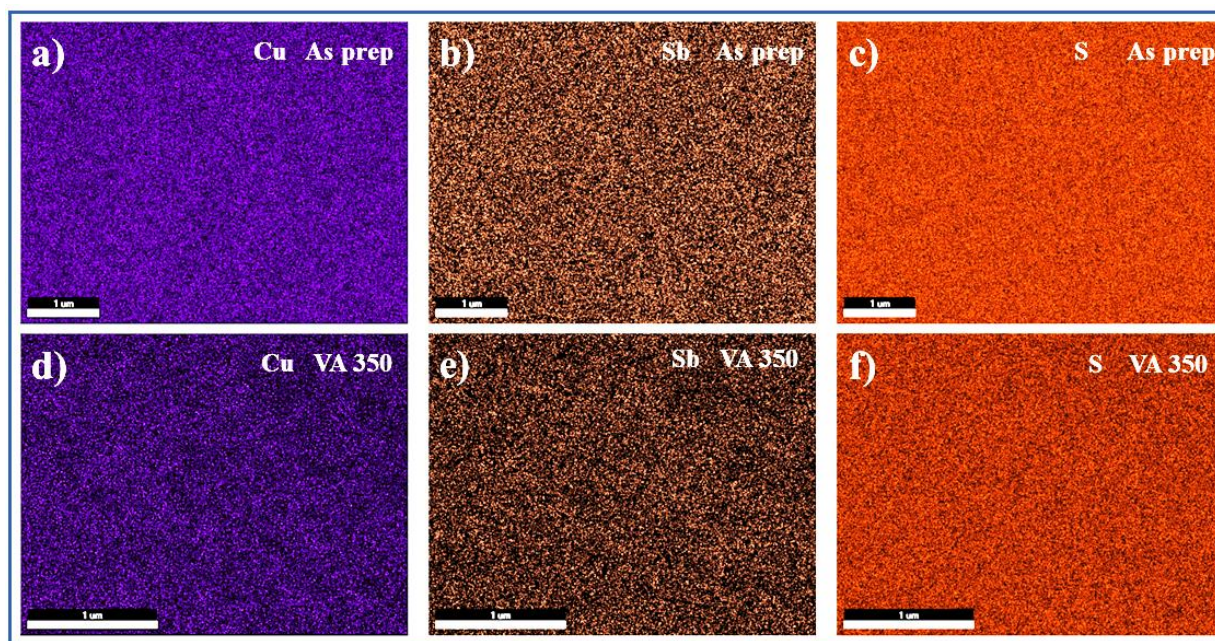
Figure 6.12 EDS mapping of Cu, Sb and S from (a-c) as prepared sample (As prep) and (d-f) vacuum annealed sample (VA 350)

Using XPS relative chemical states as well as depth-wise elemental composition, were investigated. The survey spectra and high-resolution spectra and were both recorded after one cycle of Ar+ etching. Figure 6.13 a) reveals the survey spectra of $CuSbS_2$ as prep and vacuum annealed sample (VA 350). All the procedures for calibration and data acquisition were followed as per section 6.2.

Cu 2p core level spectra of as prep (Figure 6.13b) and VA 350 (Figure 6.13e) are composed of spin-orbit doublets constituted by Cu $2p_{3/2}$ and Cu$2p_{1/2}$ at 953.6 eV and 933.8 eV, separated by $\Delta E = 19.8$ eV. The presence of Cu^+ can be determined from the peak B.Es of the core level Cu 2p spectra, and the values were consistent with previously reports[204]. Sb core level spectra of the samples are shown in Figure 6.13 (c - f). Sb 3d peaks are constituted of spin-orbit coupled $3d_{5/2}$ and $3d_{3/2}$ doublets. The peaks of $3d_{3/2}$ can be deconvoluted into two peaks: Sb^{3+} (537.9 eV), and Sb^0 (536.9 eV). The $3d_{5/2}$ peak is fitted into two distinguish peaks which are Sb^{3+} (528.5 eV) and Sb^0 (527.5 eV), with a binding energy separation of $\Delta E = 9.4$ eV, respectively[209]. Sputter induced effect by Ar^+ etching contributes to reduce Sb^{3+} to Sb^0 peak[177]. S 2p peaks are peak

fitted into the $2p_{3/2}$ (163.08 eV) and $2p_{1/2}$ (161.88 eV) components with doublet appears for sample as prep and VA 350 samples at 162.98 and 161.78 eV, which correspond to $2p_{3/2}$ and $2p_{1/2}$, respectively with ΔE of 1.2 eV[210–212]. The binding energies for Cu^{+1}, Sb^{3+} and S^{2-} ions for $CuSbS_2$ thin films were consistent with reports[201,213,214]. Figure 6.13 (h-i) shows the depth profile indicating the presence of elements distributed throughout the sample from surface to substrate.

114
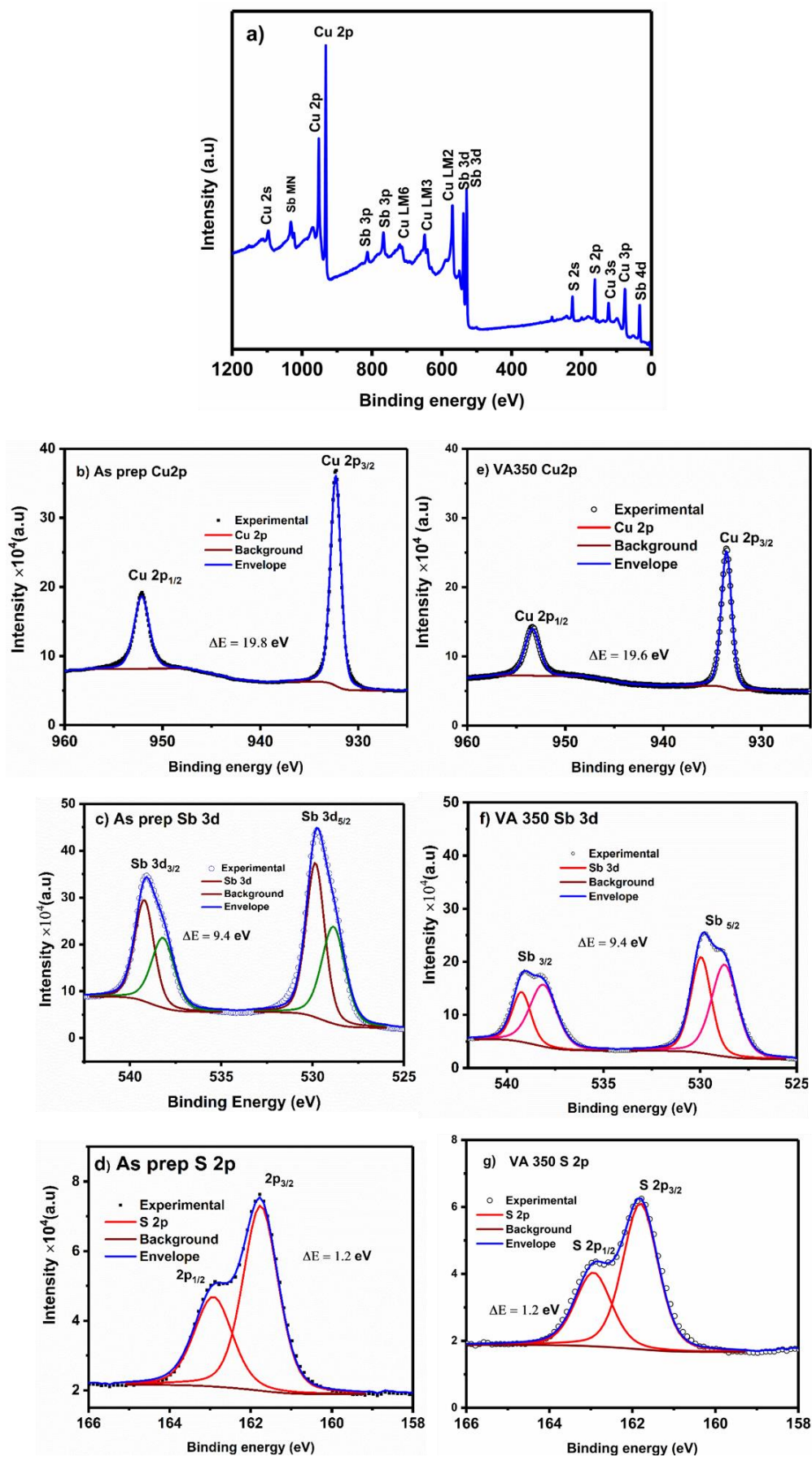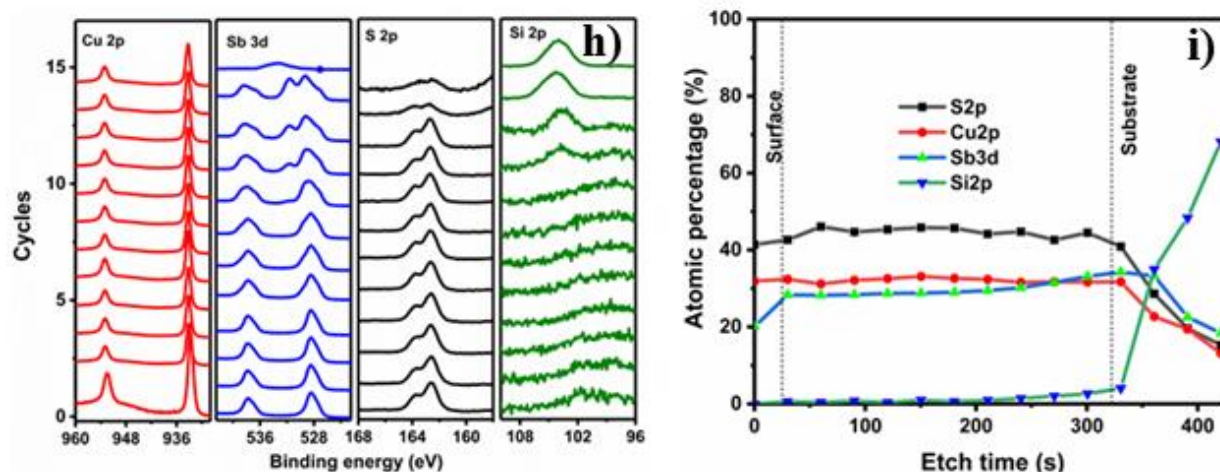
Figure 6.13. a) The survey spectra of CuSbS$_2$ thin films (As prep and VA 350), (b, c, d) High-resolution spectra of Cu 2p, Sb 3d and S 2p core levels of as prep (right column) and (e, f, g) High-resolution spectra of Cu 2p, Sb 3d and S 2p core levels of VA350. (h - i) depth profile and atomic percentage of the Cu 2p, Sb 3d and S 2s.

6.3.2 Morphology

The surface morphologies of as prepared (as prep) and vacuum annealed (VA 350) samples captured using FESEM are shown in Figure 6.14. Figure 6.14 (a) and (b) shows the as prepared sample at two different magnifications. A uniform and homogenous distribution of nano sized spherical particle can be observed on the surface. The micrographs reveal crack and pinhole free surfaces in the samples. Similar structure with uniform nanosized grains compactly distributed on the surface were reported [215,216]. For annealed sample, a compact and larger interconnected spherical grain on the surfaces was observed, as shown in figure 6.14 (c) and (d) (two magnifications). This might could be attributed to the grain coarsening or Ostwald ripening reported in spin coating and spray pyrolysis deposited thin films [217–219]. During the annealing, larger crystallites growth were improved with expense of smaller crystallites leading to the densely packed structures. This observation was confirmed in the diffraction pattern (Section **6.1** Figure **6.4).** Thermal treatments could provide sufficient energies to atoms to migrates easily among themselves which can improve the electrical properties of the thin film.

115
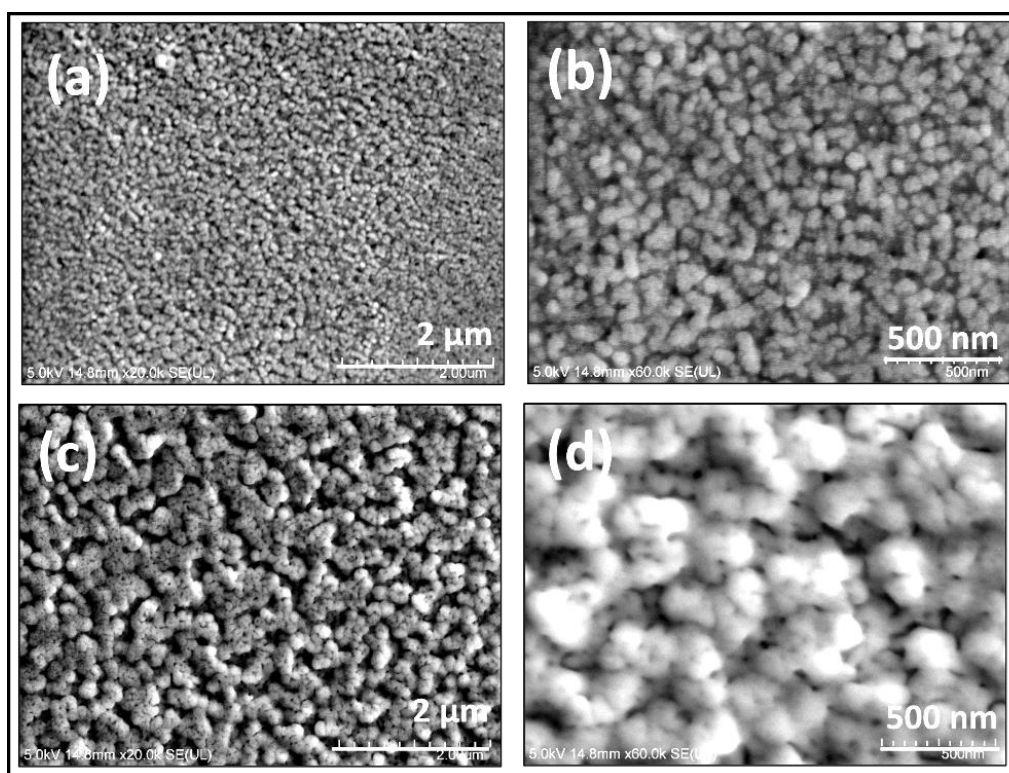
Figure 6.14 Surface morphologies of (a – b) as prepared sample, (c – d) Vacuum annealed samples (VA 350)

6.3.3 Optical properties

Figure 6.15 a) and b) displays transmittance (T) and reflectance (R) spectra along with Tauc plots $CuSbS_2$ thin films; In Figure 6.15 a) shows 70 % transmittance around visible spectra where annealed sample shows lower transmittance due to compensating reflection in the non-absorbing region (900-2500). The interference peaks in T and R spectra indicate specularly reflective homogeneous thin film quality. The optical band gap of the materials labelled : As prep, vacuum annealed samples (VA 350 and VA 400) calculated was 1.54, 1.52 and 1.51 eV respectively. Optical band gap evaluated from the $(\alpha h\upsilon)^2$ vs $h\upsilon$ (Tauc plot) signifies the direct electron transition yielding high absorption coefficient and hence high electron-hole generation rate. Such materials are suitable candidates for the photovoltaic as well as photodetectors [82,104,220] . The previous reports discussed the deposition temperature dependent band gap which varied from 1.8 – 1.2 eV $CuSbS_2$ thin films [84,221,222]. The temperature dependence on band gap can be correlated to the increase in crystallinity of the films as the substrate temperature

increases. Due to the presence of flat band in conduction band minimum indirect transition from valence band to conduction band is also predicted[84,85,223]
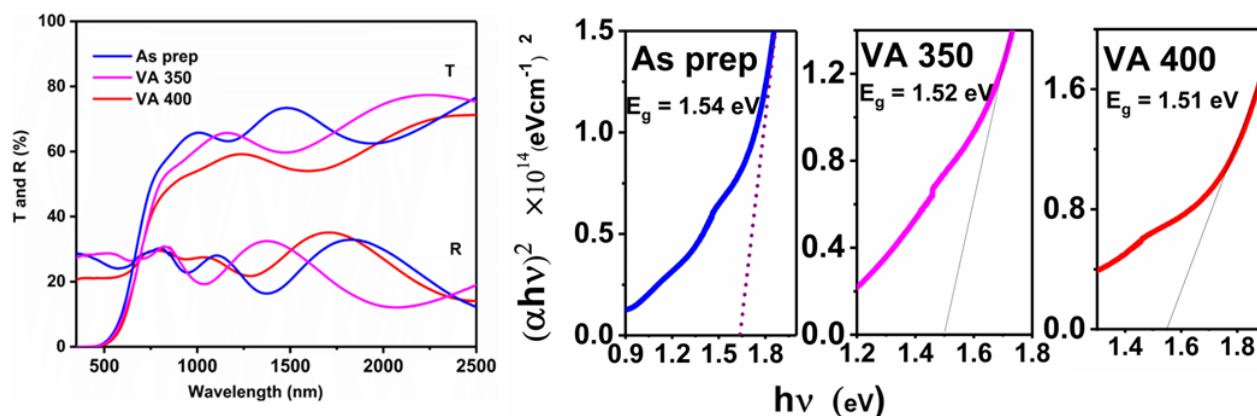
Figure 6.15 Optical properties of CuSbS$_2$ thin films; a) Transmittance (T) and reflectance (R) Vs. wavelength of as prepared samples and vacuum annealed samples (at 350 (VA350) and 400 (VA400) °C). Tauc plot calculating the optical band gap of As prep, VA 350 and VA400

6.3.4. Electrical properties

The electrical properties of as prepared and vacuum annealed samples of CuSbS$_2$ thin films measured based on Hall effect measurement are given in Table 16. As prepared sample shows lower carrier concentration compared to the vacuum annealed ones. Annealed samples VA 350 and VA 400 show higher mobility which can be attributed to the improved crystallinity of the samples. Copper vacancies have significant influence in the conductivity of copper chalcogenides and these shallow defects are the origin of intrinsic p type conductivity in such semiconductors. Copper vacancies (V$_{Cu}$) have the lowest formation energy among the other acceptor defects such as antimony vacancies, copper on antimony interstitials etc. V$_{Cu}$ have the acceptor defect where the energy state can easily ionized and generate hole carriers under room temperature and hence so the conductivity of the determined by V$_{Cu}$[104]. In the recent reports, electrical properties of the spray deposited CuSbS$_2$ thin films were varied mainly due to the substrate temperature, annealing temperature and thickness. The carrier concentration was the common factor which enhance and limits the electrical properties of films[84,85,223].

Table 16 Hall effect measurements of the CuSbS$_2$ samples.

Sample	Carrier concentration (cm^{-3}) $\times 10^{17}$	Mobility (cm^2/V. s)	Conductivity (Ωcm)$^{-1}$
As prep	2.5	5.7	0.8
VA 350	5.2	8.1	4.4
VA 400	5.8	8.8	5.1

The photo response curves of CuSbS$_2$ thin films recorded using 50 W tungsten halogen lamp with bias voltage of 1V are given. The current was recorded under illumination (10 s) and dark (10 s) (ON-OFF) conditions.
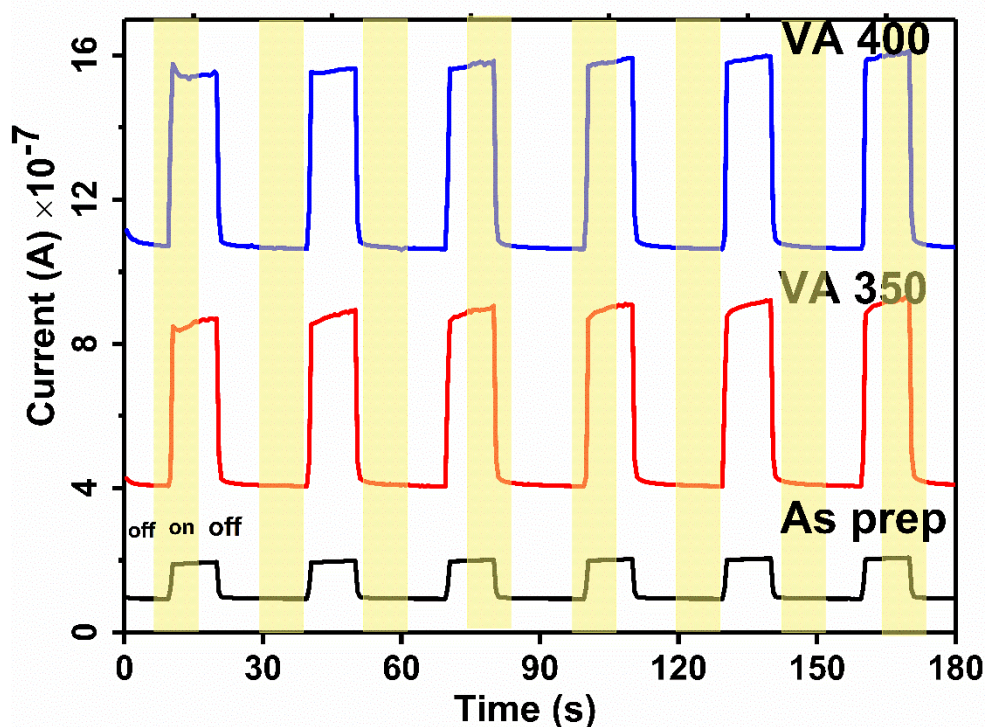
Figure 6.16 Photo response of CuSbS$_2$ samples a) as prepared, vacuum annealed samples b) 350 °C and c) 400 °C.

Figure 6.16) shows the photoresponse of as prepared sample deposited at 200 °C, vacuum annealed at 350 and 400 °C. Both dark and illuminated currents increase by one order with

annealing temperature, results were consistent with the Hall effect measurements. The higher current values may be due to improvement in crystallinity and hence improve carrier transport properties. From the photoresponse curves, the as prepared sample's rise time was calculated; 0.9 sec and for vacuum annealed sample the values decreased to 0.6 (VA 350) and 0.5 sec (VA 400). Copper chalcogenide photodetector reports antistes inversion defect (Cu_{Sb}) restrain the photo response and controlled by the preferential crystal growth or isoelectronic dopants to the films [224]. In this study, with post-thermal treatment, photo response is enhanced compared to the as prepared thin films and other reports with low photoconductivity[143,216]. Solution based solution techniques like spin coating and chemical bath deposited $CuSbS_2$ thin films were obtained conductivity 0.8 – 2.4 $(\Omega cm)^{-1}$ and the carrier concentration of 10^{16} – 10^{18} (cm^{-3}). A variation on the carrier concentration, mobility and conductivity were improved on annealing temperature and exposure time [225,226].

By correlating the analysis of the thin films formed using a given volume of precursor by varying Cu/Sb ratios in the precursor for a fixed S concentration (varying Cu for a given Sb and S: varying Cu and Sb simultaneously (S/(Cu+Sb)); very low Cu concentration for the maximum Sb and S) , it is observed two different phases of copper antimony sulfide is formed.   Thus, a selective synthesis of tetrahedrite and chalcostibite phases is achieved using ultrasonic spray pyrolysis. It was estimated that the reaction temperature and cation molar ratio determined the growth of phases. In this study, during the deposition, variation of S/Cu+Sb molar ratio determines the phase control. The change in molar ratio shifts the equilibrium conditions of phases favoring the formation of different phases. At the same time surface energy under nucleation influences the mobility of atoms, led the $CuSbS_2$ phase formation [214,227]. In the study samples annealed at 350 °C were chosen to fabricate the solar cell considering low temperature manufacture of ALL SPRAY COTAED photovoltaic devices. So, the next chapter includes the investigation of solar cell devices with structures: all spray pyrolyzed 1) ZnO/Zn (O, S)/ (Sb_2S_3)   2) ZnO/Zn (O, S)/ ($Cu_{12}Sb_4S_{13}$, 3) ZnO/Zn (O, S) / $CuSbS_2$) layers

From the analysis of electrical and optical properties of $Cu_{12}Sb_4S_{13}$ and $CuSbS_2$ thin films by ultrasonic spray, it is evident that the thin films can be incorporated to fabricate solar cells.

Chapter 7

All-Spray Pyrolysis coated photovoltaic and photodetector Devices using $Cu_{12}Sb_4S_{13}$ and $CuSbS_2$ thin films

In this chapter, characteristics of photovoltaic and photodetector devices using $Cu_{12}Sb_4S_{13}$ or $CuSbS_2$ as absorber layer and with ZnO and Zn (O, S) as window layers are explained. Photodetectors and PV devices were fabricated by ultrasonic spray pyrolysis. The major focus is to explore $Cu_{12}Sb_4S_{13}$ for device applications, which is not explored so far in literature. The device configurations are as follows; spray pyrolyzed ZnO and Zn (O, S) as window layers deposited over on commercially available FTO: FTO/ ZnO/Zn (O, S)/ Sb_2S_3 , FTO/ZnO/Zn (O, S)/$Cu_{12}Sb_4S_{13}$, FTO/ZnO/Zn (O, S)/ $CuSbS_2$. The solar cell parameters are evaluated from the respective J-V characteristics. Also, the performance of heterojunctions (Zn (O, S)/Sb_2S_3, Zn (O, S)/$Cu_{12}Sb_4S_{13}$, Zn(O, S)/$CuSbS_2$) as self-driven photodiodes are evaluated.

7.1 FTO/ ZnO/Zn (O, S)/ Sb_2S_3

Figure 7.1 a) shows the solar cell structure: FTO/ZnO/Zn (O, S)/ Sb_2S_3/C/Ag configuration. Figure 7.1 shows the schematic representation with a) J-V characteristics of the device in the dark and illumination. The device is illuminated by the solar irradiance filtered by AM 1.5G and the Ag electrode is painted from front (absorber layer) and back contact (FTO) of the devices. J-V measurements of solar device under dark and illumination   from the curve, the photovoltaic properties of the device are calculated. The results reveal that the device yields an open circuit voltage (V_{oc}) of 0.382 V and a short circuit current density (J_{sc}) of 1.3 mA/cm^2, and power conversion efficiency (η) of 0.15 %. Single p-n junction Sb_2S_3 solar cells were reported with low open circuit voltage and short circuit current density due to the intrinsic trap states act as recombination centers for the photogenerated charge carriers[228]. Hall effect measurement showed the low carrier concentration and low mobility for electron causing poor charge carrier transport and hence very low power conversion efficiency. The structural defects present in the antimony-based chalcogenides were reported to have recombination centers for the charge carriers led to inefficient charge separation. Together, large interface surface from the deposition techniques like (spin coating, chemical bath deposition etc.) results in porous p-n junction were prone to the higher interface recombination thereby the open circuit voltage diminishes[229–231].

120

Using spray pyrolysis Sb_2S_3 thin films possess high thermal stability and obtained higher open circuit voltage compared with above reports [232,233]. With insight to improve the cell performance, copper incorporated Sb_2S_3 thin films were fabricated for the photovoltaic application.

Figure 7.1 b) shows the zero biased photodetection behavior of the heterojunction under illumination using 50 W halogen lamp. The photocurrent recorded for 10 s under ON/OFF conditions (samples kept dark and illuminated for 10 sec each). The sensitivity (equation 17) and responsivity(R) of the photodetector is calculated using the equation (18)

$$R = \frac{I_{light} - I_{dark}}{A.P} \tag{18}$$

I_{light} and I_{dark} define photogenerated current under illumination and dark current respectively while R denotes the responsivity, A denotes effective area and P signifies the illumination density. The photosensitivity and responsivity of FTO/ ZnO/Zn (O, S)/ Sb_2S_3 are calculated as 123 % and 6.24×10^{-5} mAW^{-1}. The calculated rise/decay time record as 1.1/1.3 seconds, where delayed time was observed in Sb_2S_3 solar cells compared to other antimony-based chalcogenides photodetectors. The device shows a cyclic photocurrent stability over 8 cycles confirming the stability of photodetector.
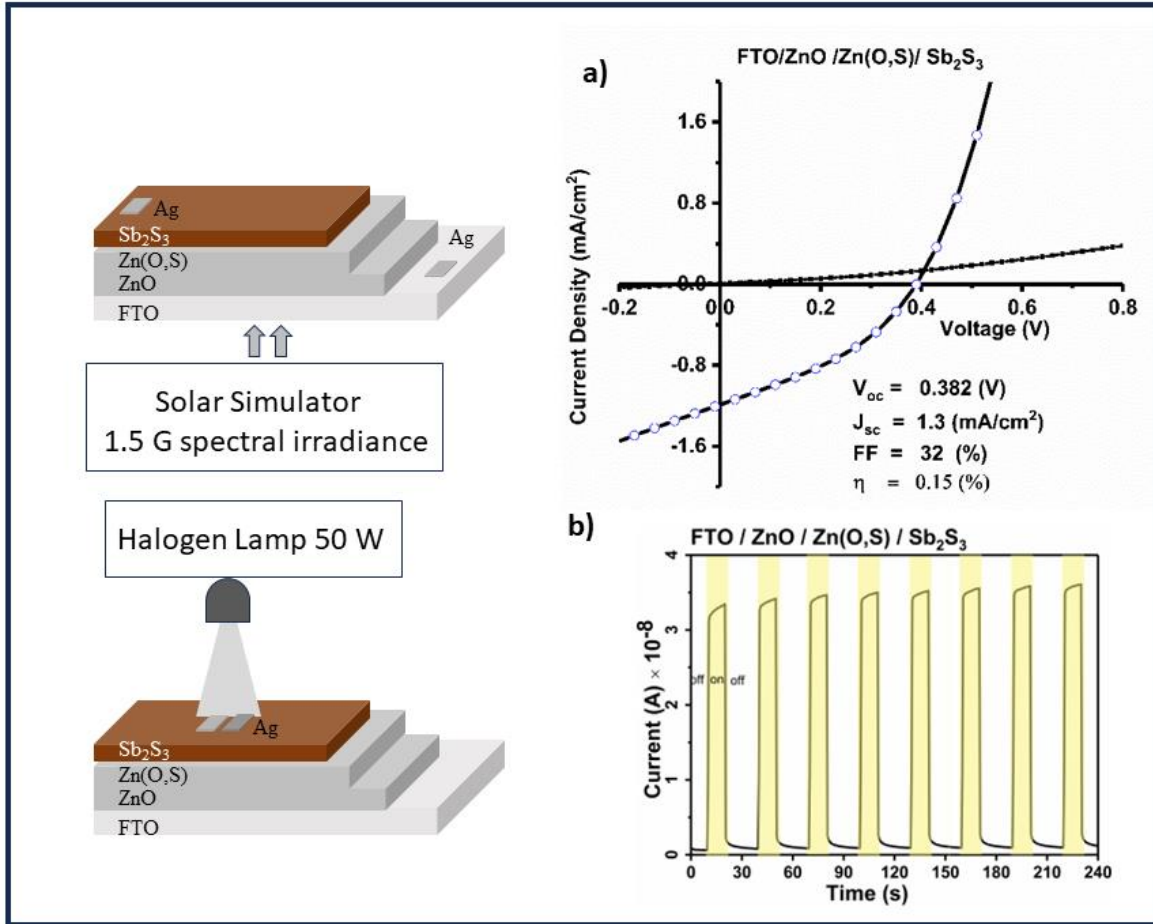
Figure 7.1 Schematic representation of cell configuration illuminated using solar irradiance with AM 1.5G a) shows the J-V characteristics of FTO/ZnO/Zn (O, S)/Sb$_2$S$_3$ heterojunction under illumination and dark. b) Photodetector measurements of the cell illuminated by 50 W halogen lamp illustrated using schematic representation.

7.2. FTO/ ZnO/Zn (O, S)/ p-Cu$_{12}$Sb$_4$S$_{13}$

From the electrical properties analysis, CAS12.5 possessed semiconducting nature whereas CAS8.8 showed metallic nature. Considering lower temperature for the device processing, phase pure samples formed by annealing at 350 °C CAS12.5 (350CAS12.5) and CAS8.8 (350CAS8.8) were incorporated to form heterojunction PV structure of FTO/ ZnO/Zn (O, S)/ p-Cu$_{12}$Sb$_4$S$_{13}$ as marked in Figure 7.2. Figure 7.2 a) shows J-V characteristics of FTO/ZnO/Zn (O, S)/350CAS12.5 heterojunction under dark and illumination. Under illumination, it results in

450 mV V_{oc}, 8.1 mA/cm^2 J_{sc} and FF (fill factor) 30 %, yielding 1.1% power conversion efficiency. FTO/ZnO/Zn (O, S)/350CAS8.8 PV measurements absorber layer which is higher conductivity improves the short circuit current density to 15.4 mA/cm^2, even though the FF value is very low.

Figure 7.2 c) shows the photodetection properties of the heterojunctions without applying any external bias. In the figure, cyclic photo response is recorded for 10 sec each under illumination ON/OFF conditions. The photoresponse reveals a steady photocurrent throughout the measurements. The rise time and decay time were measured as 0.78 and 0.8 s respectively, faster response compared to that of Sb_2S_3 based photodetector. The sensitivity and responsivity of the samples are calculated using the equation (17 & 18). FTO/ ZnO/Zn (O, S)/ 350CAS 12.5 shows 130 % and 4.52×10^{-3} mAW^{-1} while semi metallic absorber layer with device configuration FTO/ ZnO/Zn(O, S)/ 350CAS 8.8 shows 136 % and 2.32×10^{-3} mAW^{-1} sensitivity and responsivity respectively. This thesis reports the highest open circuit voltage using $Cu_{12}Sb_4S_{13}$ absorber layer, Wang *et al.* reported lower V_{oc} and J_{sc} (0.03 V and 7 mA/cm^2) due to the lower charge rectification arise from the improper band alignment and severe recombination[96]. Tamilselvan et al reported $Cu_{12}Sb_4S_{13}$ phase as hole transport layer for perovskite solar cell where better conduction band alignments to the $MAPbI_3$ layer caused improved charge collection at electrodes resulting a power conversion efficiency of 6.5%[98]. The zero-bias voltage photodetection obtained here confirms the presence of an electric field of sufficiently large in strength which can separate charge carriers generated in the depletion region. Copper incorporated devices show better photodetector parameters compared to antimony-based binary chalcogenides which can be attributed to the structural and electronic rearrangement due to the incorporation transition metal into lattice.
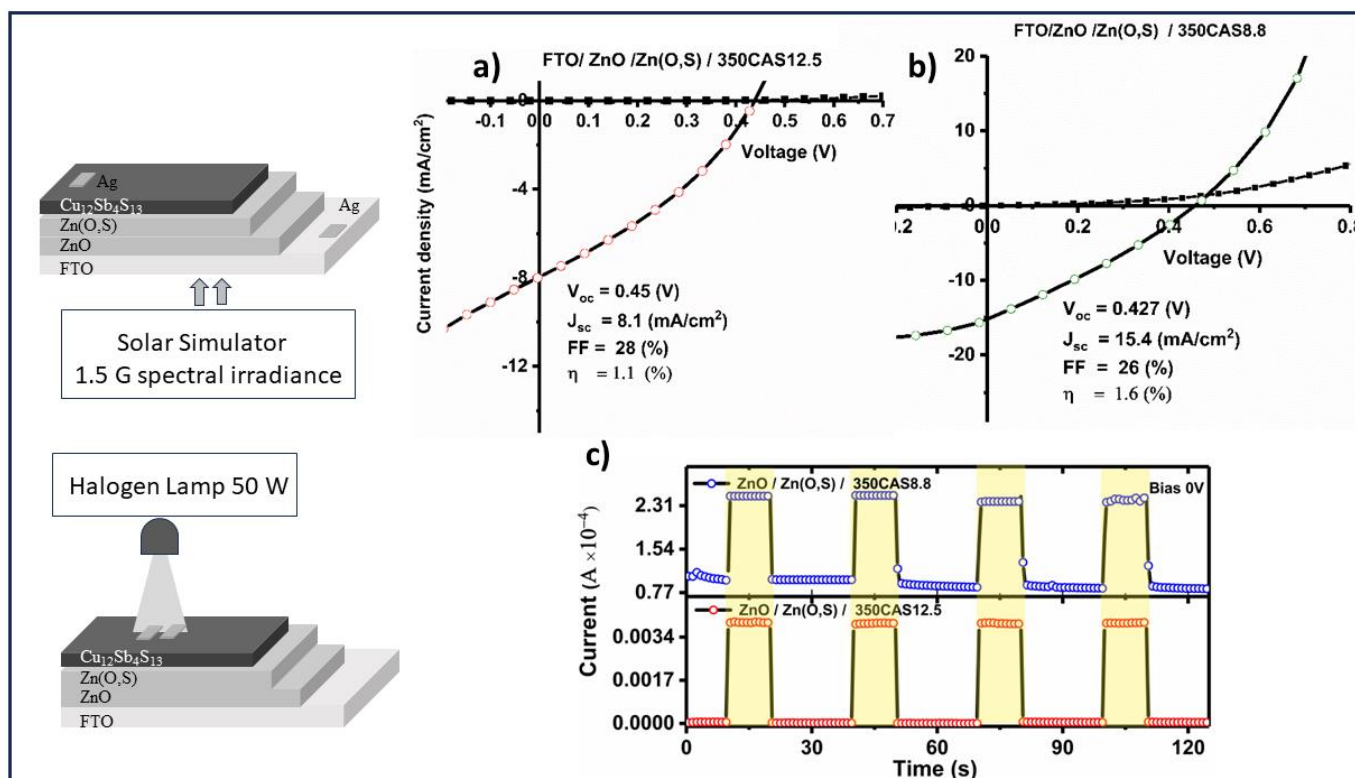
Figure 7.2 a) and b) the J-V characteristics of FTO/ ZnO/Zn (O, S)/ $Cu_{12}Sb_4S_{13}$ devices. c) Photoresponse of FTO/ ZnO/Zn (O, S)/ $Cu_{12}Sb_4S_{13}$ devices illuminated under 50 W halogen lamp.

7.3. FTO/ ZnO/Zn (O, S)/ CuSbS₂

Further, the J-V characteristics of   ALL-SPRAYED PV structure using copper antimony sulfide thin films (VA350) as absorber (FTO/ ZnO/Zn (O, S)/ $CuSbS_2$) at dark and illuminated conditions are given in Figure 7.3. The measured PV parameters were V_{oc}: 403 mV; J_{sc} : 2.5 mA/cm^2; FF : 32 % and power conversion efficiency of 0.32 %. Compared to the tetrahedrite phase, there could be observed a drop in open circuit voltage and steep decrease in the short circuit current. But compared to stibnite phase copper incorporation provides better open circuit voltage and fill factor which was evident for potential pv application. The major reason for the fall in V_{oc} could be attributed to the series resistance and conduction band offset, while the drop in short circuit current can be attributed to the low carrier concentration followed by either high density deep acceptor defects or interface recombination. The noticeable recorded efficiency in the recent past decade investigation so mentioned as follows. Septine *et al.* reported electrochemical deposition of glass/Mo/CuSbS2/CdS/ZnO:Al inverted configuration produces V_{oc} : 0.490 (v) ; J_{sc} :14.73

(mA/cm^2) ; FF : 44% and power conversion efficiency of 3.13 % [115]. In this report, the variation of thickness in absorber layer improved the power conversion efficiency and annealing temperature enhanced the short circuit current. Banu *et al.* reported spin coating deposition of glass/Mo/CuSbS$_2$/CdS/i-ZnO/n-ZnO/Al configuration produces V_{oc}: 0.470 (v); J_{sc} :15.73 (mA/cm^2); FF: 43.56% and power conversion efficiency of 3.22 %. The improved band alignment using the collecting electrode by transparent conductive oxide layer and intrinsic layer enhanced the charge separation thereby better charge collection was achieved [234]. Recent report states the chalcostibite phase (CuSbS$_2$) showed excellent hole mobility and ideal energy band gap [213,227]. Mainly the highest occupied molecular orbital (HOMO) of chalcostibite phases is suggested to have a better alignment to the HOMO of active perovskite absorber layers. This leads to the better charge transport and hence improved diffusion length as expected [98].

The photodetection performance of the photodiode is given in Figure 7.3 b). The rise time and decay time of the photodetector under illumination is calculated as 0.54 and 0.61 sec respectively. The photosensitivity and responsivity of the detector is given as 166 % and 8.4×10^{-2} mAW^{-1}.
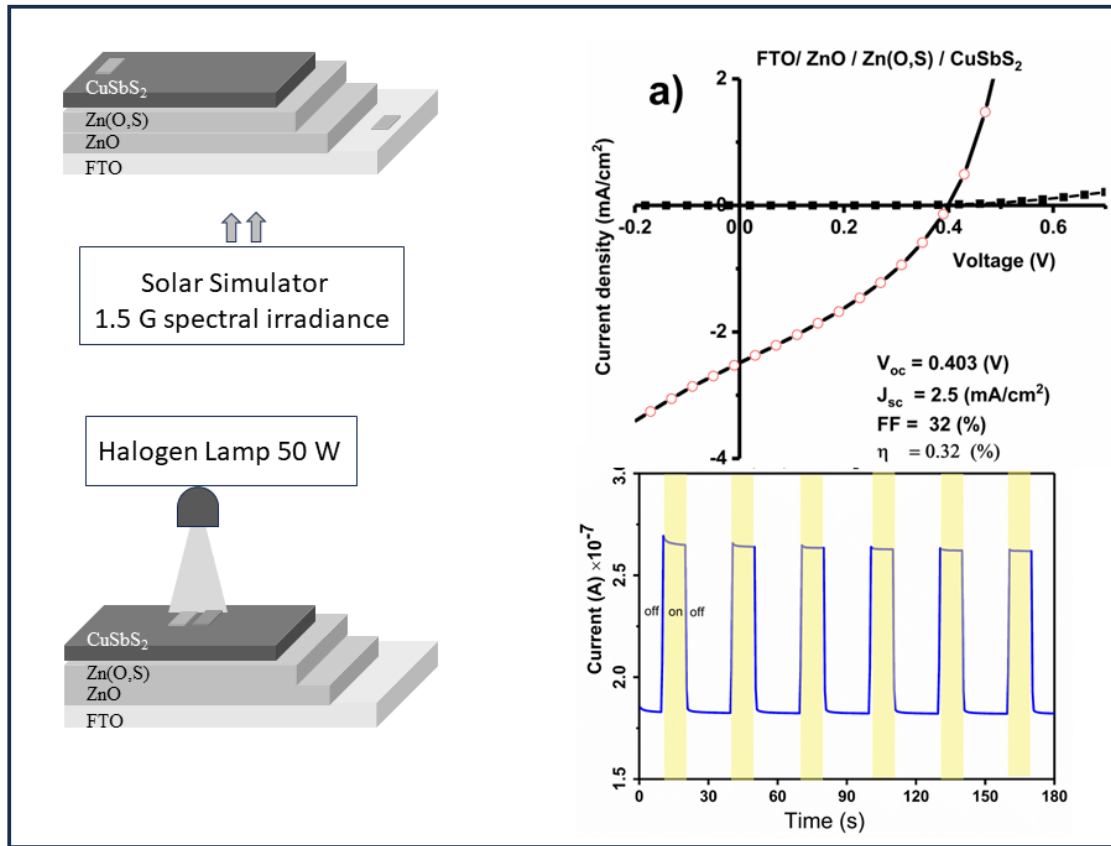
Figure 7.3 Schematic representation of FTO/ ZnO/Zn (O, S)/ CuSbS$_2$ (VA350) solar cell for J-V measurements under dark and illuminated using solar spectral irradiance using AM1.5 G.

Table 17 Summary of the photovoltaic parameters of the devices fabricated as part of this thesis.

Device structure	V_{oc}	J_{sc}	FF	Efficiency (%)	Sensitivity (%)	Responsivity (mAW^{-1})
FTO/ZnO/Zn (O, S)/Sb$_2$S$_3$	0.382	1.3	32	0.15	123	6.24×10^{-5}
FTO/ZnO/Zn (O, S)/Cu$_{12}$Sb$_4$S$_{13}$						
FTO/ZnO/Zn (O, S) /350CAS12.5	0.450	8.1	28	1.1	130	4.52×10^{-3}
FTO/ZnO/Zn (O, S) /350CAS8.8	0.427	15.4	26	1.6	136	2.32×10^{-3}
FTO/ZnO/Zn (O, S)/CuSbS$_2$						
FTO/ZnO/Zn (O, S) / 350 VA	0.403	2.5	32	0.32	166	8.4×10^{-2}

Copper antimony sulfide absorber layers were explored as photovoltaic material due to their high optical absorption coefficient, suitable band gap and high hole carrier concentration with intrinsic p-type conductivity. Difference in electronegativity and atomic size between chalcogen and transition metal results in strong hybridization especially in p and d orbitals. Especially 3d orbitals of copper influence the band structure which influence in the band gap, and alignment and degeneracy in the band edges. These factors influence the optoelectronic properties of the compounds and the incorporation of Copper into Sb$_2$S$_3$ thin films can enhance the PV performance. Tetrahedrite phase (Cu$_{12}$Sb$_4$S$_{13}$) incorporated PV structure was barely reported in a single p-n junction. Wang et, al reported spin coated thin film produces low V_{oc} due to the inhomogeneity during the deposition led to the recombination centers and mismatch in the band alignments. Together presence of deep defects introducing s trap and hence the reduced photo response as reported [96]. During the PV measurements of chalcostibite phase shortfall was mainly in the short circuit current measurements[141,214,235,236]. The low J_{sc} was measured for the devices irrespective of deposition techniques. Onset absorption of CdS window where band line ups (cliff shape) on the p- junction due to high recombination and lowered V_{oc}[80]. Replacement of CdS

with ZnO, ZnSe and ZnTe were evaluated, none of those reports reach efficiency higher than 3.2% [234] deposited using expensive hybrid ink technique. Future investigation is required for the improvement of PV devices based on copper antimony chalcogenides.

CONCLUSIONS

The present thesis achieved to develop ALL spray pyrolyzed photovoltaic structures and photodetectors using low toxic and earth abundant materials-based window and absorber layers. Sequential deposition of window layers (ZnO / Zn (O, S) and absorber films ($Cu_{12}Sb_4S_{13}$ or $CuSbS_2$) were accomplished by ultrasonic spray pyrolysis by which uniformity and homogeneity of layers were ensured. The effect of deposition parameters, annealing temperature time, and molar ratio of the precursor solution were varied for the fabrication of thin films. This thesis is the first report on ALL SPRAY COATED device -based on copper chalcogenides.

The key findings of my thesis work are:

- Highly oriented hexagonal structured ZnO thin films with direct wide band gap of 3.2 eV value and resistivity of 1.5×10^{-3} $\Omega cm^{-1,}$ the lowest reported so far, thin films were deposited. Elemental compositional analysis confirmed the uniform elemental distribution and atomic percentage throughout the samples. The theoretical simulation of ZnO unit cells on density of states and energy band diagram confirmed a wide direct band gap of 3.2 eV. From the stimulation, it was observed that the transition between band edges were mainly governed by the O 2p and Zn 3d orbitals.

- By incorporating S source in ZnO precursor solution, Zn (O, S) thin film was deposited, anion substitution for application as window layers.

- The theoretical simulation on density of states and band diagram revealed the influence of S 2p in the band edges which narrows the band gap and the influence of 2 p orbitals of O and S.

- Transparent conductive oxide/Oxysulfide layers (ZnO and Zn (O, S)) were spray deposited. Both layers were stable and exhibit excellent adhesion to the substrates.

- Orthorhombic Sb_2S_3 thin films were *in situ* grown using Sb/S precursor solutions without utilizing any complexing agent. Thin films were fabricated at different substrate temperatures and subjected to vacuum annealing resulting in better. Thin films with 1.6 eV direct optical band gap and absorption coefficient $>10^4$ cm^{-1} together with photoconductive nature for optoelectronic devices

- Simulated density of states and band diagram of orthorhombic Sb_2S_3 unit cell revealed a direct band gap of 1.6 eV, in correlation with the experimental results. The band edges were highly constituted by the Sb 3d and S 2p orbitals. Phonon spectra could be able to identify 8 IR modes and 10 Raman modes correspond to symmetric and asymmetric vibrational modes of Sb-S bonds.

- Sb_2S_3 thin films were incorporated into photovoltaic device with ZnO/Zn (O, S) transparent conductive oxide layer, with configuration: FTO / ZnO/Zn (O, S) / Sb_2S_3. The device measured a 0.382 V_{ov}, J_{sc}: 1.3 mA/cm^2 and Fill factor: 32 %, results in the power conversion efficiency of 0.15 %. The device was incorporated for photoconductive studies which measured the sensitivity and responsivity values.

- Selective synthesis of Tetrahedrite ($Cu_{12}Sb_4S_{13}$) and Chalcostibite ($CuSbS_2$) phases were achieved by the choice of copper rich and antimony rich precursor solutions.

- The tetrahedrite phase of copper antimony sulfide thin films had cubic crystal structure with good surface coverage of spherical morphology. The optical properties displayed a direct band gap of 1.4 eV direct band gap.

- Electrical conductivity tuning of semiconducting and semi metallic nature of $Cu_{12}Sb_4S_{13}$ thin films was achieved.

- Theoretical analysis of cubic $Cu_{12}Sb_4S_{13}$ unit cell displayed the influence of copper and antimony 3d orbitals with chalcogen (S) 2p orbitals at the band edges could influence the optoelectronic properties of the compound. The optical spectra revealed the electron distribution and the nature of lattice interacting with electromagnetic radiation. The complex dielectric function plot revealed energy storing capability on applied electric field at visible spectrum as well as the absorptive nature of the structure.

- Tetrahedrite phase pure thin films were incorporated to all spray pyrolyzed PV structure with configuration: FTO/ZnO/Zn (O, S)/ $Cu_{12}Sb_4S_{13}$ yielding 0.427 V_{oc}, J_{sc}: 15.4 mA/cm^2 and Fill factor: 28 %, recorded the highest efficiency ever reported with tetrahedrite phase of 1.6 %. The device operated as self-biased photodiodes with sensitivity in a wide range of wavelength UV-Vis-NIR, a relevant contribution to the development of self driven and sustainable sensors for Internet of Things.

- Polycrystalline chalcostibite $CuSbS_2$ thin films of direct band gap of 1.6 eV uniformly deposited on glass substrate. The chemical states of thin films were confirmed using XPS analysis of elemental composition, chemical state, and depth profile composition analysis.

- All spray pyrolyzed PV devices deposited using the configuration FTO / ZnO/Zn (O, S) / $CuSbS_2$ shows 0.403 V_{oc}, J_{sc}: 2.5 mA/cm^2 and Fill factor: 32 % with efficiency of 0.32 %.

- More investigation is required to optimize the device structure, thickness, morphology, annealing temperature etc. to obtain maximum efficiency.

In general, this study shows synthesis and analysis of ZnO, Zn (O, S), Sb_2S_3, $Cu_{12}Sb_4S_{13}$ and $CuSbS_2$ thin films for PV applications. The optoelectronic properties of ZnO and Zn (O, S) reveal a wide band gap material with highly conductive window layers can be used as window layer replacing toxic CdS. Selective synthesis of different phases of copper antimony chalcogenides ($Cu_{12}Sb_4S_{13}$ and $CuSbS_2$) as solar cells absorber for sustainable energy production and detection. Overall, our analyses provide scope of these materials for fabrication of PV devices with earth abundant, less toxic and cost-effective materials and devices. Further investigation is essential to improve the material properties and hence the device's performance.

References

[1]   S. Silva, I. Soares, O. Afonso, Economic and environmental effects under resource scarcity and substitution between renewable and non-renewable resources, Energy Policy. 54 (2013) 113–124. https://doi.org/10.1016/j.enpol.2012.10.069.

[2]   M. Okil, M.S. Salem, T.M. Abdolkader, A. Shaker, From Crystalline to Low-cost Silicon-based Solar Cells: a Review, Silicon. 14 (2022) 1895–1911. https://doi.org/10.1007/s12633-021-01032-4.

[3]   J. Liu, Y. Yao, S. Xiao, X. Gu, Review of status developments of high-efficiency crystalline silicon solar cells, J. Phys. D. Appl. Phys. 51 (2018) 123001. https://doi.org/10.1088/1361-6463/AAAC6D.

[4]   K. Mylvaganam, Y. Chen, W. Liu, M. Liu, L. Zhang, 21 - Hard thin films: Applications and challenges, in: M. Aliofkhazraei (Ed.), Anti-Abrasive Nanocoatings, Woodhead Publishing, 2015: pp. 543–567. https://doi.org/https://doi.org/10.1016/B978-0-85709-211-3.00021-2.

[5]   C.L. Kim, C.W. Jung, Y.J. Oh, D.E. Kim, A highly flexible transparent conductive electrode based on nanomaterials, NPG Asia Mater. 2017 910. 9 (2017) e438–e438. https://doi.org/10.1038/am.2017.177.

[6]   N. Thejo Kalyani, S.J. Dhoble, Empowering the future with organic solar cell devices, Elsevier Inc., 2018. https://doi.org/10.1016/B978-0-12-813731-4.00010-2.

[7]   S. Uchida, M. Tomiha, Y. Sanehira, Y. Fushimi, Solar cells dye-sensitized with β-CDI in electrolyte, Kobunshi Ronbunshu. 63 (2006) 62–67. https://doi.org/10.1295/koron.63.62.

[8]   M.L. Parisi, S. Maranghi, R. Basosi, The evolution of the dye sensitized solar cells from Grätzel prototype to up-scaled solar applications: A life cycle assessment approach, Renew. Sustain. Energy Rev. 39 (2014) 124–138. https://doi.org/10.1016/j.rser.2014.07.079.

[9]   J. Gong, J. Liang, K. Sumathy, Review on dye-sensitized solar cells (DSSCs): Fundamental concepts and novel materials, Renew. Sustain. Energy Rev. 16 (2012) 5848–5860. https://doi.org/10.1016/J.RSER.2012.04.044.

[10]   M. Dhonde, K. Sahu, M. Das, A. Yadav, P. Ghosh, V.V.S. Murty, Review—Recent

Advancements in Dye-Sensitized Solar Cells; From Photoelectrode to Counter Electrode, J. Electrochem. Soc. 169 (2022) 066507. https://doi.org/10.1149/1945-7111/AC741F.

[11]   G. Richhariya, A. Kumar, P. Tekasakul, B. Gupta, Natural dyes for dye sensitized solar cell: A review, Renew. Sustain. Energy Rev. 69 (2017) 705–718. https://doi.org/10.1016/j.rser.2016.11.198.

[12]   N. Suresh Kumar, K. Chandra Babu Naidu, A review on perovskite solar cells (PSCs), materials and applications, J. Mater. 7 (2021) 940–956. https://doi.org/10.1016/j.jmat.2021.04.002.

[13]   H.S. Kim, S.H. Im, N.G. Park, Organolead halide perovskite: New horizons in solar cell research, J. Phys. Chem. C. 118 (2014) 5615–5625. https://doi.org/10.1021/JP409025W.

[14]   K.A. Mazzio, C.K. Luscombe, The future of organic photovoltaics, Chem. Soc. Rev. 44 (2014) 78–90. https://doi.org/10.1039/C4CS00227J.

[15]   T. Miyasaka, A. Kulkarni, G.M. Kim, S. Öz, A.K. Jena, Perovskite Solar Cells: Can We Go Organic-Free, Lead-Free, and Dopant-Free?, Adv. Energy Mater. 10 (2020) 1902500. https://doi.org/10.1002/AENM.201902500.

[16]   A. Kojima, K. Teshima, Y. Shirai, T. Miyasaka, Organometal halide perovskites as visible-light sensitizers for photovoltaic cells, J. Am. Chem. Soc. 131 (2009) 6050–6051. https://doi.org/10.1021/ja809598r.

[17]   J.D. Poplawsky, W. Guo, N. Paudel, A. Ng, K. More, D. Leonard, Y. Yan, Structural and compositional dependence of the $CdTe_xSe_{1-x}$ alloy layer photoactivity in CdTe-based solar cells, Nat. Commun. 2016 71. 7 (2016) 1–10. https://doi.org/10.1038/ncomms12537.

[18]   T. Wang, X. Zhu, W. Li, J. Zhang, W. Wang, Incorporation of metal selenide thin films as the secondary absorber in the CdTe solar cells, J. Alloys Compd. 828 (2020) 154415. https://doi.org/10.1016/J.JALLCOM.2020.154415.

[19]   Z. Fang, X.C. Wang, H.C. Wu, C.Z. Zhao, Achievements and Challenges of CdS/CdTe Solar Cells, Int. J. Photoenergy. 2011 (2011) 297350. https://doi.org/10.1155/2011/297350.

[20]   N. Romeo, A. Bosio, V. Canevari, A. Podestà, Recent progress on CdTe/CdS thin film solar cells, Sol. Energy. 77 (2004) 795–801. https://doi.org/10.1016/J.SOLENER.2004.07.011.

[21] X. Wu, High-efficiency polycrystalline CdTe thin-film solar cells, Sol. Energy. 77 (2004) 803–814. https://doi.org/10.1016/j.solener.2004.06.006.

[22] S. Rahman, S.R. Al Ahmed, Photovoltaic performance enhancement in CdTe thin-film heterojunction solar cell with Sb_2S_3 as hole transport layer, Sol. Energy. 230 (2021) 605–617. https://doi.org/10.1016/J.SOLENER.2021.10.036.

[23] T. Feurer, P. Reinhard, E. Avancini, B. Bissig, J. Löckinger, P. Fuchs, R. Carron, T.P. Weiss, J. Perrenoud, S. Stutterheim, S. Buecheler, A.N. Tiwari, Progress in thin film CIGS photovoltaics – Research and development, manufacturing, and applications, Prog. Photovoltaics Res. Appl. 25 (2017) 645–667. https://doi.org/10.1002/PIP.2811.

[24] J. Srour, M. Badawi, F. El Haj Hassan, A. V. Postnikov, Crystal structure and energy bands of (Ga/In)Se and $Cu(In,Ga)Se_2$ semiconductors in comparison, Phys. Status Solidi. 253 (2016) 1472–1475. https://doi.org/10.1002/PSSB.201552776.

[25] A. Romeo, M. Terheggen, D. Abou-Ras, D.L. Bätzner, F.J. Haug, M. Kälin, D. Rudmann, A.N. Tiwari, Development of thin-film $Cu(In,Ga)Se_2$ and CdTe solar cells, Prog. Photovoltaics Res. Appl. 12 (2004) 93–111. https://doi.org/10.1002/PIP.527.

[26] T. Nakada, Invited Paper: CIGS-based thin film solar cells and modules: Unique material properties, Electron. Mater. Lett. 8 (2012) 179–185. https://doi.org/10.1007/S13391-012-2034-X.

[27] S. Rampino, N. Armani, F. Bissoli, M. Bronzoni, D. Calestani, M. Calicchio, N. Delmonte, E. Gilioli, E. Gombia, R. Mosca, L. Nasi, F. Pattini, A. Zappettini, M. Mazzer, 15% efficient $Cu(In,Ga)Se_2$ solar cells obtained by low-temperature pulsed electron deposition, Appl. Phys. Lett. 101 (2012). https://doi.org/10.1063/1.4755772.

[28] J. Fischer, J.K. Larsen, J. Guillot, Y. Aida, T. Eisenbarth, D. Regesch, V. Depredurand, N. Fevre, S. Siebentritt, P.J. Dale, Composition dependent characterization of copper indium diselenide thin film solar cells synthesized from electrodeposited binary selenide precursor stacks, Sol. Energy Mater. Sol. Cells. 126 (2014) 88–95. https://doi.org/10.1016/J.SOLMAT.2014.03.045.

[29] W. Riedl, J. Rimmasch, V. Probst, F. Karg, R. Guckenberger, Surface microstructure of CIS

thin films produced by rapid thermal processing, Sol. Energy Mater. Sol. Cells. 35 (1994) 129–139. https://doi.org/10.1016/0927-0248(94)90132-5.

[30] J. Ramanujam, U.P. Singh, Copper indium gallium selenide based solar cells – a review, Energy Environ. Sci. 10 (2017) 1306–1319. https://doi.org/10.1039/C7EE00826K.

[31] M.W. Bouabdelli, F. Rogti, M. Maache, A. Rabehi, Performance enhancement of CIGS thin-film solar cell, Optik (Stuttg). 216 (2020) 164948. https://doi.org/10.1016/J.IJLEO.2020.164948.

[32] Y. Tang, Copper Indium Gallium Selenide Thin Film Solar Cells, in: N. Das (Ed.), Nanostructured Sol. Cells, IntechOpen, Rijeka, 2017. https://doi.org/10.5772/65291.

[33] S.A. Vanalakar, G.L. Agawane, S.W. Shin, M.P. Suryawanshi, K. V. Gurav, K.S. Jeon, P.S. Patil, C.W. Jeong, J.Y. Kim, J.H. Kim, A review on pulsed laser deposited CZTS thin films for solar cell applications, J. Alloys Compd. 619 (2015) 109–121. https://doi.org/10.1016/J.JALLCOM.2014.09.018.

[34] P.K. Sarswat, M.L. Free, A study of energy band gap versus temperature for Cu_2ZnSnS_4 thin films, Phys. B Condens. Matter. 407 (2012) 108–111. https://doi.org/10.1016/J.PHYSB.2011.09.134.

[35] S.Y. Li, C. Hägglund, Y. Ren, J.J.S. Scragg, J.K. Larsen, C. Frisk, K. Rudisch, S. Englund, C. Platzer-Björkman, Optical properties of reactively sputtered Cu_2ZnSnS_4 solar absorbers determined by spectroscopic ellipsometry and spectrophotometry, Sol. Energy Mater. Sol. Cells. 149 (2016) 170–178. https://doi.org/10.1016/J.SOLMAT.2016.01.014.

[36] K. Ito, An Overview of CZTS-Based Thin-Film Solar Cells, in: Copp. Zinc Tin Sulfide-Based Thin-Film Sol. Cells, John Wiley & Sons, Ltd, 2014: pp. 1–41. https://doi.org/https://doi.org/10.1002/9781118437865.ch1.

[37] W. Shockley, H.J. Queisser, Detailed Balance Limit of Efficiency of p-n Junction Solar Cells, J. Appl. Phys. 32 (1961) 510–519. https://doi.org/10.1063/1.1736034.

[38] S. Chen, A. Walsh, J.-H. Yang, X.G. Gong, L. Sun, P.-X. Yang, J.-H. Chu, S.-H. Wei, Compositional dependence of structural and electronic properties of $CuZnSn(S,Se)_4$ alloys for thin film solar cells, Phys. Rev. B. 83 (2011) 125201.

https://doi.org/10.1103/PhysRevB.83.125201.

[39] H. Katagiri, N. Sasaguchi, S. Hando, S. Hoshino, J. Ohashi, T. Yokota, Preparation and evaluation of Cu_2ZnSnS_4 thin films by sulfurization of E-B evaporated precursors, Sol. Energy Mater. Sol. Cells. 49 (1997) 407–414. https://doi.org/10.1016/S0927-0248(97)00119-0.

[40] M.T. Winkler, W. Wang, O. Gunawan, H.J. Hovel, T.K. Todorov, D.B. Mitzi, Optical designs that improve the efficiency of $Cu_2ZnSn(S,Se)_4$ solar cells, Energy Environ. Sci. 7 (2014) 1029–1036. https://doi.org/10.1039/C3EE42541J.

[41] B. Müller, L. Hardt, A. Armbruster, K. Kiefer, C. Reise, Yield predictions for photovoltaic power plants: Empirical validation, recent advances and remaining uncertainties, Prog. Photovoltaics Res. Appl. 24 (2016) 570–583. https://doi.org/10.1002/PIP.2616.

[42] K. Woo, Y. Kim, W. Yang, K. Kim, I. Kim, Y. Oh, J.Y. Kim, J. Moon, Band-gap-graded $Cu_2ZnSn(S_{1-x},Se_x)_4$ Solar Cells Fabricated by an Ethanol-based, Particulate Precursor Ink Route, Sci. Reports 2013 31. 3 (2013) 1–7. https://doi.org/10.1038/srep03069.

[43] S. Chen, A. Walsh, J.H. Yang, X.G. Gong, L. Sun, P.X. Yang, J.H. Chu, S.H. Wei, Compositional dependence of structural and electronic properties of $Cu_2ZnSn(S,Se)_4$ alloys for thin film solar cells, Phys. Rev. B - Condens. Matter Mater. Phys. 83 (2011) 125201. https://doi.org/10.1103/PHYSREVB.83.125201/FIGURES/4/MEDIUM.

[44] W. Wang, M.T. Winkler, O. Gunawan, T. Gokmen, T.K. Todorov, Y. Zhu, D.B. Mitzi, Device Characteristics of CZTSSe Thin-Film Solar Cells with 12.6% Efficiency, Adv. Energy Mater. 4 (2014) 1301465. https://doi.org/10.1002/AENM.201301465.

[45] C. Malerba, M. Valentini, A. Mittiga, Cation Disorder In Cu_2ZnSnS_4 Thin Films: Effect On Solar Cell Performances, Sol. RRL. 1 (2017). https://doi.org/10.1002/solr.201700101.

[46] H. Zhang, M. Xie, S. Zhang, Y. Xiang, Fabrication of highly crystallized Cu_2SnS_3 thin films through sulfurization of Sn-rich metallic precursors, J. Alloys Compd. 602 (2014) 199–203. https://doi.org/10.1016/J.JALLCOM.2014.03.014.

[47] B. Li, Y. Xie, J. Huang, Y. Qian, Synthesis, Characterization, and Properties of Nanocrystalline Cu_2SnS_3, J. Solid State Chem. 153 (2000) 170–173.

https://doi.org/10.1006/JSSC.2000.8772.

[48] T.A. Kuku, O.A. Fakolujo, Photovoltaic characteristics of thin films of Cu_2SnS_3, Sol. Energy Mater. 16 (1987) 199–204. https://doi.org/10.1016/0165-1633(87)90019-0.

[49] A.C. Lokhande, P.T. Babar, V.C. Karade, M.G. Gang, V.C. Lokhande, C.D. Lokhande, J.H. Kim, The versatility of copper tin sulfide, J. Mater. Chem. A. 7 (2019) 17118–17182. https://doi.org/10.1039/c9ta00867e.

[50] J. Xu, X. Yang, T.L. Wong, C.S. Lee, Large-scale synthesis of Cu_2SnS_3 and $Cu_{1.8}S$ hierarchical microspheres as efficient counter electrode materials for quantum dot sensitized solar cells, Nanoscale. 4 (2012) 6537–6542. https://doi.org/10.1039/C2NR31724A.

[51] S. Dias, S.B. Krupanidhi, Solution processed Cu_2SnS_3 thin films for visible and infrared photodetector applications, AIP Adv. 6 (2016) 25217. https://doi.org/10.1063/1.4942775/22309.

[52] Y. Tan, Z. Lin, W. Ren, W. Long, Y. Wang, X. Ouyang, Facile solvothermal synthesis of Cu_2SnS_3 architectures and their visible-light-driven photocatalytic properties, Mater. Lett. 89 (2012) 240–242. https://doi.org/10.1016/J.MATLET.2012.08.117.

[53] D. Tiwari, T.K. Chaudhuri, T. Shripathi, U. Deshpande, V.G. Sathe, Microwave-assisted rapid synthesis of tetragonal Cu_2SnS_3 nanoparticles for solar photovoltaics, Appl. Phys. A Mater. Sci. Process. 117 (2014) 1139–1146. https://doi.org/10.1007/S00339-014-8484-2/FIGURES/8.

[54] H. Liu, Z. Chen, Z. Jin, Y. Su, Y. Wang, A reduced graphene oxide supported Cu_3SnS_4 composite as an efficient visible-light photocatalyst, Dalt. Trans. 43 (2014) 7491–7498. https://doi.org/10.1039/C4DT00070F.

[55] V. Maheskumar, B. Gururajan, B. Vidhya, Investigations on the structural, optical and visible light photocatalytic activity of Cu_3SnS_4 prepared by mechanical alloying, J. Mater. Sci. Mater. Electron. 28 (2017) 19081–19089. https://doi.org/10.1007/s10854-017-7862-x.

[56] G.S. Babu, Y.B.K. Kumar, Y.B.K. Reddy, V.S. Raja, Growth and characterization of Cu_2SnSe_3 thin films, Mater. Chem. Phys. 96 (2006) 442–446. https://doi.org/10.1016/J.MATCHEMPHYS.2005.07.050.

[57]   M.E. Norako, M.J. Greaney, R.L. Brutchey, Synthesis and characterization of wurtzite-phase copper tin selenide nanocrystals, J. Am. Chem. Soc. 134 (2012) 23–26. https://doi.org/10.1021/ja206929s.

[58]   J. Jeong, H. Chung, Y.C. Ju, J. Moon, J. Roh, S. Yoon, Y.R. Do, W. Kim, Colloidal synthesis of Cu_2SnSe_3 nanocrystals, Mater. Lett. 64 (2010) 2043–2045. https://doi.org/10.1016/J.MATLET.2010.07.003.

[59]   G. Marcano, C. Rincón, L.M. De Chalbaud, D.B. Bracho, G. Sánchez Pérez, Crystal growth and structure, electrical, and optical characterization of the semiconductor Cu_2SnSe_3, J. Appl. Phys. 90 (2001) 1847–1853. https://doi.org/10.1063/1.1383984.

[60]   V. Sharma, T.K. Das, P. Ilaiyaraja, C. Sudakar, Oxygen non-stoichiometry in TiO_2 and ZnO nano rods: Effect on the photovoltaic properties of dye and Sb_2S_3 sensitized solar cells, Sol. Energy. 191 (2019) 400–409. https://doi.org/10.1016/J.SOLENER.2019.09.009.

[61]   S. Hadke, M. Huang, C. Chen, Y.F. Tay, S. Chen, J. Tang, L. Wong, Emerging Chalcogenide Thin Films for Solar Energy Harvesting Devices, Chem. Rev. 122 (2022) 10170–10265. https://doi.org/10.1021/acs.chemrev.1c00301.

[62]   Y.C. Choi, D.U. Lee, J.H. Noh, E.K. Kim, S. Il Seok, Highly improved Sb_2S_3 sensitized-inorganic-organic heterojunction solar cells and quantification of traps by deep-level transient spectroscopy, Adv. Funct. Mater. 24 (2014) 3587–3592. https://doi.org/10.1002/adfm.201304238.

[63]   T. Muto, G. Larramona, G. Dennler, Unexpected performances of flat Sb_2S_3 -based hybrid extremely thin absorber solar cells, Appl. Phys. Express. 6 (2013). https://doi.org/10.7567/APEX.6.072301.

[64]   E. Zimmermann, T. Pfadler, J. Kalb, J.A. Dorman, D. Sommer, G. Hahn, J. Weickert, L.E. Schmidt-Mende Zimmermann, T. Pfadler, J. Kalb, J.A. Dorman, D. Sommer, G. Hahn, J. Weickert, L. Schmidt-Mende, Toward High-Efficiency Solution-Processed Planar Heterojunction Sb_2S_3 Solar Cells, Adv. Sci. 2 (2015) 1500059. https://doi.org/10.1002/ADVS.201500059.

[65]   O. Savadogo, K.C. Mandal, Low Cost Schottky Barrier Solar Cells Fabricated on CdSe and

Sb₂S₃ Films Chemically Deposited with Silicotungstic Acid, J. Electrochem. Soc. 141 (1994) 2871–2877. https://doi.org/10.1149/1.2059248/XML.

[66] H. Deng, Y. Zeng, M. Ishaq, S. Yuan, H. Zhang, X. Yang, M. Hou, U. Farooq, J. Huang, K. Sun, R. Webster, H. Wu, Z. Chen, F. Yi, H. Song, X. Hao, J. Tang, Quasiepitaxy Strategy for Efficient Full-Inorganic Sb₂S₃ Solar Cells, Adv. Funct. Mater. 29 (2019) 1901720. https://doi.org/10.1002/ADFM.201901720.

[67] D.H. Kim, S.J. Lee, M.S. Park, J.K. Kang, J.H. Heo, S.H. Im, S.J. Sung, Highly reproducible planar Sb₂S₃ -sensitized solar cells based on atomic layer deposition, Nanoscale. 6 (2014) 14549–14554. https://doi.org/10.1039/C4NR04148H.

[68] F. Liu, J. Li, J. Yang, Z. Han, L. Jiang, Y. Lai, J. Li, Y. He, Y. Liu, Preparation and Characterization of AgSbSe₂ Thin Films by Electrodeposition , J. Electrochem. Soc. 160 (2013) D578–D582. https://doi.org/10.1149/2.110311JES/XML.

[69] S. Cai, Z. Liu, J. Sun, R. Li, W. Fei, J. Sui, Enhancement of thermoelectric properties by Na doping in Te-free p-type AgSbSe₂, Dalt. Trans. 44 (2014) 1046–1051. https://doi.org/10.1039/C4DT03059A.

[70] W. Gao, Z. Wang, J. Huang, Z. Liu, Extraordinary Thermoelectric Performance Realized in Hierarchically Structured AgSbSe₂ with Ultralow Thermal Conductivity, ACS Appl. Mater. Interfaces. 10 (2018) 18685–18692. https://doi.org/10.1021/acsami.8b03243.

[71] S.N. Guin, A. Chatterjee, K. Biswas, Enhanced thermoelectric performance in p-type AgSbSe₂ by Cd-doping, RSC Adv. 4 (2014) 11811–11815. https://doi.org/10.1039/C4RA00969J.

[72] L. Yu, M. Han, Y. Wan, J. Jia, G. Yi, Synthesis of stoichiometric AgSbS₂ nanospheres via one-step solvothermal chemical process, Mater. Lett. 161 (2015) 447–450. https://doi.org/10.1016/J.MATLET.2015.09.011.

[73] K. Bindu, J. Campos, M.T.S. Nair, A. Snchez, P.K. Nair, Semiconducting AgSbSe₂ thin film and its application in a photovoltaic structure, Semicond. Sci. Technol. 20 (2005) 496. https://doi.org/10.1088/0268-1242/20/6/004.

[74] Y. Zhang, J. Tian, K. Jiang, J. Huang, F. Li, P. Wang, H. Fan, Y. Song, AgSbS₂ thin film

fabricated by in-situ gas-solid reaction and employed in solar cells as a light absorber, Mater. Lett. 232 (2018) 82–85. https://doi.org/10.1016/J.MATLET.2018.08.081.

[75]   J.O. González, S. Shaji, D. Avellaneda, G.A. Castillo, T.K. Das Roy, B. Krishnan, Photovoltaic structures using $AgSb(S_xSe_{1-x})_2$ thin films as absorber, Appl. Phys. A Mater. Sci. Process. 116 (2014) 2095–2105. https://doi.org/10.1007/S00339-014-8411-6/FIGURES/11.

[76]   J.O. González, S. Shaji, D. Avellaneda, A.G. Castillo, T.K.D. Roy, B. Krishnan, $AgSb(S_xSe_{1-x})_2$ thin films for solar cell applications, Mater. Res. Bull. 48 (2013) 1939–1945. https://doi.org/10.1016/J.MATERRESBULL.2013.01.040.

[77]   A. Nadukkandy, S. Shaji, D.A. Avellaneda, J.A. Aguilar-Martínez, B. Krishnan, Cubic structured silver antimony sulfide-selenide solid solution thin films for sustainable photodetection and photovoltaic application, J. Alloys Compd. 942 (2023) 169072. https://doi.org/10.1016/j.jallcom.2023.169072.

[78]   Z. Liu, J. Huang, J. Han, T. Hong, J. Zhang, Z. Liu, $CuSbS_2$: a promising semiconductor photo-absorber material for quantum dot sensitized solar cells, Phys. Chem. Chem. Phys. 18 (2016) 16615–16620. https://doi.org/10.1039/C6CP01688J.

[79]   E. Peccerillo, K. Durose, Copper—antimony and copper—bismuth chalcogenides—Research opportunities and review for solar photovoltaics, MRS Energy Sustain. 5 (2018). https://doi.org/10.1557/MRE.2018.10.

[80]   E. Peccerillo, K. Durose, Copper—antimony and copper—bismuth chalcogenides—Research opportunities and review for solar photovoltaics, MRS Energy Sustain. 5 (2018) 1–59. https://doi.org/10.1557/mre.2018.10.

[81]   L. Shi, C. Wu, J. Li, J. Ding, Selective synthesis and photoelectric properties of Cu3SbS4 and $CuSbS_2$ nanocrystals, J. Alloys Compd. 694 (2017) 132–135. https://doi.org/10.1016/J.JALLCOM.2016.09.307.

[82]   F.D. Luce, C.L. Tuttle, B.J. Skinner, Studies of sulfosalts of copper; V, Phases and phase relations in the system Cu-Sb-As-S between 350 degrees and 500 degrees C, Econ. Geol. 72 (1977) 271–289. https://doi.org/10.2113/GSECONGEO.72.2.271.

[83] M.H. Braga, J.A. Ferreira, C. Lopes, L.F. Malheiros, Phase Transitions in the Cu-Sb-S System, Mater. Sci. Forum. 587–588 (2008) 435–439. https://doi.org/10.4028/WWW.SCIENTIFIC.NET/MSF.587-588.435.

[84] T. Wada, T. Maeda, Optical properties and electronic structures of $CuSbS_2$, $CuSbSe_2$, and $CuSb(S_{1-x}Se_x)_2$ solid solution, 14 (2017) 1600196. https://doi.org/10.1002/PSSC.201600196.

[85] K. Takei, T. Maeda, T. Wada, Crystallographic and optical properties of CuSbS2and $CuSb(S_{1-x}Se_x)_2$ solid solution, in: Thin Solid Films, Elsevier, 2015: pp. 263–268. https://doi.org/10.1016/j.tsf.2014.11.029.

[86] K. Suekuni, K. Tsuruta, T. Ariga, M. Koyano, Thermoelectric properties of mineral tetrahedrites $Cu_{10}Tr_2Sb_4S_{13}$ with low thermal conductivity, Appl. Phys. Express. 5 (2012) 2–5. https://doi.org/10.1143/APEX.5.051201.

[87] H.I. Tanaka, K. Suekuni, K. Umeo, T. Nagasaki, H. Sato, G. Kutluk, E. Nishibori, H. Kasai, T. Takabatake, Metal–Semiconductor Transition Concomitant with a Structural Transformation, J. Phys. Soc. Japan. 85 (2016) 1–6.

[88] F. Mohamadkhani, M. Heidariramsheh, S. Javadpour, E. Ghavaminia, S.M. Mahdavi, N. Taghavinia, Sb_2S_3 and Cu_3SbS_4 nanocrystals as inorganic hole transporting materials in perovskite solar cells, Sol. Energy. 223 (2021) 106–112. https://doi.org/10.1016/J.SOLENER.2021.05.049.

[89] W. Lai, Y. Wang, D.T. Morelli, X. Lu, From bonding asymmetry to anharmonic rattling in $Cu_{12}Sb_4S_{13}$ tetrahedrites: When lone-pair electrons are not so lonely, Adv. Funct. Mater. 25 (2015) 3648–3657. https://doi.org/10.1002/adfm.201500766.

[90] P. Lemoine, C. Bourgès, T. Barbier, V. Nassif, S. Cordier, E. Guilmeau, High temperature neutron powder diffraction study of the $Cu_{12}Sb_4S_{13}$ and $Cu_4Sn_7S_{16}$ phases, J. Solid State Chem. 247 (2017) 83–89. https://doi.org/10.1016/j.jssc.2017.01.003.

[91] F.H. Sun, J. Dong, H. Tang, P.P. Shang, H.L. Zhuang, H. Hu, C.F. Wu, Y. Pan, J.F. Li, Enhanced performance of thermoelectric nanocomposites based on $Cu_{12}Sb_4S_{13}$ tetrahedrite, Nano Energy. 57 (2019) 835–841. https://doi.org/10.1016/j.nanoen.2018.12.090.

[92] S.G. Kwak, G.E. Lee, I.H. Kim, Effects of Se Doping on Thermoelectric Properties of Tetrahedrite $Cu_{12}Sb_4S_{13-z}Se_z$, Electron. Mater. Lett. 17 (2021) 164–171. https://doi.org/10.1007/s13391-021-00270-3.

[93] H. Hu, H.L. Zhuang, Y. Jiang, J. Shi, J.W. Li, B. Cai, Z. Han, J. Pei, B. Su, Z.H. Ge, B.P. Zhang, J.F. Li, Thermoelectric $Cu_{12}Sb_4S_{13}$-Based Synthetic Minerals with a Sublimation-Derived Porous Network, Adv. Mater. 33 (2021) 1–10. https://doi.org/10.1002/adma.202103633.

[94] C. Zhu, Q. Chen, H. Ming, X. Qin, Y. Yang, J. Zhang, D. Peng, T. Chen, D. Li, Y. Kawazoe, Improved Thermoelectric Performance of $Cu_{12}Sb_4S_{13}$ through Gd-Substitution Induced Enhancement of Electronic Density of States and Phonon Scattering, ACS Appl. Mater. Interfaces. (2021). https://doi.org/10.1021/acsami.1c03493.

[95] J. Heo, R. Ravichandran, C.F. Reidy, J. Tate, J.F. Wager, D.A. Keszler, Design meets nature: Tetrahedrite solar absorbers, Adv. Energy Mater. 5 (2015) 1–7. https://doi.org/10.1002/aenm.201401506.

[96] L. Wang, B. Yang, Z. Xia, M. Leng, Y. Zhou, D.J. Xue, J. Zhong, L. Gao, H. Song, J. Tang, Synthesis and characterization of hydrazine solution processed $Cu_{12}Sb_4S_{13}$ film, Sol. Energy Mater. Sol. Cells. 144 (2016) 33–39. https://doi.org/10.1016/j.solmat.2015.08.016.

[97] T. Alqahtani, M.D. Khan, D.J. Lewis, X.L. Zhong, P. O'Brien, Scalable synthesis of Cu–Sb–S phases from reactive melts of metal xanthates and effect of cationic manipulation on structural and optical properties, Sci. Reports 2021 111. 11 (2021) 1–17. https://doi.org/10.1038/s41598-020-80951-5.

[98] M. Tamilselvan, A.J. Bhattacharyya, Tetrahedrite ($Cu_{12}Sb_4S_{13}$) Ternary Inorganic Hole Conductor for Ambient Processed Stable Perovskite Solar Cells, ACS Appl. Energy Mater. 1 (2018) 4227–4234. https://doi.org/10.1021/acsaem.8b00844.

[99] T. Rath, A.J. MacLachlan, M.D. Brown, S.A. Haque, Structural, optical and charge generation properties of chalcostibite and tetrahedrite copper antimony sulfide thin films prepared from metal xanthates, J. Mater. Chem. A. 3 (2015) 24155–24162. https://doi.org/10.1039/C5TA05777A.

[100] S. Manolache, A. Duță, The influence of the spray deposition parameters in the photovoltaic response of the three-dimensional (3D) solar cell: TCO/ dense TiO_2 / $CuSbS_2$ / graphite, J. Optoelectron. Adv. Mater. 9 (2007) 3219–3222. https://api.semanticscholar.org/CorpusID:98407196.

[101] J.A. Ramos Aquino, D.L. Rodriguez Vela, S. Shaji, D.A. Avellaneda, B. Krishnan, Spray pyrolysed thin films of copper antimony sulfide as photovoltaic absorber, Phys. Status Solidi Curr. Top. Solid State Phys. 13 (2016) 24–29. https://doi.org/10.1002/pssc.201510102.

[102] P. Suttiyarak, A. Tubtimtae, P-type In^{3+}-doped $Cu_{12}Sb_4S_{13}$ thin films deposited by spray pyrolysis method: Investigation of structural, optical, electrical, and electrocatalytic properties, Appl. Surf. Sci. 527 (2020) 146835. https://doi.org/10.1016/j.apsusc.2020.146835.

[103] B. Yang, L. Wang, J. Han, Y. Zhou, H. Song, S. Chen, J. Zhong, L. Lv, D. Niu, J. Tang, $CuSbS_2$ as a Promising Earth-Abundant Photovoltaic Absorber Material: A Combined Theoretical and Experimental Study, Chem. Mater. 26 (2014) 3135–3143. https://doi.org/10.1021/cm500516v.

[104] B. Yang, L. Wang, J. Han, Y. Zhou, H. Song, S. Chen, J. Zhong, L. Lv, D. Niu, J. Tang, $CuSbS_2$ as a promising earth-abundant photovoltaic absorber material: A combined theoretical and experimental study, Chem. Mater. 26 (2014) 3135–3143. https://doi.org/10.1021/CM500516V/SUPPL_FILE/CM500516V_SI_001.PDF.

[105] A.W. Welch, P.P. Zawadzki, S. Lany, C.A. Wolden, A. Zakutayev, Self-regulated growth and tunable properties of $CuSbS_2$ solar absorbers, Sol. Energy Mater. Sol. Cells. 132 (2015) 499–506. https://doi.org/10.1016/J.SOLMAT.2014.09.041.

[106] M.T.S. Nair, P.K. Nair, Chemical bath deposition of CuxS thin films and their prospective large area applications, Semicond. Sci. Technol. 4 (1989) 191–199. https://doi.org/10.1088/0268-1242/4/3/009.

[107] C.A. Estrada, P.K. Nair, M.T.S. Nair, R.A. Zingaro, E.A. Meyers, Chemical Bath Deposition of ZnSe and CuSe Thin Films Using N,N-Dimethylselenourea, J. Electrochem. Soc. 141 (1994) 802–806. https://doi.org/10.1149/1.2054814/META.

[108] C.L. McCarthy, P. Cottingham, K. Abuyen, E.C. Schueller, S.P. Culver, R.L. Brutchey, Earth abundant $CuSbS_2$ thin films solution processed from thiol–amine mixtures, J. Mater. Chem. C. 4 (2016) 6230–6233. https://doi.org/10.1039/C6TC02117D.

[109] S. Suehiro, K. Horita, M. Yuasa, T. Tanaka, K. Fujita, Y. Ishiwata, K. Shimanoe, T. Kida, Synthesis of Copper–Antimony-Sulfide Nanocrystals for Solution-Processed Solar Cells, Inorg. Chem. 54 (2015) 7840–7845. https://doi.org/10.1021/acs.inorgchem.5b00858.

[110] J.A. Ramos Aquino, D.L. Rodriguez Vela, S. Shaji, D.A. Avellaneda, B. Krishnan, Spray pyrolysed thin films of copper antimony sulfide as photovoltaic absorber, Phys. Status Solidi C. 13 (2016) 24–29. https://doi.org/10.1002/pssc.201510102.

[111] D. Nagamalleswari, Y.B.K. Kumar, V. Ganesh, Effect of substrate temperature on the growth of $CuSbS_2$ thin films by chemical spray pyrolysis, Phys. B Condens. Matter. 616 (2021) 413119. https://doi.org/10.1016/j.physb.2021.413119.

[112] K. Vijayan, S.P. Vijayachamundeeswari, K. Sivaperuman, N. Ahsan, T. Logu, Y. Okada, A review on advancements, challenges, and prospective of copper and non-copper based thin-film solar cells using facile spray pyrolysis technique, Sol. Energy. 234 (2022) 81–102. https://doi.org/10.1016/j.solener.2022.01.070.

[113] R. Zhou, X. Liu, S. Zhang, L. Liu, L. Wan, H. Guo, X. Yang, Z. Cheng, L. Hu, H. Niu, X. Mao, Spray-coated copper antimony sulfide ($CuSbS_2$) thin film: A novel counter electrode for quantum dot-sensitized solar cells, Mater. Sci. Semicond. Process. 124 (2021) 105613. https://doi.org/10.1016/j.mssp.2020.105613.

[114] L. Fu, J. Yu, J. Wang, F. Xie, S. Yao, Y. Zhang, J. Cheng, L. Li, Thin film solar cells based on Ag-substituted $CuSbS_2$ absorber, Chem. Eng. J. 400 (2020). https://doi.org/10.1016/j.cej.2020.125906.

[115] W. Septina, S. Ikeda, Y. Iga, T. Harada, M. Matsumura, Thin film solar cell based on $CuSbS_2$ absorber fabricated from an electrochemically deposited metal stack, Thin Solid Films. 550 (2014) 700–704. https://doi.org/10.1016/J.TSF.2013.11.046.

[116] K.S. Gour, R. Parmar, R. Kumar, V.N. Singh, Cd-Free Zn(O,S) as Alternative Buffer Layer for Chalcogenide and Kesterite Based Thin Films Solar Cells: A Review, J. Nanosci.

Nanotechnol. 20 (2019) 3622–3635. https://doi.org/10.1166/JNN.2020.17537.

[117] F.W. De Souza Lucas, A.W. Welch, L.L. Baranowski, P.C. Dippo, H. Hempel, T. Unold, R. Eichberger, B. Blank, U. Rau, L.H. Mascaro, A. Zakutayev, Effects of Thermochemical Treatment on CuSbS$_2$ Photovoltaic Absorber Quality and Solar Cell Reproducibility, J. Phys. Chem. C. 120 (2016) 18377–18385. https://doi.org/10.1021/acs.jpcc.6b04206.

[118] P. Maiello, G. Zoppi, R.W. Miles, N. Pearsall, I. Forbes, Chalcogenisation of Cu-Sb metallic precursors into Cu$_3$Sb(Se$_x$S$_{1-x}$)$_3$, Sol. Energy Mater. Sol. Cells. 113 (2013) 186–194. https://doi.org/10.1016/j.solmat.2013.02.016.

[119] S. Banu, Y. Cho, K. Kim, S.K. Ahn, J. Gwak, A. Cho, Phase transition behavior and defect analysis of CuSbS$_2$ thin films for photovoltaic application prepared by hybrid inks, Sol. Energy. 188 (2019) 1209–1220. https://doi.org/10.1016/J.SOLENER.2019.07.019.

[120] T. Minemoto, T. Matsui, H. Takakura, Y. Hamakawa, T. Negami, Y. Hashimoto, T. Uenoyama, M. Kitagawa, Theoretical analysis of the effect of conduction band offset of window/CIS layers on performance of CIS solar cells using device simulation, Sol. Energy Mater. Sol. Cells. 67 (2001) 83–88. https://doi.org/10.1016/S0927-0248(00)00266-X.

[121] T.J. Whittles, T.D. Veal, C.N. Savory, A.W. Welch, F.W. de Souza Lucas, J.T. Gibbon, M. Birkett, R.J. Potter, D.O. Scanlon, A. Zakutayev, V.R. Dhanak, Core Levels, Band Alignments, and Valence-Band States in CuSbS$_2$ for Solar Cell Applications, ACS Appl. Mater. Interfaces. 9 (2017) 41916–41926. https://doi.org/10.1021/acsami.7b14208.

[122] W. Kohn, L.J. Sham, Self-Consistent Equations Including Exchange and Correlation Effects, Phys. Rev. 140 (1965) A1133–A1138. https://doi.org/10.1103/PhysRev.140.A1133.

[123] G. Kresse, D. Joubert, From ultrasoft pseudopotentials to the projector augmented-wave method, Phys. Rev. B. 59 (1999) 1758. https://doi.org/10.1103/PhysRevB.59.1758.

[124] J.P. Perdew, K. Burke, M. Ernzerhof, Generalized Gradient Approximation Made Simple, Phys. Rev. Lett. 77 (1996) 3865. https://doi.org/10.1103/PhysRevLett.77.3865.

[125] M. Burgelman, P. Nollet, S. Degrave, Modelling polycrystalline semiconductor solar cells, Thin Solid Films. 361 (2000) 527–532. https://doi.org/10.1016/S0040-6090(99)00825-1.

[126] K. Mukhopadhyay, P. Fermi Hilbert Inbaraj, J. Joseph Prince, Thickness optimization of CdS/ZnO hybrid buffer layer in CZTSe thin film solar cells using SCAPS simulation program, Mater. Res. Innov. 23 (2019) 319–329. https://doi.org/10.1080/14328917.2018.1475907.

[127] C. Adel, B.M. Fethi, B. Brahim, Simulation analysis of the effect graded Zn (O, S) on the performance of the ultra thin copper indium gallium diselenide (CIGS) solar cells, Int. J. Phys. Sci. 9 (2014) 250–254.

[128] M.T. Islam, A.K. Thakur, Two stage modelling of solar photovoltaic cells based on Sb_2S_3 absorber with three distinct buffer combinations, Sol. Energy. 202 (2020) 304–315. https://doi.org/10.1016/j.solener.2020.03.058.

[129] G.K. Gupta, A. Dixit, Simulation studies on photovoltaic response of ultrathin $CuSb(S/Se)_2$ ternary compound semiconductors absorber-based single junction solar cells, Int. J. Energy Res. 44 (2020) 3724–3736. https://doi.org/10.1002/er.5158.

[130] T. Otsuka, T. Kurosawa, K. Seya, Ultrasonic Atomization of Liquids, J. Acoust. Soc. Am. 34 (1962) 6–8. https://doi.org/10.1121/1.1909020.

[131] J.J. Carey, J.P. Allen, D.O. Scanlon, G.W. Watson, The electronic structure of the antimony chalcogenide series: Prospects for optoelectronic applications, J. Solid State Chem. 213 (2014) 116–125. https://doi.org/10.1016/j.jssc.2014.02.014.

[132] L. Guo, B. Zhang, S. Li, Q. Zhang, M. Buettner, L. Li, X. Qian, F. Yan, Scalable and efficient Sb_2S_3 thin-film solar cells fabricated by close space sublimation, APL Mater. 7 (2019). https://doi.org/10.1063/1.5090773.

[133] A. Bafekry, B. Mortazavi, M. Faraji, M. Shahrokhi, A. Shafique, H.R. Jappor, C. Nguyen, M. Ghergherehchi, S.A.H. Feghhi, Ab initio prediction of semiconductivity in a novel two-dimensional Sb_2X_3 (X= S, Se, Te) monolayers with orthorhombic structure, Sci. Rep. 11 (2021) 1–10. https://doi.org/10.1038/s41598-021-89944-4.

[134] A. Radzwan, A. Lawal, A. Shaari, I.M. Chiromawa, S.T. Ahams, R. Ahmed, First-principles calculations of structural, electronic, and optical properties for Ni-doped Sb_2S_3, Comput. Condens. Matter. 24 (2020). https://doi.org/10.1016/j.cocom.2020.e00477.

[135] F. Caruso, M.R. Filip, F. Giustino, Excitons in one-dimensional van der Waals materials: Sb_2S_3 nanoribbons, Phys. Rev. B - Condens. Matter Mater. Phys. 92 (2015) 1–6. https://doi.org/10.1103/PhysRevB.92.125134.

[136] T. Ben Nasr, H. Maghraoui-Meherzi, N. Kamoun-Turki, First-principles study of electronic, thermoelectric and thermal properties of Sb_2S_3, J. Alloys Compd. 663 (2016) 123–127. https://doi.org/10.1016/j.jallcom.2015.12.093.

[137] Y. Liu, K.T. Eddie Chua, T.C. Sum, C.K. Gan, First-principles study of the lattice dynamics of Sb_2S_3, Phys. Chem. Chem. Phys. 16 (2014) 345–350. https://doi.org/10.1039/c3cp53879f.

[138] T. Ketolainen, N. Macháčová, F. Karlický, Optical Gaps and Excitonic Properties of 2D Materials by Hybrid Time-Dependent Density Functional Theory: Evidences for Monolayers and Prospects for van der Waals Heterostructures, J. Chem. Theory Comput. 16 (2020) 5876–5883. https://doi.org/10.1021/acs.jctc.0c00387.

[139] T. Alzoubi, M. Moustafa, Numerical optimization of absorber and CdS buffer layers in CIGS solar cells using SCAPS, Int. J. Smart Grid Clean Energy. 8 (2019) 291–298. https://doi.org/10.12720/SGCE.8.3.291-298.

[140] M. Al-Hattab, L. Moudou, M. Khenfouch, O. Bajjou, Y. Chrafih, K. Rahmani, Numerical simulation of a new heterostructure CIGS/GaSe solar cell system using SCAPS-1D software, Sol. Energy. 227 (2021) 13–22. https://doi.org/10.1016/j.solener.2021.08.084.

[141] R. Teimouri, R. Mohammadpour, Potential application of $CuSbS_2$ as the hole transport material in perovskite solar cell: A simulation study, Superlattices Microstruct. 118 (2018) 116–122. https://doi.org/10.1016/J.SPMI.2018.03.079.

[142] M.T. Islam, A. Kumar, A.K. Thakur, Defect Density Control Using an Intrinsic Layer to Enhance Conversion Efficiency in an Optimized SnS Solar Cell, J. Electron. Mater. 50 (2021) 3603–3613. https://doi.org/10.1007/s11664-021-08881-0.

[143] Y. Rodríguez-Lazcano, M.T.S. Nair, P.K. Nair, Photovoltaic p-i-n Structure of Sb_2S_3 and $CuSbS_2$ Absorber Films Obtained via Chemical Bath Deposition, J. Electrochem. Soc. 152 (2005) G635. https://doi.org/10.1149/1.1945387.

[144] Sadanand, P.K. Singh, S. Rai, P. Lohia, D.K. Dwivedi, Comparative study of the CZTS, $CuSbS_2$ and $CuSbSe_2$ solar photovoltaic cell with an earth-abundant non-toxic buffer layer, Sol. Energy. 222 (2021) 175–185. https://doi.org/10.1016/J.SOLENER.2021.05.013.

[145] A. Purohit, S. Chander, A. Sharma, S.P. Nehra, M.S. Dhaka, Impact of low temperature annealing on structural, optical, electrical and morphological properties of ZnO thin films grown by RF sputtering for photovoltaic applications, Opt. Mater. (Amst). 49 (2015) 51–58. https://doi.org/10.1016/J.OPTMAT.2015.08.021.

[146] R. Methaapanon, S.M. Geyer, C. Hagglund, P.A. Pianetta, S.F. Bent, Portable atomic layer deposition reactor for in situ synchrotron photoemission studies, Rev. Sci. Instrum. 84 (2013). https://doi.org/10.1063/1.4773230/354578.

[147] J.G.E. Gardeniers, Z.M. Rittersma, G.J. Burger, Preferred orientation and piezoelectricity in sputtered ZnO films, J. Appl. Phys. 83 (1998) 7844–7854. https://doi.org/10.1063/1.367959.

[148] Y. Sun, T. He, H. Guo, T. Zhang, W. Wang, Z. Dai, Structural and optical properties of the S-doped ZnO particles synthesized by hydrothermal method, Appl. Surf. Sci. 257 (2010) 1125–1128. https://doi.org/10.1016/J.APSUSC.2010.08.041.

[149] X.Y. Xie, P. Zhan, L.Y. Li, D.J. Zhou, D.Y. Guo, J.X. Meng, Y. Bai, W.J. Zheng, Synthesis of S-doped ZnO by the interaction of sulfur with zinc salt in PEG200, J. Alloys Compd. 644 (2015) 383–389. https://doi.org/10.1016/J.JALLCOM.2015.04.214.

[150] L. Li, L. Fang, X.J. Zhou, Z.Y. Liu, L. Zhao, S. Jiang, X-ray photoelectron spectroscopy study and thermoelectric properties of Al-doped ZnO thin films, J. Electron Spectros. Relat. Phenomena. 173 (2009) 7–11. https://doi.org/10.1016/J.ELSPEC.2009.03.001.

[151] R. Al-Gaashani, S. Radiman, R. Al-Gaashani, S. Radiman, A.R. Daud, N. Tabet, Y. Al-Douri, XPS and optical studies of different morphologies of ZnO nanostructures prepared by microwave methods, Elsevier. (2012). https://doi.org/10.1016/j.ceramint.2012.08.075.

[152] A. Posada-Borbón, N. Bosio, H. Grönbeck, On the signatures of oxygen vacancies in O1s core level shifts, Surf. Sci. 705 (2021) 121761. https://doi.org/10.1016/J.SUSC.2020.121761.

[153] H. Nanto, T. Minami, S. Shooji, S. Takata, Electrical and optical properties of zinc oxide thin films prepared by rf magnetron sputtering for transparent electrode applications, J. Appl. Phys. 55 (1984) 1029–1034. https://doi.org/10.1063/1.333196.

[154] L. Xu, G. Zheng, J. Wang, F. Xian, Y. Liu, Stable co-emission of UV, green and red light in ZnO thin films with rapid annealing treatment, Optik (Stuttg). 127 (2016) 5942–5949. https://doi.org/10.1016/J.IJLEO.2016.04.032.

[155] H. Nanto, H. Sokooshi, T. Usuda, Smell sensor using aluminium-doped zinc oxide thin film prepared by sputtering technique, Sensors Actuators B Chem. 10 (1993) 79–83. https://doi.org/10.1016/0925-4005(93)80029-B.

[156] G. Kenanakis, N. Katsarakis, E. Koudoumas, Influence of precursor type, deposition time and doping concentration on the morphological, electrical and optical properties of ZnO and ZnO:Al thin films grown by ultrasonic spray pyrolysis, Thin Solid Films. 555 (2014) 62–67. https://doi.org/10.1016/J.TSF.2013.10.015.

[157] H.L. Ma, Z.W. Liu, D.C. Zeng, M.L. Zhong, H.Y. Yu, E. Mikmekova, Nanostructured ZnO films with various morphologies prepared by ultrasonic spray pyrolysis and its growing process, Appl. Surf. Sci. 283 (2013) 1006–1011. https://doi.org/10.1016/J.APSUSC.2013.07.060.

[158] F. Fabbri, L. Nasi, P. Fedeli, P. Ferro, G. Salviati, R. Mosca, A. Calzolari, A. Catellani, S-induced modifications of the optoelectronic properties of ZnO mesoporous nanobelts, Sci. Rep. 6 (2016) 1–8. https://doi.org/10.1038/srep27948.

[159] K.C. Yung, H. Liem, H.S. Choy, Enhanced redshift of the optical band gap in Sn-doped ZnO free standing films using the sol–gel method, J. Phys. D. Appl. Phys. 42 (2009) 185002. https://doi.org/10.1088/0022-3727/42/18/185002.

[160] M. Hjiri, M.S. Aida, O.M. Lemine, L. El Mir, Study of defects in Li-doped ZnO thin films, Mater. Sci. Semicond. Process. 89 (2019) 149–153. https://doi.org/10.1016/j.mssp.2018.09.010.

[161] E. Chikoidze, M. Nolan, M. Modreanu, V. Sallet, P. Galtier, Effect of chlorine doping on electrical and optical properties of ZnO thin films, Thin Solid Films. 516 (2008) 8146–8149.

https://doi.org/10.1016/j.tsf.2008.04.076.

[162] B.G. Choi, I.H. Kim, D.H. Kim, K.S. Lee, T.S. Lee, B. Cheong, Y.J. Baik, W.M. Kim, Electrical, optical and structural properties of transparent and conducting ZnO thin films doped with Al and F by rf magnetron sputter, J. Eur. Ceram. Soc. 25 (2005) 2161–2165. https://doi.org/10.1016/J.JEURCERAMSOC.2005.03.023.

[163] E. Chikoidze, M. Nolan, M. Modreanu, V. Sallet, P. Galtier, Effect of chlorine doping on electrical and optical properties of ZnO thin films, Thin Solid Films. 516 (2008) 8146–8149. https://doi.org/10.1016/j.tsf.2008.04.076.

[164] J. Kennedy, P.P. Murmu, J. Leveneur, A. Markwitz, J. Futter, Controlling preferred orientation and electrical conductivity of zinc oxide thin films by post growth annealing treatment, Appl. Surf. Sci. 367 (2016) 52–58. https://doi.org/10.1016/J.APSUSC.2016.01.160.

[165] H. Hagendorfer, K. Lienau, S. Nishiwaki, C.M. Fella, L. Kranz, A.R. Uhl, D. Jaeger, L. Luo, C. Gretener, S. Buecheler, Y.E. Romanyuk, A.N. Tiwari, H. Hagendorfer, K. Lienau, S. Nishiwaki, C.M. Fella, L. Kranz, A.R. Uhl, C. Gretener, S. Buecheler, Y.E. Romanyuk, A.N. Tiwari, D. Jaeger, Highly Transparent and Conductive ZnO: Al Thin Films from a Low Temperature Aqueous Solution Approach, Adv. Mater. 26 (2014) 632–636. https://doi.org/10.1002/ADMA.201303186.

[166] H. Hejin Park, R. Heasley, R.G. Gordon, Atomic layer deposition of Zn(O,S) thin films with tunable electrical properties by oxygen annealing, Appl. Phys. Lett. 102 (2013). https://doi.org/10.1063/1.4800928/124984.

[167] U.A. Shah, S. Chen, G.M.G. Khalaf, Z. Jin, H. Song, Wide Bandgap Sb_2S_3 Solar Cells, Adv. Funct. Mater. 31 (2021). https://doi.org/10.1002/adfm.202100265.

[168] S.A. Zaki, M.I. Abd-Elrahman, A.A. Abu-Sehly, Optical and electrical properties of amorphous Sb_2S_3 thin films: Effect of the film thickness, J. Non. Cryst. Solids. 552 (2021) 120318. https://doi.org/10.1016/J.JNONCRYSOL.2020.120318.

[169] J. Li, L. Xiong, X. Hu, J. Liang, C. Chen, F. Ye, J. Li, Y. Liu, W. Shao, T. Wang, C. Tao, G. Fang, Manipulating the morphology of CdS/ Sb_2S_3 heterojunction using a Mg-doped tin

oxide buffer layer for highly efficient solar cells, J. Energy Chem. 66 (2022) 374–381. https://doi.org/10.1016/J.JECHEM.2021.08.029.

[170] S. Shaji, L. V. Garcia, S.L. Loredo, B. Krishnan, J.A. Aguilar Martinez, T.K. Das Roy, D.A. Avellaneda, Antimony sulfide thin films prepared by laser assisted chemical bath deposition, Appl. Surf. Sci. 393 (2017) 369–376. https://doi.org/10.1016/j.apsusc.2016.10.051.

[171] M.Y. Versavel, J.A. Haber, Structural and optical properties of amorphous and crystalline antimony sulfide thin-films, Thin Solid Films. 515 (2007). https://doi.org/10.1016/j.tsf.2007.03.043.

[172] T. Ibn-Mohammed, S.C.L. Koh, I.M. Reaney, A. Acquaye, G. Schileo, K.B. Mustapha, R. Greenough, Perovskite solar cells: An integrated hybrid lifecycle assessment and review in comparison with other photovoltaic technologies, Renew. Sustain. Energy Rev. 80 (2017) 1321–1344. https://doi.org/10.1016/J.RSER.2017.05.095.

[173] C. Cobianu, M. Gheorghe, M. Modreanu, Y. Gutierrez, M. Losurdo, Chemically Bath Deposited Sb_2S_3 Films as Optical Phase Change Materials, Proc. Int. Semicond. Conf. CAS. 2021-October (2021) 249–252. https://doi.org/10.1109/CAS52836.2021.9604155.

[174] P. Bayliss, W. Nowacki, Refinement of the crystal structure of stibnite, Sb_2S_3 1, Zeitschrift Fur Krist. - New Cryst. Struct. 135 (1972) 308–315. https://doi.org/10.1524/zkri.1972.135.3-4.308.

[175] E. Kärber, A. Katerski, I. Oja Acik, A. Mere, V. Mikli, M. Krunks, Sb_2S_3 grown by ultrasonic spray pyrolysis and its application in a hybrid solar cell , Beilstein J. Nanotechnol. 7 (2016) 1662–1673. https://doi.org/10.3762/bjnano.7.158.

[176] D. Colombara, H. Elanzeery, N. Nicoara, D. Sharma, M. Claro, T. Schwarz, A. Koprek, M.H. Wolter, M. Melchiorre, M. Sood, N. Valle, O. Bondarchuk, F. Babbe, C. Spindler, O. Cojocaru-Miredin, D. Raabe, P.J. Dale, S. Sadewasser, S. Siebentritt, Chemical instability at chalcogenide surfaces impacts chalcopyrite devices well beyond the surface, Nat. Commun. 11 (2020) 1–14. https://doi.org/10.1038/s41467-020-17434-8.

[177] P. Abraham, S. Shaji, D.A. Avellaneda, J.A. Aguilar-Martínez, B. Krishnan, Sb_2S_3 thin

films: From first principles to in situ crystalline thin film growth by ultrasonic spray pyrolysis, Mater. Sci. Semicond. Process. 156 (2023) 107269. https://doi.org/10.1016/J.MSSP.2022.107269.

[178] A.T. Supekar, P.K. Bhujbal, S.A. Salunke, S.M. Rathod, S.P. Patole, H.M. Pathan, Bismuth sulfide and antimony sulfide-based solar cells: a review, Espublisher.Com. 19 (2023) 848. https://doi.org/10.30919/esee8c848.

[179] U. Ali Shah, G. Khalaf, H. Song, S. Chen, G. Mohamed Gomaa Khalaf, Z. Jin, U.A. Shah, S. Chen, G.M. G Khalaf, Z. Jin, H. Song, Wide Bandgap Sb_2S_3 Solar Cells, Wiley Online Libr. 31 (2021). https://doi.org/10.1002/adfm.202100265.

[180] X. Wang, R. Tang, C. Wu, C. Zhu, T. Chen, Development of antimony sulfide–selenide $Sb_2(S,Se)_3$ -based solar cells, J. Energy Chem. 27 (2018) 713–721. https://doi.org/10.1016/j.jechem.2017.09.031.

[181] Z. Chen, G. Chen, The effect of absorber thickness on the planar Sb_2S_3 thin film solar cell: Trade-off between light absorption and charge separation, Sol. Energy. 201 (2020) 323–329. https://doi.org/10.1016/j.solener.2020.02.074.

[182] J. Escorcia-García, D. Becerra, M.T.S. Nair, P.K. Nair, Heterojunction CdS/ Sb_2S_3 solar cells using antimony sulfide thin films prepared by thermal evaporation, Thin Solid Films. 569 (2014) 28–34. https://doi.org/10.1016/j.tsf.2014.08.024.

[183] J.B. Varley, V. Lordi, Electrical properties of point defects in CdS and ZnS, Appl. Phys. Lett. 103 (2013). https://doi.org/10.1063/1.4819492.

[184] A. Giri, G. Park, H. Yang, M. Pal, J. Kwak, U. Jeong, Synthesis of 2D Metal Chalcogenide Thin Films through the Process Involving Solution-Phase Deposition, Adv. Mater. 30 (2018). https://doi.org/10.1002/ADMA.201707577.

[185] V.V. Akshay, S. Benny, S.V. Bhat, Solution-processed antimony chalcogenides based thin film solar cells: A brief overview of recent developments, Sol. Energy. 241 (2022) 728–737. https://doi.org/10.1016/j.solener.2022.06.042.

[186] V. Vinayakumar, C.R.O. Hernández, S. Shaji, D.A. Avellaneda, J.A.A. Martinez, B. Krishnan, Effects of rapid thermal processing on chemically deposited antimony sulfide

thin films, Mater. Sci. Semicond. Process. 80 (2018) 9–17. https://doi.org/10.1016/j.mssp.2018.02.011.

[187] M. Medles, N. Benramdane, A. Bouzidi, K. Sahraoui, R. Miloua, R. Desfeux, C. Mathieu, Raman and optical studies of spray pyrolysed Sb_2S_3 thin films, J. Optoelectron. Adv. Mater. 16 (2014) 726–731.

[188] J. Cheng, R. Hu, K. Wang, X. Meng, Y. Li, X. Yang, X. Liao, L. Li, K.B. Chong, Air-Stable Solar Cells with 0.7 V Open-Circuit Voltage Using Selenized Antimony Sulfide Absorbers Prepared by Hydrazine-Free Solution Method, Sol. RRL. 3 (2019). https://doi.org/10.1002/solr.201800346.

[189] C. Hu, B. Zhang, B.H. Lei, S. Pan, Z. Yang, Advantageous Units in Antimony Sulfides: Exploration and Design of Infrared Nonlinear Optical Materials, ACS Appl. Mater. Interfaces. 10 (2018). https://doi.org/10.1021/acsami.8b08466.

[190] B. Minceva-Sukarova, M. Najdoski, I. Grozdanov, C.J. Chunnilall, Raman spectra of thin solid films of some metal sulfides, J. Mol. Struct. 410–411 (1997) 267–270. https://doi.org/10.1016/S0022-2860(96)09713-X.

[191] D.S. Prem Kumar, M. Ren, T. Osipowicz, R.C. Mallik, P. Malar, Tetrahedrite ($Cu_{12}Sb_4S_{13}$) thin films for photovoltaic and thermoelectric applications, Sol. Energy. 174 (2018) 422–430. https://doi.org/10.1016/j.solener.2018.08.080.

[192] F.H. Sun, C.F. Wu, Z. Li, Y. Pan, Asfandiyar, J. Dong, J.F. Li, Powder metallurgically synthesized $Cu_{12}Sb_4S_{13}$ tetrahedrites: phase transition and high thermoelectricity, RSC Adv. 7 (2017) 18909–18916. https://doi.org/10.1039/c7ra02564e.

[193] P.A. Fernandes, A. Shongalova, A.F. da Cunha, J.P. Teixeira, J.P. Leitão, J.M.V. Cunha, S. Bose, P.M.P. Salomé, M.R. Correia, Phase selective growth of $Cu_{12}Sb_4S_{13}$ and Cu_3SbS_4 thin films by chalcogenization of simultaneous sputtered metal precursors, J. Alloys Compd. 797 (2019) 1359–1366. https://doi.org/10.1016/j.jallcom.2019.05.149.

[194] U. Rout, S. Tippireddy, K. Werbach, P. Pambannan, G. Rogl, P. Rogl, R.C. Mallik, Simultaneous optimization of power factor and thermal conductivity via Te and Se double substitution in $Cu_{12}Sb_4S_{13}$ tetrahedrite, Scr. Mater. 188 (2020) 151–156.

https://doi.org/10.1016/j.scriptamat.2020.07.036.

[195] T. Rath, A.J. MacLachlan, M.D. Brown, S.A. Haque, Structural, optical and charge generation properties of chalcostibite and tetrahedrite copper antimony sulfide thin films prepared from metal xanthates, J. Mater. Chem. A. 3 (2015) 24155–24162. https://doi.org/10.1039/c5ta05777a.

[196] H. Su, Y. Xie, S. Wan, B. Li, Y. Qian, A novel one-step solvothermal route to nanocrystalline $CuSbS_2$ and Ag_3SbS_3, Solid State Ionics. 123 (1999) 319–324. https://doi.org/10.1016/s0167-2738(99)00094-6.

[197] A. Rossi, D. Atzei, S. Da Pelo, F. Frau, P. Lattanzi, K.E.R. England, D.J. Vaughan, Quantitative X-ray photoelectron spectroscopy study of enargite (Cu_3AsS_4) surface, Surf. Interface Anal. 31 (2001) 465–470. https://doi.org/10.1002/sia.1072.

[198] F. Makin, F. Alam, M.A. Buckingham, D.J. Lewis, Synthesis of ternary copper antimony sulfide via solventless thermolysis or aerosol assisted chemical vapour deposition using metal dithiocarbamates, Sci. Rep. 12 (2022) 5627. https://doi.org/10.1038/s41598-022-08822-9.

[199] E. Ciftyurek, Z. Li, K. Schierbaum, Adsorbed Oxygen Ions and Oxygen Vacancies: Their Concentration and Distribution in Metal Oxide Chemical Sensors and Influencing Role in Sensitivity and Sensing Mechanisms, Sensors (Basel). 23 (2022). https://doi.org/10.3390/S23010029.

[200] H. Idriss, On the wrong assignment of the XPS O1s signal at 531–532 eV attributed to oxygen vacancies in photo- and electro-catalysts for water splitting and other materials applications, Surf. Sci. 712 (2021) 2–7. https://doi.org/10.1016/j.susc.2021.121894.

[201] V.B. Crist, The Elements of Native Oxides, Handb. Monochromatic XPS Spectra. (2000) 548.

[202] J. van Embden, K. Latham, N.W. Duffy, Y. Tachibana, Near-Infrared Absorbing $Cu_{12}Sb_4S_{13}$ and Cu_3SbS_4 Nanocrystals: Synthesis, Characterization, and Photoelectrochemistry, J. Am. Chem. Soc. 135 (2013) 11562–11571. https://doi.org/10.1021/ja402702x.

[203] A. Zhao, Y. Wang, B. Li, D. Xiang, Z. Peng, Y. Yuan, Y. Xing, L. Yao, J. Bi, W. Li, Sulfurization of Electrodeposited Sb/Cu Precursors for CuSbS$_2$: Potential Absorber Materials for Thin-Film Solar Cells, Front. Mater. 8 (2022). https://doi.org/10.3389/FMATS.2021.818596/FULL.

[204] L. Wan, C. Ma, K. Hu, R. Zhou, X. Mao, S. Pan, L.H. Wong, J. Xu, Two-stage co-evaporated CuSbS$_2$ thin films for solar cells, J. Alloys Compd. (2016) 182–190. https://doi.org/10.1016/J.JALLCOM.2016.04.193.

[205] K. Jiang, Z. Chen, X. Meng, CuS and Cu$_2$S as Cathode Materials for Lithium Batteries: A Review, ChemElectroChem. 6 (2019) 2825–2840. https://doi.org/10.1002/CELC.201900066.

[206] Y. Fang, D. Luan, Y. Chen, S. Gao, X.W. (David) Lou, Rationally Designed Three-Layered Cu$_2$S Carbon MoS$_2$ Hierarchical Nanoboxes for Efficient Sodium Storage , Angew. Chemie. 132 (2020) 7245–7250. https://doi.org/10.1002/ANGE.201915917.

[207] P. Nieroda, J. Leszczyński, A. Mikuła, K. Mars, M.J. Kruszewski, A. Koleżyński, Thermoelectric properties of Cu$_2$S obtained by high temperature synthesis and sintered by IHP method, Ceram. Int. 46 (2020) 25460–25466. https://doi.org/10.1016/j.ceramint.2020.07.016.

[208] X. Liang, D. Jin, F. Dai, Phase Transition Engineering of Cu$_2$S to Widen the Temperature Window of Improved Thermoelectric Performance, Adv. Electron. Mater. 5 (2019). https://doi.org/10.1002/AELM.201900486.

[209] V. Vinayakumar, C.R.O. Hernández, S. Shaji, D.A. Avellaneda, J.A.A. Martinez, B. Krishnan, Effects of rapid thermal processing on chemically deposited antimony sulfide thin films, Mater. Sci. Semicond. Process. 80 (2018) 9–17. https://doi.org/10.1016/j.mssp.2018.02.011.

[210] F.E. Loranca-Ramos, C.J. Diliegros-Godines, R. Silva González, M. Pal, Structural, optical and electrical properties of copper antimony sulfide thin films grown by a citrate-assisted single chemical bath deposition, Appl. Surf. Sci. 427 (2018) 1099–1106. https://doi.org/10.1016/j.apsusc.2017.08.027.

[211] S. Majid, K.S. Ahmad, S. Sharif, Optical and structural properties of single source precursor

based pure and Cu-doped antimony sulphide thin films by physical vapour deposition assisted technique, Chem. Phys. 539 (2020) 110979. https://doi.org/10.1016/j.chemphys.2020.110979.

[212] A.D. Saragih, D.H. Kuo, T.T.A. Tuan, Thin film solar cell based on p-CuSbS2 together with Cd-free GaN/InGaN bilayer, J. Mater. Sci. Mater. Electron. 28 (2017) 2996–3003. https://doi.org/10.1007/s10854-016-5885-3.

[213] R.E. Ornelas-Acosta, S. Shaji, D. Avellaneda, G.A. Castillo, T.K. Das Roy, B. Krishnan, Thin films of copper antimony sulfide: A photovoltaic absorber material, Mater. Res. Bull. 61 (2015) 215–225. https://doi.org/10.1016/j.materresbull.2014.10.027.

[214] A.W. Welch, P.P. Zawadzki, S. Lany, C.A. Wolden, A. Zakutayev, Self-regulated growth and tunable properties of CuSbS$_2$ solar absorbers, Sol. Energy Mater. Sol. Cells. 132 (2015) 499–506. https://doi.org/10.1016/J.SOLMAT.2014.09.041.

[215] A.C.-J. of E. Materials, undefined 2023, Effect of Gamma Radiation on the Physical and Photoelectrochemical Properties of CuSbS$_2$ Thin Films Prepared via Spin-Coating Technique, Springer. 52 (2023) 6749–6759. https://doi.org/10.1007/s11664-023-10627-z.

[216] M. Yıldırım, A. Kocyigit, A. Sarılmaz, F. Ozel, The effect of the triangular and spherical shaped CuSbS$_2$ structure on the electrical properties of Au/ CuSbS$_2$/p-Si photodiode, J. Mater. Sci. Mater. Electron. 30 (2019) 332–339. https://doi.org/10.1007/S10854-018-0297-1.

[217] H. Ennaceri, M. Boujnah, A. Taleb, A. Khaldoun, R. Sáez-Araoz, A. Ennaoui, A. El Kenz, A. Benyoussef, Thickness effect on the optical properties of TiO$_2$-anatase thin films prepared by ultrasonic spray pyrolysis: Experimental and ab initio study, Int. J. Hydrogen Energy. 42 (2017) 19467–19480. https://doi.org/10.1016/j.ijhydene.2017.06.015.

[218] A.M. Teli, S.A. Bekanalkar, D.S. Patil, S.A. Pawar, T.D. Dongale, J.C. Shin, H.J. Kim, P.S. Patil, Effect of thermal annealing on physiochemical properties of spray-deposited β-MnO$_2$ thin films for electrochemical supercapacitor, J. Electroanal. Chem. 856 (2020). https://doi.org/10.1016/j.jelechem.2019.113483.

[219] M. Yang, T. Zhang, P. Schulz, Z. Li, G. Li, D.H. Kim, N. Guo, J.J. Berry, K. Zhu, Y. Zhao,

Facile fabrication of large-grain $CH_3NH_3PbI_{3-x}Br_x$ films for high-efficiency solar cells via CH_3NH_3Br-selective Ostwald ripening, Nat. Commun. 7 (2016) 12305. https://doi.org/10.1038/ncomms12305.

[220] K. Ramasamy, H. Sims, W.H. Butler, A. Gupta, Selective Nanocrystal Synthesis and Calculated ElectronicStructure of All Four Phases of Copper–Antimony–Sulfide, Chem. Mater. 26 (2014) 2891–2899. https://doi.org/10.1021/CM5005642.

[221] B. Yang, L. Wang, J. Han, Y. Zhou, H. Song, S. Chen, J. Zhong, L. Lv, D. Niu, J. Tang, $CuSbS_2$ as a Promising Earth-Abundant Photovoltaic Absorber Material: A Combined Theoretical and Experimental Study, ACS Publ. 26 (2014) 3135–3143. https://doi.org/10.1021/cm500516v.

[222] M. Birkett, C.N. Savory, M.K. Rajpalke, W.M. Linhart, T.J. Whittles, J.T. Gibbon, A.W. Welch, I.Z. Mitrovic, A. Zakutayev, D.O. Scanlon, T.D. Veal, Band gap temperature-dependence and exciton-like state in copper antimony sulphide, $CuSbS_2$, APL Mater. 6 (2018). https://doi.org/10.1063/1.5030207.

[223] M. Kumar, C. Persson, CuSbS2 and CuBiS2 as potential absorber materials for thin-film solar cells, J. Renew. Sustain. Energy. 5 (2013). https://doi.org/10.1063/1.4812448.

[224] Y. Wang, Y. Shan, W. Li, J. Shi, J. Hou, G. Zhao, N. Dai, F. Wang, Y. Fang, Y. Liu, A Molecular Precursor-Based Copper Antimony Sulfide Photodetector with Enhanced Performance by Silver Doping, Adv. Electron. Mater. 2300380 (2023) 1–10. https://doi.org/10.1002/aelm.202300380.

[225] A. Nagaoka, M. Takeuchi, K. Yoshino, S. Ikeda, S. Yasui, T. Taniyama, K. Nishioka, Growth of $CuSbS_2$ Single Crystal as an Environmentally Friendly Thermoelectric Material, Phys. Status Solidi. 216 (2019) 1800861. https://doi.org/10.1002/PSSA.201800861.

[226] F.W. de Souza Lucas, A.W. Welch, L.L. Baranowski, P.C. Dippo, H. Hempel, T. Unold, R. Eichberger, B. Blank, U. Rau, L.H. Mascaro, A. Zakutayev, Effects of Thermochemical Treatment on $CuSbS_2$ Photovoltaic Absorber Quality and Solar Cell Reproducibility, J. Phys. Chem. C. 120 (2016) 18377–18385. https://doi.org/10.1021/acs.jpcc.6b04206.

[227] S. Manolache, A. Duta, L. Isac, M. Nanu, A. Goossens, J. Schoonman, The influence of the

precursor concentration on CuSbS$_2$ thin films deposited from aqueous solutions, Thin Solid Films. 515 (2007) 5957–5960. https://doi.org/10.1016/J.TSF.2006.12.046.

[228] Z. Yang, X. Wang, Y. Chen, Z. Zheng, Z. Chen, W. Xu, W. Liu, Y. (Michael) Yang, J. Zhao, T. Chen, H. Zhu, Ultrafast self-trapping of photoexcited carriers sets the upper limit on antimony trisulfide photovoltaic devices, Nat. Commun. 2019 101. 10 (2019) 1–8. https://doi.org/10.1038/s41467-019-12445-6.

[229] M.A. Farhana, A. Manjceevan, J. Bandara, Recent advances and new research trends in Sb2S3 thin film based solar cells, J. Sci. Adv. Mater. Devices. 8 (2023) 100533. https://doi.org/10.1016/J.JSAMD.2023.100533.

[230] A.M. Salem, M. Soliman Selim, Structure and optical properties of chemically deposited Sb$_2$S$_3$ thin films, J. Phys. D. Appl. Phys. 34 (2001) 12. https://doi.org/10.1088/0022-3727/34/1/303.

[231] L. Yu, R.S. Kokenyesi, D.A. Keszler, A. Zunger, Inverse Design of High Absorption Thin-Film Photovoltaic Materials, Adv. Energy Mater. 3 (2013) 43–48. https://doi.org/10.1002/AENM.201200538.

[232] J.S. Eensalu, A. Katerski, E. Kärber, L. Weinhardt, M. Blum, C. Heske, W. Yang, I.O. Acik, M. Krunks, Semitransparent Sb$_2$S$_3$ thin film solar cells by ultrasonic spray pyrolysis for use in solar windows, Beilstein J. Nanotechnol. 10 (2019) 2396–2409. https://doi.org/10.3762/bjnano.10.230.

[233] J.S. Eensalu, K. Tõnsuaadu, I. Oja Acik, M. Krunks, Sb$_2$S$_3$ thin films by ultrasonic spray pyrolysis of antimony ethyl xanthate, Mater. Sci. Semicond. Process. 137 (2022). https://doi.org/10.1016/j.mssp.2021.106209.

[234] S. Banu, S.J. Ahn, S.K. Ahn, K. Yoon, A. Cho, Fabrication and characterization of cost-efficient CuSbS$_2$ thin film solar cells using hybrid inks, Sol. Energy Mater. Sol. Cells. C (2016) 14–23. https://doi.org/10.1016/J.SOLMAT.2016.02.013.

[235] R. Teimouri, R. Mohammadpour, Potential application of CuSbS$_2$ as the hole transport material in perovskite solar cell: A simulation study, Superlattices Microstruct. 118 (2018) 116–122. https://doi.org/10.1016/j.spmi.2018.03.079.

[236] C. Tablero, Electronic and optical property analysis of the Cu-Sb-S tetrahedrites for high-efficiency absorption devices, J. Phys. Chem. C. 118 (2014) 15122–15127. https://doi.org/10.1021/jp502045w.

List of publications

1) **Paulosutty Abraham**, Sadasivan Shaji, David Avellaneda Avellaneda, Josue Amilcar Aguilar-Martínez, Bindu Krishnan, Sb_2S_3 thin films: from first principles to in situ crystalline thin film growth by ultrasonic spray pyrolysis. https://doi.org/10.1016/j.mssp.2022.107269

2) **Paulosutty Abraham**, Sadasivan Shaji, DavidAvellaneda Avellaneda, Josue Amilcar Aguilar- Martínez, Bindu Krishnan (002) oriented ZnO and ZnO:S thin films by direct ultrasonic spray pyrolysis: A comparative analysis of structure, morphology and physical properties https://doi.org/10.1016/j.mtcomm.2023.105909

3) A. Nadukkandy, S. Devasia, Bindu Kirishnan, **P. Abraham**, S. Shaji, D. Avellaneda, J.A. Aguilar-martínez, E. Gandara, Monoclinic AgSbS2 thin films for photovoltaic applications: Computation, growth and characterization approaches, Mater. Sci. Semicond. Process. 135 (2021) 106074. https://doi.org/10.1016/j.mssp.2021.106074.

INTERNATIONAL CONFERENCES PRESENTATIONS

1) Oral presentation **in International Webinar Series, Progress and Promises in Chemical Sciences (PPCS 2021)**, CHRIST, Bengaluru, India

2) Oral presentation at **XV International Conference on Surfaces, Materials and Vacuum** 2022, Puerto Vallarta, Jalisco

3) **Poster presentation** at the XXIX **International Materials Research Congress 2021**

<div align="center">

ANNEXURE

</div>

ANNEXURE   A

Heterojunctions of Chemical bath deposited CdS and ultrasonic spray pyrolyzed Tetrahedrite copper antimony sulfide ($Cu_{12}Sb_4S_{13}$) thin films for photovoltaic and self-powered photodetector applications

Abstract

In situ growth of tetrahedrite $Cu_{12}Sb_4S_{13}$ thin films deposited using ultrasonic spray pyrolysis on the variation of S/(Cu+Sb) molar ratio. X-ray diffraction and Raman spectroscopy was employed to evaluate the phase formation. Optical properties displayed a direct band gap of 1.5 eV match the theoretical simulation on density of states and electronic band diagram on First principle calculations. $Cu_{12}Sb_4S_{13}$ thin films deposited as a variation of S/(Cu+Sb) precursor ratio spans the electrical properties from semiconducting (p) to semi-metallic (p^+) confirmed by electrochemical and hall effect measurements. The photo response and photodetection of $Cu_{12}Sb_4S_{13}$ films deposited on CdS window layer was measured. The CdS layer was fabricated using chemical bath deposition. Wavelength sensitive and self driven photodiode for UV-Vis-NIR spectrum performance was measured.
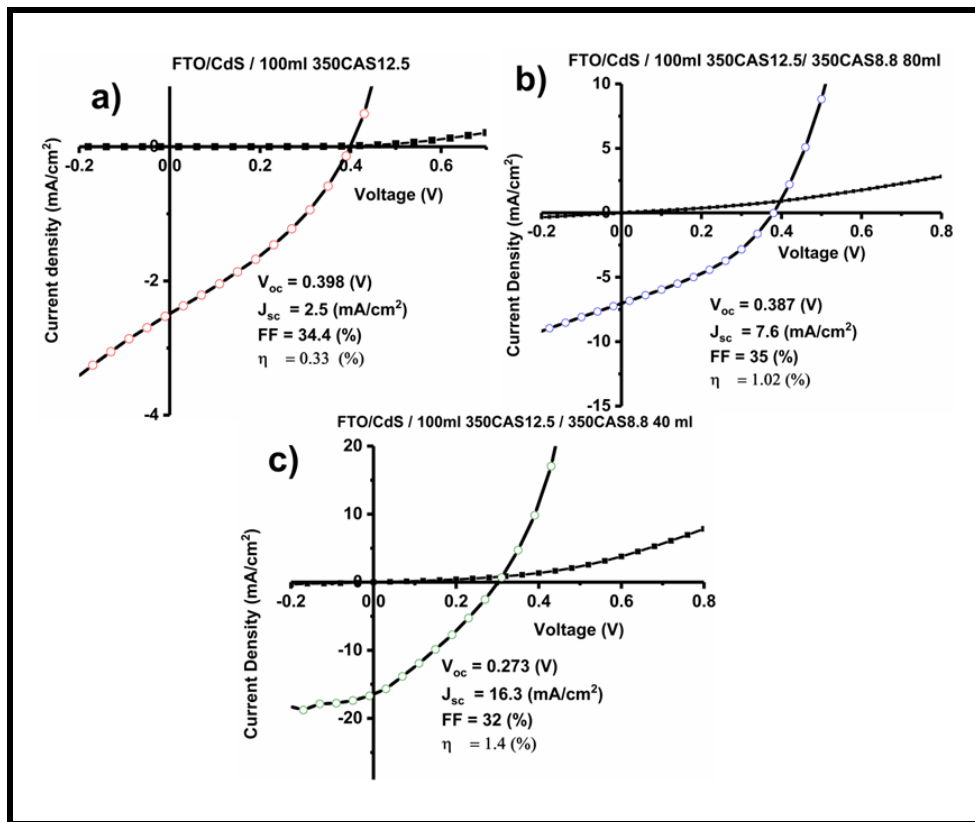
Figure 1 Photovoltaic structures of different configurations using $Cu_{12}Sb_4S_{13}$ thin films.
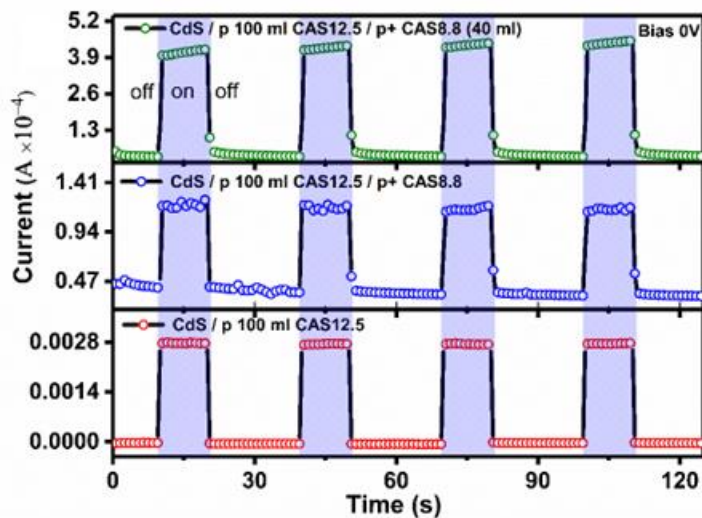

Figure 2. Zero biased photodetection and the respective cyclic measurements showing their photostability under illumination using a halogen lamp.
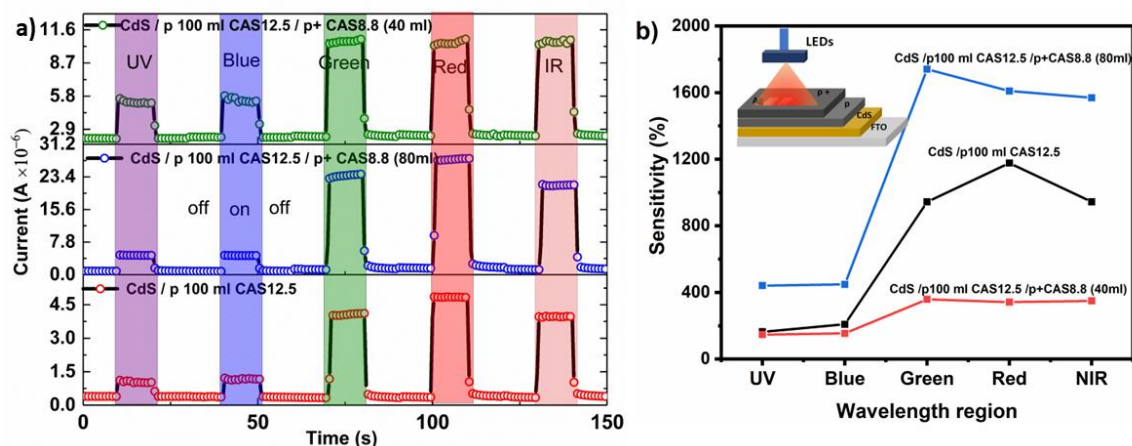
Figure 3 .Self-driven (zero bias) photodiode using the $Cu_{12}Sb_4S_{13}$ thin film deposited on CdS layer b) The photosensitivity value versus the color of LEDs (UV (400nm), blue (465 nm), green (520 nm), red (620 nm) and NIR (740 nm)

Conclusions

Phase pure tetrahedrite ($Cu_{12}Sb_4S_{13}$) thin films were deposited using single step ultrasonic spray pyrolysis at low substrate temperature (200 ℃). Thin films with electrical properties spanning from semi metallic (p) to metallic (p+) nature was deposited . FTO/CdS/p-100mlCAS12.5, FTO/CdS/100mlCAS12.5/CAS8.8 and FTO/CdS/p-$Cu_{12}Sb_4S_{13}$/p+$Cu_{12}Sb_4S_{13}$ configuration was fabricated for photovoltaic and photodetector application. The best recorded efficiency yielding the PCE = 1.4% corresponding to V_{oc}= 0.273 V, J_{sc} = 16.3 mAcm^{-2}, FF = 35%. PV device were analyzed for self driven photodiode in UV-Vis-NIR wavelength**.** This work initiates the incorporation of single step deposition of $Cu_{12}Sb_4S_{13}$ thin films for photovoltaic and photodetection application for sustainable energy conversion and detection.